



THE HONG KONG
POLYTECHNIC UNIVERSITY

香港理工大學

Pao Yue-kong Library

包玉剛圖書館

Copyright Undertaking

This thesis is protected by copyright, with all rights reserved.

By reading and using the thesis, the reader understands and agrees to the following terms:

1. The reader will abide by the rules and legal ordinances governing copyright regarding the use of the thesis.
2. The reader will use the thesis for the purpose of research or private study only and not for distribution or further reproduction or any other purpose.
3. The reader agrees to indemnify and hold the University harmless from and against any loss, damage, cost, liability or expenses arising from copyright infringement or unauthorized usage.

IMPORTANT

If you have reasons to believe that any materials in this thesis are deemed not suitable to be distributed in this form, or a copyright owner having difficulty with the material being included in our database, please contact lbsys@polyu.edu.hk providing details. The Library will look into your claim and consider taking remedial action upon receipt of the written requests.

**HYBRID FRP-CONCRETE-STEEL DOUBLE-SKIN
TUBULAR COLUMNS UNDER STATIC AND
CYCLIC LOADING**

ZHANG BING

Ph.D

The Hong Kong Polytechnic University

2014



THE HONG KONG POLYTECHNIC UNIVERSITY
Department of Civil and Environmental Engineering

**HYBRID FRP-CONCRETE-STEEL
DOUBLE-SKIN TUBULAR COLUMNS UNDER
STATIC AND CYCLIC LOADING**

ZHANG BING

A thesis submitted in partial fulfillment of the requirements for the degree of

Doctor of Philosophy

July 2014

CERTIFICATE OF ORIGINALITY

I hereby declare that this thesis is my own work and that, to the best of my knowledge and belief, it reproduces no material previously published or written, nor material that has been accepted for the award of any other degree or diploma, except where due acknowledgement has been made in the text.

(Signed)

ZHANG BING

(Name of student)

ABSTRACT

This thesis presents a systematic study on the structural behavior of hybrid FRP-concrete-steel double-skin tubular columns (hybrid DSTCs) under static and cyclic loading, with particular attention to the use of high strength concrete (HSC) and the effect of column size. A hybrid DSTC consists of a layer of concrete sandwiched between an outer tube made of FRP and an inner tube made of steel. The FRP tube, with fibers oriented close to the hoop direction, is used to confine the concrete and to enhance the shear resistance of the column. This column form was proposed by Prof. J.G. Teng to achieve excellent durability and ductility (and hence seismic resistance).

Following the introductory and the literature review chapters of the thesis, Chapters 3 and 4 present the first part of the research program concerned with the behavior of concrete filled FRP tubes (CFFTs) under cyclic axial compression. The experimental work included the concrete strength as a key variable, and was designed to supplement the very limited existing research on the cyclic compressive behavior of FRP-confined HSC. Lam and Teng's cyclic stress-strain model was critically assessed using the new test results as well as existing test results. A modified version of Lam and Teng's model, applicable to both normal strength concrete (NSC) and HSC confined with either a wet-layup FRP tube or an FRP filament-wound tube, was then proposed. The proposed model was found to provide reasonably accurate predictions of test data.

Chapters 5 and 6 present the second part of the research program which was concerned with the behavior of hybrid DSTCs filled with NSC/HSC subjected to monotonic/cyclic axial compression. Previous studies on the axial compressive behavior of hybrid DSTCs were generally limited to small-scale specimens (i.e. with a diameter < 200 mm) filled with NSC and confined with a wet-layup FRP tube. The experimental investigation was thus focused on three issues: (1) the effect of using HSC; (2) the effect of using a filament-wound FRP tube; and (3) the effect of specimen size. The test results were compared with Yu *et al.*'s model for static behavior and the stress-strain model presented in Chapter 4 for cyclic behavior. Both models were found to provide reasonably accurate predictions of test results.

Chapters 7 and 8 present the last part of the research program which was focused on the seismic behavior of hybrid DSTCs filled with NSC/HSC. A series of DSTCs were tested under combined axial compression and cyclic lateral loading. The test columns had a relatively large column section (i.e. with a diameter of 300 mm) and a realistically large void ratio (i.e. 0.73) to achieve close representation of real column behavior. The test results indicated that hybrid DSTCs possess excellent ductility and seismic resistance even when HSC with a cylinder compressive strength as high as 120 MPa is used. A numerical column model for DSTCs under combined axial compression and cyclic lateral loading was then developed, whose predictions were found to be in close agreement with the test results.

LIST OF PUBLICATIONS

JOURNAL PAPERS

Yu, T., **Zhang, B.**, Cao, Y.B. and Teng, J.G. (2012). “Behavior of hybrid FRP-concrete-steel double-skin tubular columns subjected to cyclic axial compression”, *Thin-Walled Structures*, 61, 196-203.

Zhang, B., Yu, T. and Teng, J.G. (2014). “Behaviour of concrete-filled FRP tubes under cyclic axial compression”, *Journal of Composites for Construction*, ASCE, 10.1061/(ASCE)CC.1943-5614.0000523, 04014060.

Yu, T., **Zhang, B.** and Teng, J.G. (2014). “Unified stress-strain model for FRP-confined concrete under cyclic axial compression”, *Engineering Structures*, under review.

Zhang, B., Teng, J.G. and Yu, T. (2014). “Experimental behaviour of hybrid FRP-concrete-steel double-skin tubular columns under combined axial compression and cyclic lateral loading”, *Engineering Structures*, under review.

CONFERENCE PAPERS

Zhang, B., Yu, T. and Teng, J.G. (2011). “Axial compression tests on hybrid double-skin tubular columns filled with high strength concrete”, *Proceedings, Third International Postgraduate Conference on Infrastructure and Environment*, 11-12 July, Hong Kong, China, 171-176.

Zhang, B., Teng, J.G. and Yu, T. (2012). “Behaviour of hybrid double-skin tubular columns subjected to combined axial compression and cyclic lateral loading”, *Proceedings, 6th International Conference on FRP Composites in Civil Engineering*, 13-15 June, Rome, Italy, in CD-Rom.

Yu, T., Cao, Y.B., **Zhang, B.** and Teng, J.G. (2012). “Hybrid FRP-concrete-steel double-skin tubular columns: cyclic axial compression tests”, *Proceedings, 6th International Conference on FRP Composites in Civil Engineering*, 13-15 June, Rome, Italy, in CD-Rom.

Zhang, B., Teng, J.G. and Yu, T. (2012). “Hybrid double-skin tubular columns filled with high strength concrete under axial monotonic compression”, *Proceedings, ACUN-Composites and Nanocomposites in Civil, Offshore and Mining Infrastructure*, 14-16 November, Melbourne, Australia, 89-94.

Zhang, B., Yu, T. and Teng, J.G. (2014). “Cyclic axial compression tests on concrete-filled FRP tubes”, *Proceedings, 7th International Conference on FRP Composites in Civil Engineering*, 20-22 August, Vancouver, Canada.

Teng, J.G., Zhang, S.S., Xiao, Q.G., Fernando, D. and **Zhang, B.** (2014). “Performance enhancement of bridges and other structures through the use of fiber-reinforced polymer (FRP) composites: some recent Hong Kong research”, *Proceedings, 7th International Conference on Bridge Maintenance, Safety and Management*, 7-11 July, Shanghai, China, 77-85.

ACKNOWLEDGEMENT

First and most importantly, I would like to express my heartfelt gratitude to my chief supervisor, Prof. Jin-Guang Teng for providing me with this unique opportunity to pursue my PhD study at The Hong Kong Polytechnic University. I sincerely appreciate his continuous inspiration, enlightening guidance and enthusiastic support throughout my study. The experience of being Prof. Teng's student has enriched my life and will certainly benefit me for a life-long time. I also wish to express my sincere thanks to my co-supervisor, Dr. Tao Yu, University of Wollongong, Australia, for his efforts in providing me with extensive chances of discussion and communication, for his guidance in training me in critical thinking and academic writing, and for all his continuous advice and kind encouragement.

Particularly, I am grateful to both the Research Grants Council of the Hong Kong Special Administrative Region (PolyU 5278/07E) and The Hong Kong Polytechnic University for their financial support during my study.

I would also like to express my sincere appreciation to my friends and colleagues in the Department of Civil and Environmental Engineering at The Hong Kong Polytechnic University. Firstly, many thanks go to Dr. Yue-Ming Hu, Mr. Xiao-Liang Fang, Mr. Guan Lin, Mr. Jun-Liang Zhao, Mr. Bing Fu, Dr. Yu-Lei Bai, Ms. Yue-Xin Zhang, Mr. Hang Zhou and Mr. Yu-Bo Cao for their generous help when I was preparing my experiments. Without your kind help, I would have

suffered inevitable delays and could not have finished my experimental study on schedule. I also want to thank Dr. Guang-Ming Chen, Dr. Shi-Shun Zhang, Dr. Dilum Fernando, Dr. Qiong-Guan Xiao, Dr. Wan-Yang Gao and Ms. Pan Xie for their invaluable suggestions and constructive comments for my study which benefited me greatly. I am also very grateful to Mr. Xue-Fei Nie, Mr. Tian-Sheng Shi, Mr. Yi-Nan Yang, Mr. Jun-Jie Zeng, Mr. Jiong-Yi Zhu, Mr. Jie-Kai Zhuo and Mr. Qing-Kai Wang for their help and encouragement. Particularly, I would like to thank Dr. Jian-Guo Dai and Dr. Lik Lam for their valuable suggestions during my research.

I would also want to thank the technicians of the Structural Engineering Research Laboratory of the Department of Civil and Environmental Engineering at The Hong Kong Polytechnic University, especially Mr. K.H. Wong, Mr. M.C. Ng, Mr. Y.H. Yiu, Mr. T.T. Wai and Mr. C.F. Cheung for their valuable advice and kind assistance during my experimental study.

Last but certainly not least, I would like to extend my deepest gratitude to my parents for their unconditional love and care. I would not have made it this far without their everlasting love, support and encouragement.

CONTENTS

CERTIFICATE OF ORIGINALITY	I
ABSTRACT	II
LIST OF PUBLICATIONS	IV
ACKNOWLEDGEMENT	VI
CONTENTS	VIII
LIST OF FIGURES	XVII
LIST OF TABLES	XXIV
NOTATION	XXVI
CHAPTER 1 INTRODUCTION.....	1
1.1 BACKGROUND.....	1
1.1.1 Concrete-Filled FRP Tubes.....	1
1.1.2 Hybrid FRP-Concrete-Steel Double-Skin Tubular Columns.....	3
1.2 RESERARCH OBJECTIVES.....	6
1.3 THESIS LAYOUT.....	7
1.4 REFERENCES.....	11

CHAPTER 2	LITERATURE REVIEW.....	18
2.1	INTRODUCTION.....	18
2.2	FRP COMPOSITES.....	19
2.2.1	Fabrication Methods.....	19
2.2.2	Mechanical Properties.....	21
2.2.2.1	<i>Lamination Theory</i>	21
2.2.2.2	<i>Test Methods</i>	22
2.3	FRP-CONFINED CONCRETE.....	23
2.3.1	FRP-Confined Concrete under Monotonic Axial Loading....	24
2.3.1.1	<i>Design-Oriented Stress-Strain Model</i>	26
2.3.1.2	<i>Analysis-Oriented Stress-Strain Model</i>	30
2.3.2	FRP-Confined Concrete under Cyclic Axial Loading.....	33
2.4	HYBRID FRP-CONCRETE-STEEL DOUBLE-SKIN TUBULAR COLUMNS.....	36
2.4.1	Hybrid DSTCs under Monotonic Axial Loading.....	37
2.4.2	Hybrid DSTCs under Cyclic Axial Loading.....	40
2.4.3	Hybrid DSTCs under Combined Axial Compression and Cyclic Lateral Loading.....	41
2.5	REFERENCES.....	44
CHAPTER 3	BEHAVIOR OF CONCRETE-FILLED FRP TUBES UNDER CYCLIC AXIAL COMPRESSION.....	59
3.1	INTRODUCTION.....	59
3.2	EXPERIMENTAL PROGRAM.....	61
3.2.1	Specimen Details.....	61
3.2.2	Preparation of Specimens.....	62

3.2.3	Material Properties.....	62
3.2.3.1	Concrete.....	62
3.2.3.2	FRP Tubes.....	63
3.2.4	Experimental Set-Up and Instrumentation.....	64
3.2.5	Loading Schemes.....	65
3.3	TEST RESULTS AND DISCUSSIONS.....	66
3.3.1	Test Observations.....	66
3.3.2	Axial Strains.....	66
3.3.3	Hoop Strains.....	68
3.3.4	Axial Load-Axial Strain Behavior of CFFTs.....	69
3.3.5	Axial Stress-Axial Strain Curves of Concrete.....	69
3.3.6	Key Results.....	71
3.4	COMPARISON WITH EXISTING MODELS.....	71
3.4.1	Comparison with Teng <i>et al.</i> 's (2009) Model.....	72
3.4.1.1	Teng <i>et al.</i> 's (2009) Model.....	72
3.4.1.2	Comparison.....	73
3.4.2	Comparison with Lam and Teng's (2009) Model.....	74
3.4.2.1	Lam and Teng's (2009) Model.....	74
3.4.2.2	Comparison.....	75
3.5	CONCLUSIONS.....	76
3.6	REFERENCES.....	78

CHAPTER 4	UNIFIED CYCLIC STRESS-STRAIN MODEL FOR NORMAL AND HIGH STRENGTH CONCRETE CONFINED WITH FRP.....	97
4.1	INTRODUCTION.....	97
4.2	TEST DATABASE.....	99

4.3	CYCLIC AXIAL STRESS-STRAIN MODEL.....	101
4.3.1	General.....	101
4.3.2	Key Characteristics of FRP-Confined Concrete.....	101
4.3.3	Terminology.....	102
4.3.4	Monotonic Stress-Strain Model for the Envelope Curve.....	103
4.3.5	Unloading Path.....	105
4.3.6	Plastic Strain of Envelope Cycles.....	107
4.3.7	Stress Deterioration of Envelope Cycles.....	109
4.3.8	Effect of Loading History.....	111
4.3.8.1	<i>Partial Unloading and Reloading</i>	111
4.3.8.2	<i>Plastic Strain of Internal Cycles</i>	112
4.3.8.3	<i>Stress Deterioration of Internal Cycles</i>	113
4.3.9	Reloading Path.....	115
4.3.10	Summary of the Proposed Model.....	117
4.4	PERFORMANCE OF THE PROPOSED MODEL.....	117
4.4.1	Envelope Unloading/Reloading Curves.....	117
4.4.2	Repeated Unloading/Reloading Curves.....	118
4.5	CONCLUSIONS.....	119
4.6	REFERENCES.....	121

CHAPTER 5 BEHAVIOR OF HYBRID DSTCS UNDER MONOTONIC AXIAL COMPRESSION.....135

5.1	INTRODUCTION.....	135
5.2	EXPERIMENTAL PROGRAM.....	137
5.2.1	Specimen Details.....	137
5.2.2	Preparation of Specimens.....	138
5.2.3	Material Properties	139

5.2.3.1	Concrete.....	139
5.2.3.2	FRP Tubes.....	140
5.2.3.3	Steel Tubes.....	141
5.2.4	Experimental Set-Up and Instrumentation.....	142
5.3	TEST OBSERVATIONS.....	143
5.3.1	General.....	143
5.3.2	Axial Strains.....	145
5.3.3	Hoop Strains.....	147
5.4	BEHAVIOR OF CONFINED CONCRETE.....	147
5.4.1	Axial Load-Axial Strain Curves of Hybrid DSTCs.....	147
5.4.2	Average Axial Stress of Confined Concrete in Hybrid DSTCs.....	150
5.4.3	Effect of Concrete Strength.....	151
5.4.4	Effect of Thickness of FRP Tube.....	151
5.4.5	Effect of Void Ratio.....	152
5.4.6	Effect of Specimen Size.....	153
5.4.7	Comparison between CFFTs and Hybrid DSTCs.....	153
5.4	COMPARISON WITH EXISTING MODEL.....	154
5.4.1	Yu <i>et al.</i> 's (2010) Model for Hybrid DSTCs.....	154
5.4.2	Comparisons with Yu <i>et al.</i> 's (2010) Model.....	156
5.5	CONCLUSIONS.....	157
5.6	REFERENCES.....	159

CHAPTER 6	BEHAVIOR OF HYBRID DSTCS UNDER CYCLIC AXIAL COMPRESSION.....	181
6.1	INTRODUCTION.....	181
6.2	EXPERIMENTAL PROGRAM.....	183

6.2.1	Specimen Details.....	183
6.2.2	Preparation of Specimens.....	184
6.2.3	Material Properties.....	184
6.2.3.1	<i>Concrete</i>	184
6.2.3.2	<i>FRP Tubes</i>	185
6.2.3.3	<i>Steel Tubes</i>	185
6.2.4	Experimental Set-Up and Instrumentation.....	185
6.2.5	Loading Schemes.....	185
6.3	TEST OBSERVATIONS.....	187
6.3.1	General.....	187
6.3.2	Axial Strains.....	187
6.3.3	Hoop Strains.....	188
6.4	BEHAVIOR OF CONFINED CONCRETE.....	189
6.4.1	Axial Load-Axial Strain Curves of Hybrid DSTCs.....	189
6.4.2	Axial Stress-Axial Strain Behavior of Concrete.....	189
6.4.3	Key Results.....	193
6.5	CYCLIC AXIAL STRESS-STRAIN MODEL.....	193
6.5.1	General.....	193
6.5.2	Unloading Path.....	194
6.5.3	Plastic Strain of Envelope Cycles.....	194
6.5.4	Stress Deterioration of Envelope Cycles.....	196
6.5.5	Effect of Loading History.....	196
6.5.5.1	<i>Plastic Strain of Internal Cycles</i>	197
6.5.5.2	<i>Stress Deterioration of Internal Cycles</i>	197
6.5.6	Overall Performance.....	197
6.6	CONCLUSIONS.....	198
6.7	REFERENCES.....	200

CHAPTER 7	BEHAVIOR OF HYBRID DSTCS UNDER COMBINED AXIAL COMPRESSION AND CYCLIC LATERAL LOADING.....	222
7.1	INTRODUCTION.....	222
7.2	EXPERIMENTAL PROGRAM.....	223
7.2.1	Specimen Details.....	223
7.2.2	Preparation of Specimens.....	224
7.2.3	Material Properties.....	225
7.2.3.1	<i>Concrete</i>	225
7.2.3.2	<i>FRP Tubes</i>	226
7.2.3.3	<i>Steel Tubes</i>	226
7.2.4	Testing Frame.....	227
7.2.5	Experimental Set-Up and Instrumentation.....	227
7.2.6	Loading Schemes.....	229
7.3	EXPERIMENTAL RESULTS AND DISCUSSIONS.....	231
7.3.1	General.....	231
7.3.2	Test Observations.....	231
7.3.3	Lateral Load-Lateral Displacement Curves.....	233
7.3.4	Envelope Moment-Curvature Curves.....	234
7.3.5	Curvature Distributions over the Column Height.....	235
7.3.6	Axial Displacement.....	236
7.3.7	Hoop Strain Distributions.....	237
7.3.8	Ductility of Hybrid DSTCs.....	238
7.3.9	Length of Equivalent Plastic Hinge.....	240
7.3.10	Residual Strength of Hybrid DSTCs.....	241
7.4	CONCLUSIONS.....	242
7.5	REFERENCES.....	244

CHAPTER 8	NUMERICAL SIMULATION OF HYSTERETIC BEHAVIOR OF HYBRID DSTCS.....	271
8.1	INTRODUCTION.....	271
8.2	STRESS-STRAIN MODELS.....	272
8.2.1	Confined Concrete in Hybrid DSTCs.....	272
8.2.1.1	<i>Concrete under Cyclic Compression.....</i>	<i>272</i>
8.2.1.2	<i>Concrete under Cyclic Tension.....</i>	<i>275</i>
8.2.1.3	<i>Cyclic Stress-Strain Model for Concrete.....</i>	<i>276</i>
8.2.2	Stress-Strain Model for Steel.....	276
8.2.2.1	<i>Strain Penetration.....</i>	<i>276</i>
8.2.2.2	<i>Steel under Cyclic Tension and Compression.....</i>	<i>278</i>
8.2.3	Stress-Strain Model for FRP.....	279
8.2.3.1	<i>Properties of FRP Tubes.....</i>	<i>279</i>
8.2.3.2	<i>FRP Tubes under Cyclic Tension and Compression.....</i>	<i>279</i>
8.3	NUMERICAL SIMULATIONS.....	280
8.3.1	Remarks on the Experimental Study.....	280
8.3.2	Moment-Curvature Analysis.....	281
8.3.3	Pushover Analysis.....	282
8.3.4	Hysteretic Behavior Analysis.....	284
8.4	CONCLUSIONS.....	284
8.5	REFERENCES.....	286
CHAPTER 9	CONCLUSIONS.....	298
9.1	INTRODUCTION.....	298
9.2	CONCRETE –FILLED FRP TUBES UNDER CYCLIC AXIAL	

COMPRESSION.....	299
9.3 HYBRID DSTCS UNDER MONOTONIC OR CYCLIC AXIAL COMPRESSION.....	301
9.4 HYBRID DSTCS UNDER COMBINED AXIAL COMPRESSION AND CYCLIC LATERAL LOADING.....	303
9.5 FUTURE RESEARCH.....	305
9.6 REFERENCES.....	306

LIST OF FIGURES

CHAPTER 1

Figure 1.1	Cross section of CFFTs.....	17
Figure 1.2	Cross section of hollow steel reinforced concrete columns.....	17
Figure 1.3	Cross section of steel double-skin tubular columns.....	17
Figure 1.4	Cross section of hybrid DSTCs.....	17

CHAPTER 2

Figure 2.1	Flexural and shear strengthening of concrete beams (Motavalli and Czaderski 2007).....	53
Figure 2.2	Seismic retrofitting of concrete columns (Motavalli and Czaderski 2007).....	53
Figure 2.3	FRP tubes fabricated by filament-winding.....	53
Figure 2.4	FRP products fabricated by pultrusion.....	54
Figure 2.5	FRP rebars in new construction (Berg <i>et al.</i> 2006).....	54
Figure 2.6	FRP tubes in new construction (Fam <i>et al.</i> 2003).....	54
Figure 2.7	Classification of stress-strain curves of FRP-confined concrete (from Lam and Teng 2003).....	55
Figure 2.8	Lam and Teng's (2003) model for FRP-confined concrete (from Lam and Teng 2003).....	56
Figure 2.9	Teng <i>et al.</i> 's (2009) model for FRP-confined concrete	

	(from Teng <i>et al.</i> 2009).....	56
Figure 2.10	Hybrid DSTCs under axial compression (Yu 2007).....	56
Figure 2.11	Hybrid DSTCs with HSC under axial compression (Zhang <i>et al.</i> 2011).....	57
Figure 2.12	Large-scale hybrid DSTCs under axial compression (Xie <i>et al.</i> 2011).....	57
Figure 2.13	Hybrid DSTCs with a square outer tube and a circular inner tube under axial compression (Yu and Teng 2013).....	57
Figure 2.14	Hybrid DSTCs under cyclic axial loading (Yu <i>et al.</i> 2012).....	58
Figure 2.15	Hybrid DSTCs subjected to lateral cyclic loading (Qian and Liu 2008).....	58
Figure 2.16	Hybrid DSTCs subjected to lateral cyclic loading (Han <i>et al.</i> 2010).....	58

CHAPTER 3

Figure 3.1	Preparation of specimens.....	84
Figure 3.2	Axial stress-strain behavior of control cylinders.....	84
Figure 3.3	Tensile split-disk test of FRP tubes.....	85
Figure 3.4	Tensile stress-strain curves of FRP tubes in the hoop direction..	85
Figure 3.5	Compression test of FRP tube segment.....	86
Figure 3.6	Axial stress-strain curves of FRP tubes under axial compression.....	86
Figure 3.7	Experimental set-up and instrumentation.....	87
Figure 3.8	Specimens after test.....	88
Figure 3.9	Comparison of axial strains obtained using three different methods.....	89
Figure 3.10	Hoop strain distributions.....	90

Figure 3.11	Typical axial load-axial strain curves of CFFTs.....	91
Figure 3.12	Axial stress-strain curves of concrete.....	92
Figure 3.13	Sudden increase in the hoop strain.....	93
Figure 3.14	Prediction of envelope stress-strain curves with Teng <i>et al.</i> 's (2009) model.....	94
Figure 3.15	Performance of Lam and Teng's (2009) model for envelope unloading/reloading curves.....	95
Figure 3.16	Performance of Lam and Teng's (2009) model for repeated unloading/reloading curves.....	96

CHAPTER 4

Figure 4.1	Key parameters of cyclic stress-strain curves of FRP-confined concrete (after Lam and Teng 2009).....	127
Figure 4.2	Envelope unloading curves.....	128
Figure 4.3	Slope of the unloading path at zero stress.....	129
Figure 4.4	Relationships between plastic strains and envelope unloading strains.....	129
Figure 4.5	Effect of concrete strength on the plastic strain.....	130
Figure 4.6	Performance of equations for the plastic strain of envelope cycles.....	130
Figure 4.7	Performance of equations for the stress deterioration ratio of envelope cycles.....	130
Figure 4.8	Performance of equations for the strain recovery ratio of internal cycles.....	131
Figure 4.9	Performance of equations for the stress deterioration ratio of internal cycles.....	131
Figure 4.10	Performance of the two stress-strain models for envelope	

	unloading/reloading curves: predictions based on the predicted values of $\epsilon_{pl,1}$	132
Figure 4.11	Performance of the two stress-strain models for envelope unloading/reloading curves: predictions based one experimental values of $\epsilon_{pl,1}$	133
Figure 4.12	Performance of the two stress-strain models for repeated internal unloading/reloading curves: predictions based on the experimental values of $\epsilon_{pl,1}$	134

CHAPTER 5

Figure 5.1	Molds of hybrid DSTCs.....	163
Figure 5.2	Cross-sections of different specimens.....	163
Figure 5.3	Axial stress-strain behavior of control cylinders.....	163
Figure 5.4	Tensile split-disk test of FRP tubes.....	164
Figure 5.5	Tensile stress-strain curves of FRP tubes in the hoop direction.....	164
Figure 5.6	Steel tubes after axial compression.....	165
Figure 5.7	Axial stress-axial strain curves of steel tubes.....	165
Figure 5.8	Experimental set-up and instrumentation for hybrid DSTCs of batches 1-3.....	166
Figure 5.9	Experimental set-up and instrumentation for hybrid DSTCs of batches 4-6.....	167
Figure 5.10	Specimens after test.....	168
Figure 5.11	Comparison of axial strains obtained using different methods.....	170
Figure 5.12	Hoop strain distributions.....	171
Figure 5.13	Axial load-axial strain curves of hybrid DSTCs.....	172
Figure 5.14	Development of strains during test: Specimens of Group 1.....	174
Figure 5.15	Development of strains during test: Specimens of Group 2.....	174

Figure 5.16	Development of strains during test: Specimens of Group 3.....	174
Figure 5.17	Damage localization over the cross section.....	175
Figure 5.18	Axial stress-strain curves of concrete.....	175
Figure 5.19	Effect of concrete strength on axial stress-strain curves of concrete.....	176
Figure 5.20	Effect of FRP tube thickness on axial stress-strain curves of concrete.....	177
Figure 5.21	Effect of void ratio on axial stress-strain curves of concrete.....	178
Figure 5.22	Effect of specimen size on axial stress-strain curves of concrete.....	178
Figure 5.23	Comparison of concrete behavior between hybrid DSTCs and CFFTs.....	179
Figure 5.24	Comparison of axial stress-strain curves of concrete with Yu <i>et al.</i> 's (2010) model.....	180

CHAPTER 6

Figure 6.1	Specimens after test.....	205
Figure 6.2	Hoop strain distributions.....	208
Figure 6.3	Axial load-axial strain curves of hybrid DSTCs.....	209
Figure 6.4	Cyclic axial stress-strain curves of concrete obtained using different methods.....	211
Figure 6.5	Cyclic axial stress-strain curves of concrete.....	212
Figure 6.6	Prediction of unloading curves.....	214
Figure 6.7	Relationship between plastic strains and envelope unloading strains.....	215
Figure 6.8	Effect of concrete strength on the plastic strain.....	216

Figure 6.9	Performance of equations for the plastic strain of envelope cycles.....	216
Figure 6.10	Performance of equations for the stress deterioration ratio of envelope cycles.....	216
Figure 6.11	Performance of equations for the strain recovery ratio of internal cycles.....	217
Figure 6.12	Performance of equations for the stress deterioration ratio of internal cycles.....	217
Figure 6.13	Performance of equations for envelope unloading/reloading curves.....	218
Figure 6.14	Performance of equations for repeated unloading/reloading curves.....	220

CHAPTER 7

Figure 7.1	Cross-section of hybrid DSTCs.....	251
Figure 7.2	Preparation of hybrid DSTCs before concrete casting.....	251
Figure 7.3	Axial stress-strain behavior of control cylinders.....	252
Figure 7.4	Experimental set-up.....	252
Figure 7.5	Layout of LVDTs and strain gauges.....	253
Figure 7.6	Planar layout of strain gauges on cross-section.....	253
Figure 7.7	Experimental definition of yield displacement.....	254
Figure 7.8	Cyclic loading schemes.....	254
Figure 7.9	Distributions of axial strains on cross-section in specimen D37-6-0.2.....	255
Figure 7.10	Progress of damage in specimen D37-6-0.2.....	255
Figure 7.11	Specimens after test.....	256
Figure 7.12	Damage to FRP tube, concrete and steel tube.....	258

Figure 7.13	Hysteresis curves under cyclic lateral loading.....	260
Figure 7.14	Effect of concrete strength on envelope moment-curvature curves.....	264
Figure 7.15	Effect of FRP tube thickness on envelope moment-curvature curves.....	265
Figure 7.16	Effect of axial load ratio on envelope moment-curvature curves.....	266
Figure 7.17	Effect of additional concrete infill in the steel tube on envelope moment-curvature curves.....	266
Figure 7.18	Distributions of curvature over the column height.....	267
Figure 7.19	Axial shortening versus lateral displacement during the loading process.....	268
Figure 7.20	Variations of hoop strain with lateral displacement.....	269
Figure 7.21	Definition of the yield displacement.....	270
Figure 7.22	Residual axial strength after cyclic lateral loading.....	270

CHAPTER 8

Figure 8.1	Stress-strain model for confined concrete in hybrid DSTCs.....	288
Figure 8.2	The connection detailing of the inner steel tube.....	289
Figure 8.3	Stress-strain model for reinforcing steel (Teng <i>et al.</i> 2010).....	289
Figure 8.4	The discretization of the column section.....	290
Figure 8.5	Moment-curvature analysis.....	291
Figure 8.6	Numerical models for hybrid DSTCs.....	292
Figure 8.7	Pushover analysis.....	293
Figure 8.8	Hysteretic behavior analysis.....	294

LIST OF TABLES

CHAPTER 3

Table 3.1	Details of specimens.....	82
Table 3.2	Mix proportions of concrete.....	82
Table 3.3	Cyclic loading schemes.....	83
Table 3.4	Key test results.....	83

CHAPTER 4

Table 4.1	Key information of cyclic compression tests in the database....	124
Table 4.2	Linear relationships between unloading strains and plastic strains.....	126

CHAPTER 5

Table 5.1	Details of specimens.....	161
Table 5.2	Dimensions and properties of steel tubes.....	161
Table 5.3	Mix proportions of concrete.....	161
Table 5.4	Properties of concrete.....	162
Table 5.5	Key test results.....	162

CHAPTER 6

Table 6.1	Details of specimens.....	203
Table 6.2	Cyclic loading schemes.....	203
Table 6.3	Key test results.....	204
Table 6.4	Linear relationships between unloading strains and plastic strains.....	204

CHAPTER 7

Table 7.1	Details of specimens.....	248
Table 7.2	Mix proportions of concrete.....	248
Table 7.3	Details of loading schemes.....	249
Table 7.4	Maximum readings of hoop strain gauges on FRP tubes.....	249
Table 7.5	Ductility indices of hybrid DSTCs.....	250

NOTATION

a, b, c	Parameters of equations for unloading curves;
A, B, C	Parameters of equations for reloading curves;
A_c	Area of concrete section;
A_s	Cross-sectional area of steel tube;
D'	Horizontal distance between the tips of two LVDTs in Eq. 7.2;
E_2	Slope of linear second portion of stress-strain curves of confined concrete;
E_c	Elastic modulus of unconfined concrete;
E_s	Elastic modulus of steel;
E_{sec0}	Secant modulus at compressive strength of unconfined concrete;
E_{sec1}	Slope of the initial approximately linear portion of stress-strain curves of FRP tubes under axial compression;
E_{sec2}	Secant elastic modulus at failure for of stress-strain curves of FRP tubes under axial compression;
E_{frp}	Elastic modulus of FRP tube in hoop direction;
$E_{un,0}$	Slope of an unloading path at zero stress;
E_{re}	Slope of linear portion of a reloading curve;
E_{ts}	Stiffness of tensile softening of concrete;

f'_{cc}	Compressive strength of FRP-confined concrete;
f'_{cc}^*	Peak axial stress of confined concrete under a specific constant confining pressure (i.e. actively confined concrete);
f'_{co}	Unconfined concrete strength from standard solid circular cylinder tests;
f'_{cu}	Ultimate stress of FRP-confined concrete;
f_i	Stress of cyclically loaded steel at load reversal in Eq. 6.1;
f_l	Lateral confining pressure provided by FRP tube;
f_o	Intercept of stress axis by the linear second portion of stress-strain curves of FRP-confined concrete;
f_u	Ultimate tensile strength of steel;
f_y	Yield strength of steel;
f_s	Stress of cyclically loaded steel in Eq. 6.1;
f_t	Tensile strength of concrete;
F_{all}	Peak axial load of the entire specimen;
F_c	Peak axial load taken by concrete;
H	Height of hybrid DSTCs under combined axial compression and cyclic lateral loading;
k_p	Plastic strain ratio of cyclically loaded steel in Eq. 6.1;
L_b	Horizontal distance between LVDT-9 and LVDT-10 for hybrid DSTCs under combined axial compression and cyclic lateral loading in Eq. 7.5;
L_p	Length of plastic hinge in Eq. 7.4;
l_{seg}	Length of segment for measuring average curvatures in Eq. 7.2;;

N	Constant axial load applied on column head for hybrid DSTCs under combined axial compression and cyclic lateral loading in Eq. 7.1;
n	Axial load ratio for hybrid DSTCs under combined axial compression and cyclic lateral loading in Eq. 7.1;
n_e	Number of effective cycles;
t_{frp}	Thickness of FRP tube;
t_s	Thickness of steel tube;
ε_c	Axial strain of FRP-confined concrete;
ε_{co}	Axial strain at compressive strength of unconfined concrete;
ε_{cu}	Ultimate axial strain of FRP-confined concrete;
$\varepsilon_{h,rup}$	Hoop rupture strain of FRP tube;
$\varepsilon_{h,rup1}$	Average of all hoop strain gauge readings on an FRP tube;
$\varepsilon_{h,rup2}$	Average of hoop strain gauge readings at mid-height section of an FRP tube;
ε_l	Lateral strain of confined concrete;
ε_t	Axial strain at the transition point of axial stress-axial strain curves of confined concrete;
ε_{cc}^{I*}	Axial strain at peak axial stress of actively confined concrete f_{cc}^{I*} ;
ε_h	Hoop strain of confining material;
ε_i	Yield strain of cyclically loaded steel at load reversal in Eq. 6.1;
ε_n	Initial yield strain of cyclically loaded steel in Eq. 6.1;
ε_p	Plastic strain of cyclically loaded steel in Eq. 6.1;
ε_s	Strain of cyclically loaded steel in Eq. 6.1;
ε_{un}	Unloading strain of an unloading path;

$\varepsilon_{un,env}$	Unloading strain from an envelope curve;
$\varepsilon_{un,n}$	Unloading strain of the n^{th} unloading curve;
$\varepsilon_{un,n+1}$	Unloading strain of the $(n+1)^{\text{th}}$ unloading curve;
ε_{pl}	Plastic strain of concrete;
$\varepsilon_{pl,1}$	Plastic strain of concrete of the envelope unloading curve;
$\varepsilon_{pl,n}$	Plastic strain of concrete of the n^{th} unloading curve;
ε_{re}	Reloading strain of a reloading curve;
ε_{ref}	Reference strain of an unloading curve;
$\varepsilon_{ref,1}$	Reference strain of the first reloading curve;
$\varepsilon_{ref,n}$	Reference strain of the n^{th} reloading curve;
$\varepsilon_{ref,n-1}$	Reference strain of the $(n-1)^{\text{th}}$ reloading curve;
$\varepsilon_{ret,env}$	Envelope returning strain;
ε_{tu}	Ultimate tensile strain of concrete;
ρ_K	Confinement stiffness ratio;
ρ_ε	Strain ratio;
σ_c	Axial stress of concrete;
σ_l	Lateral confining pressure;
σ_{new}	New stress on the reloading path;
$\sigma_{new,1}$	New stress on the first reloading path;
$\sigma_{new,n}$	New stress on the n^{th} reloading path;
$\sigma_{new,n-1}$	New stress on the $(n-1)^{\text{th}}$ reloading path;
σ_{un}	Unloading stress of an unloading path;

$\sigma_{un,1}$	Unloading stress of the envelope unloading curve;
$\sigma_{un,n}$	Unloading stress of the n^{th} unloading curve;
$\sigma_{un,env}$	Unloading stress of the envelope unloading curve;
σ_{re}	Reloading stress of a reloading curve;
$\sigma_{re,1}$	Reloading stress of the envelope unloading curve;
$\sigma_{re,n}$	Reloading stress of the n^{th} unloading curve;
$\sigma_{ret,env}$	Envelope returning stress;
φ	Void ratio of hybrid DSTCs;
ϕ_1	Stress deterioration ratio of the envelope cycle;
ϕ_n	Stress deterioration ratio of the n^{th} reloading curve;
$\phi_{n,ful}$	Stress deterioration ratio for the case of $\beta_{un,n} = 1$;
η	Parameter controlling the rate of change in the degree of non-linearity (i.e. the curvature) of an unloading curve;
β_{un}	Partial unloading factor of an unloading curve;
$\beta_{un,1}$	Partial unloading factor of an envelope unloading curve;
$\beta_{un,n}$	Partial unloading factor of the n^{th} unloading curve;
γ_{re}	Partial reloading factor of the reloading curve;
$\gamma_{re,n}$	Partial reloading factor of the n^{th} reloading curve;
ω_n	Strain recovery ratio;
$\omega_{n,ful}$	Strain recovery ratio for the case of $\gamma_{re,n-1} = 1$ (i.e. full reloading);
μ_δ	Displacement ductility in Eq. 7.3;
δ_u	Ultimate displacement of hybrid DSTCs under combined axial compression and cyclic lateral loading in Eq. 7.3;

δ_y	Yield displacement of hybrid DSTCs under combined axial compression and cyclic lateral loading in Eq. 7.3;
θ_p	Rotation of plastic hinge after column yielding in Eq. 7.4;
θ_u	Rotation of plastic hinge at ultimate displacement δ_u in Eq. 7.4;
θ_y	Rotation of plastic hinge at yield displacement δ_y in Eq. 7.4;
R	Radius of a confined concrete core;
Δ_1, Δ_2	LVDT readings on Side-A and Side-E of a column segment in Eq. 7.2;
Δ_u	Lateral displacement at ultimate condition in Eq. 7.4;
Δ_y	Yield displacement in Eq. 7.4.

CHAPTER 1

INTRODUCTION

1.1 BACKGROUND

1.1.1 Concrete-Filled FRP Tubes

Corrosion of steel reinforcement in concrete structures is the major reason for the deterioration of reinforced concrete structures. To overcome the deterioration problem, extensive research has been conducted on the use of FRP composites in new construction to take advantage of its excellent corrosion resistance. Concrete-filled FRP tubes (CFFTs) (Mirmiran and Shahawy 1997; Fam and Rizkalla 2001a, b) are an attractive form of hybrid compression members combining FRP and concrete in an optimal manner (Figure 1.1). A CFFT consists of an outer FRP tube filled with plain or steel bar-reinforced concrete. The FRP tube is typically manufactured using the filament-winding process (i.e. a filament-wound FRP tube), which is more suitable in real construction than FRP tube fabricated via the wet-layup method. When CFFTs are under axial compression, the concrete is under lateral confinement from the FRP tube which is in tension in the hoop direction. Due to the confinement of the FRP tube, both the strength and the ductility of the concrete can be significantly enhanced. As a result, the two brittle materials (i.e. FRP and concrete) can form a highly ductile compression member, particularly when internal steel reinforcement is also

provided in the longitudinal direction. In addition to excellent ductility and thus excellent seismic resistance, CFFTs also have excellent corrosion resistance; the steel tube is also much lighter than a corresponding steel tube. With these advantages, CFFTs are attractive for use as bridge columns and piles, which are often exposed to harsh environments (e.g. sea water). Many studies (e.g. Mirmiran and Shahawy 1997; Zhang *et al.* 2000; Fam and Rizkalla 2001a, b; Xiao 2004; Burgueño and Bhide 2006; Zhu *et al.* 2006; Ahmad *et al.* 2008; Ji *et al.* 2008; Ozbakkaloglu and Oehlers 2008; Yu and Teng 2011; Zohrevand and Mirmiran 2013) have been conducted on CFFTs in recent years.

As a structural form with a great potential for use in seismic regions, the behavior of CFFTs subjected to cyclic loading is of particular interest. The stress-strain behavior of the confined concrete in CFFTs under cyclic axial compression is particularly important for the accurate modeling of such columns under seismic loading. A number of experimental studies (e.g. Rousakis 2001; Ilki and Kumbasar 2003; Shao *et al.* 2006; Lam *et al.* 2006; Abbasnia and Ziaadiny 2010; Ozbakkaloglu and Akin 2012; Abbasnia *et al.* 2012; Abbasnia *et al.* 2013; Bai *et al.* 2013) have been conducted on the cyclic stress-strain behavior of concrete confined with an FRP wrap with fibers oriented in the hoop direction only, but no systematic experimental study has been concerned with the cyclic behavior of confined concrete in CFFTs with a filament-wound FRP tube. In addition, the shrinkage of the concrete infill in CFFTs may lead to a small initial gap between the FRP tube and the concrete, which can also have adverse effects. To the best of the author's knowledge, the only existing cyclic axial compression test on concrete-filled filament-wound FRP tubes was conducted by Mirmiran and Shahawy (1997), where only one specimen was tested. The behavior of the concrete in CFFTs is complicated by the significant axial stiffness and the Poisson's effect of the FRP tube, and the failure mode of such an FRP tube is also

different from that of an FRP wrap with only hoop fibers. In addition, the possible shrinkage gap between the FRP tube and the concrete may have adverse effects on the effectiveness of confinement.

Against this background, this thesis first presents a systematic study involving both laboratory experiments and theoretical modeling on the behavior of circular CFFTs under cyclic axial compression. The strength of concrete is treated as a key variable in the study as CFFTs offer an excellent opportunity for the use of high strength concrete (HSC) which is effectively confined by the FRP tube. This study on CFFTs was also motivated by the need to understand the cyclic stress-strain behavior of confined normal strength concrete (NSC) or HSC in hybrid FRP-steel concrete double-skin tubular columns (hybrid DSTCs), which is a key issue of the present PhD research program.

1.1.2 Hybrid FRP-Concrete-Steel Double-Skin Tubular Columns

While CFFTs possess several excellent properties as explained above, they are relatively heavy due to their solid section (Figure 1.1). In bridge engineering, reinforced concrete columns with a hollow section (Figure 1.2) are often preferred to reduce the self-weight of bridge piers because the central concrete core makes limited contributions to the resistance of the column when lateral loading is important. Therefore, in a seismic region, a hollow section is preferred as for the same amount of material, a hollow section offers a much greater resistance to lateral loading than a solid section; alternatively, for the same lateral load resistance, a hollow section leads to material savings.

For the reason given above, hollow-section reinforced concrete columns have been widely used in bridge construction. Such columns, however, suffer from

poor corrosion-resistance, especially in a harsh environment; their ductility needs to rely on heavy transverse steel reinforcement, which can be costly and lead to construction inconvenience. The cover concrete can also easily spall off during seismic loading, which compromises the seismic resistance of hollow RC columns. More recently, double-skin steel tubular columns have been explored as a new form of columns; these columns consist of an outer steel tube, an inner steel tube and a concrete infill in between (Figure 1.3). The concrete in such columns can receive confinement from both tubes, but the corrosion problem of the outer steel tube remains. In addition, the outer steel tube, as the main longitudinal reinforcement, is subjected to direct compression when the column is loaded and is thus prone to outward local buckling which may significantly reduce the strength and ductility of the column.

A novel form of structural members has recently been proposed by Teng *et al.* (2004, 2007), namely, hybrid FRP-concrete-steel double-skin tubular columns (hybrid DSTCs) (Figure 1.4). A hybrid DSTC consists of an outer tube made of FRP and an inner tube made of steel, with the space between filled with concrete. Hybrid DSTCs may be constructed in-situ or precast, with the two tubes acting as the stay-in-place form. The fibers in the FRP tube are generally oriented close to the hoop direction to confine the concrete and to enhance the shear resistance of the column. The inner void may be partially filled with concrete if desired. Compared with CCFTs (Figure 1.1), hybrid DSTCs retain the excellent corrosion resistance property but have better ductility as a result of the use of a ductile steel tube as the main longitudinal reinforcement and have lower construction costs as the FRP outer tube, which is used mainly to provide confinement, can be made very thin. Compared with hollow reinforced concrete columns (Figure 1.2), hybrid DSTCs possess better corrosion resistance due to the use of an FRP outer tube and better ductility as the concrete is effectively confined by the two tubes.

Compared with double-skin steel tubular columns (Figure 1.3), hybrid DSTCs not only have superior corrosion resistance, but also have better ductility as local bulking is not a problem for the FRP outer tube with fibers oriented close to the hoop direction.

Existing research on hybrid DSTCs has led to a good understanding of the static behavior of hybrid DSTCs through laboratory testing of small-scale columns constructed with normal strength concrete (NSC) and confined with an FRP tube fabricated using the wet-layup method. The existing work has confirmed that the concrete in this new column form is very effectively confined by the two tubes and the local buckling of the inner steel tube is either delayed or suppressed by the surrounding concrete, leading to a very ductile response (Yu 2007). Most of the work undertaken at The Hong Kong Polytechnic University prior to the project research program can be found in Teng *et al.* (2004), Yu *et al.* (2006), Teng *et al.* (2007), Yu (2007), Wong *et al.* (2008), Teng *et al.* (2010) and Yu *et al.* (2010a, 2010b, 2010c, 2010d). A design approach was proposed and adopted by the Chinese Technical Code for Infrastructure Application of FRP Composites (GB 50608 2010) based on these studies. Hybrid DSTCs have already received significant international attention and positive responses from researchers. Hollaway (2010) introduced this new form of hybrid members in detail in his review paper and commented that it “*is relatively easy to construct and is highly resistant to corrosion and earthquakes*”. Yang and Han (2008) commented that this new member form “*combines the advantages of all three constituent materials and those of the structural form of double-skin tubular columns*”. This novel form of structural members has since been studied by a number of research groups around the world, including Tsinghua University (e.g. Qian and Liu 2006; Liu 2007; Liu and Qian 2007; Qian and Liu 2008; Han *et al.* 2010), Harbin Institute of Technology (Yu 2006; Zhang 2009), Fuzhou University (Xu and Tao

2005; Wang and Tao 2009), the University of Adelaide (e.g. Ozbakkaloglu and Fanggi 2013a, 2013b; Fanggi and Ozbakkaloglu 2013), and the University of Wollongong (e.g. Yu *et al.* 2012; Yu and Teng 2013).

The excellent ductility of hybrid DSTCs means that they are particularly attractive for use in seismic regions. Therefore, their behavior under cyclic loading is of particular interest, which has received rather limited research attention. Existing work has also been focused on small-scale hybrid DSTCs constructed with NSC and confined with a wet-layup FRP tube. For practical applications, studies on large-scale hybrid DSTCs are of great importance for reliable modeling and safe design. Since hybrid DSTCs are highly ductile, and the absence of steel reinforcing bars ensures good-quality casting of HSC, they offer a promising opportunity for the use of HSC which is more brittle than NSC. HSC also facilitates the use of a large void ratio for hybrid DSTCs without compromising the contribution of concrete to its load-carrying capacity. For practical applications, wet-layup tubes cannot be used as the manual layup process is labor intensive and creates challenges for quality control. Therefore, filament-wound FRP tubes should be used together with steel tubes as the stay-in-place form. Against this background, this thesis presents a systematic research program on hybrid DSTCs under static and cyclic loading, with a strong focus on following three issues: the testing of large-scale specimens, the use of HSC, as well as the use of filament-wound FRP tubes.

1.2 RESEARCH OBJECTIVES

The research program presented in this thesis has been carried out with the following specific objectives:

1. To investigate the behavior of CFFTs under cyclic axial compression through an experimental study (Chapter 3);
2. To develop a cyclic stress-strain model that is applicable to both NSC and HSC confined with FRP (Chapter 4);
3. To investigate the behavior of hybrid DSTCs filled with NSC/HSC under monotonic axial compression through an experimental study (Chapter 5);
4. To investigate and model the behavior of hybrid DSTCs filled with NSC/HSC under cyclic axial compression (Chapter 6);
5. To investigate the behavior of hybrid DSTCs subjected to combined axial compression and cyclic lateral loading through an experimental study (Chapter 7);
6. To develop a numerical model for simulating the behavior of hybrid DSTCs subjected to combined axial compression and cyclic lateral loading (Chapter 8).

1.3 THESIS LAYOUT

The thesis consists of 9 chapters. The work presented in each chapter is briefly summarized below.

Chapter 1 explains the background to the research program, outlines the research objectives, and describes the layout of the thesis.

Chapter 2 presents an extensive literature review on topics related to the present study. First, the relevant existing knowledge about FRP composites is briefly reviewed, covering the fabrication methods for FRP composite products and methods for obtaining the mechanical properties of FRP composites. Second, the existing knowledge of FRP-confined concrete is examined in detail, with

particular attention to FRP-confined concrete in circular sections under monotonic/cyclic compression. Last, studies on hybrid DSTCs are briefly reviewed, with an emphasis on hybrid DSTCs under monotonic/cyclic compression, as well as hybrid DSTCs subjected to combined axial compression and cyclic lateral loading.

Chapter 3 presents an experimental study on the behavior of circular CFFTs under cyclic axial compression, where the strength of concrete is a key variable. The experimental program is a much needed supplement to the very limited existing research on the cyclic compressive behavior of FRP-confined HSC. The test results are compared with Teng *et al.*'s (2009) monotonic stress-strain model and Lam and Teng's (2009) cyclic stress-strain model for FRP-confined concrete, both of which have been based on test databases which are limited to concrete confined with an FRP wrap and include only a small number of tests for HSC. The comparisons show that Teng *et al.*'s (2009) monotonic stress-strain model is capable of providing accurate predictions for HSC in CFFTs, provided that the FRP tube has a sufficient circumferential stiffness to ensure a monotonically ascending axial stress-strain curve. The comparisons also show that Lam and Teng's (2009) cyclic stress-strain model may be applicable to NSC in CFFTs, but is not sufficiently accurate for HSC in CFFTs.

Chapter 4 presents a critical assessment of Lam and Teng's (2009) cyclic stress-strain model for FRP-confined concrete against the new test results of CFFTs obtained in Chapter 3 as well as those of FRP-confined concrete with wet-layup FRP tubes which were published after Lam and Teng's (2009) study. Several deficiencies are identified through the critical assessment. A cyclic stress-strain model is then proposed to correct the deficiencies of Lam and Teng's (2009) model, and to provide reasonably accurate predictions for both NSC and

HSC confined with either an FRP wrap or an FRP filament-wound tube.

Chapter 5 is concerned with experimental behavior of hybrid DSTCs under monotonic axial compression. Existing studies on the axial compressive behavior of hybrid DSTCs have generally been limited to small-scale specimens (i.e. with the diameter being smaller than 200 mm) and wet-layup FRP tubes, with only a few exceptions. In particular, there has been no experimental study on large-scale hybrid DSTCs with a filament-wound FRP tube and HSC. This chapter thus presents the first experimental study on large-scale hybrid DSTCs with a filament FRP tube under monotonic axial compression, with a strong focus on the following three issues: (1) the effect of using HSC; (2) the effect of using filament-wound tubes; and (3) the effect of specimen size. The test results are then compared with an existing stress-strain model (Yu *et al.* 2010) which was developed based on results of small-scale hybrid DSTC specimens with NSC and a wet-layup FRP tube. Yu *et al.*'s (2010) model is shown to be capable of providing reasonably accurate predictions for specimens with a bilinear ascending stress-strain curve and specimens with slight fluctuations in the axial stress-strain curve, but to slightly overestimate the results of specimens with a sudden load drop.

Chapter 6 is focused on hybrid DSTCs subjected to cyclic axial compression. Only one study (Yu *et al.* 2012) has been conducted on hybrid DSTCs under cyclic axial compression, and this study was limited to NSC, small-scale specimens (i.e. with the diameter being around 200 mm) and wet-layup FRP tubes. This chapter first presents an experimental study on hybrid DSTCs under cyclic axial compression with a strong focus on the three important issues: the use of HSC, the use of filament-wound tubes, and column size. Comparisons between the test results and the predictions from the cyclic stress-strain model proposed in Chapter

4 for FRP-confined concrete are also presented for the unloading/reloading paths. The comparisons show that the model proposed in Chapter 4 can provide reasonably predictions of the unloading/reloading paths of concrete in hybrid DSTCs.

Chapter 7 presents the first experimental study on hybrid DSTCs filled with HSC subjected to axial compression in combination with cyclic lateral loading. A relatively large column section (with a diameter of 300 mm) was chosen to allow reliable experimental modelling of real columns. The parameters examined include the concrete strength, the confinement stiffness of the FRP tube, and the axial load ratio. The test results indicate that hybrid DSTCs possess excellent ductility and seismic resistance even when HSC with a cylinder compressive of around 120 MPa is used. The test results provide valuable data needed for the formulation and verification of a theoretical model for the seismic behavior of hybrid DSTCs.

In Chapter 8, a numerical model for simulating the seismic behavior of hybrid DSTCs is presented. This numerical model was implemented into the open-source program “Open System for Earthquake Engineering Simulation” (OpenSees 2009) using its force-based “NonLinearBeamColumn” element to consider both geometric nonlinearity and material nonlinearity. The large scale hybrid DSTCs presented in Chapter 7 were simulated using the proposed numerical column model via OpenSees. Predictions of the numerical column model are shown to be in close agreement with the test results.

The thesis is concluded in Chapter 9 with a summary of the main conclusions drawn from previous chapters. Areas for the further research are also outlined.

1.4 REFERENCES

- Abbasnia, R. and Ziaadiny, H. (2010). "Behavior of concrete prisms confined with FRP composites under axial cyclic Compression", *Engineering Structures*, 32, 648-665.
- Abbasnia, R., Ahmadi, R. and Ziaadiny, H. (2012). "Effect of confinement level, aspect ratio and concrete strength on the cyclic stress-strain behavior of FRP-confined concrete prisms", *Composites Part B: Engineering*, 43, 825-831.
- Abbasnia, R., Hosseinpour, F., Rostamian, M. and Ziaadiny, H. (2013). "Cyclic and monotonic behavior of FRP confined concrete rectangular prisms with different aspect ratios", *Construction and Building Materials*, 40, 118-125.
- Ahmad, I., Zhu, Z.Y., Mirmiran, A. and Fam, A.Z. (2008). "Shear strength prediction of deep CFFT beams", *ACI Special Publication, SP-230-61* (CD-ROM), 1085-1102.
- Bai, Y.L., Dai, J.G. and Teng, J.G. (2013). "Cyclic compressive behavior of concrete confined with large rupture strain FRP composites", *Journal of Composites for Construction*, ASCE, 18(1).
- Burgueño, R. and Bhide. K. (2006). "Shear response of concrete-filled FRP composite cylindrical shells", *Journal of Structural Engineering*, ASCE, 132(6), 949-960.
- Fam, A.Z. and Rizkalla, S.H. (2001a). "Confinement model for axially loaded concrete confined by circular fiber-reinforced polymer tubes", *ACI Structural Journal*, 98(4), 451-461.
- Fam, A.Z. and Rizkalla, S.H. (2001b). "Behavior of axially loaded concrete-filled circular fiber-reinforced polymer tubes", *ACI Structural Journal*, 98(3), 280-289.
- Fanggi, B.A.L. and Ozbakkaloglu. T. (2013). "Compressive behavior of aramid

- FRP-HSC-steel double-skin tubular columns”, *Construction and Building Materials*, 48(0), 554-565.
- GB-50608. (2010). *Technical Code for Infrastructure Application of FRP Composites*, China Planning Press, China.
- Han, L.H., Tao, Z., Liao, F.Y. and Xu, Y. (2010). “Tests on cyclic performance of FRP-concrete-steel double-skin tubular columns”, *Thin-Walled Structures*, 48(6), 430-493.
- Hollaway, L.C. (2010). “A review of the present and future utilisation of FRP composites in the civil infrastructure with reference to their important in-service properties”, *Construction and Building Materials*, 24(12), 2419-2445.
- Ilki, A. and Kumbasar, N. (2003). “Compressive behavior of carbon fiber composite jacketed concrete with circular and non-circular cross sections”, *Journal of Earthquake Engineering*, 7(3), 381-406.
- Ji, G., Li, G., Li, X., Pang, S. and Jones, R. (2008). “Experimental study of FRP tube encased concrete cylinders exposed to fire”, *Composite Structures*, 85(2), 149-154.
- Lam, L., Teng, J.G., Cheung, C.H. and Xiao, Y. (2006). “FRP-confined concrete under axial cyclic compression”, *Cement and Concrete Composites*, 28, 949-958.
- Lam, L. and Teng, J.G. (2009). “Stress-strain model for FRP-confined concrete under cyclic axial compression”, *Engineering Structures*, 31(2), 308-321.
- Liu, M.X. (2007). *Studies on Key Behavior of FRP-Concrete-Steel Double Skin Tubular Columns*, PhD Thesis, Tsinghua University. (in Chinese).
- Liu, M.X. and Qian, J.R. (2007). “Moment-curvature relationships of FRP-concrete-steel tubular members”, *Journal of Tsinghua University*, 47(12), 2105-2110. (in Chinese).
- Mirmiran, A. and Shahawy, M. (1997). “Behavior of concrete columns confined

- by fiber composites”, *Journal of Structural Engineering*, ASCE, 123(5), 583-590.
- OpenSees. (2009). *Open System for Earthquake Engineering Simulation*. Pacific Earthquake Engineering Research Center, University of California, Berkeley, <http://opensees.berkeley.edu>.
- Ozbakkaloglu, T. and Oehlers. D. (2008). “Concrete-filled square and rectangular FRP tubes under axial compression”, *Journal of Composites for Construction*, ASCE, 12(4), 469-477.
- Ozbakkaloglu, T. and Akin, E. (2012) “Behavior of FRP-confined normal-and high-strength concrete under cyclic axial compression”, *Journal of Composites for Construction*, ASCE, 16, 451-463.
- Ozbakkaloglu, T. and Fanggi, B.A.L. (2013a). “Axial Compressive Behavior of FRP-Concrete-Steel Double-Skin Tubular Columns Made of Normal-and High-Strength Concrete”, *Journal of Composites for Construction*, ASCE, 18(1).
- Ozbakkaloglu, T. and Fanggi, B.A.L. (2013b). “FRP–HSC–steel composite columns: behavior under monotonic and cyclic axial compression”, *Materials and Structures*, 1-19.
- Qian, J.R. and Liu, M.X. (2006). “Experiment of FRP-concrete-steel double-skin tubular long columns under axial compressive load”, *Journal of Concrete (Theoretical Research)*, 203, 31-34. (in Chinese).
- Qian, J.R. and Liu, M.X. (2008). “Test of seismic behavior of FRP-concrete-steel double-skin tubular columns”, *China Civil Engineering Journal*, 41(3), 29-36. (in Chinese).
- Rousakis, T.C. (2001). *Experimental Investigation of Concrete Cylinders Confined by Carbon FRP Sheets Under Monotonic and Cyclic Axial Compression Load*, Research Report. 01:2, Division of Building Technology, Chalmers University of Technology, Gothenburg, Sweden.

- Shao, Y., Zhu, Z. and Mirmiran, A. (2006). "Cyclic modeling of FRP confined concrete with improved ductility", *Cement and Concrete Composites*, 28(10), 959-968.
- Teng, J.G., Yu, T. and Wong, Y.L. (2004). "Behaviour of hybrid FRP-concrete-steel double-skin tubular columns", *Proceedings, Second International Conference on FRP Composites in Civil Engineering*, 8-10 December, Adelaide, Australia, 811-818.
- Teng, J.G., Yu, T., Wong, Y.L. and Dong, S.L. (2007). "Hybrid FRP-concrete-steel tubular columns: Concept and behavior", *Construction and Building Materials*, 21(4), 846-854.
- Teng, J.G., Jiang, T., Lam, L., and Luo, Y.Z. (2009). "Refinement of a design-oriented stress-strain model for FRP-confined concrete", *Journal of Composites for Construction*, ASCE, 13(4), 269-278.
- Teng, J.G., Yu, T. and Wong, Y.L. (2010). "Hybrid FRP-concrete-steel double-skin tubular structural members", *Proceedings, Fifth International Conference on FRP Composites in Civil Engineering*, 27-29 September, Beijing, China, 26-32.
- Wang, Z.B. and Tao, Z. (2009). "Experimental behaviour of FRP-concrete-steel double-skin tubular beams", *Journal of Industrial Construction*, 39(4), 5-8. (in Chinese).
- Wong, Y.L., Yu, T., Teng, J.G. and Dong, S.L. (2008). "Behavior of FRP confined concrete in annular section columns", *Composites Part B: Engineering*, 39(3), 451-466.
- Xiao, Y. (2004). "Applications of FRP composites in concrete column", *Advances in Structural Engineering*, 7(4), 335-343.
- Xu Y. and Tao, Z. (2005). "Key issues of dynamic behavior of hybrid FRP-concrete-steel double skin tubular columns", *Journal of Fuzhou University (Natural Science)*, 33, 309-315. (in Chinese).

- Yang, Y.F. and Han, L.H. (2008). "Concrete-filled double-skin tubular columns under fire", *Magazine of Concrete Research*, 60(3), 211-222.
- Yu, T., Wong, Y.L., Teng, J.G. and Dong, S.L. (2006). "Flexural behavior of hybrid FRP-concrete-steel double-skin tubular members", *Journal of Composites for Construction*, ASCE, 10(5), 443-452.
- Yu, T. (2007). *Behavior of Hybrid FRP-Concrete-Steel Double-Skin Tubular Columns*, PhD Thesis, The Hong Kong Polytechnic University.
- Yu, T., Teng, J.G., Wong, Y.L. and Dong, S.L. (2010a). "Finite element modelling of confined concrete-I: Drucker-Prager type plasticity model", *Engineering Structures*, 32(3), 665-679.
- Yu, T., Teng, J.G., Wong, Y.L. and Dong, S.L. (2010b). "Finite element modelling of confined concrete-II: Plastic-damage model", *Engineering Structures*, 32(3), 680-691.
- Yu, T., Teng, J.G. and Wong, Y.L. (2010c). "Stress-strain behavior of concrete in hybrid double-skin tubular columns", *Journal of Structural Engineering*, ASCE, 136(4), 379-389.
- Yu, T., Wong, Y.L. and Teng, J.G. (2010d). "Behaviour of hybrid FRP-concrete-steel double-skin tubular columns subjected to eccentric compression", *Advances in Structural Engineering*, 13(5), 961-974.
- Yu, T. and Teng, J.G. (2011). "Design of concrete-filled FRP tubular columns: provisions in the Chinese technical code for infrastructure application of FRP composites", *Journal of Composites for Construction*, ASCE, 15(3), 451-461.
- Yu, T., Zhang, B., Cao, Y.B. and Teng, J.G. (2012). "Behavior of hybrid FRP-concrete-steel double-skin tubular columns subjected to cyclic axial compression", *Thin-Walled Structures*, 61, 196-203.
- Yu, T. and Teng, J.G. (2013). "Behavior of hybrid FRP-concrete-steel double-skin tubular columns with a square outer tube and a circular inner tube subjected to axial compression", *Journal of Composites for Construction*, ASCE, 17(2),

271-279.

Yu, X.W. (2006). *Research on Behaviour of Hybrid CFRP-Concrete-Steel Double-Skin Tubular Columns*, MSc Thesis. Harbin Institute of Technology Shenzhen Graduate School. (in Chinese).

Zhang, B. (2009). *Hybrid FRP-Concrete-Steel Double-Skin Tubular Columns with High Strength Concrete: Stub Column Tests*, MSc Thesis, Harbin Institute of Technology. (in Chinese).

Zhang, D.X., Huang, L.N., Wang, R.G. and Zhao, J.H. (2000). "Experimental research on the mechanical properties of concrete filled FRP tubular column", *Journal of Harbin University of Civil Engineering and Architecture*, 1(33), 73-76.

Zhu, Z., Ahmad, I. and Mirmiran, A. (2006). "Seismic performance of concrete-filled FRP tube columns for bridge substructure", *Journal of Bridge Engineering*, ASCE, 11(3), 359-370.

Zohrevand, P. and Mirmiran, A. (2013). "Seismic response of ultra-high performance concrete-filled FRP tube columns." *Journal of Earthquake Engineering*, 17(1), 155-170.

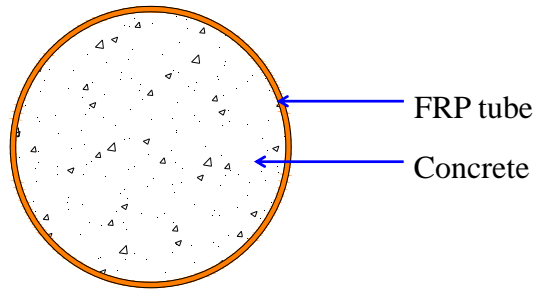


Figure 1.1: Cross section of CFFTs

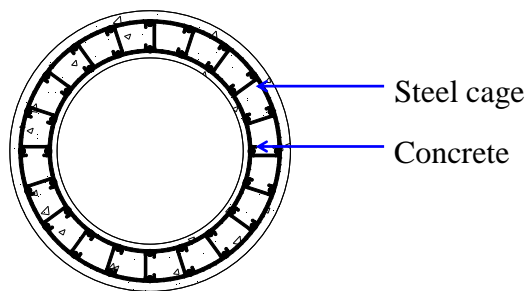


Figure 1.2: Cross section of hollow steel reinforced concrete columns

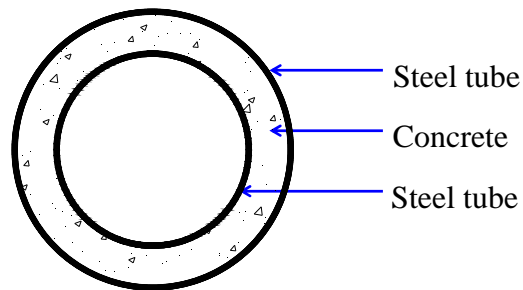


Figure 1.3: Cross section of steel double-skin tubular columns

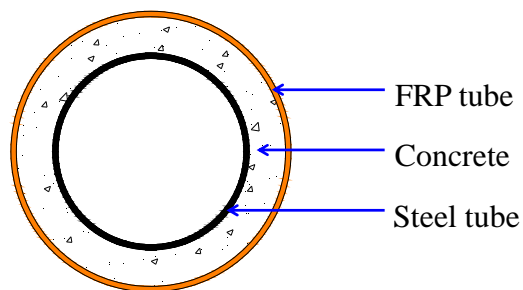


Figure 1.4: Cross section of hybrid DSTCs

CHAPTER 2

LITERATURE REVIEW

2.1 INTRODUCTION

This chapter presents a review of existing knowledge pertinent to hybrid FRP-concrete-steel double-skin tubular columns (hybrid DSTCs). In a hybrid DSTC, the FRP tube, containing fibers oriented close to the hoop direction, offers mechanical resistance primarily in the hoop direction to confine the concrete and to enhance the shear resistance of the column. Therefore, the existing knowledge of FRP composites is first reviewed, including fabrication techniques for FRP composites and products, applications in civil engineering, and methods for obtaining their mechanical properties. As the first part of the present research program was concerned with the experimental behaviour and theoretical modelling of FRP-confined concrete under cyclic axial compression, existing knowledge of FRP-confined concrete is then examined, with particular attention to monotonic stress-strain models and cyclic stress-strain models for FRP-confined concrete. Then, previous studies on hybrid DSTCs under monotonic/cyclic axial compression are summarized, which have generally been limited to small-scale specimens filled with NSC (i.e. with a diameter < 200 mm) and confined with a wet-layup FRP tube. Finally, the very limited existing work on the seismic behavior of hybrid DSTCs subjected to combined axial compression and cyclic lateral loading is briefly discussed.

2.2 FRP COMPOSITES

FRP composites are formed by embedding continuous fibers (e.g. carbon fibers, glass fibers and aramid fibers) in a resin matrix (e.g. epoxy, polyester and vinyl ester resins) which binds the fibers together (Teng *et al.* 2003). FRP composites have many advantages over traditional materials, such as high strength, high stiffness, a long fatigue life, a small density, corrosion resistance, environmental stability and flexibility, etc. The widely used FRP composites include glass FRP (GFRP), carbon FRP (CFRP) and aramid FRP (AFRP).

FRP composites have found many applications in different areas, such as in the aircraft industry (e.g. the fuselage and wings for the Boeing 787 “Dreamliner”), the automobile industry (e.g. the engine hood, dash board and other parts of a car), the energy industry (e.g. the composite blade for a wind turbine tower; insulators in electricity transmission tower), the military industry (e.g. antennae shields for radars; various applications in military vessels and weapons), civil infrastructures (e.g. composite pipes used for water transportation), as well as sports equipment (e.g. badminton bats and tennis bats).

2.2.1 Fabrication Methods

In civil engineering applications, FRP composite products are commonly fabricated in two ways: in-situ fabrication and prefabrication in a factory.

For the retrofitting of an existing structure, the installation of FRP strengthening systems is generally carried out on-site, and the wet-layup method is the more commonly used method for preparing the FRP. In a wet-layup process, fibers or woven fabrics are mixed with a resin material (generally an epoxy resin) for

external bonding to concrete beams (i.e. flexural strengthening or shear strengthening) (Figure 2.1) or for wrapping around existing columns (i.e. enhancing the ductility and seismic behaviour) (Figure 2.2). This method leads to handling flexibility on-site as FRP composites are light in weight and flexible compared with traditional retrofitting materials (e.g. steel plate or steel shells).

Factory prefabrication generally refers to the filament winding and the pultrusion techniques, which produce FRP products with better quality control and are more suitable for mass production. Filament winding is a common fabrication technique for composite cylindrical structures (e.g. FRP tubes), involving the winding of resin-bathed filaments under a certain amount of tension over a cylindrical mould with the fiber volume ratio, the fiber angle and the stacking sequence well controlled (Figure 2.3). The pultrusion technique is a continuous manufacturing process utilized to make profiles with a constant cross-section (e.g. FRP bars, FRP plates or other section forms with fibers only in the longitudinal direction) (Figure 2.4).

With decreases in the cost of raw materials, FRP composites have found increasing applications both in the retrofitting of existing structures [e.g. external bonding of FRP to concrete beams for flexural strengthening or shear strengthening (Figure 2.1); wrapping FRP on columns to enhance their seismic performance (Figure 2.2)] and in constructing new structures [e.g. using FRP bars in reinforced concrete structures (Figure 2.5); using filament-wound FRP tubes to construct FRP-confined concrete columns (Figure 2.6)].

2.2.2 Mechanical Properties

2.2.2.1 Lamination Theory

It is well known that FRP composites possess a linear-elastic stress-strain behaviour when it is loaded in tension in the direction of fibers. The material properties of FRP composites can be estimated based on the classical lamination theory (Daniel and Ishai 1994), in which the mechanical properties of FRP composites are estimated based on the properties of the two constituent materials (i.e. fibers and resin). The analysis process generally includes two steps (Daniel and Ishai 1994): (1) estimating the mechanical properties of an FRP lamina (one plane or curved layer of unidirectional fibers or woven fabric in a resin matrix) based on the material properties of the fibers and the resin; the lamina is an orthotropic material with three principal material axes [the direction of the fibers (longitudinal), the direction normal to the fibers in the plane of the lamina (in-plane transverse) and the direction normal to the plane of lamina]; (2) evaluating the mechanical properties of an FRP laminate (a laminate is made up of two or more unidirectional laminas stacked together at different directions) based on the mechanical properties of a lamina (Yu 2007). The first step is referred to as micro-mechanical analysis and the second step is referred to as macro-mechanical analysis in the classical lamination theory, which is described in detail in Daniel and Ishai (1994).

Based on these analyses, constitutive equations can be derived for FRP composites. It should be noted that, in the lamination theory, the material properties of the fibers and the resin (i.e. Young's moduli, shear moduli, Poisson's ratios, tensile strengths, compressive strengths and shear strengths, etc.) are crucial for estimating the mechanical properties of FRP composites. However,

these basic material properties of the fibers and the resin may be not available to researchers. Thus, difficulties arise in estimating the mechanical properties of FRP composites using this method.

2.2.2.2 Test Methods

Alternatively, the mechanical properties of FRP composites can be assessed by direct experimental testing following well-established test standards for FRP composites. There are various testing standards for FRP composites, such as the test method for determining the in-plane tensile properties of FRP composites given by ASTM D3039/D3039M (2008), the test method for obtaining the in-plane shear response of FRP composites given by ASTM D3518/D3518M (1994), the test method for acquiring the longitudinal compressive properties of FRP tubes given by GB/T 5350 (2005), the test method for determining the apparent hoop tensile strength of plastic or reinforced plastic pipe by the split disk method given by ASTM D2290 (2008), as well as the test method for determining the in-plane compressive properties of FRP composites given by ASTM D3410/D3410M (2003). In the research program presented in the present thesis, the testing standards of ASTM D2290 (2008) and GB/T 5350 (2005) were adopted for determining the hoop tensile properties and the longitudinal compressive properties of filament-wound FRP tubes.

As described in ASTM D2290 (2008), the test specimen shall be a full-diameter, full-wall thickness ring cut from the original pipe. The specimen should then be loaded through a self-aligning split disk apparatus, which applies a tensile force to the ring-shape specimen. An apparent tensile strength rather than a true tensile strength is obtained from this test because some bending exists in the ring during the test at the split of the test fixture. This bending in the ring is caused by the gap

between the two half-circular disk sections induced by the tensile force. Based on the split disk test, the apparent tensile strength of the specimen can be obtained by dividing the tensile force with the section area under tension. By installing bi-directional strain gauge rosettes on the ring specimen, strains can also be obtained, thus the Young's modulus and the Poisson's ratio for the ring can be determined.

In GB/T 5350 (2005), a simple method is given for obtaining the longitudinal compressive properties of FRP tubes by compressing short tube specimens in a universal testing machine. With the installation of bi-directional strain rosettes on the specimen, the compressive strength, the compressive strain, the Young's modulus and the Poisson's ratio can also be determined.

2.3 FRP-CONFINED CONCRETE

In civil engineering, one important application of FRP composites is to provide confinement for concrete, both in the retrofitting of existing reinforced concrete columns using the wet-layup method or in the construction of new columns using filament-wound FRP tubes. In experimental studies on FRP-confined concrete, the following three methods have been used to prepare the FRP jacket: (1) forming of the FRP jacket by manually wrapping and resin impregnation of fiber sheets on hardened concrete as is done in retrofit applications (referred to as wet-layup FRP tubes or FRP wraps) (e.g. Xiao and Wu 2000; Teng and Lam 2004; Yu 2007); (2) prefabrication by manually wrapping and resin impregnation of fiber sheets on a mold which is removed after the resin has cured (referred to as prefabricated wet-layup FRP tubes) (e.g. Ozbakkaloglu and Akin 2012); (3) prefabrication using the filament-winding process (referred to as filament-wound FRP tubes) (e.g. Fam *et al.* 2003). FRP-confined concrete with FRP jackets formed using method (2)

and (3) have also been referred to as concrete-filled FRP tubes (CFFTs), as the concrete is cast into prefabricated FRP tubes.

2.3.1 FRP-Confined Concrete under Monotonic Axial Loading

Over the past two decades, extensive research has been conducted on FRP-confined concrete under monotonic axial compression (e.g. Mirmiran and Shahawy 1997; Karbhari and Gao 1997; Samaan *et al.* 1998; Saafi *et al.* 1999; Spoelstra and Monti 1999; Toutanji 1999; Xiao and Wu 2000; Xiao and Wu 2003; Fam and Rizkalla 2001; Teng and Lam 2002a, 2002b, 2003, 2004; Teng and Lam 2004; Binici 2005; Jiang and Teng 2007; Teng *et al.* 2007; Eid and Paultre 2007; Teng *et al.* 2009; Fahmy and Wu 2010; Xiao *et al.* 2010; Wei and Wu 2012). Detailed reviews of existing studies on FRP-confined concrete in circular sections can be found in Lam and Teng (2002) and Ozbakkaloglu and Lim (2013).

In early studies, the stress-strain model developed for steel-confined concrete (Mander *et al.* 1988) was directly adopted for FRP-confined concrete (e.g. Saadatmanesh *et al.* 1994; Seible *et al.* 1995), which was found to be inadequate in later studies. FRP-confined concrete is different from steel-confined concrete in the nature of behavior. For steel-confined concrete, the lateral confining pressure is constant when the steel is in plastic flow (i.e. active confinement); by contrast, for FRP-confined concrete, the lateral confinement provided by FRP increases continuously with the applied load due to the linear-elastic stress-strain curve of FRP (i.e. passive confinement). When FRP-confined concrete is subjected to axial compression, the concrete expands laterally, which loads the FRP jacket in hoop tension. As a result, the dilation of concrete in FRP-confined concrete can be effectively restrained by the FRP jacket.

The ultimate condition of FRP-confined concrete is reached when the FRP jacket ruptures under hoop tension. It was assumed in early studies (e.g. Samaan *et al.* 1998; Saffi *et al.* 1999; Toutanji 1999) that when the FRP jacket ruptures, its hoop tensile stress is equal to the tensile strength of the FRP material obtained from material tests (i.e. flat coupon tests, ASTM D3039/D3039M 2008). However, subsequent studies showed that the rupture strains/strengths of FRP measured in tests on such FRP-confined concrete cylinders are substantially lower than those obtained from flat coupon tests (e.g. Xiao and Wu 2000; Shahawy *et al.* 2000; Lam and Teng 2003). A systematic study was carried out by Lam and Teng (2004) to clarify this issue, in which three types of tests (i.e. flat coupon tensile tests, FRP ring split-disk tests, and FRP-confined concrete axial compression tests) were conducted to obtain the rupture strain of the FRP jacket. Based on their experimental results, Lam and Teng's (2004) identified three causes for this phenomenon: (1) the deformation localization of cracked concrete; (2) the curvature of the FRP jacket; and (3) the existence of an overlapping zone (for FRP-confined concrete cylinders with the FRP jacket formed using the wet-layup method). It was also recommended by Lam and Teng (2003) that a unified stress-strain model for concrete confined by different types of FRP should be based on the actual hoop rupture strain of the FRP jacket, but not the ultimate tensile strain from flat coupon tests.

It has also been well recognized that FRP-confined concrete has a monotonically ascending bi-linear shape stress-strain curve when the confinement stiffness of the FRP jacket exceeds a certain threshold (referred to as sufficient confinement) (Lam and Teng 2003). In this case, both the compressive strength and the ultimate strain of the confined concrete are reached simultaneously and are significantly enhanced. However, the stress-strain curve may have a post-peak descending branch if the confinement provided by the FRP jacket is insufficient, in which

case the compressive strength is reached before the ultimate strain. As shown in Figure 2.7, three types of stress-strain curves are possible for FRP-confined concrete as classified by Lam and Teng (2003): (a) the increasing type; (b) the decreasing type with $f'_{cu} > f'_{co}$; and (c) the decreasing type with $f'_{cu} < f'_{co}$ (f'_{cu} is the ultimate stress of FRP-confined concrete; and f'_{co} is the unconfined concrete strength).

Many stress-strain models have been proposed for predicting the behavior of FRP-confined concrete, which can be classified into two categories: (a) design-oriented models in closed-form expressions (e.g. Karbhari and Gao 1997; Samaan *et al.* 1998; Saafi *et al.* 1999; Toutanji 1999; Xiao and Wu 2000; Lam and Teng 2003; Xiao and Wu 2003; Teng *et al.* 2009); (b) analysis-oriented models which predict stress-strain curves using an incremental numerical procedure (e.g. Mirmmiran and Shahawy 1996; Spoelstra and Monti 1999; Fam and Rizkalla 2001; Chun and Park 2002; Harries and Kharel 2002; Marques *et al.* 2004; Binici 2005; Jiang and Teng 2007; Teng *et al.* 2007). Ozbakkaloglu *et al.* (2013) presented a comprehensive review and systematic assessment of 88 existing models for FRP-confined concrete in circular sections.

2.3.1.1 Design-Oriented Stress-Strain Models

In design-oriented stress-strain models, the compressive strength, the ultimate axial strain as well as the stress-strain curve of FRP-confined concrete are predicted using closed-form equations based directly on the interpretation and regression analysis of experimental results (Lam and Teng 2003). Therefore, the accuracy of design-oriented models depends heavily on the reliability and the size of the experimental database, as well as the variables or parameters selected for inclusion in the closed-form equations.

Many design-oriented stress-strain models are available in open literature (Yu 2007; Ozbakkaloglu *et al.* 2013). Samman *et al.* (1998) proposed a single complex equation to predict the complete bilinear stress-strain behaviour of FRP-confined concrete in both the axial and the lateral directions. Xiao and Wu (2000) proposed a bilinear stress-strain model with two straight lines based on their own tests on FRP-confined concrete columns together with equations derived from the theory of elasticity. Saafi *et al.*'s (1999) model, modified from Toutanji's (1999) model, approximates the stress-strain curve of FRP-confined concrete with two curved lines. In Lam and Teng (2003), a parabolic first portion together with a linear second portion was proposed to form their model for FRP-confined concrete. Lam and Teng's (2003) model was based on a large database containing test results of 76 FRP-confined concrete specimens assembled from the open literature. Lam and Teng's (2003) model has received extensive citations and numerous positive comments by the international scientific community and has been adopted by the design guidelines/codes of the UK, US and China due to its simplicity and accuracy. Teng *et al.* (2009) formulated a refined version of the design-oriented model proposed by Lam and Teng (2003); this refined version includes more accurate expressions for the ultimate axial strain and the compressive strength.

Lam and Teng's (2003) model for FRP-confined concrete has a parabolic first portion plus a linear second portion with a smooth transition at axial strain ε_t as shown in Figure 2.8. The first parabolic portion is given by:

$$\sigma_c = E_c \varepsilon_c - \frac{(E_c - E_2)^2}{4f'_{co}} \varepsilon_c^2 \quad \text{for } 0 \leq \varepsilon_c \leq \varepsilon_t \quad (2.1)$$

and the linear second portion is given:

$$\sigma_c = f'_{co} + E_2 \varepsilon_c \quad \text{for } \varepsilon_t \leq \varepsilon_c \leq \varepsilon_{cu} \quad (2.2)$$

where σ_c and ε_c are the axial stress and the axial strain of FRP-confined concrete, respectively; f'_{co} and E_c are the compressive strength and the elastic modulus of unconfined concrete, respectively.

The slope of the linear second portion E_2 is given by:

$$E_2 = \frac{f'_{cc} - f'_{co}}{\varepsilon_{cu}} \quad (2.3)$$

where f'_{cc} and ε_{cu} are the compressive strength and the ultimate axial strain of FRP-confined concrete, respectively.

The strain at the transition point ε_t is given by:

$$\varepsilon_t = \frac{2f'_{co}}{E_c - E_2} \quad (2.4)$$

The compressive strength f'_{cc} and ultimate axial strain ε_{cu} of FRP-confined concrete are defined by:

$$\frac{f'_{cc}}{f'_{co}} = \begin{cases} 1 + 3.3 \frac{f_l}{f'_{co}} & f_l/f'_{co} \geq 0.07 \\ 1 & f_l/f'_{co} < 0.07 \end{cases} \quad (2.5)$$

and

$$\frac{\varepsilon_{cu}}{\varepsilon_{co}} = 1.75 + 12 \frac{f_l}{f'_{co}} \left(\frac{\varepsilon_{h,rup}}{\varepsilon_{co}} \right)^{0.45} \quad (2.6)$$

where ε_{co} is the axial strain at the compressive strength of unconfined concrete, and $\varepsilon_{h,rup}$ is the FRP hoop rupture strain obtained from FRP-confined concrete. f_l is the lateral confining pressure provided by the FRP jacket at hoop rupture failure and can be found from:

$$f_l = \frac{E_{frp} t_{frp} \varepsilon_{h,rup}}{R} \quad (2.7)$$

where E_{frp} and t_{frp} are the elastic modulus and thickness of the FRP jacket, and R is the radius of the confined concrete core.

Lam and Teng's (2003) model can yield accurate predictions for FRP-confined concrete with sufficient confinement (defined by them as meeting the condition of $f_l/f'_{co} \geq 0.07$) and it reduces directly to idealized stress-strain curves adopted by existing design codes for unconfined concrete.

As shown in Figure 2.9, Teng *et al.* (2009) refined Lam and Teng's (2003) model based on additional test data and proposed the following equations for the ultimate condition of FRP-confined concrete:

$$\frac{f'_{cc}}{f'_{co}} = \begin{cases} 1 + 3.5(\rho_K - 0.01)\rho_\varepsilon & \rho_K \geq 0.01 \\ 1 & \rho_K < 0.01 \end{cases} \quad (2.8)$$

and

$$\frac{\varepsilon_{cu}}{\varepsilon_{co}} = 1.75 + 6.5\rho_K^{0.8}\rho_\varepsilon^{1.45} \quad (2.9)$$

The ratio between the confining pressure f_l (the pressure provided by the FRP jacket when it fails by rupture due to hoop tensile stresses) and the unconfined concrete strength f'_{co} is referred to as the confinement ratio. The confinement ratio f_l/f'_{co} can be expressed as the product of the confinement stiffness ratio ρ_K and the strain ratio ρ_ε :

$$\frac{f_l}{f'_{co}} = \frac{E_{frp}t_{frp}\varepsilon_{h,rupt}}{f'_{co}R} = \rho_K\rho_\varepsilon \quad (2.10)$$

$$\rho_K = \frac{E_{frp}t_{frp}}{(f'_{co}/\varepsilon_{co})R} \quad (2.11)$$

$$\rho_\varepsilon = \frac{\varepsilon_{h,rupt}}{\varepsilon_{co}} \quad (2.12)$$

Teng *et al.* (2009) also proposed a refinement for the linear second portion after

the smooth transition ε_t as shown in Eq. 2.13, which caters for stress-strain curves with a descending branch as shown in Figure 2.9.

$$\sigma_c = \begin{cases} f'_{co} + E_2 \varepsilon_c & \rho_K \geq 0.01 \\ f'_{co} - \frac{f'_{co} - f'_{cu}}{\varepsilon_{cu} - \varepsilon_{co}} (\varepsilon_c - \varepsilon_{co}) & \rho_K < 0.01 \end{cases} \quad \varepsilon_t \leq \varepsilon_c \leq \varepsilon_{cu} \quad (2.13)$$

It should be noted that f'_{cu} in Eq. 2.13 is found from Eq. 2.14, which predicts the axial stress at the ultimate axial strain, but not the compressive strength f'_{cc} of FRP-confined concrete; actually, the two values are the same unless the stress-strain curve has a descending branch (Teng *et al.* 2009).

$$f'_{cu} = 1 + 3.5(\rho_K - 0.01)\rho_\varepsilon \quad (2.14)$$

2.3.1.2 Analysis-Oriented Stress-Strain Models

In analysis-oriented stress-strain models, the stress-strain curves of FRP-confined concrete are generated via an incremental numerical procedure, in which the responses of the concrete core and the FRP jacket as well as their interaction are considered in an explicit manner. The success of an analysis-oriented model depends on the close representation of the lateral deformation characteristics of unconfined, actively confined, and FRP-confined concrete (Teng *et al.* 2007). Analysis-oriented models are capable of predicting not only the response of sufficiently confined concrete with a bilinear stress-strain curve, but also that of insufficiently confined concrete with a stress-strain curve featuring a descending branch. The majority of analysis-oriented models found in the open literature (e.g. Mirmiran and Shahawy 1996; Spoelstra and Monti 1999; Fam and Rizkalla 2001; Chun and Park 2002; Harries and Kharel 2002; Marques *et al.* 2004; Binici 2005; Teng *et al.* 2007; Jiang and Teng 2007) have been based on active confinement model for concrete, force equilibrium and displacement

compatibility in the radial direction between the FRP jacket and the concrete core (Yu 2007).

The analysis-oriented model proposed by Teng *et al.* (2007) is given by Eqs. 2.15 ~ 2.21, where compressive stresses and strains in the concrete as well as tensile hoop stresses/strains in the FRP jacket are taken to be positive. The peak axial stress f_{cc}^{I*} and the corresponding axial strain ε_{cc}^{I*} of confined concrete under a specific constant confining pressure (i.e. actively confined concrete) can be found from Eq. 2.15 and Eq. 2.16, respectively.

$$\frac{f_{cc}^{I*}}{f_{co}'} = 1 + 3.5 \frac{\sigma_l}{f_{co}'} \quad (2.15)$$

$$\frac{\varepsilon_{cc}^{I*}}{\varepsilon_{co}} = 1 + 1.75 \frac{\sigma_l}{f_{co}'} \quad (2.16)$$

where σ_l is the lateral confining pressure and can be related to the hoop strain ε_h of the confining material by Eq. 2.17, which is further related to the lateral strain of the confined concrete through Eq. 2.18.

$$\sigma_l = \frac{E_{frp} t_{frp} \varepsilon_h}{R} \quad (2.17)$$

$$\varepsilon_h = -\varepsilon_l \quad (2.18)$$

The relationship between the axial strain ε_c and the lateral strain ε_l of confined concrete is described by the following equation:

$$\begin{aligned} \phi \left(\frac{-\varepsilon_l}{\varepsilon_{co}} \right) &= \frac{\varepsilon_c}{\varepsilon_{co}} / \left(1 + 8 \frac{\sigma_l}{f_{co}'} \right) \\ &= 0.85 \left\{ \left[1 + 0.75 \left(\frac{-\varepsilon_l}{\varepsilon_{co}} \right) \right]^{0.7} - \exp \left[-7 \left(\frac{-\varepsilon_l}{\varepsilon_{co}} \right) \right] \right\} \end{aligned} \quad (2.19)$$

The axial stress-strain curve of FRP-confined concrete can then be found from Eqs. 2.20 and 2.21, which was originally proposed by Popovics (1973) and used in Mander *et al.*'s (1998) model for steel-confined concrete.

$$\frac{\sigma_c}{f'_{cc}} = \frac{(\varepsilon_c/\varepsilon'_{cc})r}{r - 1 + (\varepsilon_c/\varepsilon'_{cc})r} \quad (2.20)$$

$$r = \frac{E_c}{E_c - f'_{cc}/\varepsilon'_{cc}} \quad (2.21)$$

The incremental numerical procedure for generating the axial stress-strain curves of FRP-confined concrete using Teng *et al.*'s (2007) model can be described as follows: (1) for a given axial strain of concrete ε_c , the corresponding lateral strain ε_l can be determined with Eq. 2.19; (2) based on the conditions of force equilibrium (Eq. 2.17) and displacement compatibility (Eq. 2.18) in the radial direction between the concrete core and the FRP jacket, the corresponding lateral confining pressure σ_l can be obtained; (3) based on the axial strain ε_c and the obtained lateral confining pressure σ_l , the axial stress f'_{cc} and the corresponding axial strain ε'_{cc} of confined concrete can be found from Eqs. 2.15 and 2.16, respectively; (4) the axial stress σ_c corresponding to the given axial strain ε_c can then be calculated with Eqs. 2.20 and 2.21, and thus a point on the stress-strain curve of FRP-confined concrete is obtained; (5) by repeating steps (1)~(4), the whole stress-strain curves of FRP-confined concrete is generated. The incremental procedure should be terminated when the hoop strain ε_h exceeds the rupture strain of the FRP jacket, $\varepsilon_{h,rupt}$ (Teng *et al.* 2007).

Based on additional test data, Jiang and Teng (2007) presented a thorough assessment of the performance of eight analysis-oriented stress-strain models for FRP-confined concrete (i.e. Mirmmiran and Shahawy 1996; Spoelstra and Monti 1999; Fam and Rizkalla 2001; Chun and Park 2002; Harries and Kharel 2002; Marques *et al.* 2004; Binici 2005; Teng *et al.* 2007). All these models employ an active confinement model as the base model. Teng *et al.*'s (2007) model was identified to be the most accurate model among these eight models, even though it overestimates the axial stress at ultimate axial strain for weakly-confined concrete

and to a lesser extent for moderately-confined concrete. A nonlinear equation for the strain at the peak axial stress (Eq. 2.22) is proposed in Jiang and Teng (2007) to replace Eq. 2.16 in the original model presented in Teng *et al.* (2007). This refinement significantly improved the performance of Teng *et al.*'s (2007) model for weakly-confined concrete. This improved model has also been referred to as Jiang and Teng's (2007) model.

$$\frac{\varepsilon_{cc}^{\prime*}}{\varepsilon_{co}} = 1 + 1.75\left(\frac{\sigma_l}{f'_{co}}\right)^{1.2} \quad (2.22)$$

2.3.2 FRP-Confined Concrete under Cyclic Axial Loading

Columns incorporating FRP-confined concrete have great potential for use in seismic regions. Therefore, the behaviour of FRP-confined concrete under cyclic axial compression is of great interest. A number of studies have been conducted on the cyclic stress-strain behavior of FRP-confined concrete (e.g. Mirmiran and Shahawy 1997; Rodrigues and Silva 2001; Rousakis 2001; Ilki and Kumbasar 2003; Shao *et al.* 2006; Lam *et al.* 2006; Lam and Teng 2009; Abbasnia and Ziaadiny 2010; Abbasnia *et al.* 2012; Wang *et al.* 2012; Ozbakkaloglu and Akin 2012; Abbasnia *et al.* 2013a, 2013b; Bai *et al.* 2013). To the best of the authors' knowledge, only four cyclic stress-strain models have been proposed for FRP-confined concrete in circular columns (i.e. concrete under uniform FRP confinement) (i.e. Shao *et al.* 2006; Lam and Teng 2009; Wang *et al.* 2012; Bai *et al.* 2013).

Shao *et al.* (2006) presented a total of 24 FRP-confined concrete stub columns, which were tested in uniaxial compression with loading and unloading at different displacement levels; the parameters examined included FRP types, the FRP jacket thickness and loading patterns. Based on a regression analysis of their test results,

a stress-strain model was developed (Shao *et al.* 2006). While this model is capable of predicting the reloading paths reasonably closely, it consistently overestimates the plastic strains and can not accurately capture the shape of the unloading paths (Lam and Teng 2006). Shao *et al.*'s (2006) model is also incapable of predicting the cumulative effect of loading history on the plastic strain and the stress deterioration of concrete (Lam and Teng 2006; Ozbakkaloglu and Akin 2012). Wang *et al.* (2012) reported experimental results of 30 CFRP-confined large-scale concrete columns of circular section subjected to monotonic/cyclic axial loading, among which the majority specimens were FRP-confined steel reinforced concrete. A cyclic stress-strain model was proposed for FRP-confined concrete as well as concrete subjected to combined confinement from FRP and hoop steel. This model also does not consider the cumulative effect of repeated loading cycles. Bai *et al.*'s (2013) model is specifically for concrete confined with FRP possessing a large rupture strain (around 6%); it includes most of the components (e.g. unloading/reloading paths) of Lam and Teng's (2009) model but a different envelope stress-strain curve to reflect the effect of this special type of FRP.

Lam and Teng's (2009) cyclic stress-strain model was based on a test database available to them at that time, and was shown to capture all the key characteristics of and provide reasonably accurate predictions for cyclically loaded FRP-confined concrete. Lam and Teng's (2009) model consists of the following major components: (a) a monotonic stress-strain model (Lam and Teng 2003) for FRP-confined concrete to predict the envelope curve; (b) new algebraic expressions for predicting unloading and reloading paths; (c) predictive equations for determining the plastic strain and the stress deterioration of confined concrete. This model caters for all possible unloading/reloading scenarios and can thus be directly used in numerical simulations without additional development (e.g. Teng

et al. 2010). The equations describing the cyclic stress-strain model proposed by Lam and Teng (2009) are described in detail and critically assessed in Chapter 4.

Although Lam and Teng's (2009) model was developed on the basis of a relatively large database, a few significant issues could not be well resolved using the test database available to them at that time. The test database was limited to concrete confined with wet-layup FRP wraps. The calibration of the model for high strength concrete (HSC) was based on a limited amount of test data from one single study (i.e. Rousakis 2001). A recent study by Ozbakkaloglu and Akin (2012) has shown that the performance of Lam and Teng's (2009) model for HSC is not as good as its performance for NSC. In addition, while Lam and Teng's (2009) model has considered the cumulative effect of loading history in their model, their proposed equations were based on limited test data with the maximum number of repeated loading cycles at a given unloading point being three.

Against this background, Chapter 3 presents an experimental study on the behavior of concrete confined with circular FRP tubes under cyclic axial compression, with particular attention to specimens with HSC and the number of repeated loading cycles at a given unloading point. As prefabricated filament-wound FRP tubes were used as the confining material, these specimens are also referred to as CFFTs. This experimental program is a much needed supplement to the very limited existing research on the cyclic compressive behavior of FRP-confined HSC. Furthermore, Chapter 4 presents a critical assessment of Lam and Teng's (2009) model against the new test results as well as those published after Lam and Teng's (2009) work in order to develop an improved cyclic stress-strain model for FRP-confined concrete.

2.4 HYBRID FRP-CONCRETE-STEEL DOUBLE-SKIN TUBULAR COLUMNS

Hybrid DSTCs are a novel form of structural members proposed by Prof. J.G. Teng of The Hong Kong Polytechnic University (PolyU) (Teng *et al.* 2004, 2007). A hybrid DSTC consists of an outer tube made of FRP and an inner tube made of steel, with the space between filled with concrete (Figure 1.4). In Teng *et al.* (2007), the rationale of the new column form with its expected advantages is explained in detail. Since then, a large amount of research has been conducted on this novel form of columns at PolyU (e.g. Teng *et al.* 2004, 2007; Yu 2007; Wong *et al.* 2008; Yu *et al.* 2010a, 2010b; Xie *et al.* 2011) as well as other universities around the world, including Tsinghua University (e.g. Qian and Liu 2006, 2008; Han *et al.* 2010), Harbin Institute of Technology (Yu 2006; Zhang 2009), Fuzhou University (Xu and Tao 2005; Wang and Tao 2009), the University of Adelaide (e.g. Ozbakkaloglu and Fanggi 2013a, 2013b; Fanggi and Ozbakkaloglu 2013), and the University of Wollongong (e.g. Yu *et al.* 2012; Yu and Teng 2013).

At PolyU, a major research program on hybrid DSTCs has been ongoing. This research program covers the following aspects: (1) use of high strength concrete (HSC); (2) use of filament-wound FRP tubes; (3) effect of specimen size; (4) behavior of hybrid DSTCs under cyclic axial compression; and (5) behavior of hybrid DSTCs under combined axial compression and cyclic lateral loading. Existing knowledge of hybrid DSTCs under monotonic/cyclic axial compression, as well as hybrid DSTCs under combined axial compression and cyclic lateral loading are briefly reviewed below.

2.4.1 Hybrid DSTCs under Monotonic Axial Loading

Since the invention of hybrid DSTCs (Teng *et al.* 2004, 2007), a large number of experimental studies have been undertaken by the research group led by Prof. Teng at PolyU. Many aspects of the axial compressive behavior of hybrid DSTCs have been studied, covering the illustration of basic behavior, finite element modelling and the development of a stress-strain model for the confined concrete in hybrid DSTCs (e.g. Teng *et al.* 2004, 2007; Yu 2007; Wong *et al.* 2008; Yu *et al.* 2010a, 2010b; Zhang *et al.* 2011; Xie *et al.* 2011).

Yu's (2007) PhD thesis presents the first systematic study of hybrid DSTCs, in which 18 small-scale hybrid DSTC specimens with a characteristic diameter (the outer diameter of the annular concrete section) of 152.5 mm and a height of 305 mm were tested under monotonic axial compression (Figure 2.10). These specimens had wet-layup FRP tubes and had concrete cylinder strengths ranging from 36.7 MPa ~ 46.7 MPa. The experimental investigation and the modelling work conducted by Yu (2007) can also be found in a number of papers (Teng *et al.* 2004, 2007; Wong *et al.* 2008; Yu *et al.* 2010a, 2010b; Yu and Teng 2013). Teng *et al.* (2004) introduced the new hybrid column with the first series of stub column tests under monotonic axial compression. In Teng *et al.* (2007), the rationale of the new column form together with its expected advantages is explained. The test results given in Teng *et al.* (2007) confirmed that the concrete in this new form of columns is very effectively confined by the two tubes and the local buckling of the inner steel tube is either delayed or suppressed by the surrounding concrete, leading to a very ductile response. Wong *et al.* (2008) presented a systematic experimental study on hybrid DSTCs and compared their behavior with that of two other types of columns (i.e. FRP-confined solid columns and FRP-confined hollow columns), which showed that the presence of an inner void reduces the

beneficial effect of external FRP confinement, but the loss of confinement effectiveness can almost be completely compensated for through the provision of a suitable inner steel tube. Yu *et al.* (2010a) examined the behavior of confined concrete in hybrid DSTCs using a finite-element model to investigate the effects of several key parameters on stress-strain behavior (i.e. the stiffness of the FRP tube, the stiffness of the steel tube, and the size of the inner void). A simple stress-strain model for confined concrete in hybrid DSTCs was then proposed based on both experimental results and finite-element results for practical use (Yu *et al.* 2010a). Based on these investigations, a design approach was proposed and adopted by the Chinese Technical Code for Infrastructure Application of FRP Composites (GB 50608 2010).

Zhang *et al.* (2011) presented the first series of axial compression tests on hybrid DSTCs with high strength concrete (HSC), where six hybrid DSTCs were tested (characteristic diameter: 204 mm; height: 400 mm; concrete strength: 83.5 MPa; wet-layup FRP tubes). Zhang *et al.*'s (2011) test results indicated that hybrid DSTCs with HSC can still possess excellent ductility if the FRP tube has a sufficiently large hoop strain capacity (Figure 2.11).

Xie *et al.* (2011) presented the first study on the axial compressive behavior of large-scale hybrid DSTCs, where three specimens were tested (characteristic diameter: 400 mm; height: 800 mm; concrete strengths: 29.3 MPa~40.1 MPa; wet-layup FRP tubes). Xie *et al.*'s (2011) tests confirmed the excellent ductility of large-scale hybrid DSTCs (Figure 2.12).

Yu and Teng (2013) presented the first ever study on hybrid DSTCs with a square outer tube and a circular inner tube (width of square concrete cross-section: 150 mm; height: 300 mm; concrete strength: 37.5 MPa; wet-layup FRP tubes). In

practical applications, square hybrid DSTCs may be needed for aesthetic reasons. The experimental results showed that the concrete in these square hybrid DSTCs is effectively confined by the two tubes, and the behavior of confined concrete is similar to that of concrete in FRP-confined square columns (Figure 2.13).

Hybrid DSTCs have also attracted research attentions from other researchers (e.g. Qian and Liu 2008; Ozbakkaloglu and Fanggi 2013a, 2013b; Fanggi and Ozbakkaloglu 2013). In Qian and Liu (2008), 10 hybrid DSTCs [characteristic diameter: 190 mm; height: 500 mm; concrete strengths: 23.7 MPa~32.5 MPa; filament-wound FRP tubes (with fibers at ± 60 or ± 80 degrees to the longitudinal axis)] were tested, and the results showed that FRP tubes with ± 80 degrees fibers lead to better performance.

In Ozbakkaloglu and Fanggi (2013a, 2013b) and Fanggi and Ozbakkaloglu (2013), three series of tests were conducted on small-scale hybrid DSTCs (characteristic diameter: 150 mm; height: 300 mm; concrete strengths: 36.7 MPa ~113.8 MPa; prefabricated wet-layup FRP tubes). In Ozbakkaloglu and Fanggi (2013a, 2013b), the effect of additional concrete infill in the inner steel tube, was studied as an important parameter. The filling of the inner steel tube with concrete resulted in a small decrease in the ultimate axial strain and a small increase in the ultimate stress of confined concrete in hybrid DSTCs. Fanggi and Ozbakkaloglu (2013) presented another experimental study on hybrid DSTCs with AFRP tubes. One pair of hybrid DSTCs in their tests was fabricated with a square inner steel tube. From their experimental study, it was found that, the confinement to the concrete in hybrid DSTCs with a square inner steel tube is less effective than that in corresponding hybrid DSTCs with a circular inner steel tube.

The above review indicates that existing studies on the axial compressive

behavior of hybrid DSTCs have generally been limited to small-scale specimens (i.e. with the characteristic diameter being smaller than 200 mm) and wet-layup FRP tubes, with only a few exceptions. In particular, there has been no experimental study on large-scale hybrid DSTCs built with a filament-wound FRP tube and HSC. As part of the on-going programme of hybrid DSTCs in PolyU, a systematic experimental campaign on hybrid DSTCs under monotonic axial compression was completed as part of the research program presented in this PhD thesis, with a strong focus on three issues: (1) the use of HSC; (2) the use of filament-wound FRP tubes; and (3) the testing of large-scale specimens.

2.4.2 Hybrid DSTCs under Cyclic Axial Loading

To the best of the author's knowledge, only two studies have been conducted on hybrid DSTCs under cyclic axial compression (i.e. Yu *et al.* 2012; Ozbakkaloglu and Fanggi 2013b), and no cyclic stress-strain model has been developed for the confined concrete in hybrid DSTCs yet.

Yu *et al.* (2012) presented the first ever study on the behavior of circular hybrid DSTCs under cyclic axial compression (Figure 2.14). In total, 6 identical hybrid DSTCs filled with NSC (characteristic diameter: 205 mm; height: 400 mm; concrete strength: 43.9 MPa; wet-layup FRP tubes) were tested under cyclic axial compression following three different loading schemes (i.e. full unloading/reloading; partial unloading; partial reloading); two specimens were prepared for each loading scheme. The experimental results showed that hybrid DSTCs are very ductile under cyclic loading and their envelope axial load-strain curve is almost the same as the corresponding monotonic axial stress-strain curve. It has also been shown that repeated unloading/reloading cycles have a cumulative detrimental effect on the permanent strain and the stress deterioration of confined

concrete in hybrid DSTCs. Yu *et al.* (2012) also presented comparisons between the test results and predictions from two existing stress-strain models. Yu *et al.*'s (2010) monotonic stress-strain model was found to provide acceptable but conservative predictions of the experimental envelope curves of these hybrid DSTCs. Yu *et al.* (2012) also confirmed that Lam and Teng's (2009) cyclic stress-strain model provides reasonably accurate predictions of the experimental unloading/reloading cycles.

Ozbakkaloglu and Fanggi (2013b) reported cyclic compression tests on six small-scale hybrid DSTCs with additional concrete infill in the steel inner tube (characteristic diameter: 150 mm; height: 300 mm; concrete strengths: 42.5 MPa and 82.4 MPa; prefabricated wet-layup FRP tubes). The study was only concerned with hybrid DSTCs with an inner void, so Ozbakkaloglu and Fanggi's (2013b) work is not further discussed in this PhD thesis.

Against this background, an experimental study on hybrid DSTCs under cyclic axial compression was undertaken as part of the present PhD research program, and the results are presented later in this thesis. The study was focused on the following three aspects: (1) the use of HSC; (2) the use of filament-wound FRP tubes; and (3) the testing of large-scale specimens.

2.4.3 Hybrid DSTCs under Combined Axial Compression and Cyclic Lateral Loading

The excellent ductility of hybrid DSTCs means that they are particularly attractive for use in seismic regions. Therefore, their behavior under cyclic lateral loading is of significant interest. Existing work on the seismic behavior of hybrid DSTCs has been rather limited. To the best of the authors' knowledge, only Qian and Liu

(2008) and Han *et al.* (2010) conducted cyclic lateral loading tests on small-scale hybrid DSTCs (i.e. with the characteristic diameter of the columns being smaller than 200 mm) constructed with NSC. Both of them suffer from significant limitations, although they also provided useful conclusions for the planning of the present experimental programme.

Qian and Liu's (2008) study employed cantilever specimens with a characteristic diameter of 194 mm and a height (the distance between the loading point and the upper surface of the footing) of 1000 mm, leading to a shear-span ratio of 5.15 (Figure 2.15). Filament-wound FRP tubes were used to construct the column specimens. FRP tubes with fibers oriented at both ± 60 degrees and ± 80 degrees were used, leading to the conclusion that the latter tubes were more effective in confining the concrete than the former tubes. A number of void ratios were covered by the test programme, but only the largest void ratio used (0.74) is realistically large. However, due to the small column diameter, the annular concrete layer in columns with a void ratio of 0.74 was only 25 mm, which can create difficulties with concrete casting. The concrete strength was not a parameter in the study: the concrete cylinder compressive strengths ranged from around 36 to around 42 MPa (converted from their cube tests by a factor of 0.79). Despite these limitations, their study did confirm that hybrid DSTCs possess excellent seismic performance as the outer FRP tube provides effective confinement to the inner concrete and prevents the concrete from spalling during cyclic lateral loading.

In Han *et al.*'s (2010) study, eight hybrid DSTCs were tested, including four columns with a square section and another four columns with a circular section. All specimens had a concrete cylinder compressive strength of around 38 MPa (converted from their cube tests by a factor of 0.79). These specimens were tested

horizontally with two pinned ends under a vertical cyclic load. The four circular columns had a characteristic diameter of 150 mm and a length of 1500, leading to a shear-span ratio of 5.0 (Figure 2.16). The FRP tube for these columns were made via the wet-layup process from bi-directional carbon fiber sheets with nearly the same material properties in the hoop and the longitudinal directions, which is a significant shortcoming of these tests in terms of understanding the behavior of real columns which are likely to have FRP tubes with the fibres oriented close to the hoop direction to achieve better structural performance. These circular columns had a void ratio of 0.5, which is also far smaller than desirable values in practice (from around 0.7 to 0.8). When the void ratio is 0.5, only a quarter of the concrete is removed compared to a solid section, and the steel tube is too close to the centre to be effective in resisting bending actions.

To address the limitations of the studies conducted by Qian and Liu (2008) and Han *et al.* (2010) as mentioned above, an experimental study was planned and executed as part of the present PhD research program. The following aspects were taken into account in the planning of the experimental study: (1) hybrid DSTCs filled with HSC should be the focus as the two previous studies were limited to DSTCs filled with NSC; (2) all DSTCs should have a realistically large void ratio (between 0.7 and 0.8); (3) a reasonably large section size should be used so that the concrete layer is not too small for concrete casting even with a realistically large void ratio; (4) filament-wound GFRP tubes with fibers oriented close to the hoop direction should be used; (5) self-compacting concrete should be used to enhance the casting quality of concrete and given that self-compacting concrete is also a likely option in real projects. Numerical simulations of the seismic behavior of hybrid DSTCs has not been attempted before, so a numerical simulation study was also planned as part of the present PhD research program.

2.5 REFERENCES

- Abbasnia, R. and Ziaadiny, H. (2010). "Behavior of concrete prisms confined with FRP composites under axial cyclic Compression", *Engineering Structures*, 32, 648-665.
- Abbasnia, R., Ahmadi, R. and Ziaadiny, H. (2012). "Effect of confinement level, aspect ratio and concrete strength on the cyclic stress-strain behavior of FRP-confined concrete prisms", *Composites Part B: Engineering*, 43, 825-831.
- Abbasnia, R., Hosseinpour, F., Rostamian, M. and Ziaadiny, H. (2013a). "Cyclic and monotonic behavior of FRP confined concrete rectangular prisms with different aspect ratios", *Construction and Building Materials*, 40, 118-125.
- Abbasnia, R., Hosseinpour, F., Rostamian, M. and Ziaadiny, H. (2013b). "Effect of corner radius on stress-strain behavior of FRP confined prisms under axial cyclic compression", *Engineering Structures*, 40, 529-535.
- ASTM D2290-08. (2008). *Standard Test Method for Apparent Hoop Tensile Strength of Plastic or Reinforced Plastic Pipe by Split Disk Method*, American Society for Testing and Materials (ASTM), Philadelphia, USA.
- ASTM D3039/D3039M-08. (2008). *Standard Test Method for Tensile Properties of Polymer Matrix Composite Materials*, American Society for Testing and Materials (ASTM), Philadelphia, USA.
- ASTM D3410/D3410M-03. (2003). *Standard Test Method for Compressive Properties of Polymer Matrix Composite Materials with Unsupported Gage Section by Shear Loading*, American Society for Testing and Materials (ASTM), Philadelphia, USA.
- ASTM D3518/D3518M-94. (1994). *Standard Test Method for In-Plane Shear Response of Polymer Matrix Composite Materials by Tensile Test of a $\pm 45^\circ$ Laminate*, American Society for Testing and Materials (ASTM), Philadelphia,

USA.

- Bai, Y.L., Dai, J.G. and Teng, J.G. (2013). “Cyclic compressive behavior of concrete confined with large rupture strain FRP composites”, *Journal of Composites for Construction*, ASCE, 18(1).
- Berg, A.C., Bank, L.C., Oliva, M.G. and Russell, J.S. (2006). “Construction and cost analysis of an FRP reinforced concrete bridge deck”, *Construction and Building Materials*, 20(8), 515-526.
- Binici, B. (2005). “An analytical model for stress-strain behavior of confined concrete”, *Journal of Structural Engineering*, ASCE, 27(7), 1040-1051.
- Chun, S.S. and Park, H.C. (2002). “Load carrying capacity and ductility of RC columns confined by carbon fiber reinforced polymer”, *Proceedings, 3rd International Conference on Composites in Infrastructure* (CD-Rom).
- Daniel, I.M. and Ishai, O. (2006). *Engineering Mechanics of Composite Materials*, New York, N.Y. Oxford University Press.
- Eid, R. and Paultre, P. (2007). “Plasticity-based model for circular concrete columns confined with fibre-composite sheets”, *Engineering Structures*, 29(12), 3301-3011.
- Fahmy, M. and Wu, Z. (2010). “Evaluating and proposing models of circular concrete columns confined with different FRP composites”, *Composites Part B: Engineering*, 41(3), 199-213.
- Fam, A.Z. and Rizkalla, S.H. (2001). “Confinement model for axially loaded concrete confined by circular fiber-reinforced polymer tubes”, *ACI Structural Journal*, 98(4), 451-461.
- Fam, A., Pando, M., Filz, G. and Rizkalla, S. (2003). “Precast piles for Route 40 bridge in Virginia using concrete filled FRP tubes”, *PCI journal*, 48(3), 32-45.
- Fanggi, B.A.L. and Ozbakkaloglu, T. (2013). “Compressive behavior of aramid FRP–HSC–steel double-skin tubular columns”, *Construction and Building*

- Materials*, 48, 554-565.
- GB-50608. (2010). *Technical Code for Infrastructure Application of FRP Composites*, China Planning Press, China.
- Han, L.H., Tao, Z., Liao, F.Y. and Xu, Y. (2010). “Tests on cyclic performance of FRP-concrete-steel double-skin tubular columns”, *Thin-Walled Structures*, 48(6), 430-493.
- Harries K.A. and Kharel, G. (2002). “Behavior and modeling of concrete subject to variable confining pressure”, *ACI Materials Journal*, 99(2), 180-189.
- Ilki, A. and Kumbasar, N. (2003). “Compressive behavior of carbon fiber composite jacketed concrete with circular and non-circular cross sections”, *Journal of Earthquake Engineering*, 7(3), 381-406.
- Jiang, T. and Teng, J.G. (2007). “Analysis-oriented stress-strain models for FRP-confined concrete”, *Engineering Structures*, 29(11), 2968-2986.
- Karbhari, V.M. and Gao, Y. (1997). “Composite jacketed concrete under uniaxial compression-verification of simple design equations”, *Journal of Materials in Civil Engineering*, ASCE, 9(4), 185-193.
- Lam, L. and Teng, J.G. (2002). “Strength models for fiber-reinforced plastic-confined concrete”, *Journal of Structural Engineering*, ASCE, 128(5), 612-623.
- Lam, L. and Teng, J.G. (2003). “Design-oriented stress-strain model for FRP-confined concrete”, *Construction and Building Materials*, 17(6), 471-489.
- Lam, L. and Teng, J.G. (2004). “Ultimate Condition of Fiber Reinforced Polymer-Confined Concrete”, *Journal of Composites for Construction*, ASCE, 8, 539-548.
- Lam, L. and Teng, J.G. (2006). “FRP-confined concrete under axial cyclic compression”, *Cement and Concrete Composites*, 28(10), 949-958.
- Lam, L. and Teng, J.G. (2009). “Stress-strain model for FRP-confined concrete

- under cyclic axial compression”, *Engineering Structures*, 31(2), 308-321.
- Mander, J.B., Priestley, M.J.N. and Park, R. (1988). “Theoretical stress–strain model for confined concrete”, *Journal of Structural Engineering*, ASCE, 114(8), 1804-1826.
- Marques, S.P.C., Marques D.C.D.S.C., Lins, da. Silva. J. and Cavalcante, M.A.A. (2004). “Model for analysis of short columns of concrete confined by fiber-reinforced polymer”, *Journal of Composites for Construction*, ASCE, 8(4), 332-340.
- Mirmiran, A. and Shahawy, M. (1996). “A new concrete-filled hollow FRP composite column”, *Composites Part B: Engineering*, 27B(3),263-268.
- Mirmiran, A. and Shahawy, M. (1997). “Behavior of concrete columns confined by fiber composites”, *Journal of Structural Engineering*, ASCE, 123(5), 583-590.
- Motavalli, M. and Czaderski, C. (2007). “FRP composites for retrofitting of existing civil structures in Europe: state-of-the-art review”, *Proceedings, International Conference of Composites and Polycon*, American Composites Manufacturers Association, Tampa, FL, USA.
- Ozbakkaloglu, T. and Akin, E. (2012). “Behavior of FRP-confined normal-and high-strength concrete under cyclic axial compression”, *Journal of Composites for Construction*, ASCE, 16, 451-463.
- Ozbakkaloglu, T. and Lim, J.C. (2013). “Axial compressive behavior of FRP-confined concrete: Experimental test database and a new design-oriented model”, *Composites Part B: Engineering*, 55, 607-634.
- Ozbakkaloglu, T., Lim, J. C. and Vincent, T. (2013). “FRP-confined concrete in circular sections: review and assessment of stress–strain models”, *Engineering Structures*, 49, 1068-1088.
- Ozbakkaloglu, T. and Fanggi, B.A.L. (2013a). “Axial Compressive Behavior of FRP-Concrete-Steel Double-Skin Tubular Columns Made of Normal-and

- High-Strength Concrete”, *Journal of Composites for Construction*, ASCE, 18(1).
- Ozbakkaloglu, T. and Fanggi, B.A.L. (2013b). “FRP-HSC-steel composite columns: behavior under monotonic and cyclic axial compression”, *Materials and Structures*, 1-19.
- Popovics, S. (1973). “A numerical approach to the complete stress-strain curve of concrete”, *Cement and Concrete Research*, 3(5), 583-599.
- Qian, J.R. and Liu, M.X. (2006). “Experiment of FRP-concrete-steel double-skin tubular long columns under axial compressive load”, *Journal of Concrete (Theoretical Research)*, 203, 31-34. (in Chinese).
- Qian, J.R. and Liu, M.X. (2008). “Test of seismic of FRP-concrete-steel double-skin tubular columns”, *China Civil Engineering Journal*, 41(3), 29-36. (in Chinese).
- Rodrigues, C.C. and Silva, M.G. (2001). “The behavior of GFRP reinforced concrete columns under monotonic and cyclic axial compression”, *Composites in Constructions: Proceedings of International Conference*, A.A. Balkema, Lisse, Netherlands, 245-250.
- Rousakis, T.C. (2001). “Experimental investigation of concrete cylinders confined by carbon FRP sheets under monotonic and cyclic axial compression load”, *Research Report. 01:2*, Div. of Building Technology, Chalmers Univ. of Technology, Gothenburg, Sweden.
- Saadatmanesh, H., Ehsani, M.R. and Li, M.W. (1994). “Strength and ductility of concrete columns externally reinforced with fiber composite straps”, *ACI Structural Journal*, 91(4), 434-447.
- Saafi, M., Toutanji, H.A. and Li, Z. (1999). “Behavior of concrete columns confined with fiber reinforced polymer tubes”, *ACI Materials Journal*, 96(4), 500-509.
- Samaan, M., Mirmiran, A. and Shahawy, M. (1998). “Modeling of concrete

- confined by fiber composites”, *Journal of Structural Engineering*, ASCE, 124(9), 1025-1031.
- Seible, F., Burgueno, A., Abdallah, M.G. and Nuismer, R. (1995). “Advanced composites carbon shell system for bridge columns under seismic loads”, Proceedings, *National Seismic Conference on Bridges and Highways*, San Diago, USA.
- Shahawy, M., Mirmiran, A. and Beitelman. T. (2000). “Tests and modeling of carbon-wrapped concrete columns”, *Composites Part B: Engineering*, 31(6), 471-480.
- Shao, Y., Zhu, Z. and Mirmiran, A. (2006). “Cyclic modeling of FRP confined concrete with improved ductility”, *Cement and Concrete Composites*, 28(10), 959–968.
- Spoelstra, M.R. and Monti, G. (1999). “FRP-confined concrete model”, *Journal of Composites for Construction*, ASCE, 3(3), 143-150.
- Teng, J.G. and Lam, L. (2002). “Compressive behavior of carbon fiber reinforced polymer confined concrete in elliptical columns”, *Journal of Structural Engineering*, ASCE, 128(12), 1535-1543.
- Teng, J.G., Chen, J.F., Smith, S.T. and Lam, L. (2003). “Behaviour and strength of FRP-strengthened RC structures: a state-of-the-art review”, *Proceedings of the Institution of Civil Engineering Structures and Buildings*, 156(1), 51-62.
- Teng, J.G., Yu, T. and Wong, Y.L. (2004). “Behaviour of hybrid FRP-concrete-steel double-skin tubular columns”, *Proceedings, Second International Conference on FRP Composites in Civil Engineering*, 8-10 December, Adelaide, Australia, 811-818.
- Teng, J. G., Huang, Y. L., Lam, L. and Ye, L. P. (2007). “Theoretical model for fiber reinforced polymer-confined concrete”, *Journal of Composites for Construction*, ASCE, 11(2), 201-210.
- Teng, J.G., Yu, T., Wong, Y.L. and Dong, S.L. (2007). “Hybrid FRP-concrete-steel

- tubular columns: concept and behavior”, *Construction and Building Materials*, 21(4), 846-854.
- Teng, J.G., Jiang, T., Lam, L. and Luo, Y.Z. (2009). “Refinement of a design-oriented stress-strain model for FRP-confined concrete”, *Journal of Composites for Construction*, ASCE, 13(4), 269-278.
- Teng, J.G., Yu, T. and Wong, Y.L. (2010). “Hybrid FRP-concrete-steel double-skin tubular structural members”, *Proceedings, Fifth International Conference on FRP Composites in Civil Engineering*, 27-29 September, Beijing, China, 26-32.
- Toutanji, H.A. (1999). “Stress-strain characteristics of concrete columns externally confined with advanced fiber composite sheets”, *ACI Materials Journal*, 96(3), 397-404.
- Wang, Z.B. and Tao, Z. (2009). “Experimental behaviour of FRP-concrete-steel double-skin tubular beams”, *Journal of Industrial Construction*, 39(4), 5-8. (in Chinese).
- Wang, Z.Y., Wang, D.Y., Simth, S.T. and Lu, D.G. (2012). “Experimental testing and analytical modeling of CFRP-confined large circular RC columns subjected to cyclic axial compression”, *Engineering Structures*, 40, 67-74.
- Wei, Y.Y. and Wu, Y.F. (2012). “Unified stress-strain model of concrete for FRP-confined columns”, *Construction and Building Materials*, 26(1), 381-392.
- Wong, Y.L., Yu, T., Teng, J.G. and Dong, S.L. (2008). “Behavior of FRP confined concrete in annular section columns”, *Composites Part B: Engineering*, 39(3), 451-466.
- Xiao, Q.G., Teng, J.G. and Yu, T. (2010). “Behavior and modeling of confined high-strength concrete”, *Journal of Composites for Construction*, ASCE, 14(3), 249-259.
- Xiao, Y. and Wu, H. (2000). “Compressive behavior of concrete confined by

- carbon fiber composite jackets”, *Journal of Materials in Civil Engineering*, ASCE, 12(2), 139–146.
- Xiao, Y. and Wu, H. (2003). “Compressive behavior of concrete confined by various types of FRP composites jackets”, *Journal of Reinforced Plastics and Composites*, 22(13), 1187-1202.
- Xie, P., Yu, T., Wong, Y.L. and Teng, J.G. (2011). “Compressive behavior of large-scale hybrid FRP-concrete-steel double-skin tubular columns”, *Advanced Materials Research*, 243, 1138-1144.
- Xu, Y. and Tao, Z. (2005). “Key issues of dynamic behavior of hybrid FRP-concrete-steel double skin tubular columns”, *Journal of Fuzhou University (Natural Science)*, 33, 309-315. (in Chinese).
- Yu, T., Wong, Y.L., Teng, J.G. and Dong, S.L. (2006). “Flexural behaviour of hybrid FRP-concrete-steel double-skin tubular members”, *Journal of Composites for Construction*, ASCE, 10(5), 443-452.
- Yu, T. (2007). *Behavior of Hybrid FRP-Concrete-Steel Double-Skin Tubular Columns*, PhD Thesis, The Hong Kong Polytechnic University.
- Yu, T., Teng, J.G. and Wong, Y.L. (2010a). “Stress-strain behavior of concrete in hybrid double-skin tubular columns”, *Journal of Structural Engineering*, ASCE, 136(4), 379-389.
- Yu, T., Wong, Y.L. and Teng, J.G. (2010b). “Behaviour of hybrid FRP-concrete-steel double-skin tubular columns subjected to eccentric compression”, *Advances in Structural Engineering*, 13(5), 961-974.
- Yu, T., Teng, J.G., Wong, Y.L. and Dong, S.L. (2010c). “Finite element modelling of confined concrete-I: Drucker-Prager type plasticity model”, *Engineering Structures*, 32(3), 665-679.
- Yu, T., Teng, J.G., Wong, Y.L. and Dong, S.L. (2010d). “Finite element modelling of confined concrete-II: Plastic-damage model”, *Engineering Structures*, 32(3), 680-691.

- Yu, T. and Teng, J.G. (2011). “Design of concrete-filled FRP tubular columns: provisions in the Chinese technical code for infrastructure application of FRP composites”, *Journal of Composites for Construction*, ASCE, 15(3), 451-461.
- Yu, T., Zhang, B., Cao, Y.B. and Teng, J.G. (2012). “Behavior of hybrid FRP-concrete-steel double-skin tubular columns subjected to cyclic axial compression”, *Thin-Walled Structures*, 61, 196-203.
- Yu, T. and Teng, J.G. (2013). “Behavior of hybrid FRP-concrete-steel double-skin tubular columns with a square outer tube and a circular inner tube subjected to axial compression”, *Journal of Composites for Construction*, ASCE, 17(2), 271-279.
- Yu, X.W. (2006). *Research on Behaviour of Hybrid CFRP-Concrete-Steel Double-Skin Tubular Columns*, MSc Thesis, Harbin Institute of Technology Shenzhen Graduate School. (in Chinese).
- Zhang, B. (2009). *Hybrid FRP-Concrete-Steel Double-Skin Tubular Columns with High Strength Concrete: Stub Column Tests*, MSc Thesis, Harbin Institute of Technology. (in Chinese).
- Zhang, B., Yu, T. and Teng, J.G. (2011). “Axial compression tests on hybrid double-skin tubular columns filled with high strength concrete”, *Proceedings, Third International Postgraduate Conference on Infrastructure and Environment*, 11-12 July, Hong Kong, China, 171-176.



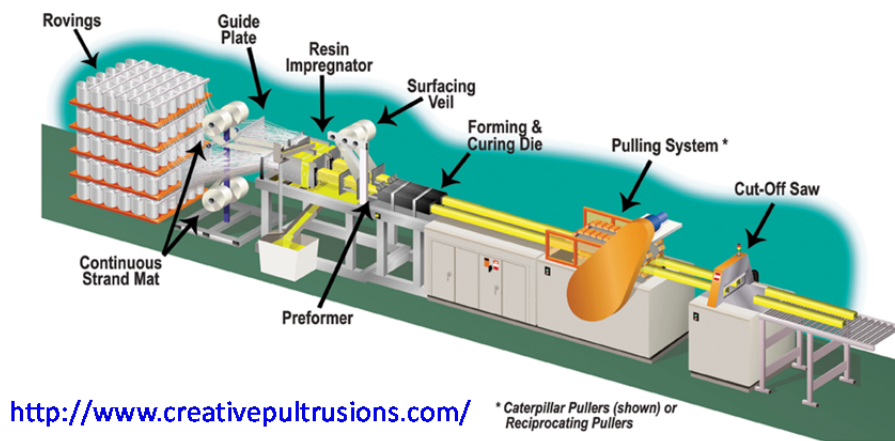
Figure 2.1: Flexural and shear strengthening of concrete beams
(Motavalli and Czaderski 2007)



Figure 2.2: Seismic retrofitting of concrete columns
(Motavalli and Czaderski 2007)



Figure 2.3: FRP tubes fabricated by filament-winding



<http://www.fastecinternational.com/>

Figure 2.4: FRP products fabricated by pultrusion

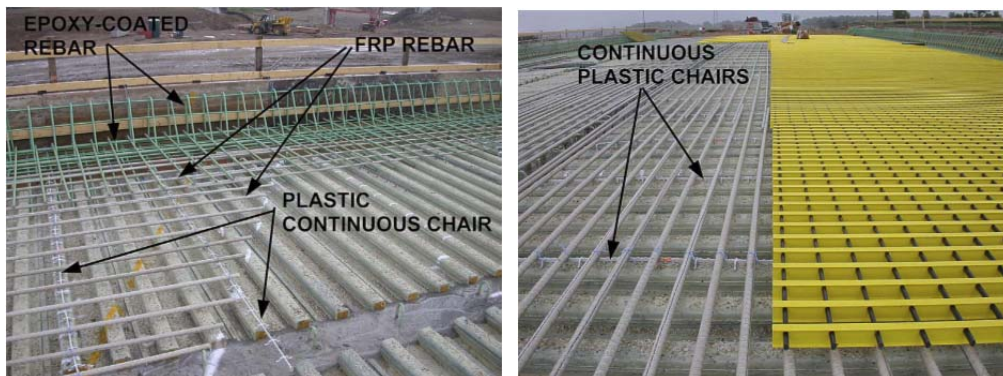
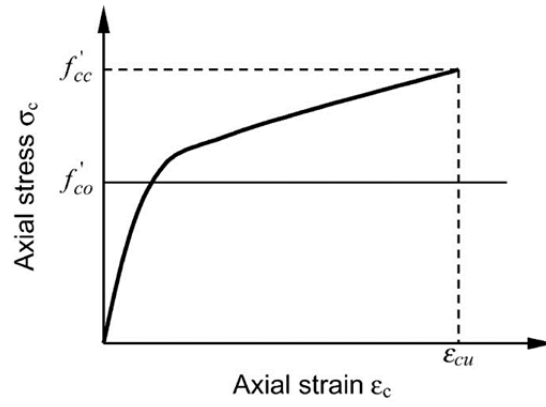


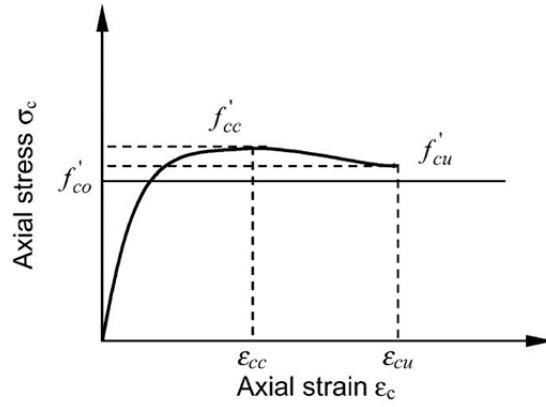
Figure 2.5: FRP rebars in new construction (Berg *et al.* 2006)



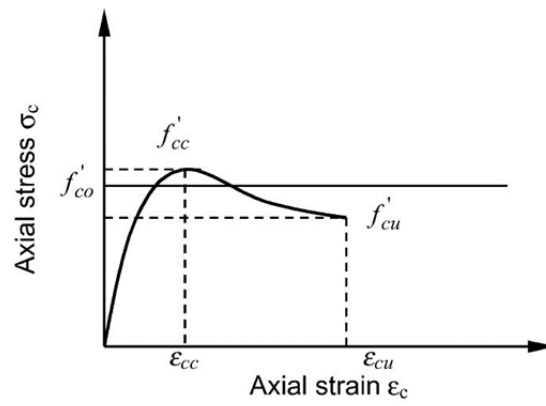
Figure 2.6: FRP tubes in new construction (Fam *et al.* 2003)



(a) Increasing type



(b) Decreasing type with $f'_{cu} > f'_{co}$



(c) Decreasing type with $f'_{cu} < f'_{co}$

Figure 2.7: Classification of stress-strain curves of FRP-confined concrete (from Lam and Teng 2003)

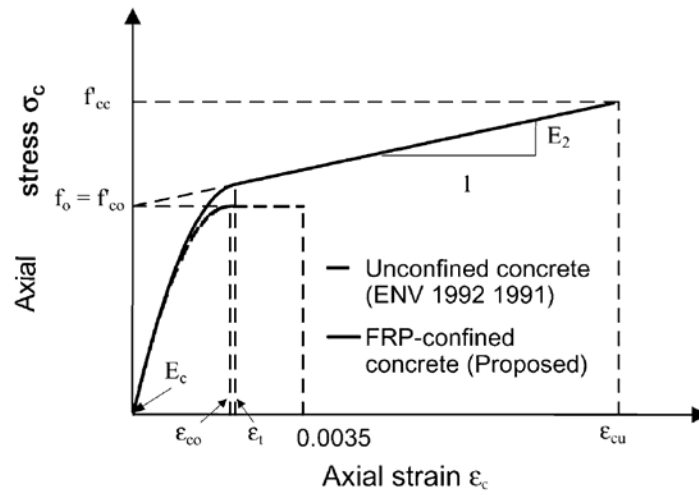


Figure 2.8: Lam and Teng's (2003) model for FRP-confined concrete (from Lam and Teng 2003)

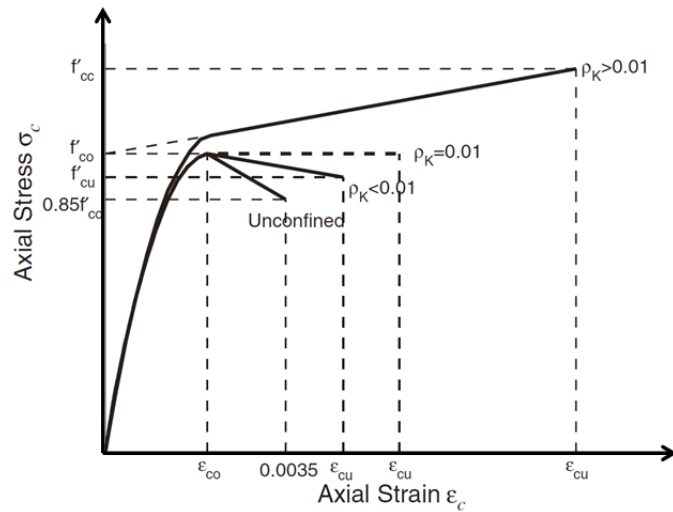


Figure 2.9: Teng *et al.*'s (2009) model for FRP-confined concrete (from Teng *et al.* 2009)

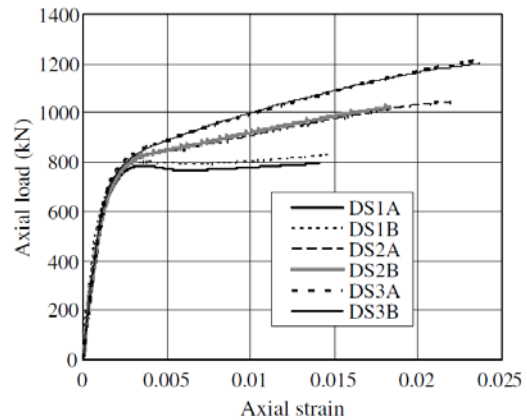


Figure 2.10: Hybrid DSTCs under axial compression (Yu 2007)

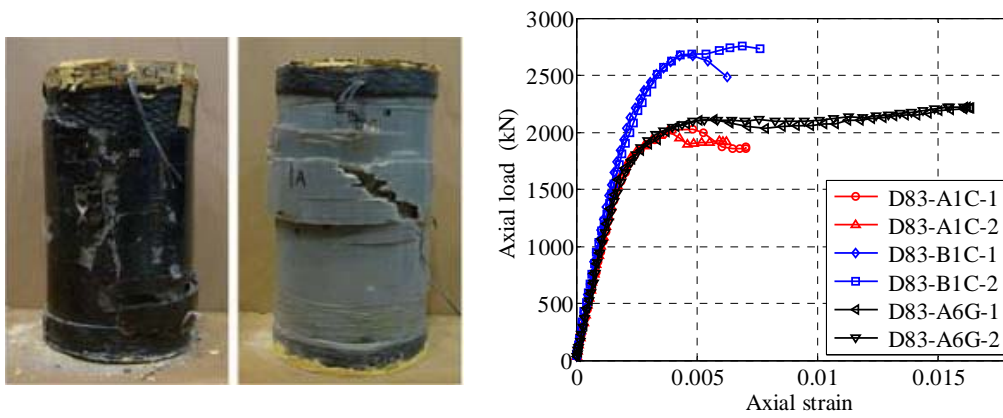


Figure 2.11: Hybrid DSTCs with HSC under axial compression (Zhang *et al.* 2011)

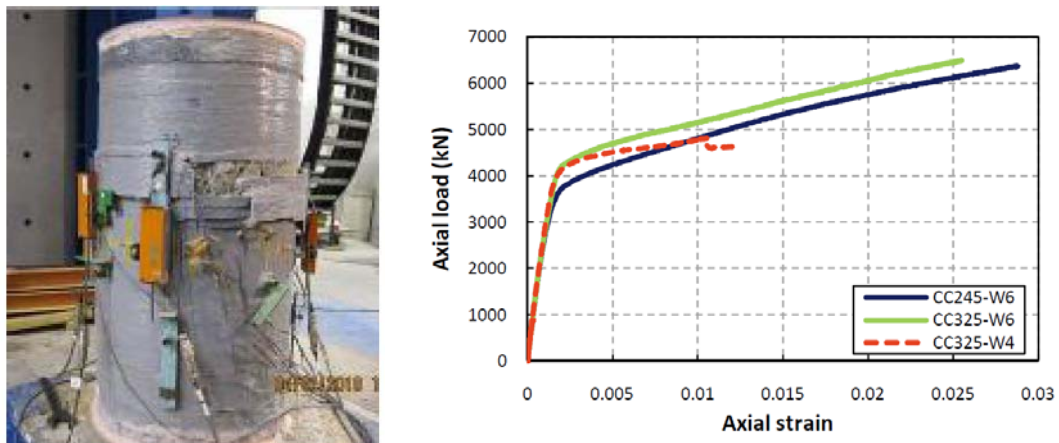


Figure 2.12: Large-scale hybrid DSTCs under axial compression (Xie *et al.* 2011)

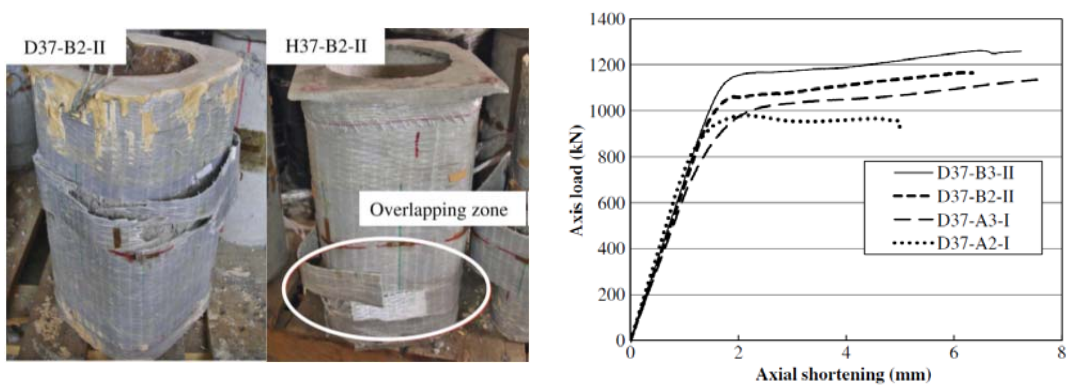


Figure 2.13: Hybrid DSTCs with a square outer tube and a circular inner steel tube under axial compression (Yu and Teng 2013)

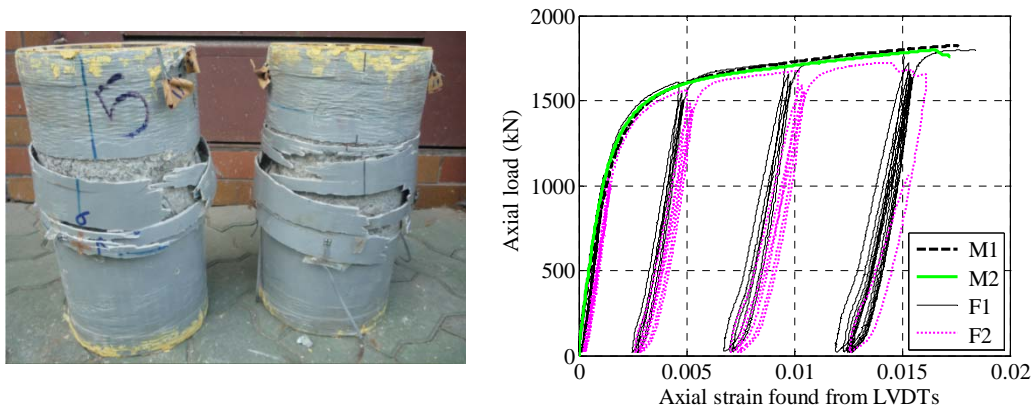


Figure 2.14: Hybrid DSTCs under cyclic axial loading
(Yu *et al.* 2012)



Figure 2.15: Hybrid DSTCs subjected to lateral cyclic loading
(Qian and Liu 2008)

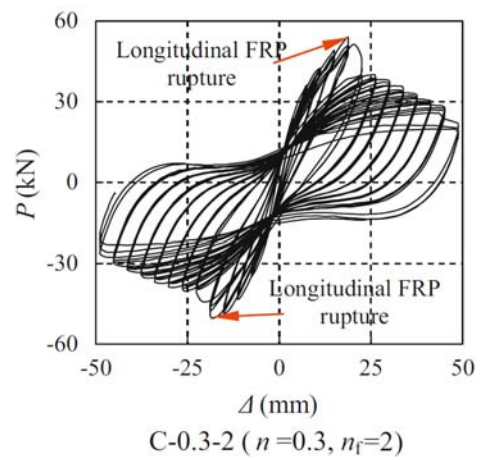


Figure 2.16: Hybrid DSTCs subjected to lateral cyclic loading
(Han *et al.* 2010)

CHAPTER 3

BEHAVIOR OF CONCRETE-FILLED FRP TUBES UNDER CYCLIC AXIAL COMPRESSION

3.1 INTRODUCTION

Concrete-filled FRP tubes (CFFTs) (Mirmiran and Shahawy 1997; Fam and Rizkalla 2001a, b) are an attractive form of hybrid compression members combining FRP and concrete in an optimal manner. A CFFT consists of an outer FRP tube filled with plain or steel-reinforced concrete. The FRP tube is typically manufactured through a filament-winding process (i.e. filament-wound FRP tube). When a concrete-filled FRP tube is under compression, the axially-compressed concrete is also subjected to lateral confinement from the FRP tube which is in tension in the circumferential (or hoop) direction. This lateral confinement from the FRP tube can increase both the strength and the ductility of the concrete significantly. As a result, a highly ductile compression member can be formed from the two brittle materials, namely, FRP and concrete, even when steel reinforcement is completely absent. In addition to excellent ductility and thus excellent seismic resistance, the advantages of CFFTs include their excellent corrosion resistance and the lightweight nature of FRP tubes compared to steel tubes. With these advantages, concrete-filled FRP tubes are attractive for use as bridge columns and piles, both of which are commonly exposed to severe outdoor

environments (e.g. sea water). Many studies have been conducted on CFFTs over recent years, with the respective focuses on the axial compressive behavior (e.g. Mirmiran and Shahawy 1997; Zhang *et al.* 2000; Fam and Rizkalla 2001a, 2001b; Ozbakkaloglu and Oehlers 2008), flexural behavior (e.g. Burgueño and Bhide 2006), seismic behavior (e.g. Zhu *et al.* 2006; Zohrevand and Mirmiran 2013), fatigue behavior (e.g. Ahmad *et al.* 2008), behavior under fire (e.g. Ji *et al.* 2008), as well as design procedures (e.g. Yu and Teng 2011) and review of the literature (e.g. Xiao 2004).

As a structural form with great potential for use in seismic regions, the behavior of CFFTs subject to cyclic loading is of particular importance. The stress-strain behavior of the confined concrete in CFFTs under cyclic axial compression is particularly important for the accurate modeling of such columns under seismic loading. A number of experimental studies (Rousakis 2001; Ilki and Kumbasar 2003; Shao *et al.* 2006; Lam *et al.* 2006; Abbasnia and Ziaadiny 2010; Ozbakkaloglu and Akin 2012; Abbasnia *et al.* 2012, 2013; Bai *et al.* 2013) have been conducted on the cyclic stress-strain behavior of concrete confined by an wet-layup FRP tube with fibers oriented in the hoop direction only (referred to as “FRP wrap” for concision in this chapter), but no systematic experimental study has been concerned with the confined concrete in CFFTs with a filament-wound FRP tube. To the best of the authors’ knowledge, the only existing cyclic axial compression test on concrete-filled filament-wound FRP tubes was conducted by Mirmiran and Shahawy (1997), where only one specimen was tested. The behavior of the concrete in CFFTs is complicated by the significant axial stiffness and Poisson’s effect of the FRP tube, and the failure mode of such an FRP tube is also different from that of an FRP wrap with only hoop fibers. In addition, the shrinkage of the concrete infill in CFFTs may lead to a small initial gap between the FRP tube and the concrete, which can also have adverse effects. Against this

background, this chapter presents an experimental study on the behavior of circular CFFTs under cyclic axial compression. The experimental program included the strength of concrete as a key variable, as CFFTs offer an ideal opportunity for the use of high strength concrete (HSC) because of the confinement from the tube. The experimental program is thus also a much needed supplement to the very limited existing research on the cyclic compressive behavior of FRP-confined HSC. Only two studies by Rousakis (2001) and Ozbakkaloglu and Akin (2012) where FRP wraps were used..

3.2 EXPERIMENTAL PROGRAM

3.2.1 Specimen Details

A total of 15 concrete-filled filament-wound FRP tubes were prepared and tested. All the specimens had a characteristic diameter of 200 mm (diameter of the concrete core) and a height of 400 mm. These columns were cast in 3 batches (batches 1 to 3) with 3 different concrete mix ratios respectively to produce 3 different concrete grades. Each batch included two groups of specimens which were confined with two different types of filament-wound FRP tubes respectively. Each group included two or three nominally identical specimens among which one was tested under monotonic compression while the other one or two were tested under cyclic compression. For the group with two cyclically loaded specimens, two different loading schemes were used as discussed later. Each specimen was given a name, which starts with the letter “S” to represent “specimen”, followed by a two- or three-digit number to represent the unconfined concrete strength, and then a number which defines the thickness (in mm) of the FRP tube, together with two letters “FW” indicating that the tube is made using the filament-winding process. This is then followed by a letter “M” or “C” to

represent “monotonic” or “cyclic” compression. The last number “1” or “2” in some specimens is used to differentiate two nominally identical specimens which were tested under two different cyclic loading schemes respectively. The details of all specimens are summarized in Table 3.1.

3.2.2 Preparation of Specimens

In the preparation of these specimens, the FRP tube was used as the mold for casting concrete (Figure 3.1). A 25 mm wide carbon FRP circumferential strip was provided near each end of a CFFT specimen to avoid unexpected failure there. Both ends of the specimen were then capped with high strength gypsum to achieve flat and smooth end surfaces which were perpendicular to the specimen axis.

3.2.3 Material Properties

3.2.3.1 Concrete

Self-compacting concrete was used for all the specimens. A previous study by the authors’ group (i.e. Yu *et al.* 2013) has demonstrated that the behavior of FRP-confined self-compacting concrete is generally similar to that of FRP-confined normal concrete. In batch 1, the concrete was prepared with ordinary Portland cement, fly ash, super plasticizer (S.P.), river sand, and granite aggregate with a maximum nominal size of 10 mm. In batches 2 and 3, silica fume was added to achieve the high strengths required. The mix proportions used are summarized in Table 3.2. Three plain concrete cylinders (152.5 mm x 305 mm) were tested for each batch to determine the concrete properties following ASTM C39/C39M (2011). The elastic modulus, compressive strength and compressive

strain at peak stress of the concrete averaged from the concrete cylinder tests are given in Table 3.1. The axial stress-axial strain curves for these concrete cylinders are shown in Figure 3.2.

3.2.3.2 FRP Tubes

Three types of prefabricated filament-wound glass FRP (GFRP) tubes were used in the present study. These tubes were manufactured using the same batches of raw materials (i.e. fibers and resin), and were designed to have the same nominal volume ratio and the same angles of fibers (i.e. ± 80 degrees to the longitudinal axis of the tube respectively), for the same mechanical properties. The only difference among the three types of FRP tubes is in their thicknesses, which were measured to be 2.2 mm, 4.7 mm and 9.5 mm, respectively. Based on their actual thicknesses, the actual fiber volume ratios in the three types of tubes were found to be slightly different (i.e. 0.452, 0.466 and 0.482 respectively). In the present study, only selected tubes were tested under hoop tension and axial compression respectively. Appropriate small adjustments were made to the mechanical properties obtained from tests to consider the difference in the actual fiber volume ratio when these values were used for other types of tubes.

Tensile split-disk tests on 5 FRP rings were conducted following ASTM D2290-08 (2008) as shown in Figure 3.3. The 5 FRP rings, each having a uniform height of 35 mm, were cut from the same FRP tube with a thickness of 4.7 mm. Six hoop strain gauges with a gauge length of 20 mm were installed, among which two were centered at the two gaps, whereas the nearer edges of the other four gauges were located at 15 mm away from the gaps. The readings of the two strain gauges at the gaps were found to be lower due to the effect of bending there.

The experimental tensile stress-strain curves are shown in Figure 3.4, where the tensile stress was obtained by dividing the applied tensile force by two times the cross-section area of the ring, while the tensile strain was averaged from the four hoop strain gauges away from the gaps to eliminate any effects from local bending at the gaps. Figure 3.4 shows that the FRP tube has a linear stress-strain relationship in the hoop direction. The average rupture strain and secant elastic modulus at failure are 1.49% and 45.9 GPa, respectively.

Compression tests on 5 FRP rings were conducted following GB/T5350-2005 (2005) as shown in Figure 3.5. The 5 FRP rings all had a height of 60 mm and were cut from the same FRP tube with a thickness of 9.5 mm. They were tested on an MTS machine with a displacement control rate of 0.036 mm/min. Figure 3.6 shows the experimental stress-strain curves. The stress is shown to increase linearly with the strain until an axial strain of around 0.004, after which the FRP tube segment exhibits significantly nonlinear behavior before the final failure of the tube segment due mainly to failure of the resin matrix. The average secant elastic modulus at an axial strain of 0.004, which represents the slope of the approximately linear initial portion, was found to be 15.6 GPa and is referred to as $E_{sec,1}$. The average ultimate axial stress, ultimate axial strain and secant elastic modulus at failure (referred to as $E_{sec,2}$) are 95.1MPa, 0.95% and 10.0 GPa respectively.

3.2.4 Experimental Set-Up and Instrumentation

For each specimen, eight axial strain gauges, among which four had a gauge length of 20 mm while the other four had a gauge length of 100 mm, were installed at the mid-height of the FRP tube (Figure 3.7). The use of two different gauge lengths was to clarify any possible effect of the gauge length on the

measured axial strains. Three groups of hoop strain gauges with a gauge length of 20 mm were installed at 3 different heights of the FRP tube respectively: mid-height; 100 mm lower than the mid-height; 100 mm higher than the mid-height. Each group included four hoop strain gauges evenly distributed over the circumference (Figure 3.7). In addition, 4 LVDTs were used to obtain the total axial shortening of each specimen. The axial load was applied on both the FRP tube and the concrete simultaneously. All compression tests were carried out using a column testing facility with a displacement control rate of 0.24 mm/min. All test data, including the strains, loads, and displacements, were recorded simultaneously by a data logger.

3.2.5 Loading Schemes

For the groups (i.e. S54-2FW, S54-4FW and S104-4FW) with two cyclically loaded specimens, one was subjected to type C1 loading while the other was subjected to type C2 loading. Both the type C1 and type C2 loading schemes were designed for full unloading/reloading cycles where the unloading of each cycle was terminated at a zero load and the reloading of each cycle was terminated at the unloading displacement of the same cycle (i.e. where the unloading starts) or after reaching the envelope curve. For type C1 loading, a single unloading/reloading cycle was applied at each of several prescribed unloading displacement values before failure. For type C2 loading, a number (9-12) of repeated unloading/reloading cycles were applied at a single prescribed unloading displacement value. For the groups (i.e. S84-4FW, S84-9FW and S104-9FW) with only one cyclically loaded specimen, the specimen was subjected to a combination of type C1 and C2 loading: a single unloading/reloading cycle was applied at each of the first several prescribed unloading displacement values while a number (9-12) of repeated cycles were applied at the last prescribed unloading

displacement value. All the loading schemes were executed manually with the use of the displacement averaged from the 4 LVDTs (Figure 3.7) and the load readings of the column testing facility as the controlling parameters. Details of the loading schemes are summarized in Table 3.3.

3.3 TEST RESULTS AND DISCUSSIONS

3.3.1 Test Observations

All the specimens were tested to failure except for the specimens with a 9 mm FRP tube (i.e. groups S84-9FW and S104-9FW). The tests for these specimens were terminated at an axial load of 8000 kN because of the loading capacity limitation of the column testing facility. All specimens after test are shown in Figure 3.8.

The failure processes of all specimens were similar, indicating that different loading schemes had little effect on this process. As the loading process progressed, white patches along the fiber directions appeared on the outer surface of the tube, indicating local damage in the resin because of the dilation of the concrete inside. These white patches developed continuously until the rupture of fibers which occurred nearby. It is worth noting that the rupture of fibers, starting from the outermost ply, was a progressive process accompanied with continuous snapping noises. This is different from the sudden failure of concrete confined with a wet-layup FRP wrap with unidirectional fibers in the hoop direction.

3.3.2 Axial Strains

There are three ways to obtain the axial strain of a specimen: (1) the average

reading from the four 20 mm axial strain gauges at the mid-height (referred to as SG-20 axial strain); (2) the average reading from the four 100 mm axial strain gauges at the mid-height (referred to as SG-100 axial strain); and (3) the average strain over the whole height of the specimen based on the average overall axial shortening of the four LVDTs (referred to as nominal axial strain).

Figure 3.9 shows a comparison between the axial strains obtained in the three different ways for the specimens tested under axial monotonic compression. The SG-20 and the SG-100 axial strains shown in Figure 3.9 were all averaged from the readings of four axial strain gauges except for specimen S104-9FW-M. In specimen S104-9FW-M, one of the 100 mm axial strain gauges was damaged, so the SG-100 strains for this specimen were from the three surviving axial strain gauges. Figure 3.9a shows that the SG-20 and the SG-100 axial strains are generally in close agreement. For the specimens with the lowest concrete strength (i.e. specimens in the S54 series), the nominal axial strain also agrees closely with the SG-20 and the SG-100 axial strains (Figures 3.9b and 3.9c). However, for the specimens in the other two series (i.e. specimens in the S84 and S104 series), such agreement is only observed before a threshold strain value (around 0.004 for the S84 series and around 0.005 for the S104 series), beyond which the nominal axial strain becomes significantly larger than the axial strain gauge readings (i.e. both the SG-20 and the SG-100 strains), indicating that significant localized deformation occurred outside the 100 mm mid-height region of the column. This observation is probably due to the brittleness of HSC, which led to more localized and non-uniform damage of concrete.

As the axial strain gauges were attached on the external surface of the FRP tube, and significant slips may have existed between the FRP tube and the concrete especially after the development of significant localized deformation of concrete,

the axial strain gauge readings cannot simply be assumed to closely reflect the strain state of the confined concrete. In the subsequent sections, the axial strain of the confined concrete is represented by the nominal axial strain. It should be noted that the nominal axial strain represents the average deformation of the concrete over the column height, where the deformation near the ends is expected to be different from that near the mid-height because of the lateral constraints from the two ends. The existence of such differences, as well as the other possible deformation of the loading system, generally leads to slightly larger strains as measured by LVDTs especially in the initial stage of loading. However, this effect is believed to be small, given the fact that the nominal axial strain agrees closely with the mid-height axial strain gauge reading for the specimens in the S54 series (Figure 3.9).

3.3.3 Hoop Strains

Making use of readings from the three groups of hoop strain gauges located at 3 different heights of the FRP tube, the hoop strain distributions at the ultimate state of all the 15 specimens are shown in Figure 3.10, except for specimens in groups S84-9FW and S104-9FW which were not tested to failure as mentioned earlier. For these specimens, the hoop strains at the time when the tests were terminated are shown in Figure 3.10. It is evident that a considerable scatter exists in the hoop strain readings. Such scatters appear to be less pronounced for the mid-height section than the other two sections (i.e. sections 1 and 3) (Figure 3.7), indicating that the lateral expansion of concrete is more uniform in the mid-height region. While the maximum hoop strain and the minimum hoop strain were found to be typically not at the mid-height section, the average hoop strain reading at the mid-height section ($\epsilon_{h,rup2}$) is very close to and generally slightly higher than the average reading of the three groups of hoop strain gauges ($\epsilon_{h,rup1}$) (Table 3.4).

The average hoop rupture strain appears to be smaller for specimens with a higher concrete strength and/or a weaker tube.

3.3.4 Axial Load-Axial Strain Behavior of CFFTs

Typical axial load-axial strain curves of the CFFT specimens are shown in Figure 3.11. Figure 3.11 shows that the specimens all had an approximately bilinear load-strain curve (for monotonically loaded specimens) or envelope curve (for cyclically loaded specimens), but for some specimens with a very high strength concrete (e.g. specimen S104-4FW-M), there is a slight drop in the load in the transition zone between the two approximately linear portions of the curve. Such a slight load drop, however, was not found in specimens with a relatively low concrete strength (e.g. specimen S54-2FW-M), or specimens with a very strong FRP tube (e.g. specimen S104-9FW-M). It is thus believed that such a load drop is due to the brittleness of HSC when it is subjected to insufficient confinement. It does not appear to be caused by the less intimate contact between the concrete and the FRP tube in a CFFT, as such a load drop is also a common observation in HSC confined with an FRP wrap (Cui and Sheikh 2009; Ozbakkaloglu and Akin 2012).

3.3.5 Axial Stress-Axial Strain Curves of Concrete

The axial stress-strain curves of the FRP-confined concrete in CFFTs are shown in Figure 3.12 for all the specimens, where those of cyclically loaded specimens are compared with the curve of the corresponding specimen under monotonic compression. The axial stress of the concrete was found as the axial load carried by the concrete section divided by its cross-sectional area. The axial load carried by the concrete section is assumed to be equal to the difference between the axial load carried by the specimen and the axial load carried by the FRP tube at the

same axial strain. One main difference between the FRP tube in a CFFT and an FRP wrap is that the former generally has a considerable axial stiffness and its direct contribution to the axial load capacity cannot be ignored. In the present study, the load carried by the FRP tube in CFFTs was found from axial compression tests on hollow FRP tubes. When the axial strain of a specimen exceeds the ultimate strain of the corresponding hollow FRP tube tests, it is assumed that the load resisted by the FRP tube is equal to its ultimate load because of the support from the concrete core (Figure 3.11a). It is further assumed that in the unloading process, the load taken by the FRP tube reduces proportionally to the total axial load acting on the specimen, and reaches zero at the same time as the total load becomes zero; in the reloading process, the load taken by the FRP tube increases proportionally to the total axial load taken by the specimen, and reaches the previous load taken by FRP tube when unloading initiates (Figure 3.11b). While these assumptions may lead to small errors in the estimated load taken by the FRP tube, such small errors are believed to have negligible effects on the obtained axial stress-strain curve of the confined concrete, due to the much smaller cross-sectional area of the FRP tube.

It is evident from Figure 3.12 that the envelope curves of all the specimens subjected to cyclic axial compression are almost the same as the corresponding monotonic axial stress-strain curves. This observation is consistent with that from Lam *et al.*'s (2006) tests on FRP-confined NSC, where FRP wraps formed via a wet-layup process were used. Similar to the axial load-strain curves, Figure 3.12 also shows that all the monotonic stress-strain curves have an approximately bilinear shape with a second ascending branch, except for the specimens with HSC and a 4.0 mm GFRP tube (i.e. S84-4FW-M and S104-4FW-M). For these two specimens, there is a slight fluctuation in the stress-strain curve at an axial strain of around 0.006, which is associated with a sudden increase in the hoop

strain (Figure 3.13). This phenomenon, as discussed above, is believed to be due to the brittleness of HSC and the use of a FRP tube which is not sufficiently stiff in the circumferential direction.

Figure 3.12 also shows that the cyclic stress-strain curves of concrete in CFFT's possess the following key characteristics, which are the same as those of concrete confined with an FRP wrap (Lam and Teng 2009): (1) the loading history has a cumulative effect on both the plastic strain and stress deterioration; (2) the unloading path is generally nonlinear with a continuously decreasing slope while the reloading path is approximately linear.

3.3.6 Key Results

The key test results of all 15 specimens are summarized in Table 3.4. In this table, F_{all} is the peak axial load of the specimen from the test; F_c is the peak axial load taken by the concrete; f'_{cc} is the peak axial stress of the confined concrete; ϵ_{cu} is the ultimate axial strain of the concrete at the rupture of the FRP tube. The peak axial stress f'_{co} and the strain at peak stress ϵ_{co} of unconfined concrete were used to normalize the ultimate axial stress and the ultimate axial strain, respectively.

3.4 COMPARISON WITH EXISTING MODELS

It has been shown in Figure 3.12 that the envelope curves of specimens subjected to cyclic axial compression are almost the same as the axial stress-strain curves of the corresponding monotonically loaded specimens. In this section, the experimental envelope stress-strain curves are compared with predictions from an accurate monotonic stress-strain model proposed by Teng *et al.* (2009). Teng *et*

al.'s (2009) model is a refined version of a well-recognized model developed by the same research group (Lam and Teng 2003). The test database, on which Lam and Teng's (2003) and Teng *et al.*'s (2009) models have been based, is however generally limited to normal strength concrete (with only one group of specimens having the maximum unconfined strength of 55.2 MPa) and concrete confined with an FRP wrap. The comparison presented in this section thus allows a quantitative assessment of the differences which may be caused by the use of HSC and/or a filament-wound tube in the monotonic behavior of FRP-confined concrete.

The experimental results are also compared with a cyclic stress-strain model proposed by Lam and Teng (2009), which is again based on test results of concrete confined with an FRP wrap. Lam and Teng (2009) mentioned that their model is expected to be applicable to HSC in terms of the unloading/reloading paths, but the calibration of the model for HSC was based on limited test data from one single study (i.e. Rousakis 2001). The comparison presented in this section thus allows further examination of the applicability of this model to HSC and when HSC is confined by an FRP tube. It should be noted that in Lam and Teng (2009), Lam and Teng's (2003) stress-strain model is used to predict the envelope stress-strain curve. In the present study, the comparison with Lam and Teng's (2009) model is limited to the unloading/reloading paths.

3.4.1 Comparison with Teng *et al.*'s (2009) Model

3.4.1.1 Teng *et al.*'s (2009) Model

Teng *et al.*'s (2009) model consists of a parabolic first portion and a linear second portion. Compared with Lam and Teng's (2003) model, Teng *et al.*'s (2009) model

includes more accurate expressions for the ultimate axial strain and the compressive strength. These new expressions allow the effects of confinement stiffness and the jacket strain capacity to be separately reflected and account for the effect of confinement stiffness explicitly instead of reflecting it through the confinement ratio.

Readers may refer to Teng *et al.* (2009) for more details of the model. It should be noted that Teng *et al.* (2009) proposed two versions of the model, but both versions predict the same stress-strain curves for concrete without a descending branch in the stress-strain curve. Predictions of the two versions are thus the same for the specimens tested in the present study.

3.4.1.2 Comparison

Comparisons between the predictions of Teng *et al.*'s (2009) model and the test results are given in Figure 3.14. In making the predictions, the material properties summarized in Table 3.1 were used and $\varepsilon_{h,rupt1}$ was adopted as the FRP hoop rupture strain. It is evident that the predictions agree very well with the experimental results except for the initial slope for some specimens. The difference in the initial slope is due to the use of strains calculated from the total axial shortenings (i.e. LVDT readings) in establishing the experimental curves. As explained earlier, the strains from LVDTs are generally larger than those at mid-height in the initial stage of loading. If the actual axial strains of concrete at mid-height are used, it can be expected that the predicted initial slopes will be in closer agreement with the experimental results.

The above comparison suggests that there is no obvious difference between the stress-strain behavior of concrete confined with an FRP wrap and that confined

with filament-wound FRP tube. The comparison also suggests that Teng *et al.*'s (2009) model, although developed based on test data of normal strength concrete, can provide accurate predictions for FRP-confined HSC with sufficient confinement. Despite the overall good performance of Teng *et al.*'s (2009) model for HSC, it is also noted that this model fails to predict the slight stress fluctuation in the transition zone between the two portions of the stress-strain curve for some specimens (e.g. Figures 3.14b and 3.14c). Considering that the magnitude of this stress drop may become greater when the circumferential stiffness of the confining FRP wrap/tube becomes smaller (Cui and Sheikh 2009; Ozbakkaloglu and Akin 2012), the applicability of Teng *et al.*'s (2009) model needs to be further examined for HSC confined by a weak FRP wrap/tube.

3.4.2 Comparison with Lam and Teng's (2009) Model

3.4.2.1 Lam and Teng's (2009) Model

Lam and Teng's (2009) model provides explicit equations to describe the cyclic stress-strain history of FRP-confined concrete. In Lam and Teng's (2009) model, the unloading curves, being the paths experienced by the concrete when its strain reduces, can be divided into envelope unloading paths (i.e. unloading paths starting from the envelope curve) and internal unloading paths (i.e. the previous reloading path does not reach the envelope curve). Envelope unloading paths depend only on the unloading stress and the unloading strain, while internal unloading paths depend also on the prior loading history. The reloading curves, being the paths experienced by the concrete when its strain increases, may or may not reach the envelope curve. When unloading/reloading cycles are repeated within the envelope curve, they are defined as internal cycles and are numbered so that the effects of previous internal cycles on subsequent cycles can be considered.

In Lam and Teng's (2009) model, empirical equations are also given for the key parameters determining unloading/reloading curves, including the stress deterioration rule and the plastic strain which is defined as the strain value at the intersection of an unloading path and the strain axis. The cumulative effect of the loading history is considered in these equations. Readers may refer to Lam and Teng (2009) for more details of the model.

3.4.2.2 Comparison

Predictions from Lam and Teng's (2009) model are compared with the present test results in terms of the envelope unloading/reloading behavior in Figure 3.15. In making the predictions, the experimental envelope curves were used together with Lam and Teng's (2009) model, so that any difference between the predictions and the experimental unloading/reloading cycles comes only from the cyclic stress-strain model.

Figure 3.15 shows that predictions from Lam and Teng's (2009) model generally deviate from the experimental results, and it is evident that such deviations become much more pronounced for concrete with a higher strength. Considering that the predictions for the S54 series still appear to be reasonable, it may be concluded that Lam and Teng's (2009) model is applicable to normal strength concrete filled FRP tubes, but not CFFTs with HSC. This is probably due to the fact that the development of Lam and Teng's (2009) model relied heavily on the experimental results by Lam et al. (2006) which only covered a small range of concrete strengths (i.e. 38.9 MPa and 41.1 MPa). A recent experimental study by Ozbakkaloglu and Akin (2012), where concrete cylinders confined with an FRP wrap were tested under cyclic axial compression, also showed that the

performance of Lam and Teng's (2009) model for HSC is not as good as its performance for normal strength concrete. Apparently, revisions are needed before Lam and Teng's (2009) model can accurately predict the envelope unloading/reloading curves of FRP-confined HSC.

Predictions from Lam and Teng's (2009) model are compared with the present test results in terms of the repeated unloading/reloading cycles in Figure 3.16. In order to assess these unloading/reloading cycles clearly, each cycle is shown with the corresponding predicted cycle individually to avoid the over-crowding of curves at the same unloading strain. Only comparisons for the 1st, 4th, 7th and the last cycles are shown in Figure 3.16, as comparisons for other cycles are similar. In making the predictions, the envelope unloading strain $\varepsilon_{un,env}$ and the envelope unloading stress $\sigma_{un,env}$, as well as the experimental plastic strains of envelope cycles $\varepsilon_{pl,1}$ were used so that the comparisons in Figure 3.16 reflect only the accuracy of the model for predicting the cumulative effect of loading history. It is evident that Lam and Teng's (2009) model generally provides reasonable predictions, but the performance of the model becomes slightly worse for specimens with a higher concrete strength.

3.5 CONCLUSIONS

This chapter has presented an experimental study on the cyclic axial behavior of CFFTs, where the strength of concrete is a key variable. The test results have also been compared with Teng *et al.*'s (2009) monotonic stress-strain model and Lam and Teng's (2009) cyclic stress-strain model, both of which have been based on test databases which are limited to concrete confined with an FRP wrap formed by wet-layup method and include only a small number of tests for HSC. The results and discussions allow the following conclusions to be drawn:

- (1) The rupture of fibers in a filament-wound FRP tube, starting from the outermost ply, is a progressive process which is different from the failure of concrete confined with an FRP wrap.
- (2) The cyclic axial stress-strain behavior of concrete in CFFTs is generally similar to that of concrete confined with an FRP wrap.
- (3) Teng *et al.*'s (2009) monotonic stress-strain model is capable of providing accurate predictions for HSC in CFFTs, given that the FRP tube has a sufficient circumferential stiffness.
- (4) Lam and Teng's (2009) cyclic stress-strain model may be applicable to normal strength concrete in CFFTs, but not HSC in CFFTs.

3.6 REFERENCES

- Abbasnia, R. and Ziaadiny, H. (2010). "Behavior of concrete prisms confined with FRP composites under axial cyclic Compression", *Engineering Structures*, 32, 648-665.
- Abbasnia, R., Ahmadi, R. and Ziaadiny, H. (2012). "Effect of confinement level, aspect ratio and concrete strength on the cyclic stress-strain behavior of FRP-confined concrete prisms", *Composites Part B: Engineering*, 43, 825-831.
- Abbasnia, R., Hosseinpour, F., Rostamian, M. and Ziaadiny, H. (2013). "Cyclic and monotonic behavior of FRP confined concrete rectangular prisms with different aspect ratios", *Construction and Building Materials*, 40, 118-125.
- Ahmad, I., Zhu, Z.Y., Mirmiran, A. and Fam, A.Z. (2005). "Shear strength prediction of deep CFFT beams", *ACI Special Publication SP-230-61* (CD-ROM), 1085-1102.
- ASTM C39/C39M. (2011). *Standard Test Method for Compressive Strength of Cylindrical Concrete Specimens*, American Society for Testing and Materials, Philadelphia, USA.
- ASTM D2290-08. (2008). *Standard Test Method for Apparent Hoop Tensile Strength of Plastic or Reinforced Plastic Pipe by Split Disk Method*, American Society for Testing and Materials, Philadelphia, USA.
- Bai, Y.L., Dai, J.G. and Teng, J.G. (2013). "Cyclic compressive behavior of concrete confined with large rupture strain FRP composites", *Journal of Composites for Construction*, ASCE, 18(1).
- Burgueño, R. and Bhide. K. (2006). "Shear response of concrete-filled FRP composite cylindrical shells", *Journal of Structural Engineering*, ASCE, 132(6), 949-960.
- Cui, C. and Sheikh. S. (2010). "Experimental study of normal- and high-strength

- concrete confined with fiber-reinforced polymers”, *Journal of Composites for Construction*, ASCE, 14(5), 553-561.
- Fam, A.Z. and Rizkalla, S.H. (2001a). “Confinement model for axially loaded concrete confined by circular fiber-reinforced polymer tubes”, *ACI Structural Journal*, 98(4), 451-461.
- Fam, A.Z. and Rizkalla, S.H. (2001b). “Behavior of axially loaded concrete-filled circular fiber-reinforced polymer tubes”, *ACI Structural Journal*, 98(3), 280-289.
- GB/T5350-2005. (2005). *Fiber-Reinforced Thermosetting Plastic Composites Pipe: Determination for Longitudinal Compressive Properties*, The Standards Press of China.
- Ilki, A. and Kumbasar, N. (2003). “Compressive behavior of carbon fiber composite jacketed concrete with circular and non-circular cross sections”, *Journal of Earthquake Engineering*, 7(3), 381-406.
- Ji, G., Li, G., Li, X., Pang, S. and Jones, R. (2008). “Experimental study of FRP tube encased concrete cylinders exposed to fire”, *Composite Structures*, 85(2), 149-154.
- Lam, L. and Teng, J.G. (2003). “Design-oriented stress-strain model for FRP-confined concrete”, *Construction and Building Materials*, 17(6-7), 471-489.
- Lam, L., Teng, J.G., Cheung, C.H. and Xiao, Y. (2006). “FRP-confined concrete under axial cyclic compression”, *Cement and Concrete Composites*, 28, 949-958.
- Lam, L. and Teng, J.G. (2009). “Stress-strain model for FRP-confined concrete under cyclic axial compression”, *Engineering Structures*, 31(2), 308-321.
- Mirmiran, A. and Shahawy, M. (1997). “Behavior of concrete columns confined by fiber composites”, *Journal of Structural Engineering*, ASCE, 123(5), 583-590.

- Ozbakkaloglu, T. and Akin, E. (2012) “Behavior of FRP-confined normal-and high-strength concrete under cyclic axial compression”, *Journal of Composites for Construction*, ASCE, 16, 451-463.
- Ozbakkaloglu, T. and Oehlers, D. (2008). “Concrete-filled square and rectangular FRP tubes under axial compression”, *Journal of Composites for Construction*, ASCE, 12(4), 469-477.
- Rousakis, T.C. (2001). *Experimental Investigation of Concrete Cylinders Confined by Carbon FRP Sheets Under Monotonic and Cyclic Axial Compression Load*, Research Report. 01:2, Division of Building Technology, Chalmers University of Technology, Gothenburg, Sweden.
- Shao, Y., Zhu, Z. and Mirmiran, A. (2006). “Cyclic modeling of FRP confined concrete with improved ductility”, *Cement and Concrete Composites*, 28(10), 959-968.
- Teng, J.G., Jiang, T., Lam, L. and Luo, Y.Z. (2009). “Refinement of a design-oriented stress-strain model for FRP-confined concrete”, *Journal of Composites for Construction*, ASCE, 13(4), 269-278.
- Wang, Z.Y., Wang, D.Y., Simth, S.T. and Lu, D.G. (2012). “Experimental testing and analytical modeling of CFRP-confined large circular RC columns subjected to cyclic axial compression”, *Engineering Structures*, 40, 67-74.
- Xiao, Y. (2004). “Applications of FRP composites in concrete column”, *Advances in Structural Engineering*, 7(4), 335-343.
- Yu, T. and Teng, J.G. (2011). “Design of concrete-filled FRP tubular columns: provisions in the Chinese technical code for infrastructure application of FRP composites”, *Journal of Composites for Construction*, ASCE, 15(3), 451-461.
- Yu, T., Fang, X.L. and Teng, J.G. (2013). “FRP-confined self-compacting concrete under axial compression”, *Journal of Materials in Civil Engineering*, ASCE, in press.
- Zhang, D.X., Huang, L.N., Wang, R.G. and Zhao, J.H. (2000). “Experimental

research on the mechanical properties of concrete filled FRP tubular column”, *Journal of Harbin University of Civil Engineering and Architecture*, 1(33), 73-76.

Zhu, Z., Ahmad, I. and Mirmiran, A. (2006). “Seismic performance of concrete-filled FRP tube columns for bridge substructure”, *Journal of Bridge Engineering*, ASCE, 11(3), 359-370.

Zohrevand, P. and A. Mirmiran (2013). “Seismic response of ultra-high performance concrete-filled FRP tube columns”, *Journal of Earthquake Engineering*, 17(1), 155-170.

Table 3.1: Details of specimens

Specimen	Loading type	FRP tube thickness		Concrete properties		
		t_{frp} (mm)	f'_{co} (MPa)	E_c (GPa)	ϵ_{co} (%)	
S54-2FW-M	Monotonic	2.2	batch 1	27.8	0.25	
S54-2FW-C1,2	Cyclic					
S54-4FW-M	Monotonic	4.7	54.1			
S54-4FW-C1,2	Cyclic					
S84-4FW-M	Monotonic	4.7	batch 2	33.1	0.27	
S84-4FW-C	Cyclic					
S84-9FW-M	Monotonic	9.5	84.6			
S84-9FW-C	Cyclic					
S104-4FW-M	Monotonic	4.7	batch 3	36.5	0.31	
S104-4FW-C1,2	Cyclic					
S104-9FW-M	Monotonic	9.5	104.4			
S104-9FW-C	Cyclic					

Table 3.2: Mix proportions of concrete

Batch	Water cement ratio	Water	Cement	Fly ash	Silica fume	Super plasticizer*	Coarse aggregate	Sand
1	0.35	175	300	200	---	9	829	796
2	0.29	174	377	203	29	11	793	762
3	0.23	155	442	170	68	16	819	712

*The brand of the super plasticizer is "Grace HK", and the product model is "ADVA109".

Table 3.3: Cyclic loading schemes

Specimen	Unloading displacement (mm) found from LVDTs								
	Step 1	Step 2	Step 3	Step 4	Step 5	Step 6	Step 7	Step 8	Step 9
S54-2FW-C1	0.94	1.94	2.91	3.92	4.91	5.93	6.94	---	---
S54-2FW-C2	5.96(10) *	---	---	---	---	---	---	---	---
S54-4FW-C1	1.09	2.01	4.09	6.11	8.13	10.11	12.09	14.12	16.18
S54-4FW-C2	12.14(10)*	---	---	---	---	---	---	---	---
S84-4FW-C	1.05	2.07	3.13	4.26	5.10	6.27(11) *	---	---	---
S84-9FW-C	1.03	2.03	4.09	6.20	8.42	10.43(9) *	---	---	---
S104-4FW-C1	1.03	1.97	2.95	4.11	5.13	6.10	7.10	8.22	9.49
S104-4FW-C2	7.05(12) *	---	---	---	---	---	---	---	---
S104-9FW-C	1.03	2.02	4.07	6.08	8.47(10) *	---	---	---	---

*The number in the bracket is the number of repeated cycles imposed at that prescribed unloading displacement.

Table 3.4: Key test results

Specimen	F_{all}	F_c	f'_{cc}	ϵ_{cu}	$\frac{f'_{cc}}{f'_{co}}$	$\frac{\epsilon_{cu}}{\epsilon_{co}}$	$\epsilon_{h,rup1}$	$\epsilon_{h,rup2}$
	(kN)	(kN)	(MPa)	(%)			(%)	(%)
S54-2FW-M	3312	3179	101.3	2.25	1.87	8.73	1.43	1.61
S54-2FW-C1	2833	2700	86.0	1.76	1.59	6.83	1.08	1.12
S54-2FW-C2	2917	2785	88.7	1.89	1.64	7.33	1.11	1.18
S54-4FW-M	5734	5447	173.5	4.93	3.21	19.1	1.95	2.01
S54-4FW-C1	5366	5078	161.7	4.42	2.99	17.2	1.68	1.82
S54-4FW-C2	5294	5006	159.4	4.43	2.95	17.2	1.69	1.76
S84-4FW-M	5189	4901	156.1	2.20	1.85	8.00	1.17	1.27
S84-4FW-C	5069	4782	152.3	2.39	1.80	8.69	1.10	1.08
S84-9FW-M	8011	7417	236.2	3.17	2.79	11.5	1.12	1.21
S84-9FW-C	8012	7418	236.2	3.22	2.79	11.7	1.05	1.18
S104-4FW-M1	6215	5927	188.8	2.64	1.81	8.48	1.19	1.21
S104-4FW-C1	5927	5640	179.6	2.58	1.72	8.29	1.32	1.44
S104-4FW-C2	5551	5263	167.6	2.38	1.61	7.64	1.09	1.13
S104-9FW-M	8019	7424	236.4	2.61	2.26	8.38	0.94	0.91
S104-9FW-C	8019	7424	236.4	2.61	2.26	8.38	0.93	0.91

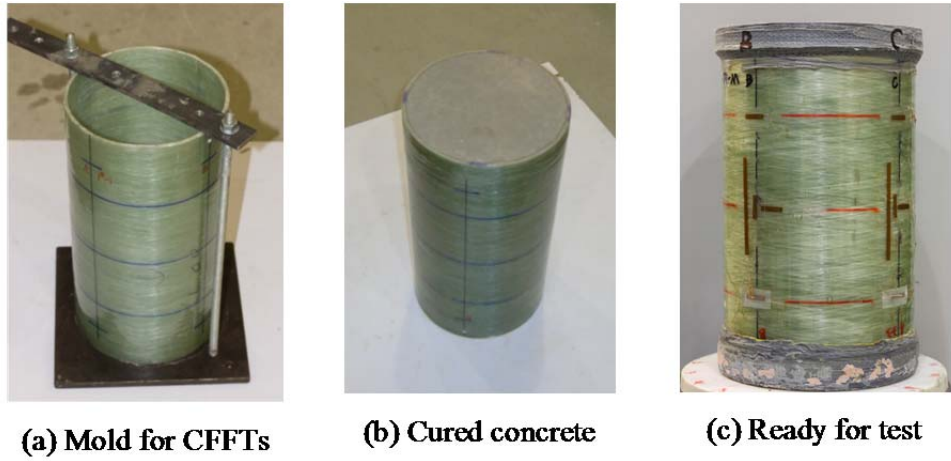


Figure 3.1: Preparation of specimens

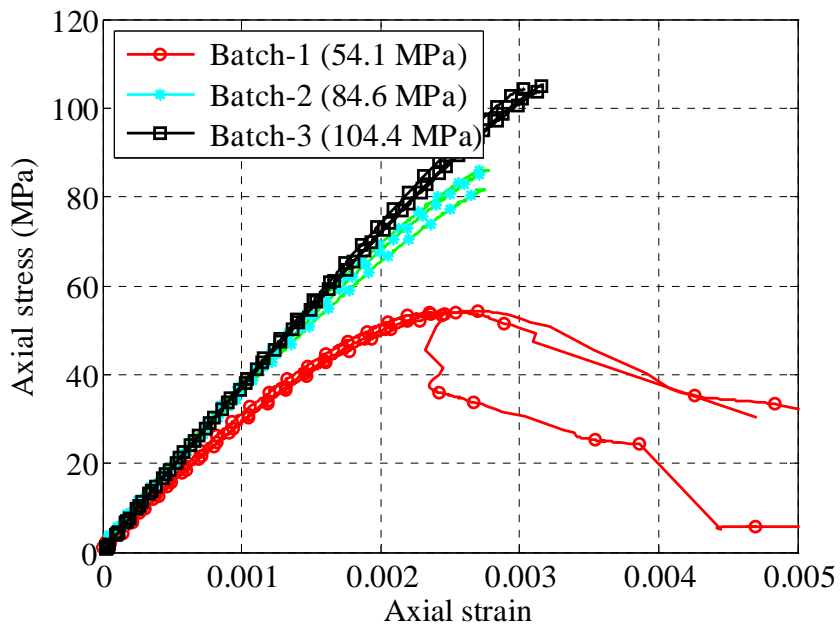
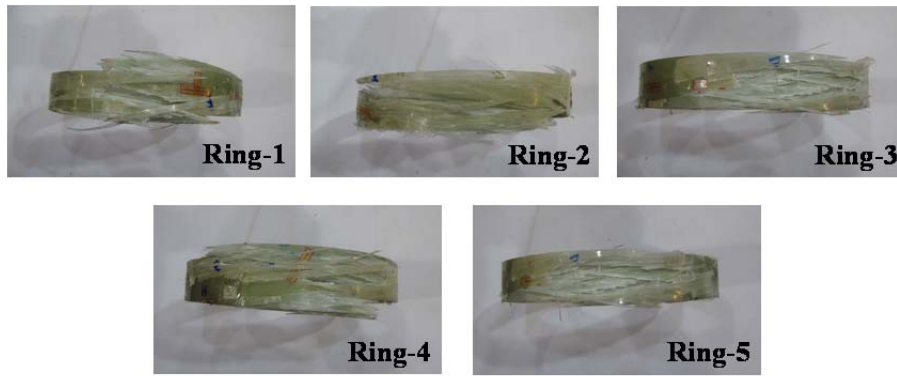
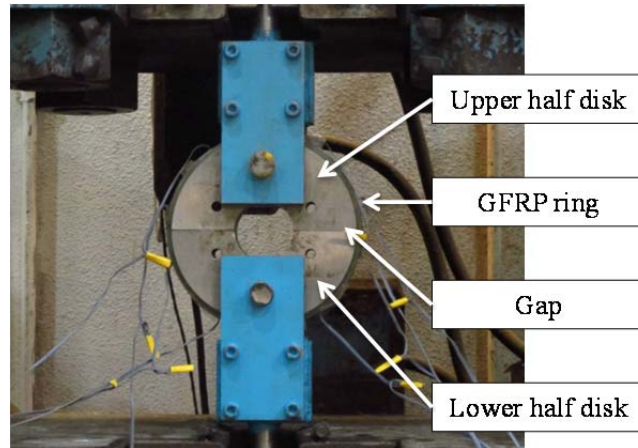


Figure 3.2: Axial stress-strain behavior of control cylinders



Failed specimens

Figure 3.3: Tensile split-disk test of FRP tubes

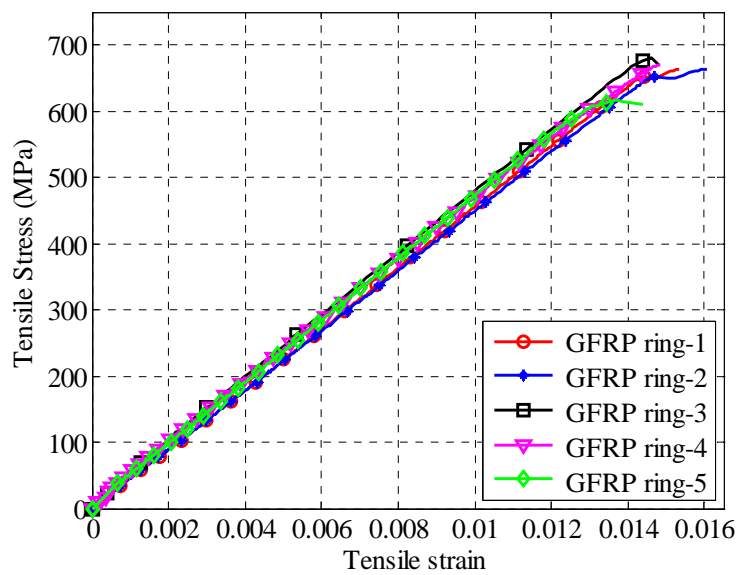
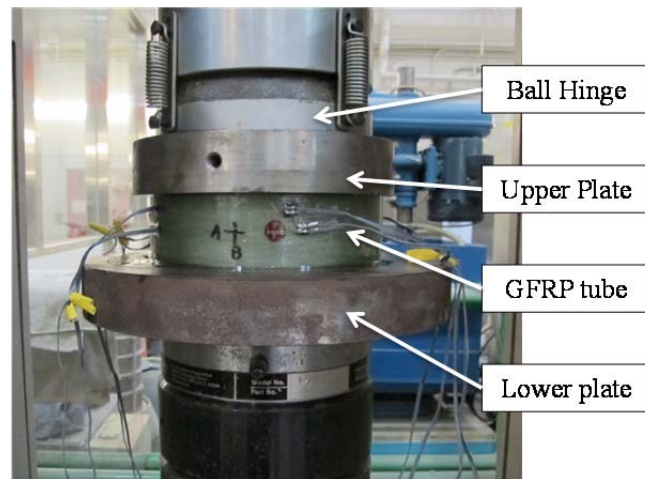


Figure 3.4: Tensile stress-strain curves of FRP tubes in the hoop direction



Failed specimens

Figure 3.5: Compression test of FRP tube segment

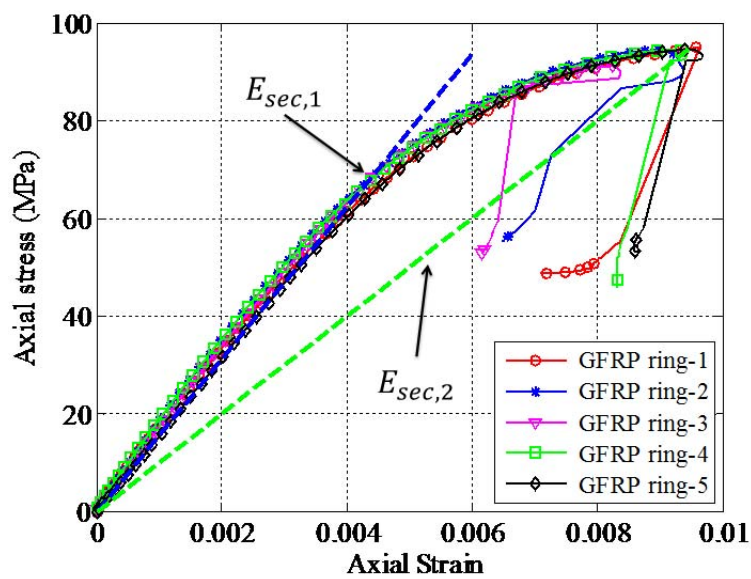
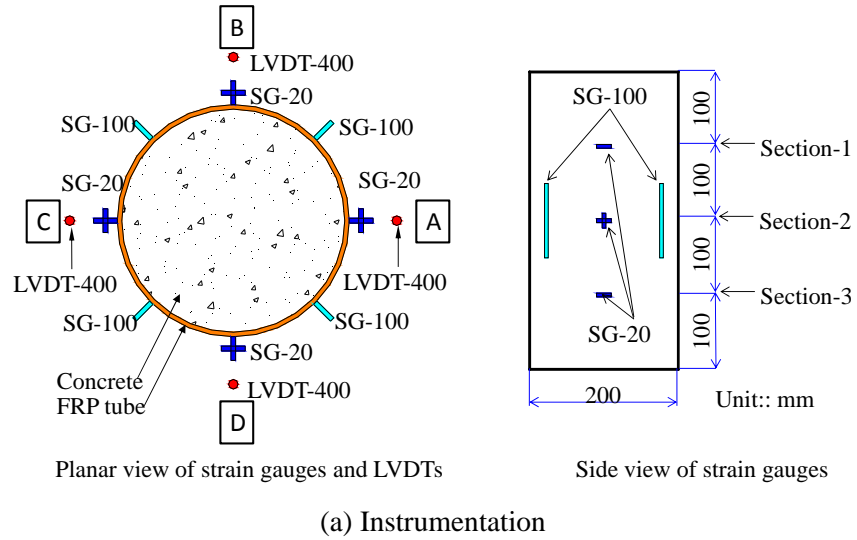


Figure 3.6: Axial stress-strain curves of FRP tubes under axial compression



(b) Experimental set-up

Figure 3.7: Experimental set-up and instrumentation



S54-2FW-M



S54-2FW-C1



S54-2FW-C2



S54-4FW-M



S54-4FW-C1



S54-4FW-C2

(a) Failed specimens of batch 1



S84-4FW-M



S84-4FW-C



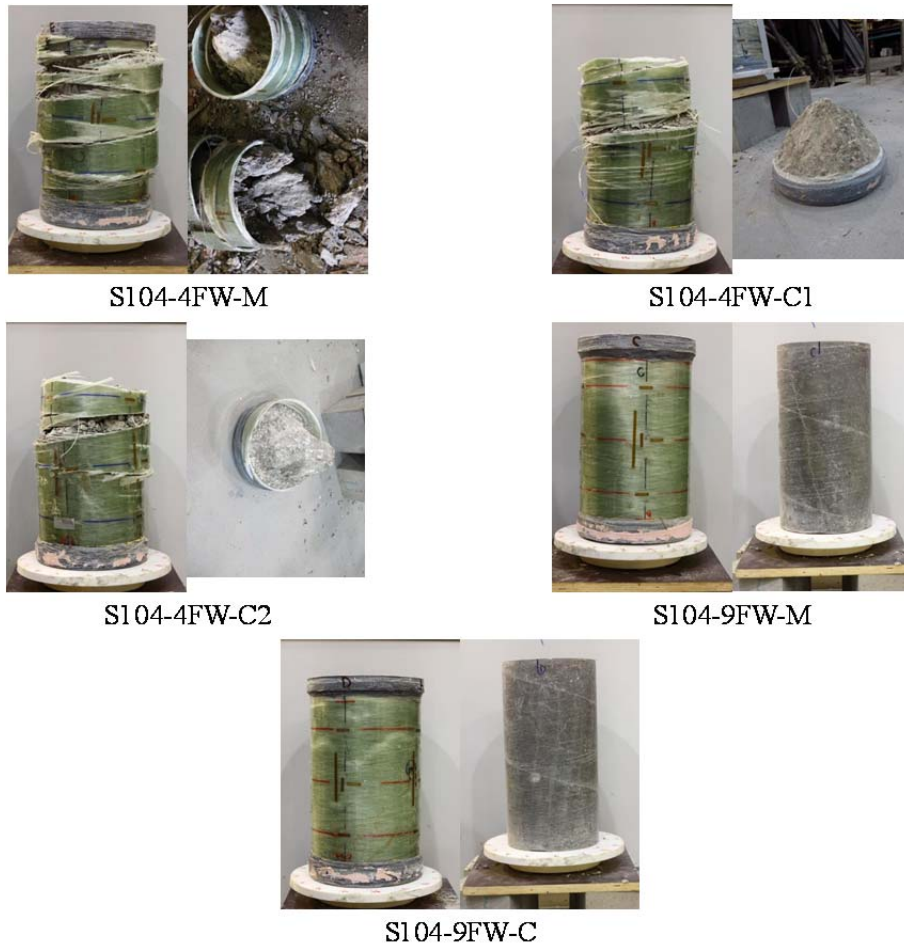
S84-9FW-M



S84-9FW-C

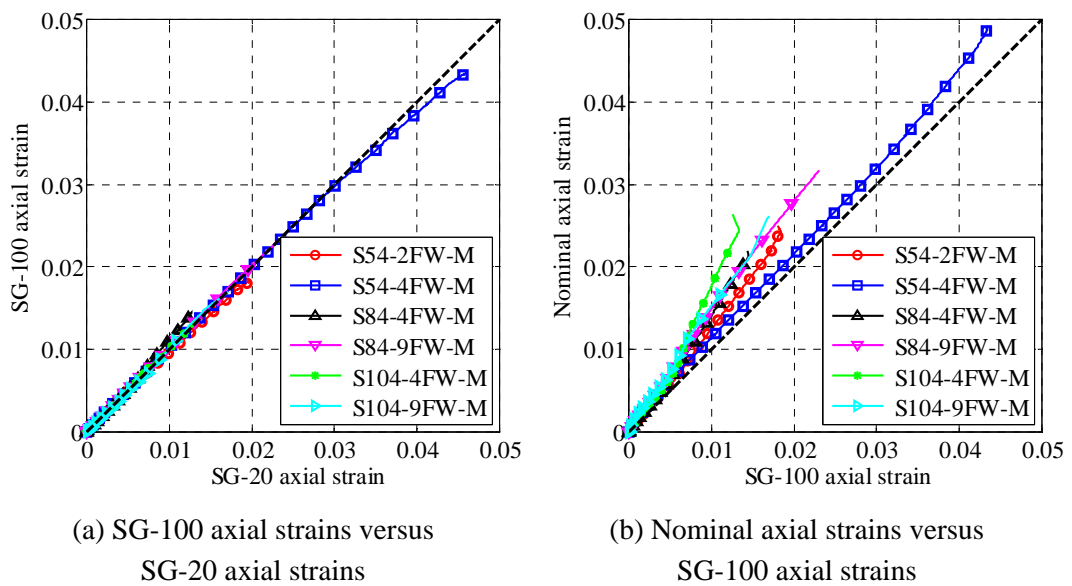
(b) Failed specimens of batch 2

Figure 3.8: Specimens after test



(c) Failed specimens of batch 3

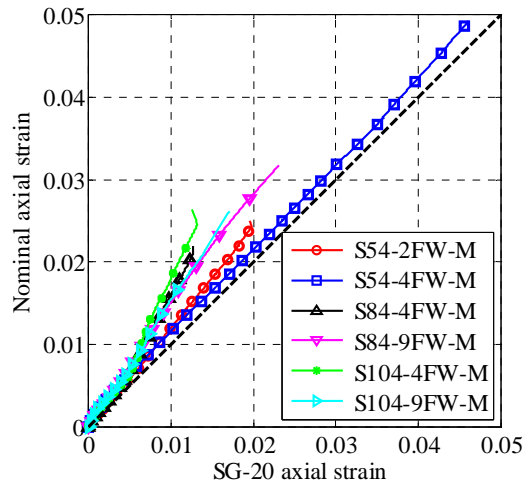
Figure 3.8: Specimens after test (continued)



(a) SG-100 axial strains versus SG-20 axial strains

(b) Nominal axial strains versus SG-100 axial strains

Figure 3.9: Comparison of axial strains obtained using three different methods



(c) Nominal axial strains versus SG-20 axial strains

Figure 3.9: Comparison of axial strains obtained using three different methods (continued)

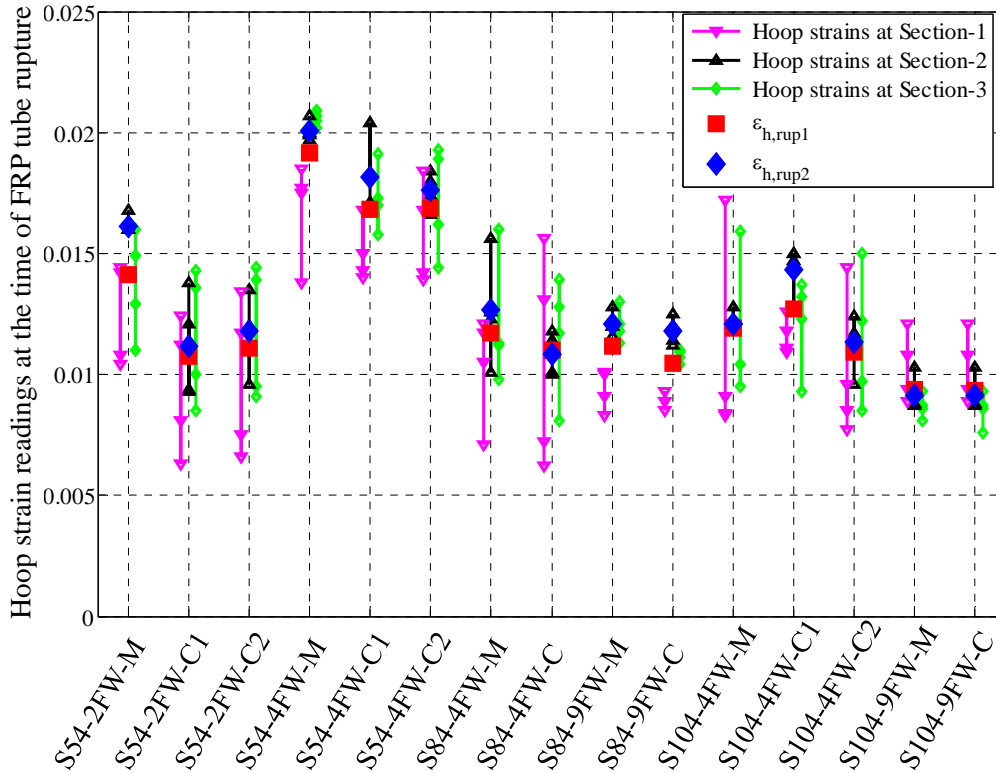
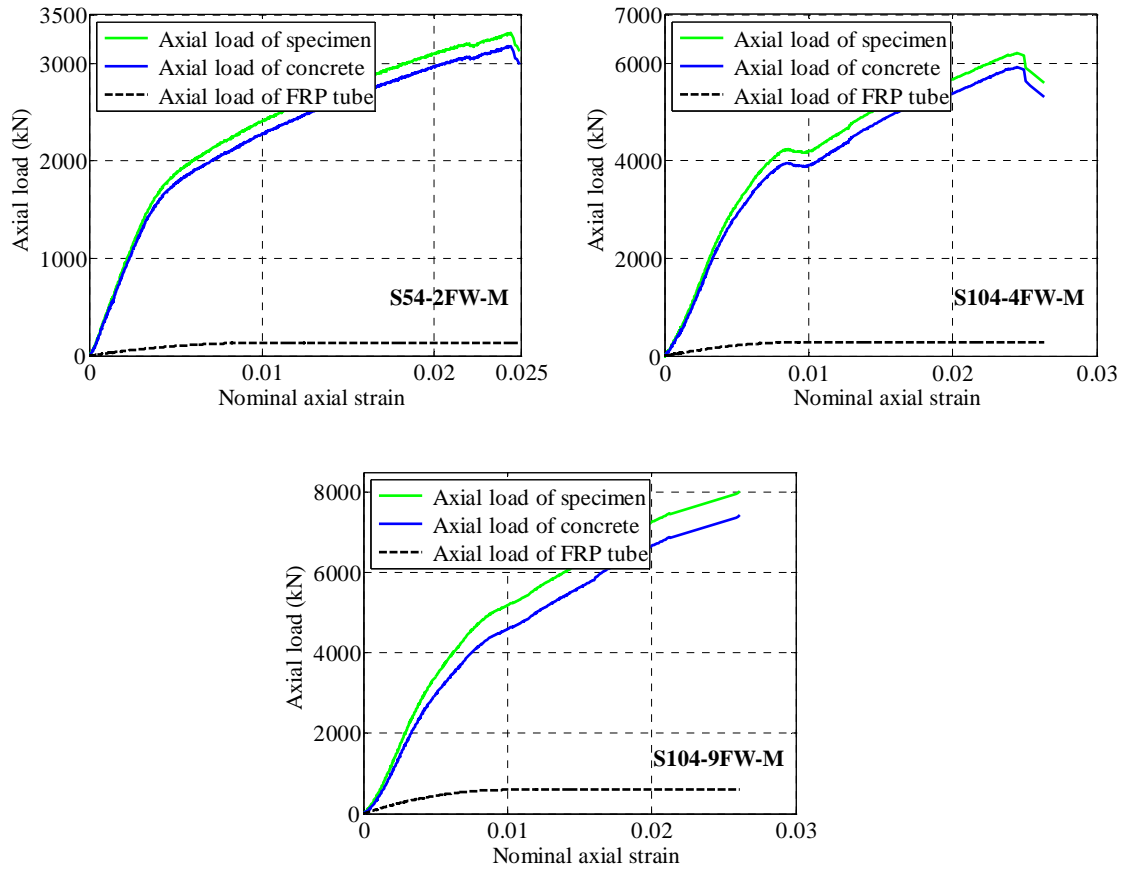
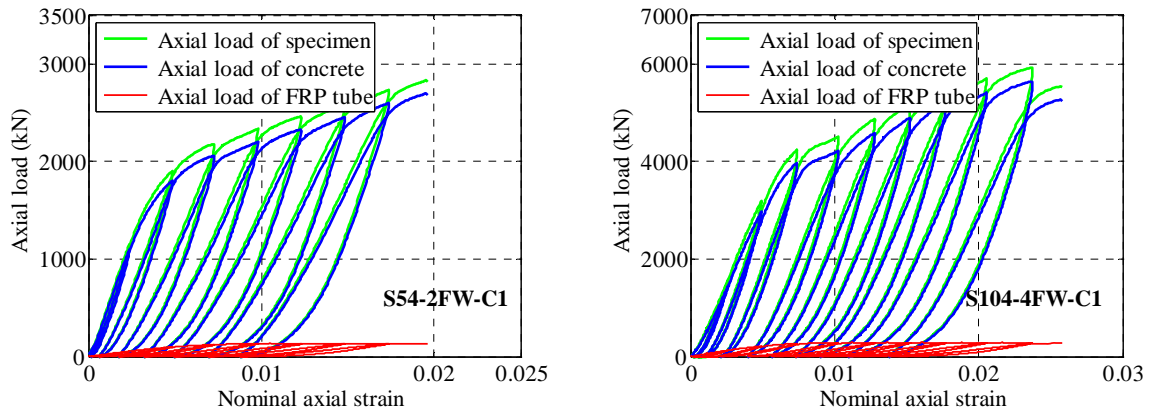


Figure 3.10: Hoop strain distributions

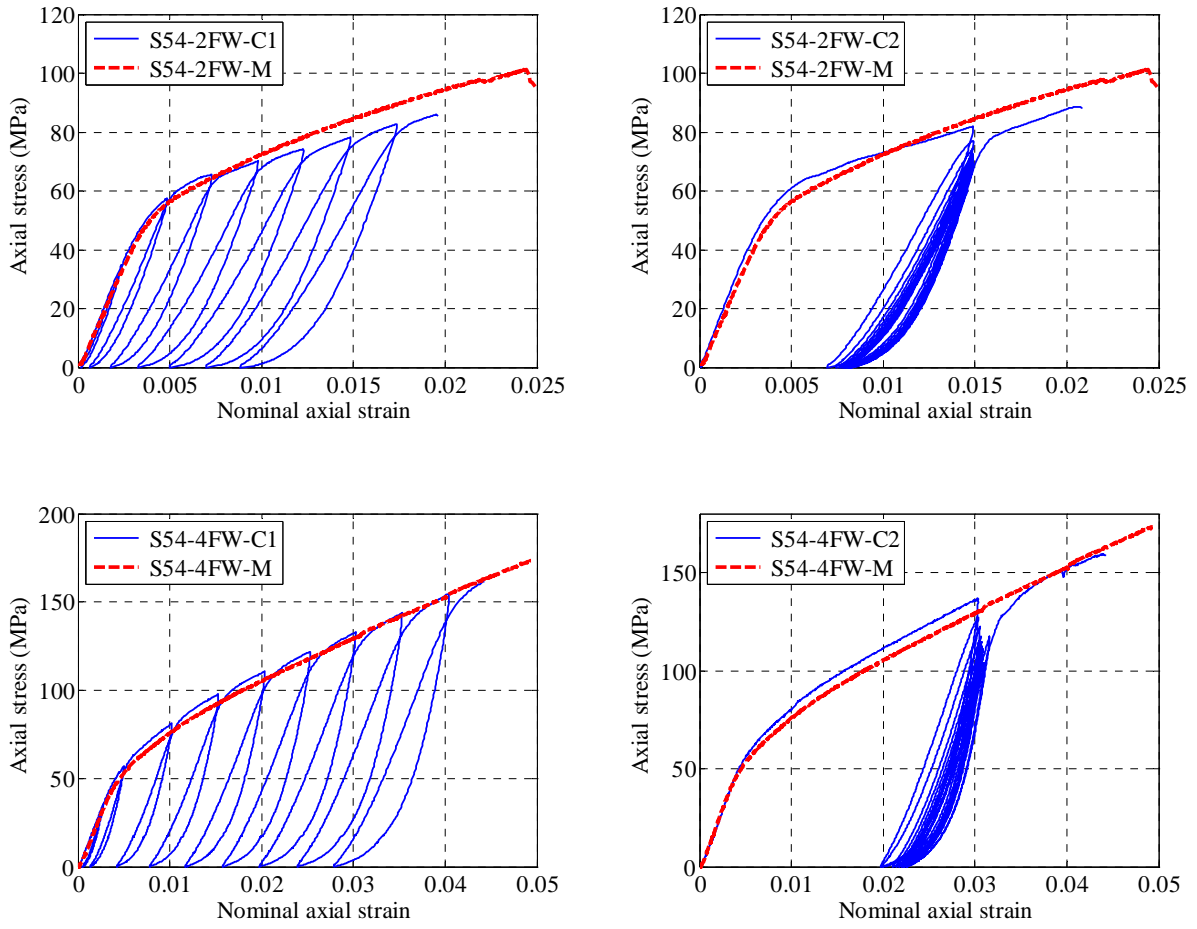


(a) CFFTs subjected to monotonic axial compression

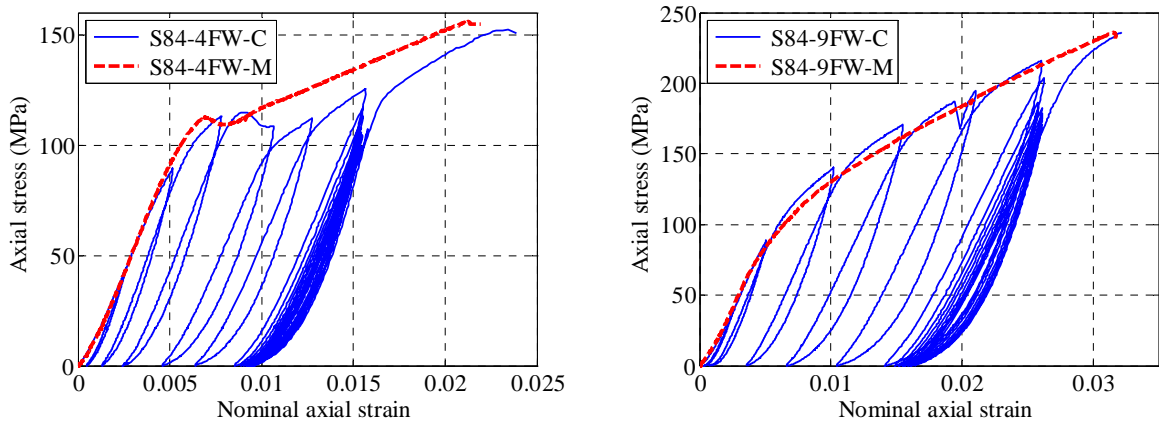


(b) CFFTs subjected to cyclic axial compression

Figure 3.11: Typical axial load-axial strain curves of CFFTs

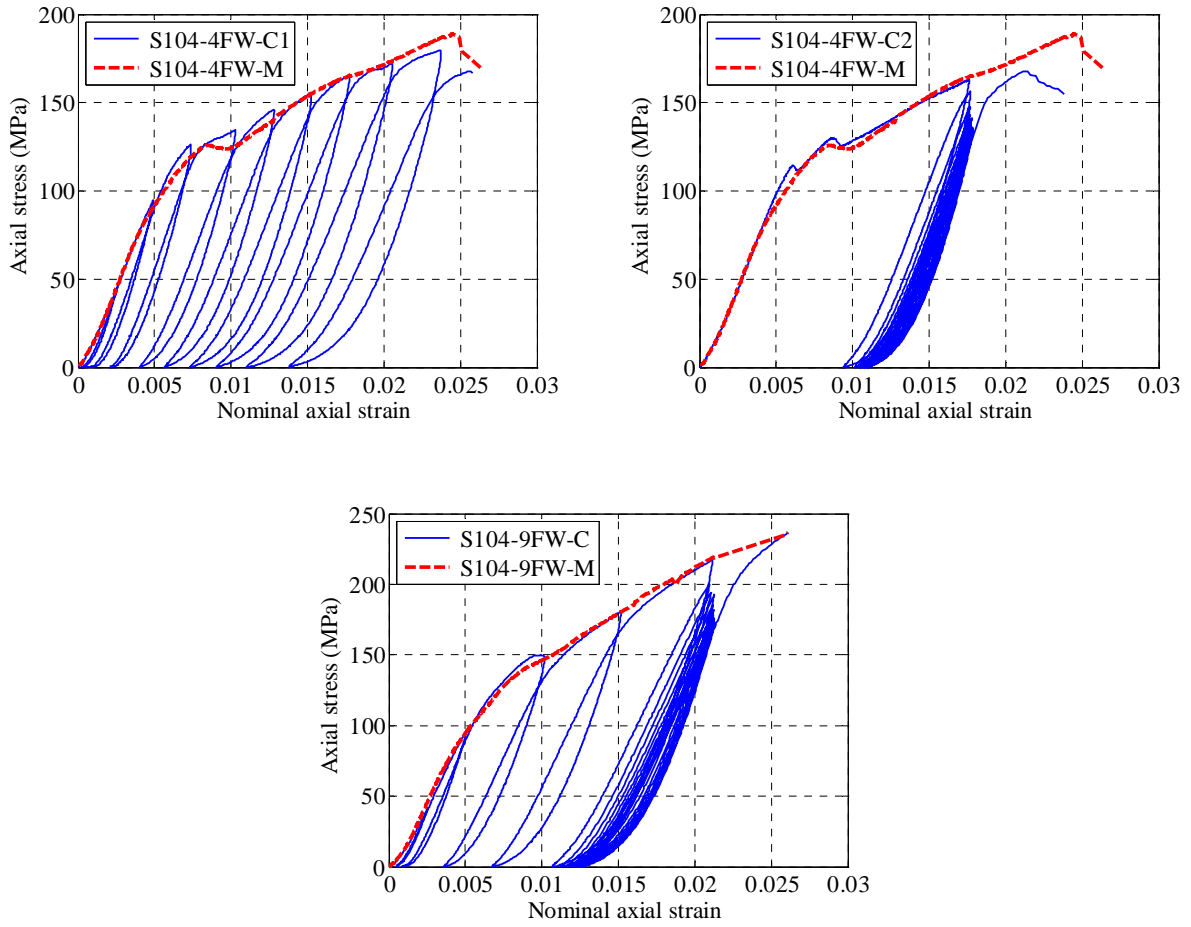


(a) Specimens of batch 1



(b) Specimens of batch 2

Figure 3.12: Axial stress-strain curves of concrete



(c) Specimens of batch 3

Figure 3.12: Axial stress-strain curves of concrete (continued)

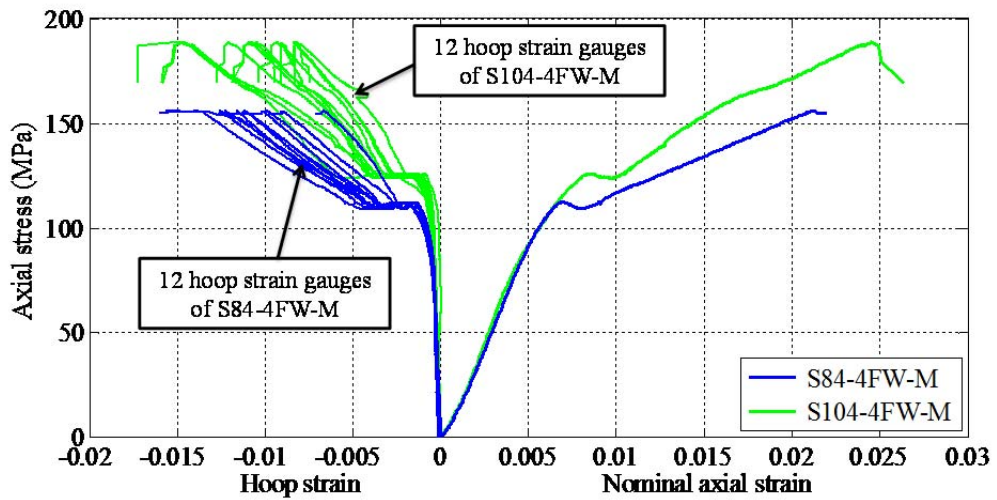
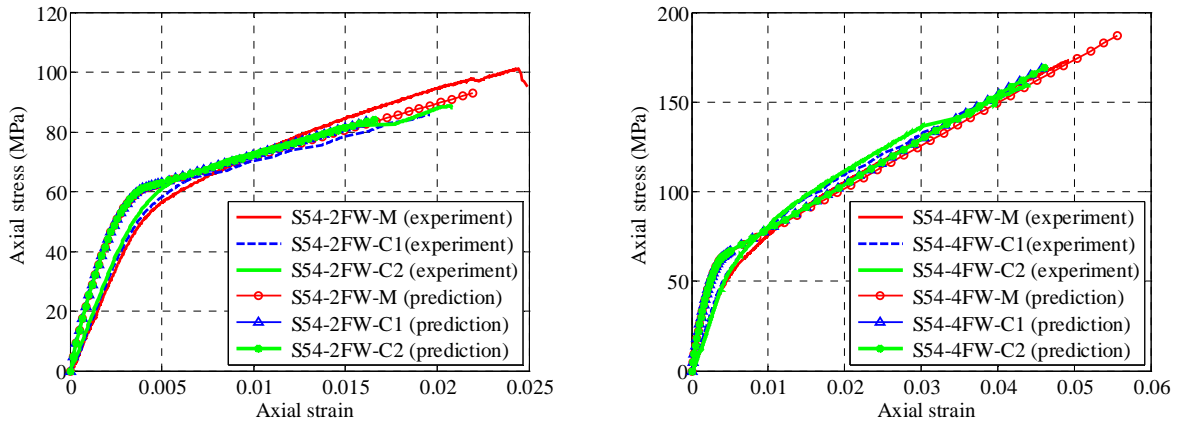
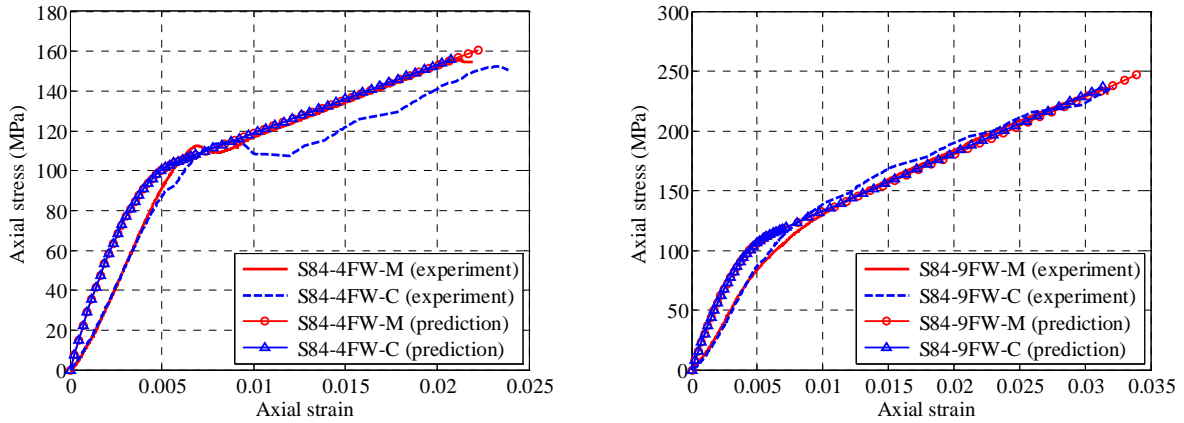


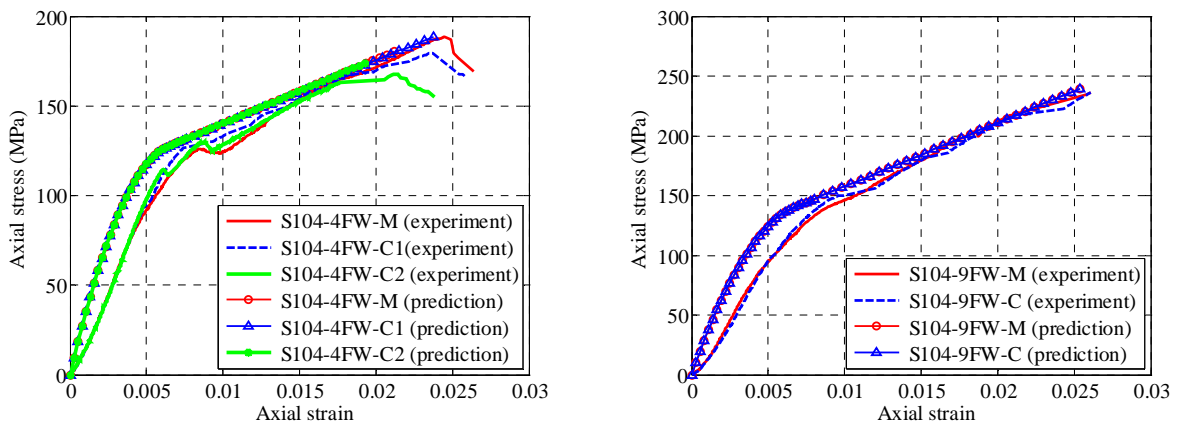
Figure 3.13: Sudden increase in the hoop strain



(a) Specimens of batch 1

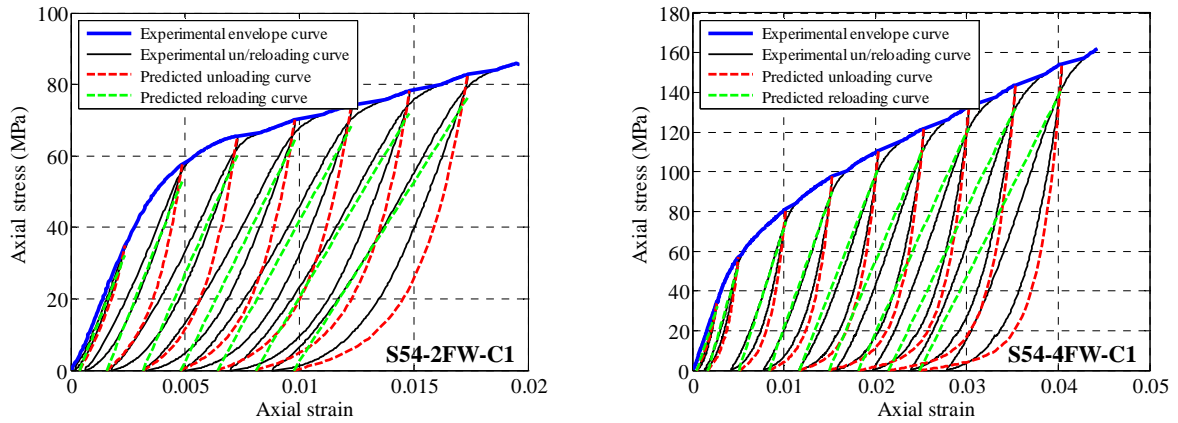


(b) Specimens of batch 2

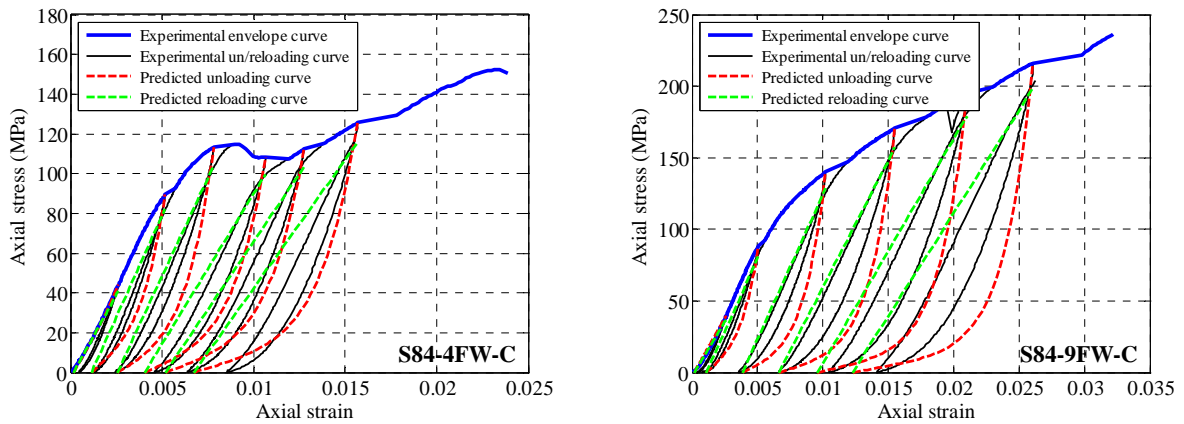


(c) Specimens of batch 3

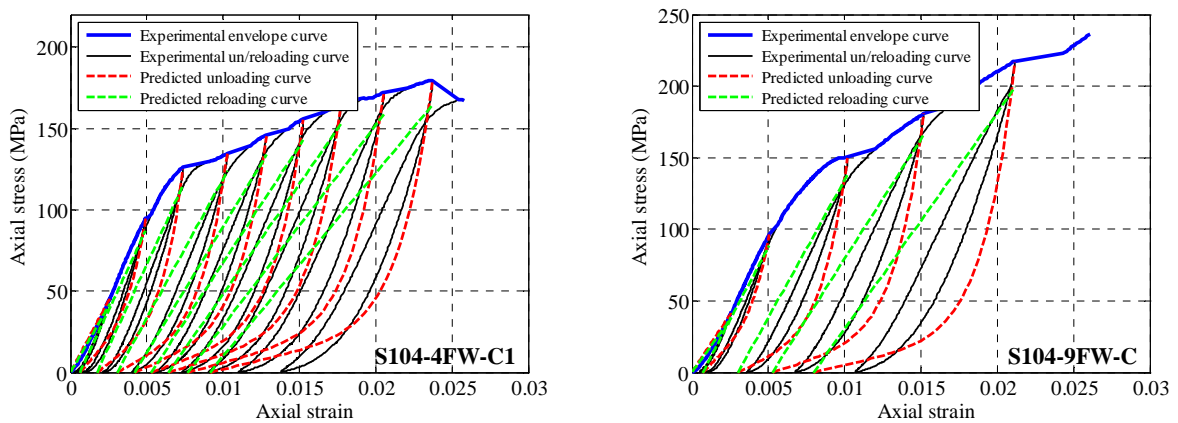
Figure 3.14: Prediction of envelope stress-strain curves with Teng *et al.*'s (2009) model



(a) Specimens of batch 1

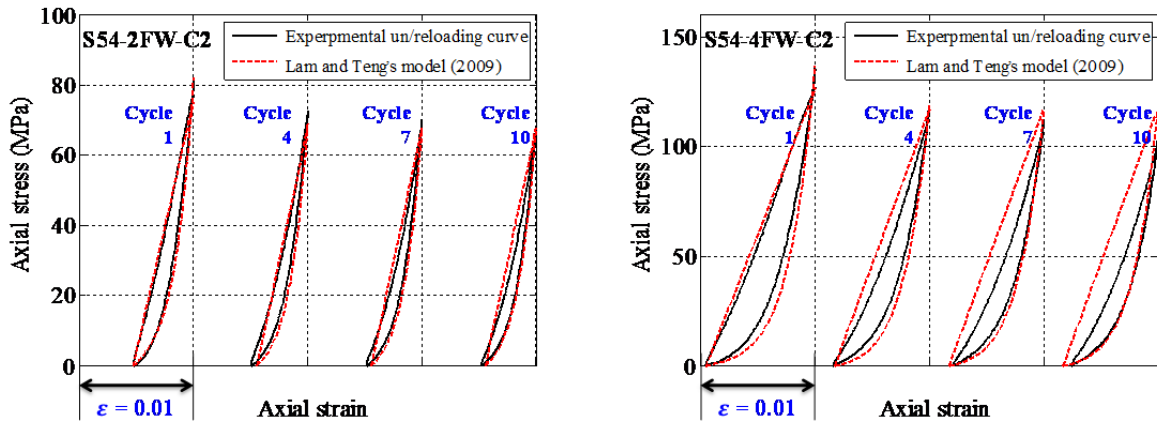


(b) Specimens of batch 2

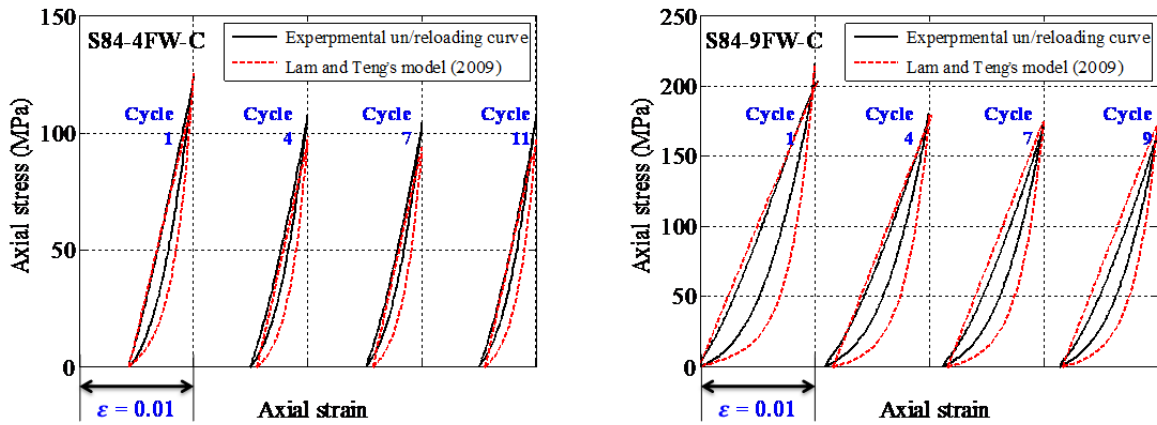


(c) Specimens of batch 3

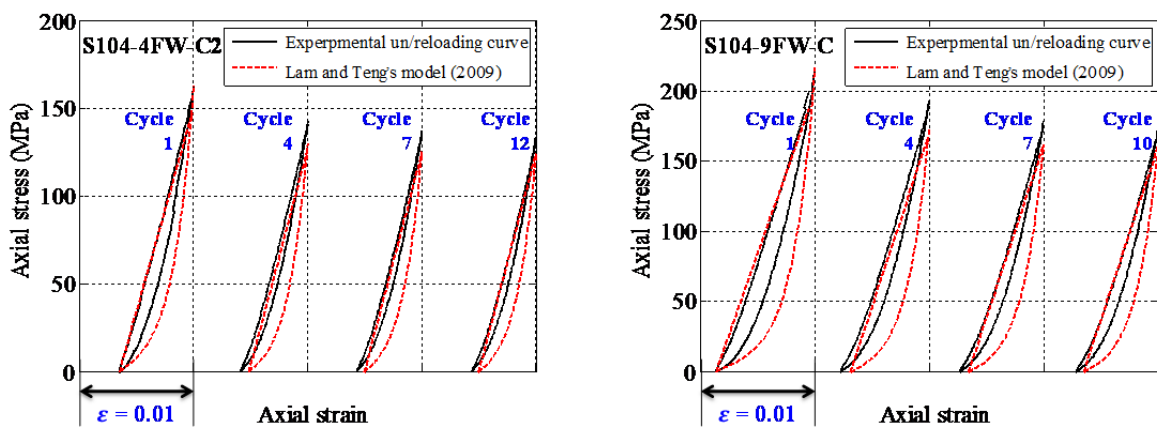
Figure 3.15: Performance of Lam and Teng's (2009) model for envelope unloading/reloading curves



(a) Specimens of batch 1



(b) Specimens of batch 2



(c) Specimens of batch 3

Figure 3.16: Performance of Lam and Teng's (2009) model for repeated unloading/reloading cycles

CHAPTER 4

UNIFIED CYCLIC STRESS-STRAIN MODEL FOR NORMAL AND HIGH STRENGTH CONCRETE CONFINED WITH FRP

4.1 INTRODUCTION

Fiber reinforced polymer (FRP) with fibers oriented completely or predominantly in the hoop direction have been widely used in civil engineering for strengthening/retrofitting concrete columns (Teng *et al.* 2002; Hollaway and Teng 2008). Due to the confinement provided by FRP tube, both the compressive strength and the ultimate compressive strain of concrete can be significantly enhanced (Lam and Teng 2002; Teng and Lam 2004). The use of FRP as a confining material has also been explored in new construction, where FRP is typically adopted in the form of a tube to confine the concrete infill with or without additional steel reinforcement (i.e. concrete-filled FRP tubes or CFFTs) (Teng *et al.* 2007; Yu and Teng 2011). In both types of applications, the stress-strain behavior of the FRP-confined concrete needs to be properly understood and modeled before a safe and economical design approach can be developed. The stress-strain behavior of FRP-confined concrete under cyclic axial compression is of particular importance for the accurate modeling of such columns under seismic loading.

A number of experimental studies (Rousakis 2001; Ilki and Kumbasar 2003; Shao *et al.* 2006; Lam *et al.* 2006; Abbasnia and Ziaadiny 2010; Ozbakkaloglu and Akin 2012; Abbasnia *et al.* 2012, 2013; Bai *et al.* 2013) have been conducted on the cyclic stress-strain behavior of concrete confined with an FRP wrap. Chapter 3 presents the first systematic experimental study on the cyclic compressive behavior of CFFTs with filament-wound FRP tube, where the cyclic stress-strain behavior of the confined concrete was a focus of the study. The study showed that the cyclic axial stress-strain behavior of concrete in CFFTs is generally similar to that of concrete confined with an FRP wrap (i.e. wet-layup FRP tube), suggesting that a cyclic stress-strain model for the confined concrete suitable for both types of applications can be developed.

To the best of my knowledge, only four cyclic stress-strain models have been proposed for FRP-confined concrete in circular columns (i.e. concrete under uniform FRP confinement) (i.e. Shao *et al.* 2006; Lam and Teng 2009; Wang *et al.* 2012; Bai *et al.* 2013). Shao *et al.*'s (2006) model was shown to be inadequate in predicting unloading paths and incapable of predicting the cumulative effect of loading history on the stress-strain response of concrete (Lam *et al.* 2006). Wang *et al.*'s (2012) model is for FRP-confined concrete as well as concrete subjected to combined confinement from FRP and hoop steel reinforcement; this model also does not consider the cumulative effect of repeated loading cycles. Lam and Teng's (2009) model was based on a test database assembled by them and was shown to capture all the key characteristics of and provide reasonably accurate predictions for cyclically loaded FRP-confined concrete. Bai *et al.*'s (2013) model is specifically for concrete confined with FRP possessing a large rupture strain (around 6%); it includes most of the components (e.g. unloading/reloading paths) of Lam and Teng's (2009) model but a different envelope stress-strain curve to reflect the effect of this special type of FRP.

Although Lam and Teng's (2009) model was developed on the basis of a relatively large database, a few significant issues could not be well resolved using the test database available to them at that time. The test database was limited to concrete confined with an FRP wrap (i.e. wet-layup FRP tube). The calibration of the model for high strength concrete (HSC) was based on limited test data from one single study (i.e. Rousakis 2001). A recent study by Ozbakkaloglu and Akin (2012) has, however, shown that the performance of Lam and Teng's (2009) model for HSC is not as good as its performance for normal strength concrete (NSC). In addition, while Lam and Teng (2009) has considered the cumulative effect of loading history in their model, their proposed equations were based on limited test data with the maximum number of repeated loading cycles at a given unloading point being three.

Against this background, this chapter presents a critical assessment of Lam and Teng's (2009) model against the new test results of CFFTs obtained in Chapter 3 as well as those of concrete confined with an FRP wrap which were published after Lam and Teng's (2009) study. An improved cyclic stress-strain model is then proposed on the basis of this assessment. The proposed model is a unified model in two senses: (1) it is applicable to both concrete confined with an FRP wrap and concrete in CFFTs; (2) it is applicable to both FRP-confined NSC and HSC. This chapter is concerned only with concrete confined with conventional FRP (e.g. glass FRP and carbon FRP) with a rupture strain less than 3%, so Bai *et al.*'s (2013) work is not further discussed in the chapter.

4.2 TEST DATABASE

In the present study, a test database was assembled from the studies of Rousakis (2001), Ilki and Kumbasar (2003), Lam *et al.* (2006), Ozbakkaloglu and Akin

(2012), Wang *et al.* (2012) and new test results in Chapter 3. Test results from the first three studies were also used by Lam and Teng (2009) for the development of their cyclic stress-strain model. Except for new test in Chapter 3 where CFFTs with a filament-wound FRP tube were tested, all the tests were conducted on circular solid cylinders confined with an FRP wrap (i.e. wet-layup FRP tube). The present study is concerned with concrete confined with FRP only, so the majority of the specimens reported in Wang *et al.* (2012), which had transverse steel reinforcement, are excluded from the test database. Key information of the tests is given in Table 4.1, while readers may refer to the original papers for more details. In Table 4.1, the thickness given for wet-layup FRP wraps is the nominal thickness, while that for filament-FRP tubes is the actual thickness; their respective elastic moduli are both based on the thicknesses listed in Table 4.1. The compressive strength of unconfined concrete was obtained from compression tests on standard plain concrete cylinders (152.5 mm x 305 mm), except for the tests of Rousakis (2001). For Rousakis's (2001) tests, the unconfined concrete strengths were converted from the data obtained from the standard cube compression test (CEB-FIP Model Code 1990).

All specimens were subjected to a single unloading/reloading cycle at each prescribed unloading displacement/load level except two specimens tested by Lam *et al.* (2006) and six specimens tested in Chapter 3. As indicated in Table 4.1, the two specimens (i.e. specimens CI-RC and CII-RC) tested by Lam *et al.* (2006) were subjected to 3 unloading/reloading cycles at each prescribed unloading displacement level and the six specimens tested in Chapter 3 were subjected to 9~12 unloading/reloading cycles at a prescribed unloading displacement level.

Linear variable displacement transducers (LVDTs) were used to obtain axial strains in all the studies. For the specimens in Rousakis (2001), Ilki and Kumbasar

(2003), Ozbakkaloglu and Akin (2012) and Chapter 3, LVDTs were used to measure the total axial shortenings of specimens; for the specimens in Lam *et al.* (2006), the LVDTs covered the 120 mm mid-height region of specimens; for the specimens in Wang *et al.* (2012), the LVDTs covered the 204 mm mid-height region. It has been shown (Lam *et al.* 2006; Chapter 3) that the strains obtained from total axial shortenings are generally similar to but slightly larger than those obtained from LVDTs covering a certain length of the mid-height region, especially in the initial stage of loading, but this effect is generally very small for the later loading stage. Lam and Teng (2009) also found that their model was generally applicable to the test database assembled by them despite the different methods of obtaining axial strains.

4.3 CYCLIC AXIAL STRESS-STRAIN MODEL

4.3.1 General

In this section, Lam and Teng's (2009) cyclic stress-strain model is first critically assessed against the test data of the new database as described above, with the focus being on its applicability to HSC and concrete in CFFTs. The key components of Lam and Teng's (2009) model are examined separately, based on which revisions are proposed, leading to an improved stress-strain model.

4.3.2 Key Characteristics of FRP-Confined Concrete

Lam and Teng's (2009) model was proposed based on and can capture the following key characteristics of the experimental cyclic stress-strain behaviour of concrete confined with an FRP wrap: (1) the envelope curve is basically the same as the monotonic stress-strain curve; (2) the loading history has a cumulative

effect on both the plastic strain and stress deterioration; (3) the unloading path is generally nonlinear with a continuously decreasing slope while the reloading path is approximately linear. It is shown in Chapter 3 that the cyclic stress-strain behaviour of concrete (including HSC) in CFFTs also possesses the same three characteristics, suggesting that the framework of Lam and Teng's (2009) model can be retained in developing an improved stress-strain model.

4.3.3 Terminology

The cyclic stress-strain history consists of unloading curves and reloading curves. The unloading curves are defined as the paths that the concrete experiences when its strain reduces. Unloading paths can be further divided into envelope unloading paths (i.e. unloading paths starting from the envelope curve) and internal unloading paths (i.e. the previous reloading path does not reach the envelope curve). They should be both independent of the subsequent terminating point. However, internal unloading paths are dependent on the prior loading history. The stress and strain where an unloading curve starts are named the unloading stress σ_{un} and the unloading strain ε_{un} respectively. For envelope unloading, the two terms are denoted by $\sigma_{un,env}$ and $\varepsilon_{un,env}$ respectively. The strain value at the intersection of an unloading path with the strain axis is defined as the plastic strain ε_{pl} . The reloading curves are defined as the paths that the concrete experiences when its strain increases. Similar to unloading paths, reloading paths are also independent of the subsequent terminating point where the concrete once again starts to unload or the concrete reaches the envelope curve. The stress and strain where a reloading curve starts are named the reloading stress σ_{re} and the reloading strain ε_{re} respectively. The stress and strain where a reloading curve meets with the corresponding envelope curve are referred as envelope returning stress $\sigma_{ret,env}$ and strain $\varepsilon_{ret,env}$ respectively.

The internal cycles, which are defined as those cycles repeated within the envelope curve, need to be numbered so that the effects of previous internal cycles on subsequent cycles can be considered. Envelope unloading is always regarded as the first cycle (i.e. $n = 1$). When the subsequent unloading stress is not greater than the present envelope unloading stress $\sigma_{un,env}$, the cycle number needs to be updated (i.e. $n = n + 1$). The number will be reset to zero when a subsequent unloading stress is greater than this envelope unloading stress $\sigma_{un,env}$. It is possible to encounter an unloading stress which is larger than the corresponding envelope unloading stress $\sigma_{un,env}$, but is smaller than the envelope returning stress $\sigma_{ret,env}$. Unloading from such an unloading stress is treated as an envelope unloading cycle following Lam and Teng (2009).

The definitions of σ_{un} , ε_{un} , $\sigma_{un,env}$, $\varepsilon_{un,env}$, ε_{pl} , σ_{re} , ε_{re} , $\sigma_{ret,env}$ and $\varepsilon_{ret,env}$ for both envelope and internal cycles are illustrated in Figure 4.1.

4.3.4 Monotonic Stress-Strain Model for the Envelope Curve

In Lam and Teng's (2009) model, Lam and Teng's (2003) monotonic stress-strain model was adopted to predict the envelope curve of FRP-confined concrete under cyclic compression. A refined version of this design-oriented model was proposed by Teng *et al.* (2009), which includes more accurate expressions for the ultimate axial strain and the compressive strength. Chapter 3 showed that Teng *et al.*'s (2009) model can provide accurate predictions for envelope stress-strain curves of concrete in CFFT. Teng *et al.*'s (2009) model is therefore adopted in the present stress-strain model for the envelope curve.

Teng *et al.*'s (2009) model consists of a parabolic first portion plus a linear second portion with a smooth transition at ε_t , and is described as follows:

$$\sigma_c = E_c \varepsilon_c - \frac{(E_c - E_2)^2}{4f'_{co}} \varepsilon_c^2 \quad \text{for } 0 \leq \varepsilon_c < \varepsilon_t \quad (4.1)$$

and

$$\sigma_c = \begin{cases} f'_{co} + E_2 \varepsilon_c & \rho_K \geq 0.01 \\ f'_{co} - \frac{f'_{co} - f'_{cu}}{\varepsilon_{cu} - \varepsilon_{co}} (\varepsilon_c - \varepsilon_{co}) & \rho_K < 0.01 \end{cases} \quad \text{for } \varepsilon_t \leq \varepsilon_c \leq \varepsilon_{cu} \quad (4.2)$$

where σ_c and ε_c are the axial stress and axial strain of concrete respectively; f'_{co} and E_c are the compressive strength and elastic modulus of unconfined concrete, respectively. The slope of the linear second portion, E_2 is given by:

$$E_2 = \frac{f'_{cc} - f'_{co}}{\varepsilon_{cu}} \quad (4.3)$$

where f'_{cc} and ε_{cu} are the compressive strength and ultimate axial strain of FRP-confined concrete, respectively. The strain at the transition point ε_t is given by:

$$\varepsilon_t = \frac{2f'_{co}}{E_c - E_2} \quad (4.4)$$

The compressive strength f'_{cc} and ultimate axial strain ε_{cu} of FRP-confined concrete are defined by:

$$\frac{f'_{cc}}{f'_{co}} = \begin{cases} 1 + 3.5(\rho_K - 0.01)\rho_\varepsilon & \rho_K \geq 0.01 \\ 1 & \rho_K < 0.01 \end{cases} \quad (4.5)$$

and

$$\frac{\varepsilon_{cu}}{\varepsilon_{co}} = 1.75 + 6.5\rho_K^{0.8}\rho_\varepsilon^{1.45} \quad (4.6)$$

The ratio between the confining pressure f_l (the pressure provided by the FRP jacket when it fails by rupture due to hoop tensile stresses) and the unconfined concrete strength f'_{co} is referred as the confinement ratio. The confinement ratio f_l/f'_{co} can be expressed as the product of the confinement stiffness ratio ρ_K and

the strain ratio ρ_ε as shown follows:

$$\frac{f_l}{f'_{co}} = \frac{E_{frp} t_{frp} \varepsilon_{h,rup}}{f'_{co} R} = \rho_K \rho_\varepsilon \quad (4.7)$$

$$\rho_K = \frac{E_{frp} t_{frp}}{(f'_{co}/\varepsilon_{co})R} \quad (4.8)$$

$$\rho_\varepsilon = \frac{\varepsilon_{h,rup}}{\varepsilon_{co}} \quad (4.9)$$

where E_{frp} and t_{frp} are the elastic modulus and thickness of the FRP jacket, ε_{co} is the axial strain at the compressive strength of unconfined concrete, $\varepsilon_{h,rup}$ is the FRP hoop rupture strain, and R is the radius of the confined concrete core. It should be noted that f'_{cu} in Eq. 4.2 is found from Eq. 4.10, which predicts the axial stress at the ultimate axial strain, but not the compressive strength f'_{cc} of FRP-confined concrete; actually, the two values are the same unless the stress-strain curve has a descending branch (Teng *et al.* 2009).

$$\frac{f'_{cu}}{f'_{co}} = 1 + 3.5(\rho_K - 0.01)\rho_\varepsilon \quad (4.10)$$

4.3.5 Unloading Path

An unloading path is defined as the stress-strain path that the concrete experiences when its strain reduces. Lam and Teng (2009) proposed the following equations (Eqs. 4.11-4.16) for both internal and envelope unloading, which are adopted in the present model:

$$\sigma_c = a\varepsilon_c^\eta + b\varepsilon_c + c \quad (4.11)$$

with

$$a = \frac{\sigma_{un} - E_{un,0}(\varepsilon_{un} - \varepsilon_{pl})}{\varepsilon_{un}^{\eta} - \varepsilon_{pl}^{\eta} - \eta\varepsilon_{pl}^{\eta-1}(\varepsilon_{un} - \varepsilon_{pl})} \quad (4.12)$$

$$b = E_{un,0} - \eta\varepsilon_{pl}^{\eta-1}a \quad (4.13)$$

$$c = -a\varepsilon_{pl}^{\eta} - b\varepsilon_{pl} \quad (4.14)$$

$$\eta = 350\varepsilon_{un} + 3 \quad (4.15)$$

$$E_{un,0} = \min\left(\frac{0.5f'_{co}}{\varepsilon_{un}}, \frac{\sigma_{un}}{\varepsilon_{un} - \varepsilon_{pl}}\right) \quad (4.16)$$

in which, σ_c and ε_c are the axial stress and axial strain of concrete respectively; and $E_{un,0}$ is the slope of the unloading path at zero stress (Figure 4.1).

Figure 4.2 shows a comparison between the predictions of the above equations and the experimental envelope unloading curves from new tests in Chapter 3. In making the predictions, the experimental ε_{un} , σ_{un} and ε_{pl} were used so that the comparison in Figure 4.2 reflects only the performance of the equations for the unloading path (i.e. Eqs. 4.11-4.16). Figure 4.2 shows that Eqs. 4.11-4.16 provide reasonably accurate predictions for specimens S54-2FW-C1 and S54-4FW-C1, but the predictions deviate significantly from the experimental results for the remaining specimens which had higher unconfined strengths. This observation suggests that Lam and Teng's (2009) model may be applicable to FRP-confined NSC, but revisions are needed before Lam and Teng's (2009) model can accurately predict the unloading paths of FRP-confined HSC. This is probably due to the fact that the development of Lam and Teng's (2009) model relied heavily on the experimental results by Lam et al. (2006) which only covered a small range of

concrete strengths (i.e. 38.9 MPa and 41.1 MPa).

In Lam and Teng's (2009) model, two parameters are used to control the shape of the unloading path: (1) parameter η which controls the rate of change in the degree of non-linearity (or the curvature) of an unloading path with the unloading strain; (2) parameter $E_{un,0}$ which controls the slope of the unloading path at zero stress. Lam and Teng (2009) proposed Eq. 4.16 for $E_{un,0}$ where the unconfined concrete strength f'_{co} is already a parameter. Figure 4.3 compares the predictions of Eq. 4.16 with the experimental results, and demonstrates its applicability to HSC. The inaccuracy of Lam and Teng's (2009) model for HSC is therefore believed to be mainly due to their equation for η (i.e. Eq. 4.15) which does not reflect the effect of unconfined concrete strength f'_{co} . Based on the experimental results in Chapter 3, the following equation was derived through a trial and error process, with f'_{co} being an additional controlling parameter:

$$\eta = 40(350\varepsilon_{un} + 3)/f'_{co} \quad (4.17)$$

Eq. 4.17 reduces to Eq. 4.15 when f'_{co} is equal to 40 MPa. Figure 4.2 shows that the use of the new equation leads to much better predictions than the use of Eq. 4.15 in Lam and Teng (2009), especially for specimens S84-4FW-C, S84-9FW-C, S104-4FW-C1 and S104-9FW-C.

4.3.6 Plastic Strain of Envelope Cycles

Lam and Teng (2009) proposed the following equation to predict the plastic strain of envelope unloading curves $\varepsilon_{pl,1}$, where the unconfined concrete strength f'_{co} and the envelope unloading strain $\varepsilon_{un,env}$ are the two controlling parameters:

$$\varepsilon_{pl,1} = \begin{cases} 0 & 0 < \varepsilon_{un,env} \leq 0.001 \\ [1.4(0.87 - 0.004f'_{co}) - 0.64](\varepsilon_{un,env} - 0.001) & 0.001 < \varepsilon_{un,env} < 0.0035 \\ (0.87 - 0.004f'_{co})\varepsilon_{un,env} - 0.0016 & 0.0035 \leq \varepsilon_{un,env} \leq \varepsilon_{cu} \end{cases} \quad (4.18)$$

In Lam and Teng (2009), the development of Eq. 4.18 was based on: (1) the experimental observation that the plastic strain is independent of the confinement level and has a linear relationship with the envelope unloading strain; (2) the limited test results by Rousakis (2001), Ilki and Kumbasar (2003) and Lam et al. (2006) among which only Rousakis's (2001) study covered HSC. While the first observation has been continuously supported by new test results (e.g. Wang et al. 2012; Ozbakkaloglu and Akin 2012), a recent experimental study on FRP-confined HSC by Ozbakkaloglu and Akin (2012) suggested that the unconfined concrete strength does not appear to have a considerable effect on the envelope plastic strain. Ozbakkaloglu and Akin (2012) also showed that Eq. 4.18 provides reasonably accurate predictions for their test results on NSC, but underestimates the plastic strain of envelope unloading curves $\varepsilon_{pl,1}$ significantly based on their test results for HSC.

To clarify this issue, the plastic strains obtained from new tests in Chapter 3 are shown against the corresponding envelope unloading strains in Figure 4.4, where the trend lines for $\varepsilon_{un,env} > 0.0035$ are also shown. Table 4.2 summarizes the statistical characteristics of the trend lines for specimens in Table 4.1 including the three studies used in Lam and Teng (2009). Figure 4.4 confirms the linear relationship between the plastic strain $\varepsilon_{pl,1}$ and the envelope unloading strain $\varepsilon_{un,env}$. Table 4.2, however, suggests that such a linear relationship is not significantly affected by the unconfined concrete strength. The coefficient a (i.e. the slope of the trend line) is further shown against the unconfined concrete

strength in Figure 4.5, which clearly indicates that this coefficient is similar for most specimens covering a range of unconfined concrete strength from 24.5 MPa to 105 MPa. The only exceptions appear to be the three HSC specimens tested by Rousakis (2001) which had a lower a value. It should be noted that these three specimens were also the only HSC specimens used in Lam and Teng (2009) in developing Eq. 4.18, which includes the unconfined concrete strength as a controlling parameter. For further comparison, the predictions of Eq. 4.18 are also shown in Figure 4.6a, and are seen to significantly underestimate the experimental results of FRP-confined HSC from most studies including the present study.

Based on the experimental results summarized in Table 4.2, the following equations are proposed for the plastic strain of envelope curves, where the unconfined strength is not used as a parameter:

$$\varepsilon_{pl,1} = \begin{cases} 0 & 0 < \varepsilon_{un,env} \leq 0.001 \\ 0.184\varepsilon_{un,env} - 0.0002 & 0.001 < \varepsilon_{un,env} \leq 0.0035 \\ 0.703\varepsilon_{un,env} - 0.002 & 0.0035 < \varepsilon_{un,env} \leq \varepsilon_{cu} \end{cases} \quad (4.19)$$

In the development of Eq. 4.19, the two coefficients a and b are obtained by averaging the a and b values listed in Table 4.2 for all the specimens. Figure 4.6b shows that Eq. 4.19 can provide reasonably accurate predictions for the majority of the test results and is far superior to Eq. 4.18 proposed by Lam and Teng (2009).

4.3.7 Stress Deterioration of Envelope Cycles

It has been commonly observed (e.g. Lam *et al.* 2006) that the new stress $\sigma_{new,1}$ on the first reloading path at the envelope unloading strain is lower than the envelope unloading stress. This phenomenon is referred to as stress deterioration.

Lam and Teng (2009) proposed the following equations for the stress deterioration ratio ϕ_1 of envelope cycles:

$$\phi_1 = \begin{cases} 1 & 0 < \varepsilon_{un,env} \leq 0.001 \\ 1 - 80(\varepsilon_{un,env} - 0.001) & 0.001 < \varepsilon_{un,env} < 0.002 \\ 0.92 & 0.002 \leq \varepsilon_{un,env} \leq \varepsilon_{cu} \end{cases} \quad (4.20)$$

where ϕ_1 is defined as

$$\phi_1 = \frac{\sigma_{new,1}}{\sigma_{un,env}} \quad (4.21)$$

The performance of Eq. 4.20 is shown in Figure 4.7 against the experimental results in Chapter 3 and two other studies published after Lam and Teng (2009). Figure 4.7 shows that Eq. 4.20 provides reasonably accurate predictions except for the envelope unloading strains $\varepsilon_{un,env}$ which are between 0.001 and 0.035. For this range of $\varepsilon_{un,env}$, the predictions of Eq. 4.20 appear to be on the lower bound. In order to address this deficiency of Eq. 4.20, the following equations are proposed based on all the available test data:

$$\phi_1 = \begin{cases} 1 & 0 < \varepsilon_{un,env} \leq 0.001 \\ 1 - 32(\varepsilon_{un,env} - 0.001) & 0.001 < \varepsilon_{un,env} \leq 0.0035 \\ 0.92 & 0.0035 < \varepsilon_{un,env} \leq \varepsilon_{cu} \end{cases} \quad (4.22)$$

The predictions of Eq. 4.22 are shown to be better than Lam and Teng's (2009) equation, especially for the cases where $0.001 < \varepsilon_{un,env} \leq 0.0035$ (Figure 4.7). The use of 0.0035 instead of 0.002 as a threshold is also consistent with the equation for the plastic strain (i.e. Eq. 4.19).

4.3.8 Effect of Loading History

It is evident from Lam *et al.* (2006) on concrete confined with an FRP wrap and the new test results in Chapter 3 on CFFTs that the loading history has a cumulative effect on both the plastic strain and stress deterioration. The cumulative effect of loading history is considered in Lam and Teng's (2009) model, but their proposed equations were based on only data from Lam *et al.* (2006) where the maximum number of repeated loading cycles at a given unloading point was three. In this section, Lam and Teng's (2009) equations are evaluated against new test results in Chapter 3 where the maximum number of repeated loading cycles ranged from 9 to 12. Revisions to Lam and Teng's (2009) equations are then proposed wherever necessary.

4.3.8.1 Partial Unloading and Reloading

In some cases, an unloading curve is terminated before reaching the zero stress point, or a reloading curve is terminated before reaching the reference strain (defined in Eq. 4.25, normally equal to the envelope unloading strain). These cases are referred to as partial unloading and partial reloading respectively. In the present study, the following definitions for the partial unloading factor $\beta_{un,n}$ and the partial reloading factor $\gamma_{re,n}$ are used to consider the effect of partial unloading/reloading, following Lam and Teng (2009):

$$\beta_{un,1} = \frac{\sigma_{un,env} - \sigma_{re,1}}{\sigma_{un,env}} \quad n = 1$$

$$\beta_{un,n} = \frac{\sigma_{un,n} - \sigma_{re,n}}{\sigma_{new,n-1}} \quad n > 2 \quad (4.23)$$

$$\gamma_{re,n} = \frac{\varepsilon_{un,n+1} - \varepsilon_{pl,n}}{\varepsilon_{ref,n} - \varepsilon_{pl,n}} \quad (n = 1, 2, 3, \dots) \quad (4.24)$$

where $\varepsilon_{un,n}$, $\sigma_{un,n}$, $\varepsilon_{pl,n}$ and $\sigma_{new,n}$ are the unloading strain, unloading stress, plastic strain, new stress at the reference strain of the n^{th} loading cycle respectively; the reference strain point is defined by:

$$\begin{aligned} \varepsilon_{ref,1} &= \varepsilon_{un,env} & n &= 1 \\ \varepsilon_{ref,n} &= \max(\varepsilon_{ref,n-1}, \varepsilon_{un,n}) & n &> 2 \end{aligned} \quad (4.25)$$

$$\begin{aligned} \sigma_{ref,1} &= \sigma_{un,env} & n &= 1 \\ \sigma_{ref,n} &= \begin{cases} \sigma_{ref,1} & \varepsilon_{un,n} \leq \varepsilon_{ref,n-1} \\ \sigma_{un,n} & \varepsilon_{un,n} > \varepsilon_{ref,n-1} \end{cases} & n &> 2 \end{aligned} \quad (4.26)$$

The following conditions proposed by Lam and Teng (2009) for effective unloading/reloading cycles are also adopted in the present study:

$$\beta_{un} \geq 0.7 \text{ and } \gamma_{re} \geq 0.7 \quad (4.27)$$

4.3.8.2 Plastic Strain of Internal Cycles

Lam and Teng (2009) proposed the following equations for plastic strains of internal cycles:

$$\omega_n = \frac{\varepsilon_{un,n} - \varepsilon_{pl,n}}{\varepsilon_{un,n} - \varepsilon_{pl,n-1}} \quad n \geq 2 \quad (4.28)$$

$$\omega_n = \min \left\{ \omega_{n,ful} - 0.25(\gamma_{re,n-1} - 1), 1 \right\} \quad n \geq 2 \quad (4.29)$$

$$\begin{aligned} \omega_{n,ful} \quad (2 \leq n_e \leq 5) &= \begin{cases} 1 \\ 1 + 400(0.0212n_e - 0.12)(\varepsilon_{un,env} - 0.001) \\ 0.0212n_e + 0.88 \end{cases} \\ & \quad \begin{aligned} & 0 < \varepsilon_{un,env} \leq 0.001 \\ & 0.001 < \varepsilon_{un,env} < 0.0035 \\ & 0.0035 \leq \varepsilon_{un,env} \leq \varepsilon_{cu} \end{aligned} \end{cases} \quad (4.30)$$

in which $\varepsilon_{un,n}$ and $\varepsilon_{pl,n}$ are the unloading strain and plastic strain of the n^{th} loading cycle respectively from an envelope unloading strain $\varepsilon_{un,env}$, with $n=1$ representing the envelope cycle; ω_n is the strain recovery ratio; $\omega_{n,ful}$ is the strain recovery ratio for the case of $\gamma_{re,n-1} = 1$ (i.e. full reloading); and n_e is the number of effective cycles. Lam and Teng (2009) proposed that Eq. 4.30 is only applicable when $2 \leq n_e \leq 5$, and that $\omega_{n,ful} = 1$ when $n_e \geq 6$.

The predictions of Eq. 4.30 are compared with the new test results of Chapter 3 in Figure 4.8. The test results presented in Lam et al. (2006) are also shown in Figure 4.8 for comparison. Figure 4.8 shows that Eq. 4.30 generally provides reasonably accurate predictions when $n_e < 5$ for both concrete confined with an FRP wrap and concrete in CFFTs, but overestimates the test results when $n_e \geq 6$. This is understandable as Eq. 4.30 was developed based on the limited test results with the maximum n_e being 3. In order to address this deficiency of Lam and Teng's (2009) model, the following equations are proposed for ω_n based on regression analysis of the mean $\omega_{n,ful}$ values from all the available test data (Figure 4.8):

$$\omega_{n,ful} (n_e \geq 2) = \begin{cases} 1 & 0 < \varepsilon_{un,env} \leq 0.001 \\ 1 - 32(\varepsilon_{un,env} - 0.001)/(n_e - 1) & 0.001 < \varepsilon_{un,env} \leq 0.0035 \\ -0.08/(n_e - 1) + 1 & 0.0035 < \varepsilon_{un,env} \leq \varepsilon_{cu} \end{cases} \quad (4.31)$$

4.3.8.3 Stress Deterioration of Internal Cycles

Lam and Teng (2009) proposed the following equations for stress deterioration ratios of internal cycles:

$$\phi_n = \frac{\sigma_{new,n}}{\sigma_{ref,n}} \quad (4.32)$$

$$\phi_n = \min \left\{ \begin{array}{l} 1 \\ \phi_{n,ful} - 0.2(\beta_{un,n} - 1) \end{array} \right. \quad n \geq 2 \quad (4.33)$$

$$\phi_{n,ful} (2 \leq n_e \leq 5) = \begin{cases} 1 \\ 1 + 1000(0.013n_e - 0.075)(\varepsilon_{un,env} - 0.001) \\ \quad 0.013n_e + 0.925 \end{cases} \quad (4.34)$$

$$\begin{array}{l} 0 < \varepsilon_{un,env} \leq 0.001 \\ 0.001 < \varepsilon_{un,env} < 0.002 \\ 0.002 \leq \varepsilon_{un,env} \leq \varepsilon_{cu} \end{array}$$

in which ϕ_n is the stress deterioration ratio of the n^{th} loading cycle from an envelope unloading strain $\varepsilon_{un,env}$; $\phi_{n,ful}$ is the stress deterioration ratio for the case of $\beta_{un,n} = 1$. Lam and Teng (2009) proposed Eq. 4.34 for use when $2 \leq n_e \leq 5$, and that $\phi_{n,ful} = 1$ when $n_e \geq 6$.

The predictions of Eq. 4.34 are compared with the new test results of Chapter 3 in Figure 4.9. The test results presented in Lam et al. (2006) are also shown in Figure 4.9 for comparison. Similar to the observation for Lam and Teng's (2009) equations for plastic strains, Eq. 4.34 generally provides reasonably accurate predictions when $n_e < 5$, but overestimates the test results when $n_e \geq 6$. In order to address this deficiency of Lam and Teng's (2009) model, the following equations (Eq. 4.35) are proposed for $\phi_{n,ful}$ based on regression analysis of the mean $\phi_{n,ful}$ values from all the available test data:

$$\phi_{n,ful} = \begin{cases} 1 \\ 1 - 80(\varepsilon_{un,env} - 0.001)/n_e \\ \quad -0.08/n_e + 1 \end{cases} \quad \begin{array}{l} 0 < \varepsilon_{un,env} \leq 0.001 \\ 0.001 < \varepsilon_{un,env} \leq 0.002 \\ 0.002 < \varepsilon_{un,env} \leq \varepsilon_{cu} \end{array} \quad (4.35)$$

4.3.9 Reloading Path

A reloading path is defined as the stress-strain path that the concrete traces as its strain increases from a starting point on an unloading path. Lam and Teng (2009) proposed equations for the reloading path based on the test observation that the major part of each reloading path of FRP-confined concrete resembles a straight line. In Lam and Teng's (2009) model, the reloading path consists of a linear first portion from the reloading strain ε_{re} to the reference strain ε_{ref} , and a possible short parabolic portion for the remaining part to meet smoothly with the envelope curve.

The linear portion of the reloading path is defined as follows:

$$\sigma_c = \sigma_{re} + E_{re}(\varepsilon_c - \varepsilon_{re}) \quad \varepsilon_{re} \leq \varepsilon_c \leq \varepsilon_{ref} \quad (4.36)$$

where the slope of the linear portion is found from:

$$E_{re} = (\sigma_{new} - \sigma_{re})/(\varepsilon_{ref} - \varepsilon_{re}) \quad \varepsilon_{re} \leq \varepsilon_c \leq \varepsilon_{ref} \quad (4.37)$$

In most cases, the linear portion is followed by a parabolic curve from the reference strain point to the envelope returning point. For some cases, the reloading path has only a straight line which returns to the envelope curve directly at the envelope unloading point. These cases are (Lam and Teng 2009): (1) $\varepsilon_{un,env} \leq 0.001$; (2) $n = 1$; $\varepsilon_{un,env} > 0.001$; $\sigma_{re,1} > 0.85\sigma_{un,env}$; and (3) $n > 1$; $\varepsilon_{un,env} > 0.001$; $\sigma_{re,n} > 0.85\sigma_{un,env}$.

The parabolic portion of the reloading path is given as follows:

$$\sigma_c = A\varepsilon_c^2 + B\varepsilon_c + C \quad \varepsilon_{ref} \leq \varepsilon_c \leq \varepsilon_{ret,env} \quad (4.38)$$

For cases where the reloading path returns to the parabolic first portion of the envelope curve, the parameter A is as follows:

$$A = \frac{(E_c - E_2)^2(E_{re}\varepsilon_{ref} - \sigma_{new}) + (E_c - E_2)^2 f'_{co}}{4(\sigma_{new} - E_c\varepsilon_{ref})f'_{co} + (E_c - E_2)^2 \varepsilon_{ref}^2}$$

$$\varepsilon_{ret,env} = \frac{E_c - B}{2A + \left(\frac{E_c - E_2}{f'_{co}}\right)^2} < \varepsilon_t \quad (4.39)$$

For cases where the reloading path returns to the linear section portion of the envelope curve, the parameter A is as follows:

$$A = \frac{(E_c - E_2)^2}{4(\sigma_{new} - f'_{co} - E_2\varepsilon_{ref})} \quad \varepsilon_{ret,env} = \frac{E_c - B}{2A} \geq \varepsilon_t \quad (4.40)$$

The other two parameters, B and C, are as follows:

$$B = E_{re} - 2A\varepsilon_{ref} \quad (4.41)$$

$$C = \sigma_{new} - A\varepsilon_{ref}^2 - B\varepsilon_{ref} \quad (4.42)$$

Apparently, the new stress σ_{new} , which determines the slope of the linear portion, is a key parameter for the reloading path. Given that σ_{new} is accurately predicted by the new equations proposed in the present study (Eqs. 4.21-4.22, 4.32-4.33, 4.35), it is reasonable to expect that Eqs. 4.36-4.42 can also provide close predictions for the test results of FRP-confined HSC whose reloading paths also have a major part resembling a straight line. Eqs. 4.36-4.42 are therefore adopted in the proposed model.

4.3.10 Summary of the Proposed Model

To summarize, the proposed cyclic stress-strain model for FRP-confined concrete include:

- (1) Teng *et al.*'s (2009) model (Eqs. 4.1-4.10) for the envelope stress-strain curve;
- (2) Lam and Teng's (2009) equations (Eqs. 4.11-4.14) for the unloading path, with their original equation (Eq. 4.16) for $E_{un,0}$ and the newly proposed Eq. 4.17 for η ;
- (3) Eqs. 4.19 and 4.22 proposed herein for the plastic strain and stress deterioration ratio of envelope cycles, respectively;
- (4) Lam and Teng's (2009) equations (Eqs. 4.23-4.27) for partial unloading and reloading;
- (5) Lam and Teng's (2009) equations (Eqs. 4.28-4.29) for the plastic strain of internal cycles, with the newly proposed Eq. 4.31 for $\omega_{n,ful}$;
- (6) Lam and Teng's (2009) equations (Eqs. 4.32-4.33) for stress deteriorations of internal cycles, with the newly proposed Eq. 4.35 for $\phi_{n,ful}$; and
- (7) Lam and Teng's (2009) equations (Eqs. 4.36-4.42) for the reloading path.

The process of generating cyclic stress-strain curves is similar to that explained in Lam and Teng (2009).

4.4 PERFORMANCE OF THE PROPOSED MODEL

4.4.1 Envelope Unloading/Reloading Curves

The predictions of the proposed model are compared with the experimental results of Chapter 3 in Figure 4.10 for envelope unloading/reloading cycles. The

predictions of Lam and Teng's (2009) model are also shown for comparison. It is evident from Figure 4.10 that the proposed model is superior to Lam and Teng's (2009) model, especially for specimens in the S84 and S104 series. The proposed model generally provides reasonably accurate predictions, but considerable errors are also seen for some specimens (i.e. specimens S84-9FW-C and S104-9FW-C). The errors are found to be mainly from the inaccuracy in predicting the envelope plastic strain, $\varepsilon_{pl,1}$. The equation proposed in the present study (i.e. Eq. 4.19) for $\varepsilon_{pl,1}$ is based on a regression analysis of all the available test data while there is considerable scatter in the test data (Figure 4.6). When the experimental envelope strains of the three specimens (i.e. specimens S54-2FW-C1, S84-9FW-C and S104-9FW-C) are used, Figure 4.11 shows that the proposed model compares very well with the test results and is far superior to Lam and Teng's (2009) model.

4.4.2 Repeated Unloading/Reloading Curves

Figure 4.12 shows comparisons between the experimental results and the predictions of the two models [i.e. the proposed model and Lam and Teng's (2009) model] for repeated unloading/reloading cycles. In order to assess these unloading/reloading cycles clearly, each cycle is shown with the corresponding predicted cycle individually to avoid the over-crowding of curves at the same unloading strain. Only the 1st, 4th, 7th, and the last cycles are examined here. In Figure 4.12, the experimental plastic strains of envelope cycles $\varepsilon_{pl,1}$ are used instead of Eq. 4.19, in order to eliminate the effect of inaccuracy in this equation. Again, the proposed model is shown to be superior to Lam and Teng's (2009) model especially for specimens in the S84 and S104 series, suggesting that the proposed revisions for $\omega_{n,ful}$ and $\phi_{n,ful}$ can capture the effect of loading history.

As evident from the development process of the proposed model, the proposed model basically reduces to and provide very similar predictions as Lam and Teng's (2009) model when the concrete strength is equal to 40 MPa and/or when the number of repeated cycles is smaller than 3. That is, the proposed model is as accurate as, if not more accurate than, Lam and Teng's (2009) model for the results reported in Lam *et al.* (2006), where NSC cylinders confined with an FRP wrap (i.e. wet-layup FRP tube) were tested.

4.5 CONCLUSIONS

An improved cyclic stress-strain model for FRP-confined concrete has been presented in the chapter. The development of the proposed model has been based on a critical assessment of Lam and Teng's (2009) model by making use of a large test database containing new test results on both concrete in filament-wound FRP tubes and concrete confined with an FRP wrap (i.e. wet-layup FRP tube), which were published after Lam and Teng (2009). The assessment revealed that:

- (1) The degree of non-linearity of unloading paths of FRP-confined HSC is different from that of FRP-confined NSC. Lam and Teng's (2009) model cannot provide accurate predictions for the unloading paths of FRP-confined HSC.
- (2) The relationship between the plastic strain $\varepsilon_{pl,1}$ and the envelope unloading strain $\varepsilon_{un,env}$ does not seem to be significantly affected by the unconfined concrete strength. Lam and Teng's (2009) equations, which take the unconfined concrete strength as a key parameter, fail to predict $\varepsilon_{pl,1}$ closely for FRP-confined HSC.
- (3) Lam and Teng's (2009) model is inaccurate in predicting the effect of repeated loading cycles (i.e. $\omega_{n,ful}$ and $\phi_{n,ful}$).

The proposed cyclic stress-strain model corrects the above deficiencies of Lam and Teng's (2009) model, and can provide reasonably accurate predictions for both NSC and HSC confined with either an FRP wrap or an FRP filament-wound tube.

4.6 REFERENCES

- Abbasnia, R. and Ziaadiny, H. (2010). "Behavior of concrete prisms confined with FRP composites under axial cyclic Compression", *Engineering Structures*, 32, 648-665.
- Abbasnia, R., Ahmadi, R. and Ziaadiny, H. (2012). "Effect of confinement level, aspect ratio and concrete strength on the cyclic stress-strain behavior of FRP-confined concrete prisms", *Composites Part B: Engineering*, 43, 825-831.
- Abbasnia, R., Hosseinpour, F., Rostamian, M. and Ziaadiny, H. (2013). "Cyclic and monotonic behavior of FRP confined concrete rectangular prisms with different aspect ratios", *Construction and Building Materials*, 40, 118-125.
- Bai, Y.L., Dai, J.G. and Teng, J.G. (2013). "Cyclic compressive behavior of concrete confined with large rupture strain FRP composites", *Journal of Composites for Construction*, ASCE, 18(1), 04013025.
- CEB-FIP. *CEB-FIP Model Code*, Comite Euro-International Du Beton. London, (UK), Thomas Telford, 1990.
- Hollaway, L.C. and Teng, J.G. (2008). *Strengthening and Rehabilitation of Civil Infrastructures Using FRP Composites*, Woodhead Publishing Limited, Cambridge, U.K.
- Ilki, A. and Kumbasar, N. (2003). "Compressive behavior of carbon fiber composite jacketed concrete with circular and non-circular cross sections", *Journal of Earthquake Engineering*, 7(3), 381-406.
- Lam, L. and Teng, J.G. (2002). "Strength models for fiber-reinforced plastic-confined concrete", *Journal of Structure Engineering*, ASCE, 128(5), 612-623.
- Lam, L. and Teng, J.G. (2003). "Design-oriented stress-strain model for FRP-confined concrete", *Construction and Building Materials*, 17(6-7),

471-489.

Lam, L., Teng, J.G., Cheung, C.H. and Xiao, Y. (2006). "FRP-confined concrete under axial cyclic compression", *Cement and Concrete Composites*, 28, 949-958.

Lam, L. and Teng, J.G. (2009). "Stress-strain model for FRP-confined concrete under cyclic axial compression", *Engineering Structures*, 31(2), 308-321.

Ozbakkaloglu, T. and Akin, E. (2012). "Behavior of FRP-confined normal-and high-strength concrete under cyclic axial compression", *Journal of Composites for Construction*, ASCE, 16, 451-463.

Rousakis, T.C. (2001). *Experimental Investigation of Concrete Cylinders Confined by Carbon FRP Sheets Under Monotonic and Cyclic Axial Compression Load*, Research Report 01:2, Division of Building Technology, Chalmers Univ. of Technology, Gothenburg, Sweden.

Shao, Y., Zhu, Z. and Mirmiran, A. (2006). "Cyclic modeling of FRPconfined concrete with improved ductility", *Cement and Concrete Composites*, 28(10), 959-968.

Teng, J.G., Chen, J.F., Smith, S.T. and Lam, L. (2002). *FRP strengthened RC Structures*, Wiley, New York.

Teng, J.G. and Lam, L. (2004). "Behavior and modeling of fiber reinforced polymer-confined concrete", *Journal of Structural Engineering*, ASCE, 130(11), 1713-1723.

Teng, J.G., Huang, Y.L., Lam, L. and Ye, L.P. (2007). "Theoretical model for fiber reinforced polymer-confined concrete", *Journal of Composites for Construction*, ASCE, 11(2), 201-210.

Teng, J.G., Jiang, T., Lam, L. and Luo, Y.Z. (2009). "Refinement of a design-oriented stress-strain model for FRP-confined concrete", *Journal of Composites for Construction*, ASCE, 13(4), 269-278.

Wang, Z.Y., Wang, D.Y., Simth, S.T. and Lu, D.G. (2012). "Experimental testing

and analytical modeling of CFRP-confined large circular RC columns subjected to cyclic axial compression”, *Engineering Structures*, 40, 67-74.

Yu, T. and Teng, J.G. (2011). “Design of concrete-filled FRP tubular columns: provisions in the Chinese technical code for infrastructure application of FRP composites”, *Journal of Composites for Construction*, ASCE, 15(3), 451-461.

Table 4.1: Key information of cyclic compression tests in the database

Specimen	Concrete strength f'_{co} (MPa)	Thickness of FRP t (mm)	Elastic modulus of FRP E_{frp} (GPa)	FRP hoop rupture strain $\epsilon_{h,rup}$	Ultimate axial strain ϵ_{cu}	Confined concrete strength f'_{cc} (MPa)
Rousakis (2001): 150mm in diameter; 300 mm in height; wet-layup FRP wraps						
20c1L1C	26.5	0.17	CFRP: 377 GPa in hoop direction	0.00639	0.0153	44.1
20c1L2C	26.5	0.34		0.00569	0.0208	61.6
20c1L3C	26.5	0.51		0.00435	0.0244	70.2
40c1L2C	49.5	0.34		0.00540	0.0133	79.2
40c1L3C	49.5	0.51		0.00615	0.0181	104.0
60ac1L1C	65.5	0.17		0.00517	0.0068	79.2
60ac1L2C	65.5	0.34	0.00513	0.0102	90.3	
60ac1L3C	65.5	0.51	0.00559	0.0153	117.2	
60ac1L5C	65.5	0.85	0.00526	0.0181	137.9	
80c1L1C	68.5	0.17	0.00663	0.0076	83.2	
80c1L2C	68.5	0.34	0.00598	0.0098	107.2	
80c1L3C	68.5	0.51	0.00391	0.0110	108.2	
100c1L1C	95.0	0.17	0.00333	0.0056	97.6	
100c1L2C	95.0	0.34	0.00154	0.0053	98.2	
100c1L3C	95.0	0.51	0.00443	0.0098	129.6	
Ilki and Kumbasar (2003): 150mm in diameter; 300 mm in height; wet-layup FRP wraps						
3-14-S	32.0	0.165	CFRP: 230 GPa in hoop direction	0.0079	0.0144	47.2
3-15-S	32.0	0.495		0.0108	0.0392	91.0
3-18-S	32.0	0.825		0.0100	0.0432	107.7
Lam <i>et al.</i> (2006) : 152mm in diameter; 305 mm in height; wet-layup FRP wraps						
CI-SC1	41.1	0.165	CFRP: 250 GPa in hoop direction	0.0132	0.0134	60.2
CI-SC2	41.1	0.165		0.0103	0.0117	56.8
CI-RC ^a	41.1	0.165		0.0113	0.0120	56.5
CII-SC1	38.9	0.33	CFRP: 247 GPa in hoop direction	0.0122	0.0244	81.5
CII-SC2	38.9	0.33		0.0108	0.0189	78.2
CII-RC ^a	38.9	0.33		0.0122	0.0234	85.6

^a Specimens tested by Lam *et al.* (2006) which were subjected to 3 unloading/reloading cycles at each prescribed unloading displacement level;

^b Specimens tested in Chapter 3 which were subjected to 9~12 unloading/reloading cycles at a prescribed unloading displacement level.

Table 4.1: Key information of cyclic compression tests in the database (continued)

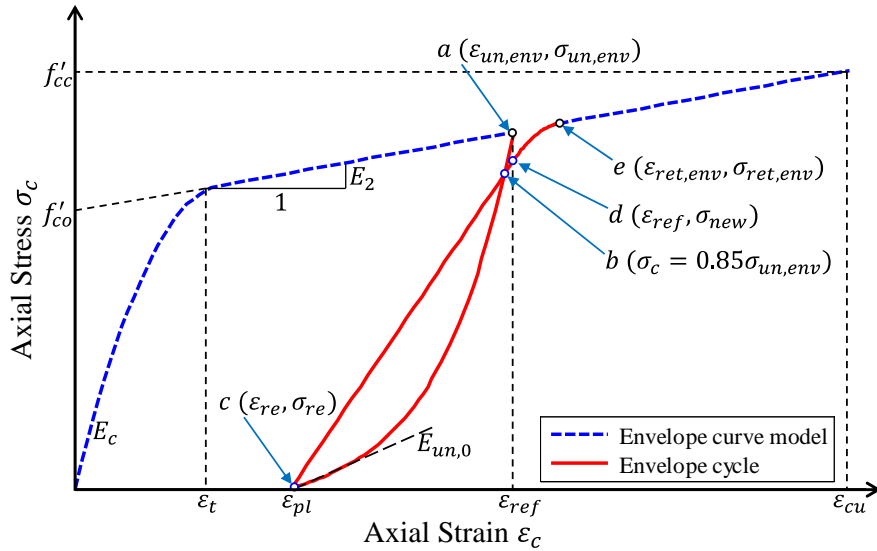
Specimen	Concrete strength f'_{co} (MPa)	Thickness of FRP t (mm)	Elastic modulus of FRP E_{frp} (GPa)	FRP hoop rupture strain $\epsilon_{h,rup}$	Ultimate axial strain ϵ_{cu}	Confined concrete strength f'_{cc} (MPa)
Ozbakkaloglu and Akin (2012): 152mm in diameter; 305 mm in height; wet-layup FRP wraps						
N-A-2L-C1	38.0	0.400	AFRP: 120 GPa in hoop direction	0.0150	0.0225	64.3
N-A-2L-C2	39.0	0.400		0.0156	0.0225	64.3
N-A-3L-C1	39.0	0.600		0.0176	0.0404	97.4
N-A-3L-C2	39.0	0.600		0.0202	0.0443	104.5
H-A-4L-C1	100.0	0.800		0.0124	0.0182	136.4
H-A-4L-C2	102.0	0.800		0.0110	0.0163	125.4
H-A-6L-C1	104.0	1.20		0.0116	0.0187	157.2
H-A-6L-C2	106.0	1.20		0.0145	0.0213	170.9
Wang <i>et al.</i> (2012): 204mm in diameter; 612 mm in height; wet-layup FRP wraps						
C2H0L1C	24.5	0.167	CFRP: 244 GPa in hoop direction	0.0145	0.0194	42.3
C2H0L2C	24.5	0.334		0.0136	0.0382	66.8
New test results (Chapter 3): 200mm in diameter; 400 mm in height; filament-wound FRP tubes						
S54-2FW-C1	54.1	2.2	GFRP: 45.9 GPa in hoop direction	0.0108	0.0176	86.0
S54-2FW-C2 ^b	54.1	2.2		0.0111	0.0189	88.7
S54-4FW-C1	54.1	4.7		0.0168	0.0442	161.7
S54-4FW-C2 ^b	54.1	4.7		0.0169	0.0443	159.4
S84-4FW-C ^b	84.6	4.7		0.0110	0.0239	152.3
S84-9FW-C ^b	84.6	9.5		0.0105	0.0322	236.2
S104-4FW-C1	84.6	4.7		0.0132	0.0258	179.6
S104-4FW-C2 ^b	104.4	4.7		0.0109	0.0238	167.6
S104-9FW-C ^b	104.4	9.5		0.0093	0.0261	236.4

^a Specimens tested by Lam *et al.* (2006) which were subjected to 3 unloading/reloading cycles at each prescribed unloading displacement level;

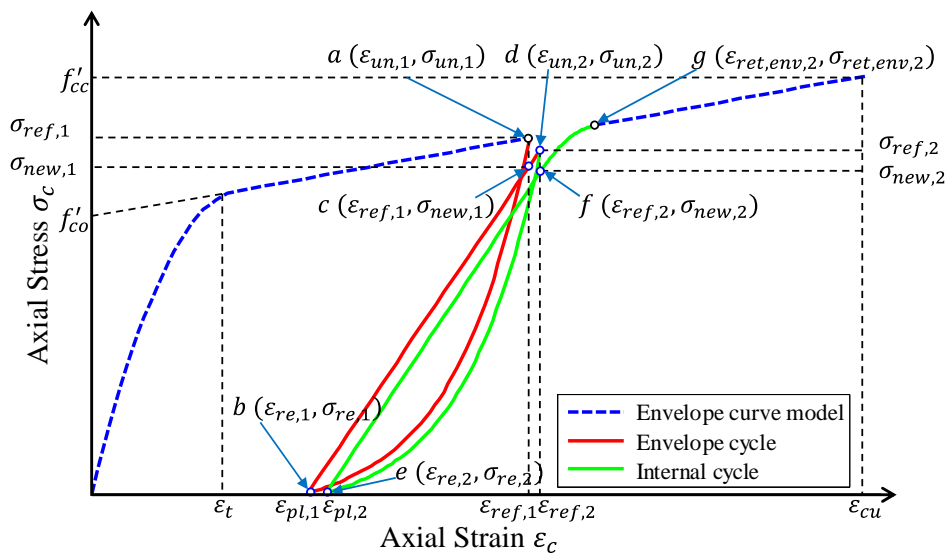
^b Specimens tested in Chapter 3 which were subjected to 9~12 unloading/reloading cycles at a prescribed unloading displacement level.

Table 4.2: Linear relationships between unloading strains and plastic strains

Source of test data	Unconfined concrete strength f'_{co} (MPa)	$\varepsilon_{pl,1} = a\varepsilon_{un,env} + b$		R^2
		a	b	
Rousakis (2001)	26.5	0.744	-0.0006	0.987
	49.5	0.737	-0.0020	0.981
	65.5	0.601	-0.0015	0.981
	68.5	0.603	-0.0015	0.968
	95.0	0.467	-0.0013	0.999
Ilki and Kumbasar (2003)	32.0	0.713	-0.0019	0.994
Lam <i>et al.</i> (2006)	38.9	0.714	-0.0016	0.998
	41.1	0.703	-0.0014	0.996
Ozbakkaloglu and Akin (2012)	38.0~39.0	0.736	-0.0016	0.999
	39.0	0.743	-0.0017	0.999
	100.0~102.0	0.805	-0.0021	0.996
	104.0~106.0	0.775	-0.0022	0.998
	100.0	0.760	-0.0020	0.995
Wang <i>et al.</i> (2012)	105.0~109.0	0.760	-0.0023	0.999
	24.5	0.815	-0.002	0.999
New test results (Chapter 3)	54.1	0.665	-0.0030	0.993
	54.1	0.764	-0.0034	0.998
	84.6	0.708	-0.0027	0.989
	84.6	0.638	-0.0028	0.996
	104.4	0.695	-0.0031	0.997
	104.4	0.614	-0.0024	0.998

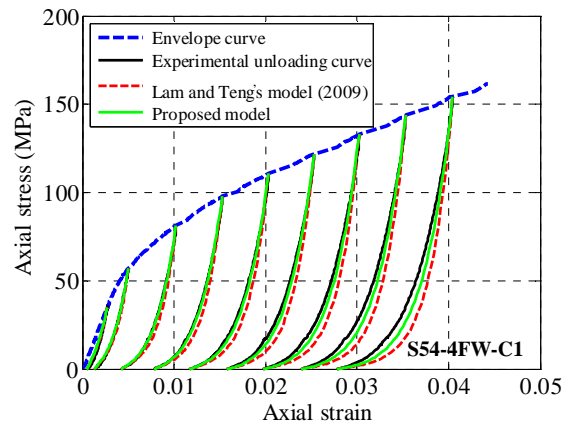
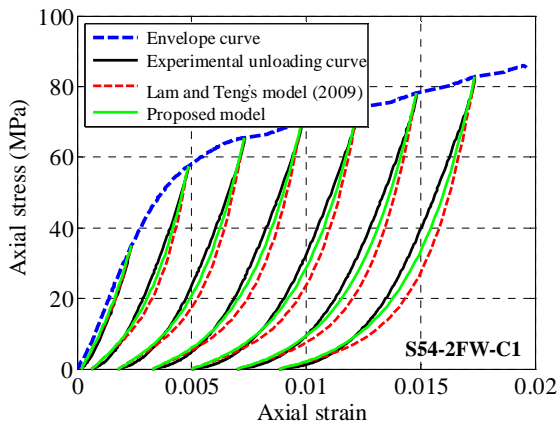


(a) Envelope cycle

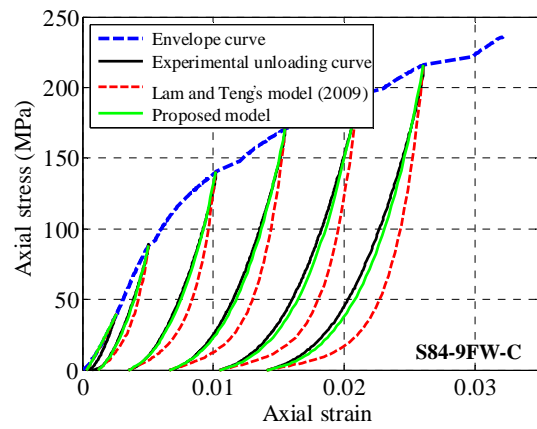
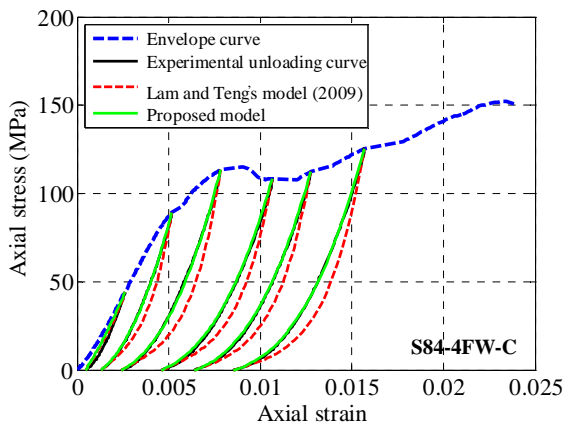


(b) Internal cycles

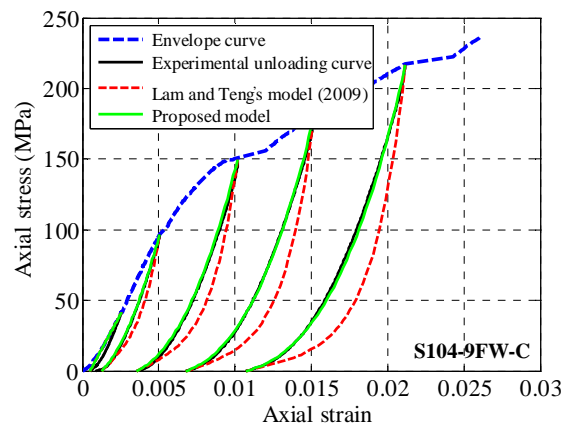
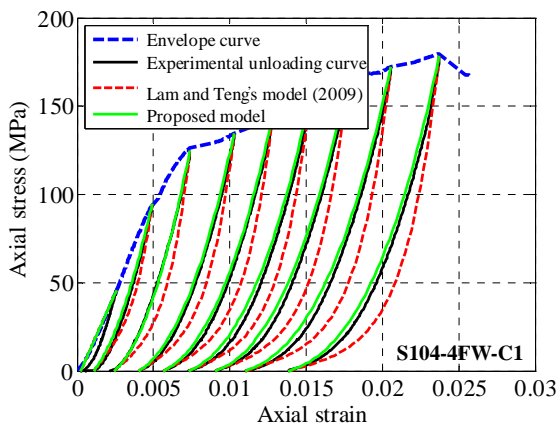
Figure 4.1: Key parameters of cyclic stress-strain curves of FRP-confined concrete (after Lam and Teng 2009)



(a) Specimens of batch 1



(b) Specimens of batch 2



(c) Specimens of batch 3

Figure 4.2: Envelope unloading curves

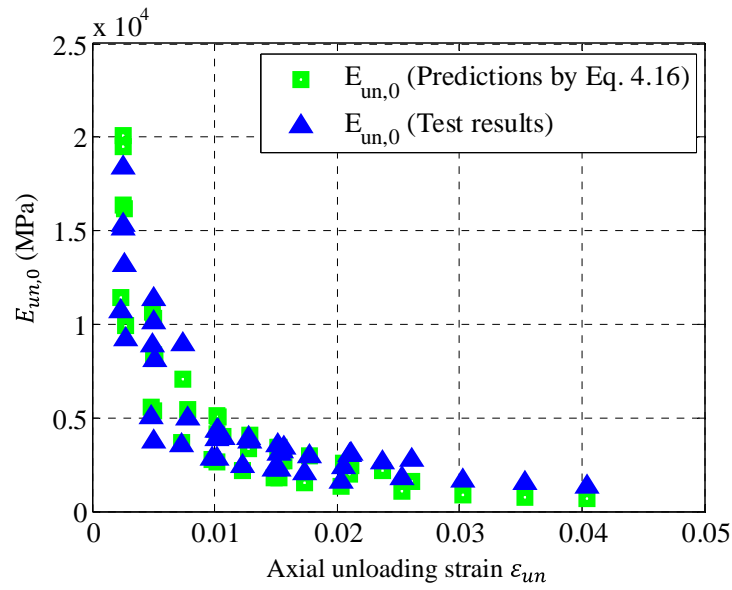


Figure 4.3: Slope of the unloading path at zero stress

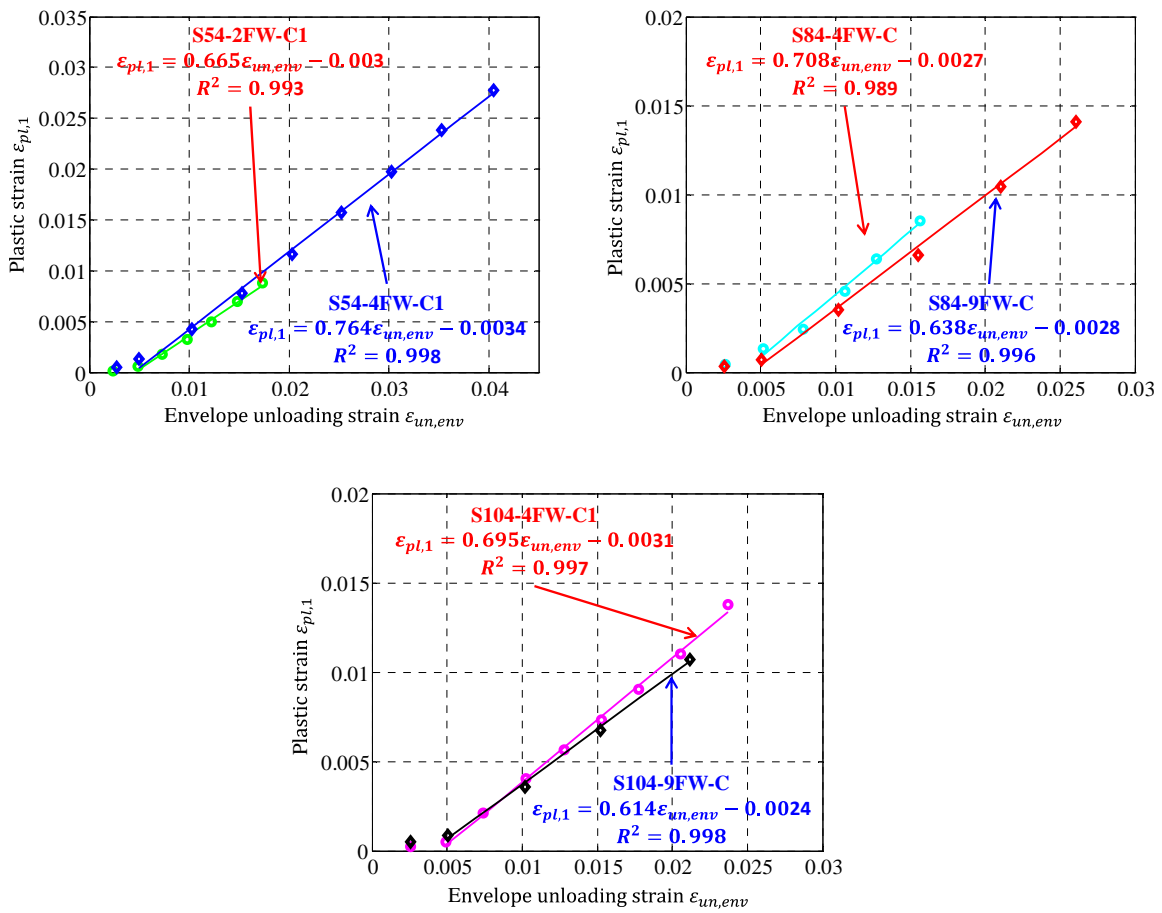


Figure 4.4: Relationships between plastic strains and envelope unloading strains

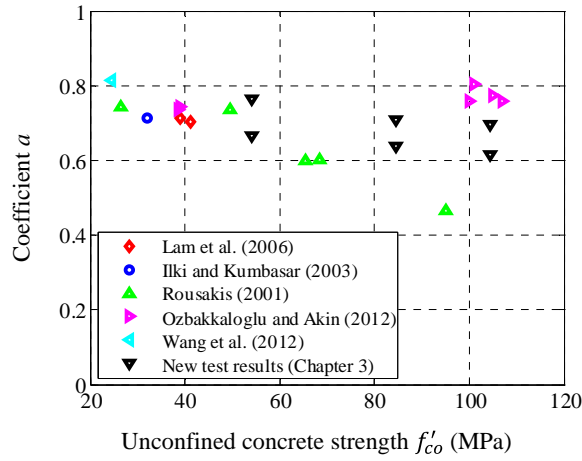


Figure 4.5: Effect of concrete strength on the plastic strain

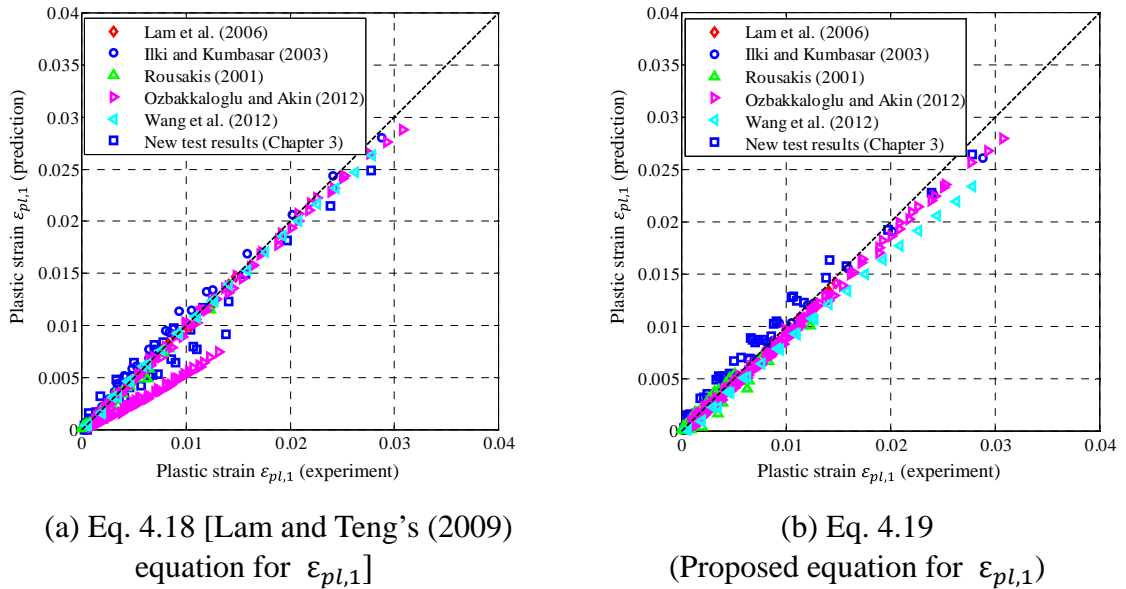


Figure 4.6: Performance of equations for the plastic strain of envelope cycles

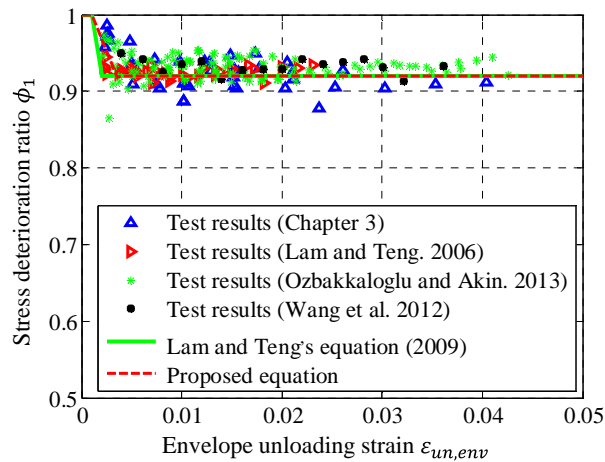


Figure 4.7: Performance of equations for the stress deterioration ratio of envelope cycles

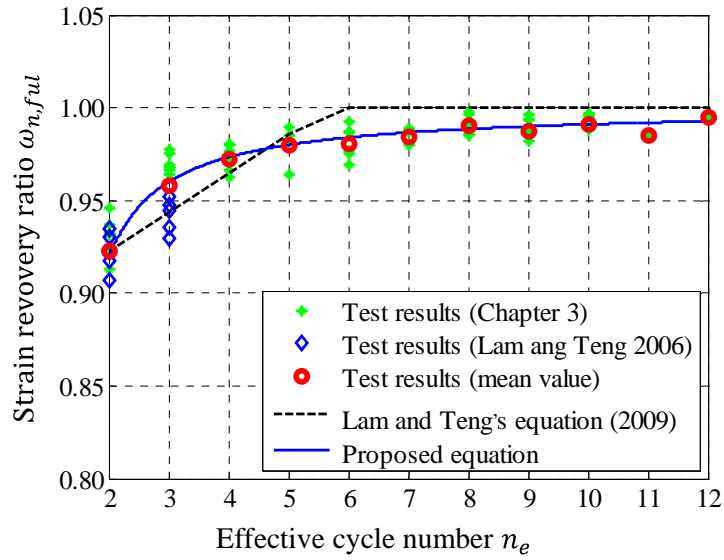


Figure 4.8: Performance of equations for the strain recovery ratio of internal cycles

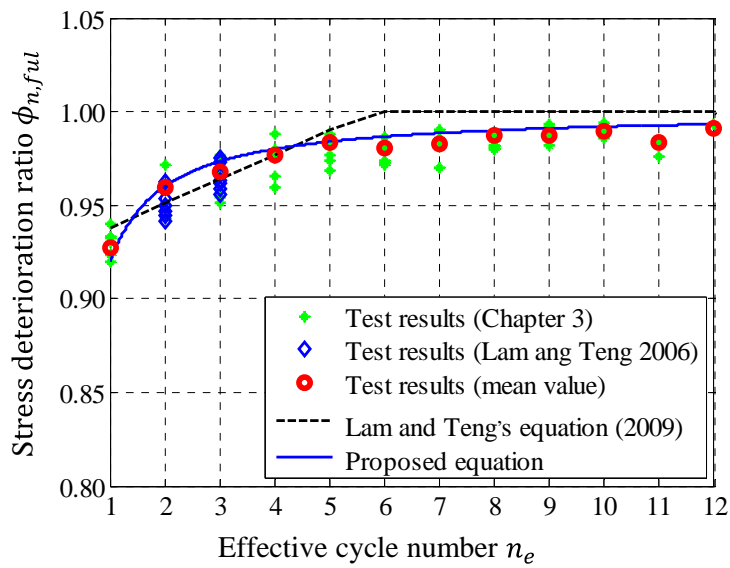
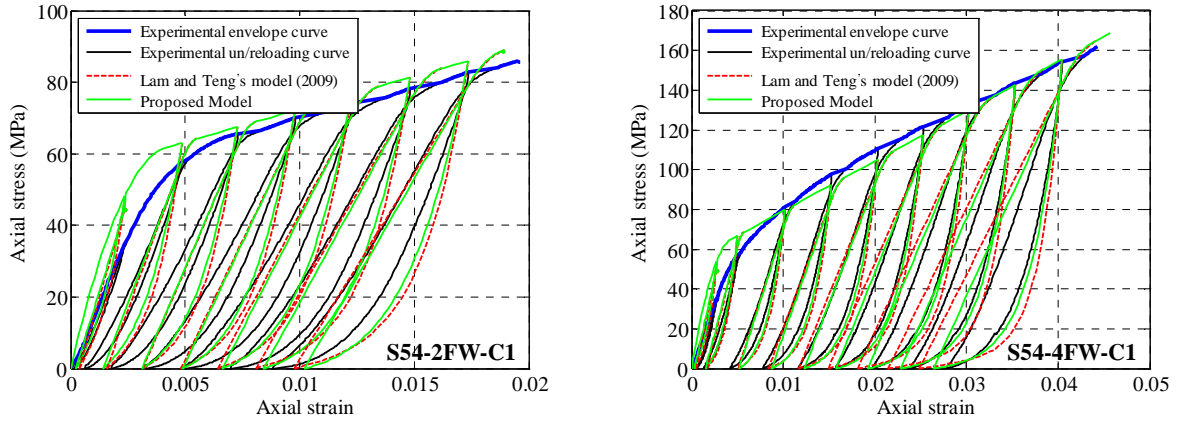
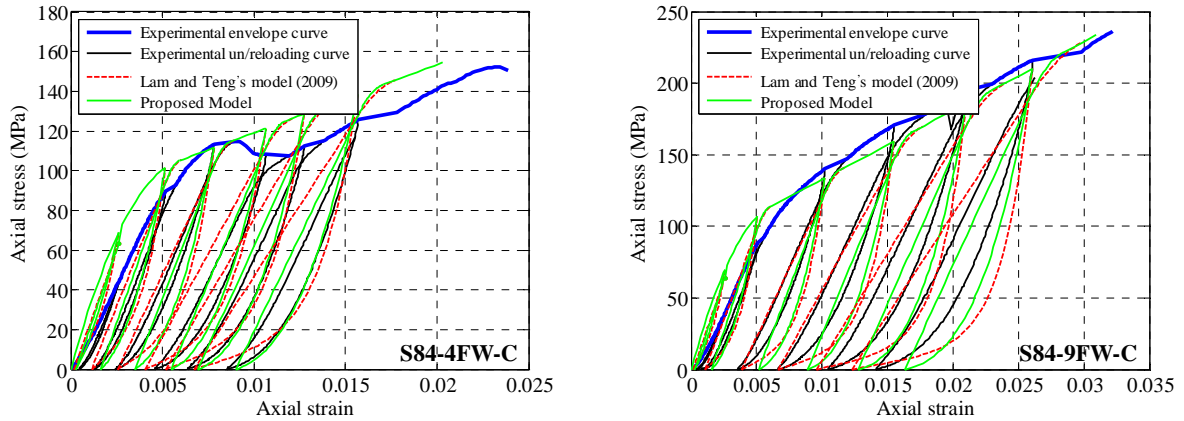


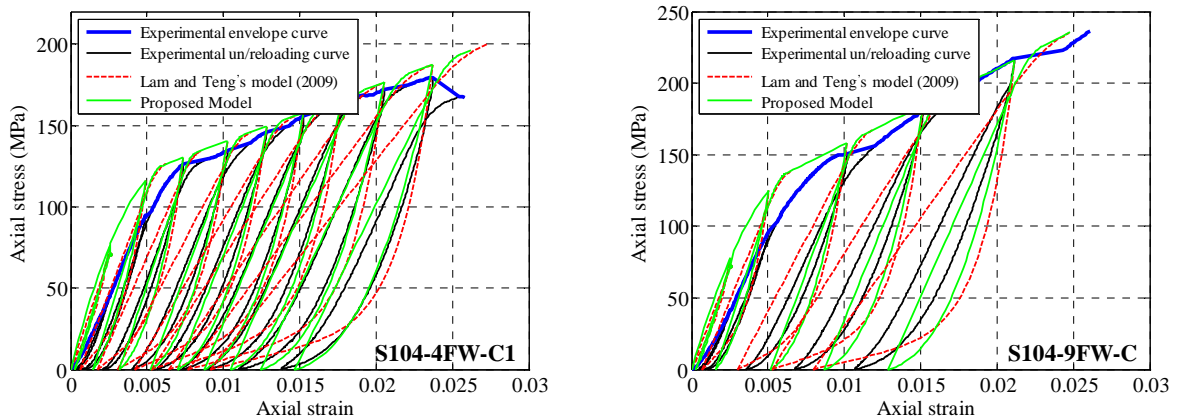
Figure 4.9: Performance of equations for the stress deterioration ratio of internal cycles



(a) Specimens of batch 1

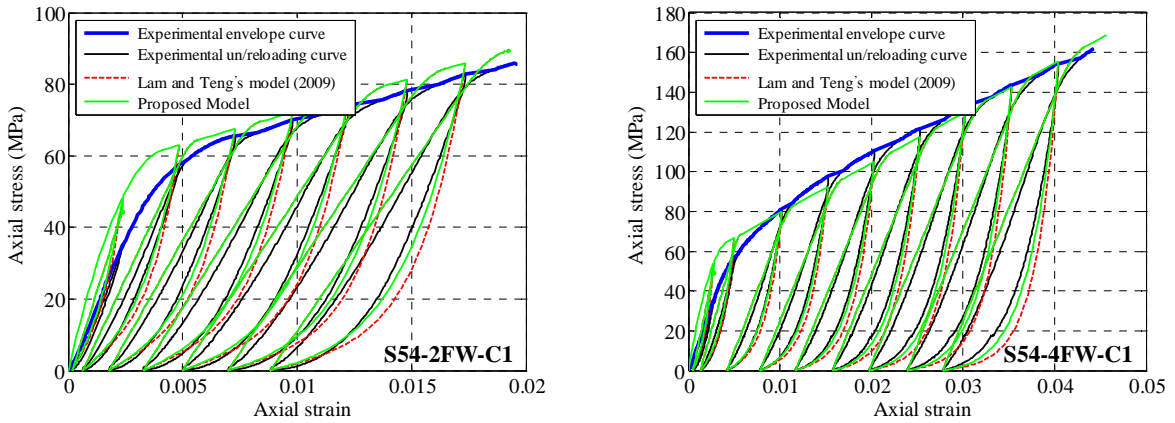


(b) Specimens of batch 2

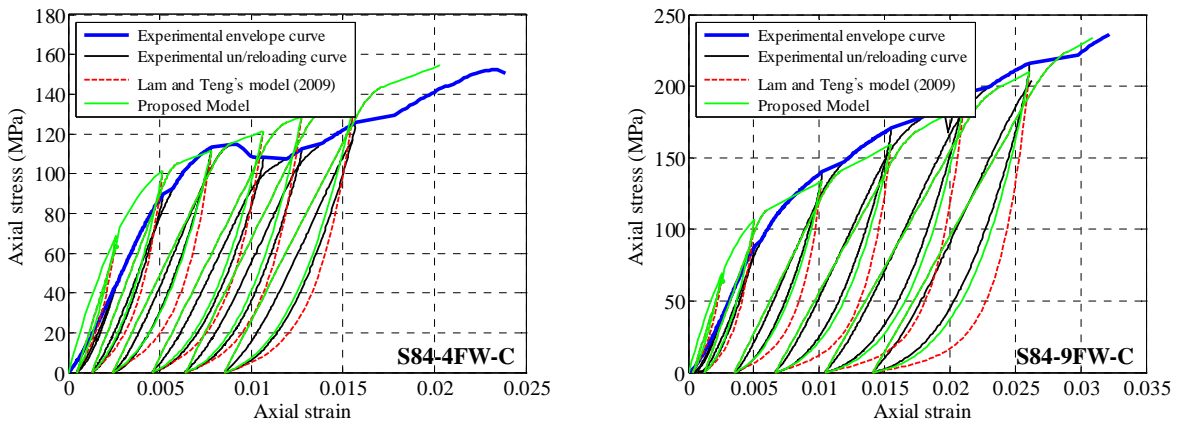


(c) Specimens of batch 3

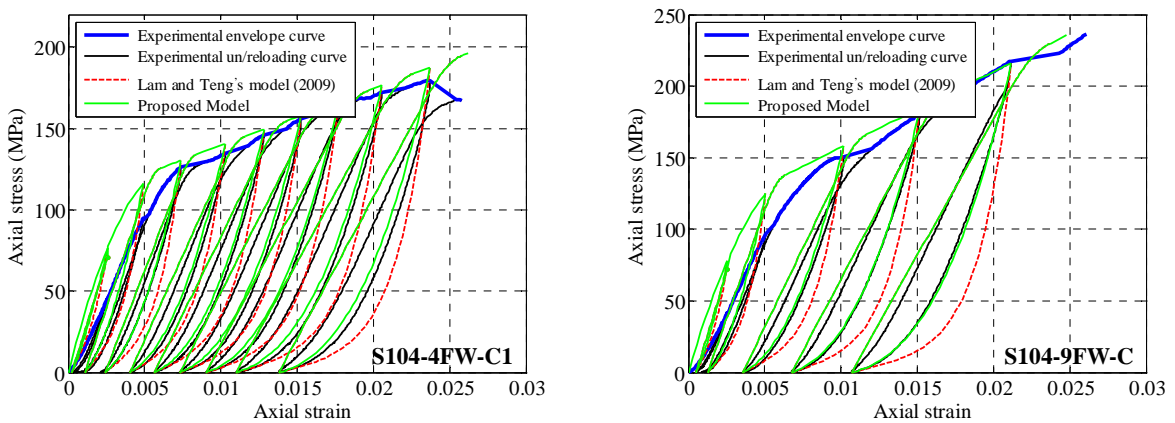
Figure 4.10: Performance of the two stress-strain models for envelope unloading/reloading curves: predictions based on the predicted values of $\epsilon_{pl,1}$



(a) Specimens of batch 1

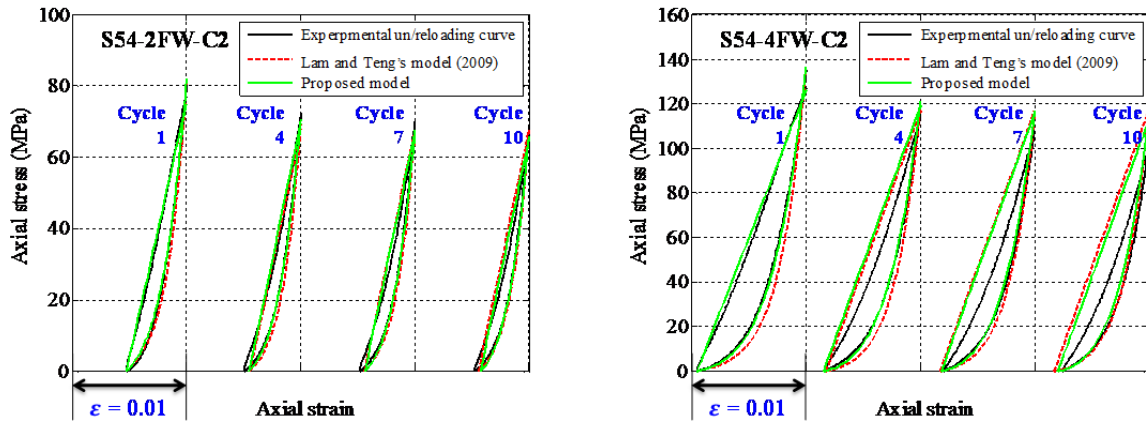


(b) Specimens of batch 2

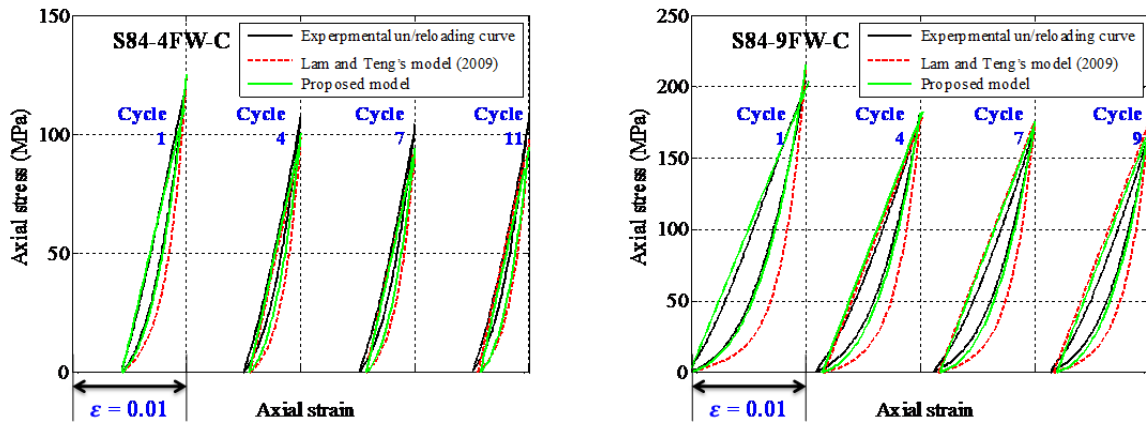


(c) Specimens of batch 3

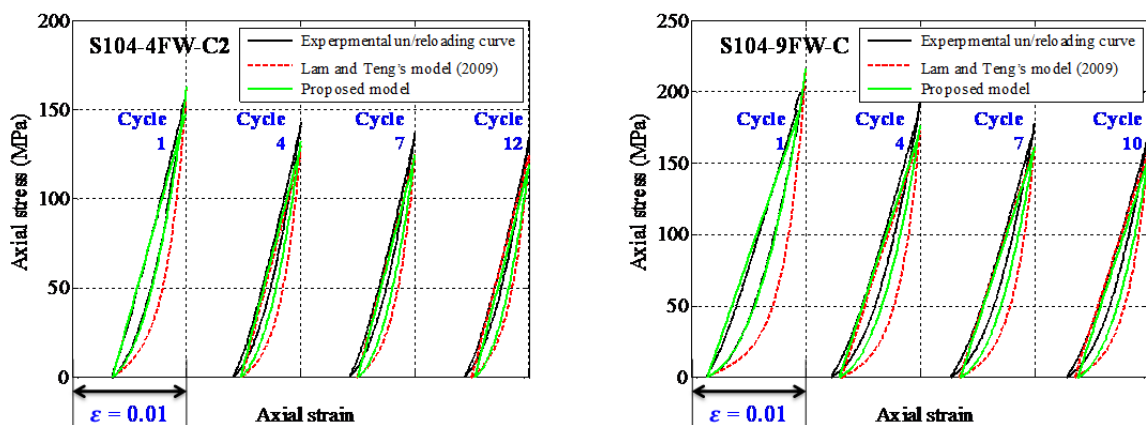
Figure 4.11: Performance of the two stress-strain models for envelope unloading/reloading curves: predictions based on experimental values of $\epsilon_{pl,1}$



(a) Specimens of batch 1



(b) Specimens of batch 2



(c) Specimens of batch 3

Figure 4.12: Performance of the two stress-strain models for repeated internal unloading/reloading curves: predictions based on the experimental values of $\epsilon_{pl,1}$

CHAPTER 5

BEHAVIOR OF HYBRID DSTCS UNDER MONOTONIC AXIAL COMPRESSION

5.1 INTRODUCTION

Since the invention of hybrid FRP-concrete-steel double-skin tubular columns (hybrid DSTCs) (Teng *et al.* 2004, 2007), a large number of experimental studies have been undertaken by the author's research group. The axial compressive behavior of hybrid DSTCs has been studied step by step in recent years (Teng *et al.* 2007; Yu 2007; Wong *et al.* 2008; Zhang *et al.* 2011; Xie *et al.* 2011). Yu's (2007) PhD thesis presented the first systematic study of hybrid DSTCs, in which 18 small-scale hybrid DSTC specimens with a characteristic diameter (the outer diameter of the annular concrete section) of 152.5 mm and a height of 305 mm were tested under monotonic axial compression. These specimens had FRP tubes formed in the same way as FRP wraps used to strengthen concrete columns (i.e. wet-layup FRP tubes) and had concrete cylinder strengths ranging from 36.7 MPa ~ 46.7 MPa. For the first time, Yu's (2007) study explained the confinement mechanism and demonstrated the excellent ductility of hybrid DSTCs (Teng *et al.* 2007; Yu 2007; Wong *et al.* 2008). Zhang *et al.* (2011) presented the first series of axial compression tests on hybrid DSTCs with high strength concrete (HSC), where six hybrid DSTCs were tested (characteristic diameter: 204 mm; height:

400 mm; concrete strength: 83.5 MPa; wet-layup FRP tubes). Zhang *et al.*'s (2011) test results indicated that hybrid DSTCs with HSC can still possess excellent ductility if the FRP tube has a sufficiently large hoop strain capacity. Xie *et al.* (2011) presented the first study on the axial compressive behavior of large-scale hybrid DSTCs, where three specimens were tested (characteristic diameter: 400 mm; height: 800 mm; concrete strengths: 29.3 MPa~40.1 MPa; wet-layup FRP tubes). Xie *et al.*'s (2011) tests confirmed the excellent ductility of large-scale hybrid DSTCs.

Hybrid DSTCs have also received extensive research attention from other researchers (e.g., Qian and Liu 2008; Ozbakkaloglu and Fanggi 2013a, 2013b; Fanggi And Ozbakkaloglu 2013). Qian and Liu (2008) presented results from axial compression tests of 10 hybrid DSTCs [characteristic diameter: 190 mm; height: 500 mm; concrete strengths: 23.7 MPa~32.5 MPa; filament-wound FRP tubes (with fibers at ± 60 or ± 80 degrees to the longitudinal axis)]. More recently, Ozbakkaloglu and his co-workers (Ozbakkaloglu and Fanggi 2013a, 2013b; Fanggi And Ozbakkaloglu 2013) reported three series of experimental studies on hybrid DSTCs (characteristic diameter: 150 mm; height: 300 mm; concrete strengths: 36.7 MPa ~113.8 MPa; prefabricated wet-layup FRP tubes) with the concrete strength as an important variable. These test results further confirmed the excellent ductility of hybrid DSTCs with HSC.

Existing studies on the axial compressive behavior of hybrid DSTCs have generally been limited to small-scale specimens (i.e. with the diameter being smaller than 200 mm) and wet-layup FRP tubes, with only a few exceptions. In particular, there has been no experimental study on large-scale hybrid DSTCs with a filament-wound FRP tube and HSC. Since hybrid DSTCs are highly ductile and the absence of any steel bars in the column ensures good-quality casting of HSC,

hybrid DSTCs provide a promising opportunity for the use of HSC which is much more brittle than normal strength concrete (NSC). For new construction, filament-wound FRP tubes should be used as the stay-in-place form for concrete casting. This chapter presents an experimental study of hybrid DSTCs under monotonic axial compression, with a particular focus on three issues: (1) the use of HSC; (2) the use of filament-wound FRP tubes; and (3) the testing of large-scale specimens. The test results are also compared with an existing model, Yu *et al.*'s (2010) model, which was developed based on test results of small-scale hybrid DSTCs with NSC and a wet-layup FRP tube.

5.2 EXPERIMENTAL PROGRAM

5.2.1 Specimen Details

A total of 12 hybrid DSTCs were prepared and tested as detailed in Table 5.1. These specimens were casted in 6 different batches respectively. Hybrid DSTCs of batches 1-3 were cast together with the three batches of CFFTs presented in Chapter 3 respectively. For all 12 hybrid DSTCs, corresponding hybrid DSTCs were also fabricated and tested under cyclic axial compression, the results of which are presented in Chapter 6.

As shown in Table 5.1, the specimens of batches 1-3 had a characteristic diameter of 200 mm and a height of 400 mm, while specimens of batches 4-6 were large-scale specimens with a characteristic diameter of 300 mm and a height of 600 mm. The void ratio φ refers to the ratio of the inner diameter D_s to the outer diameter D of the annular concrete section. A realistically large void ratio for hybrid DSTCs is between 0.7 and 0.8 (GB 50608 2010), which saves around 49%~64% of the concrete compared to solid concrete columns. The majority of

hybrid DSTCs in the present study was designed with a large void ratio (i.e. 0.73 and 0.795), with only one exception (i.e. specimen D84-4FW-MB with a void ratio of 0.60) to investigate the effect of void ratio. Three types of steel tubes were used, which are referred to as type A, type B and type C steel tubes respectively for ease of discussion (Table 5.2). Filament-wound GFRP tubes with the fibers being at ± 80 degrees to the longitudinal axis were adopted.

The naming system for these hybrid DSTCs is similar to that for the CFFTs as presented in Chapter 3. Each specimen was given a name, which starts with the letter “D” to represent “hybrid DSTCs”, followed by a two- or three-digit number to represent the unconfined concrete strength, and then a number which defines the thickness (in mm) of the FRP tube, together with two letters “FW” indicating that the tube is made using the filament-winding process. This is then followed by a letter “M” to represent monotonic axial loading; the last number “1” or “2” in some of the specimens is to differentiate two nominally identical specimens. The information of the inner steel tube is not given in the specimen name for brevity, except for the specimen with a type B steel tube and thus a smaller void ratio (i.e. D84-4FW-MB), for which a letter “B” is added to the end of its name.

5.2.2 Preparation of Specimens

All steel tubes of the same type were first cut from the same long steel tube. Precise machining was carried out to make sure both ends of each steel tube were perpendicular to its longitudinal axis. All glass FRP (GFRP) tubes used were fabricated by the same manufacturer using the same raw material (i.e., fibers and resin) and the same machine. The FRP tubes were also cut and machined into the designed length. Both the outer FRP tube and the inner steel tube were fixed concentrically and perpendicularly to a bottom steel plate to form the mold

(Figure 5.1). Before casting the concrete, strain gauges were installed on the mid-height of the inner steel tube; the lead wires of strain gauges passed through predrilled holes near the top end of the FRP tube.

Typical cross sections of hybrid DSTCs are shown in Figure 5.2. After curing of the concrete, both the upper and the lower ends of each specimen were strengthened with an additional 3-ply carbon FRP strip (25 mm in width for specimens of batches 1-3, but 40 mm in width for specimens of batches 4-6) in order to avoid unexpected failure there. Both ends of the specimen were then capped with high strength gypsum to achieve flat and smooth end surfaces which were perpendicular to the specimen axis.

5.2.3 Material Properties

5.2.3.1 Concrete

Self-compacting concrete was used for all the specimens to guarantee the quality of casting. The mix proportions used are summarized in Table 5.3. In batches 1, 4 and 5, the concrete was prepared with ordinary Portland cement, fly ash, super plasticizer (S.P.), river sand, and granite aggregate with a maximum nominal size of 10 mm. In the other batches, silica fume was added to achieve the targeted high strengths. Three concrete control cylinders (152.5 mm x 305 mm) were prepared and tested for each batch of concrete to determine the concrete properties. The concrete properties were obtained during the testing period of the specimens following ASTM C39/C39M (2011). The average concrete elastic modulus E_c , compressive strength f'_{co} and the corresponding strain ϵ_{co} obtained from these tests are given in Table 5.4. The stress-strain curves of all control cylinders are shown in Figure 5.3.

5.2.3.2 FRP Tubes

For the FRP tubes with a diameter of 200 mm, three types of prefabricated filament-wound glass FRP (GFRP) tubes were used, which were the same as those used in the CFFTs presented in Chapter 3. These tubes were manufactured using the same batches of raw materials (i.e. fibers and resin), and were designed to have the same nominal volume ratio and the same angles of fibers, for the same mechanical properties. Based on the tensile split-disk tests following ASTM D2290-08 (2008), the average rupture strain and secant elastic modulus E_{frp} at failure in the hoop direction were 1.486% and 45.9 GPa, respectively (see Section 3.2.3.2, Figures 3.3 and 3.4). Based on the compression tests following GB/T5350 (2005), the average ultimate axial stress, axial strain and secant elastic modulus at failure were 95.1MPa, 0.95% and 10.0 GPa respectively (see Section 3.2.3.2, Figures 3.5 and 3.6).

For the FRP tubes with a diameter of 300 mm, two types of prefabricated filament-wound GFRP tubes were used. The two types of FRP tubes differed only in the thickness: one had a thickness t_{frp} of 6.0 mm and the other had a thickness t_{frp} of 10 mm. The volume ratio and the angles of the fibers in all these tubes were 0.559 and ± 80 degrees to the longitudinal axis of the tube respectively. As a consequence, the two types of tubes were assumed to have the same mechanical properties, with only a small longitudinal stiffness. Tensile split-disk tests on 5 FRP rings from the 6.0 mm tube were conducted following ASTM D2290-08 (2008) (Figure 5.4). The 5 FRP rings all had a width of 35 mm. Six hoop strain gauges with a gauge length of 20 mm were installed, among which two were centered at the two gaps, whereas the centers of the other four gauges were located at 25 mm away from the gaps. The readings of the two strain gauges at the gaps were found to be lower due to the effect of bending there. All

the FRP rings failed in a brittle manner by the rupture of fibers at or near the disk gap. The experimental tensile stress-strain curves are shown in Figure 5.5, where the tensile stresses were obtained by dividing the applied tensile force by two times the cross-section area of the ring, while the tensile strains were averaged from the four hoop strain gauges away from the gap to eliminate any effects from local bending. Figure 5.5 shows that the FRP tube had a linear stress-strain relationship in the hoop direction. The average hoop rupture strain and secant elastic modulus at failure E_{frp} were 1.55% and 43.6 GPa, respectively. The compressive properties of the tubes in the longitudinal direction were assumed to be the same as the 200 mm tubes presented above. As the 300 mm tubes had fibers oriented in directions which were the same as those of the 200 mm tubes and were close to the hoop direction, their compressive stiffness and strength in the longitudinal direction were expected to be small and similar to those of the 200 mm tubes. The above assumption is thus believed to have only minor effects on the analysis of test data presented in this chapter.

5.2.3.3 Steel Tubes

For each type of steel tubes, tensile tests on three steel coupons were conducted following BS 18 (1987). The average elastic modulus E_s , the average yield stress f_y and the average ultimate stress f_u obtained from these tests are summarized in Table 5.2. The tests showed that all the steel had a long yield plateau after the stress reached the proportional limit, which was then followed by a strain-hardening branch until failure.

In addition, for each type of steel tubes, three hollow steel tubes were tested under monotonic axial compression (for two of the three tubes) or cyclic axial compression (for one of the three tubes). These hollow tubes had the same height

as those used in hybrid DSTCs (i.e. 400 mm for types A and B, 600 mm for type C). For each of these steel tubes, four bi-direction rosettes with a gauge length of 10 mm were installed at the mid-height of the steel tube; four LVDTs were installed to measure the axial shortening. All these steel tubes showed large plastic deformation until local buckling occurred in the elephant's foot mode as shown in Figure 5.6. The axial stress-axial strain curves of these specimens are shown in Figure 5.7, with the axial strain being calculated from the LVDTs. The slope of the unloading/reloading path of the cyclic stress-strain curve found from the cyclic axial compression test was almost the same as the elastic modulus of the steel (i.e. no stiffness degradation).

5.2.4 Experimental Set-Up and Instrumentation

As shown in Figure 5.8, for hybrid DSTCs in batches 1-3, four LVDTs (LVDT-400) were used to measure the total axial shortening of each specimen. For the outer GFRP tube, eight axial strain gauges, among which four had a gauge length of 20 mm (i.e. SG-20) while the other four had a gauge length of 100 mm (i.e. SG-100), were installed at the mid-height of the column. The use of two different gauge lengths was to clarify any possible effect of the gauge length on the axial strain measurements. Three groups of hoop strain gauges with a gauge length of 20 mm were installed at 3 different heights of the FRP tube respectively: mid-height; 100 mm lower than the mid-height; 100 mm higher than the mid-height. Each group included four hoop strain gauges evenly distributed over the circumference. In addition, 2 strain gauge rosettes with a gauge length of 10 mm were attached at the mid-height of the inner steel tube.

As shown in Figure 5.9, for specimens of batches 4-6, eight LVDTs were installed to measure the axial deformation of each specimen. Of the eight LVDTs, four (i.e.

LVDT-320) were used to measure the shortening of the 320 mm mid-height region, while the other four (i.e. LVDT-600) were used to measure the total shortening of the specimen. For the outer GFRP tube, eight axial strain gauges, which were the same as those for the specimens of batches 1-3, were installed at the mid-height of the column. Five groups of hoop strain gauges with a gauge length of 20 mm were installed at 5 different heights of the FRP tube respectively: mid-height; 80 mm lower than the mid-height; 80 mm higher than the mid-height; 160 mm lower than the mid-height; 160 mm higher than the mid-height. The group installed at the mid-height included eight hoop strain gauges, while the other groups each included four hoop strain gauges, which were all evenly distributed over the circumference. In addition, 2 strain gauge rosettes with a gauge length of 10 mm were attached on the mid-height of the inner steel tube.

A large testing facility (maximum capacity: 10000 kN) was used to conduct the axial compression test with a displacement control rate of 0.24 mm/min (for specimens with a height of 400 mm) or 0.36 mm/min (for specimens with a height of 600 mm). The axial load was applied on both the FRP tube, the steel tube and the concrete simultaneously. All test data, including strains, loads, and displacements, were recorded simultaneously by a data logging system.

5.3 TEST OBSERVATIONS

5.3.1 General

At the early stage of testing, no obvious phenomenon was observed on the FRP tubes; readings of both the vertical and the hoop strain gauges were quite uniform, indicating that the specimens were loaded concentrically. For the specimens with NSC (i.e. specimens D40-6FW-M, D54-2FW-M and D54-4FW-M), the axial load

increased continuously with the axial strain until the final rupture of FRP tube. For the other specimens where HSC was used, there was a load fluctuation or a sudden load drop at an axial strain of around 0.005, after which the strain gauge readings became quite scattered, especially for the specimens with a sudden load drop. The load fluctuation/sudden load drop was generally associated with a large noise, suggesting that severe damage might have occurred in the concrete infill. After the load fluctuation/sudden load drop, the axial load taken by these specimens increased again until the final rupture of FRP tube.

As the loading process progressed, white patches along the fiber directions appeared on the outer surface of FRP tube, indicating local damage in the resin. These white patches were seen to develop continuously until the rupture of fibers which occurred nearby. Progressive snapping of fibers was noticed in the final stage of test, until the explosive rupture of FRP tube associated with a big noise.

After the test, the GFRP tube, the concrete and the inner steel tube were carefully examined (see Figure 5.10); localization of damage was found for all the specimens. The damage of FRP tube was due to the combined action of axial compression and hoop tension caused by the dilation of concrete, and was distributed over the column height. The rupture of FRP occurred at places where concentrated damage occurred. As expected, the concrete layer also suffered severe crushing at the locations where FRP ruptured; severe inward deformation/buckling of the inner steel tube was also observed at the same locations. For some specimens, folding of the inner steel tube was noted (e.g., specimens D84-9FW-M, D104-4FW-M, and D104-9FW-M).

5.3.2 Axial Strains

As mentioned earlier, both LVDTs and strain gauges were used to measure the axial deformation of the specimens during the test, which provided several ways to obtain the axial strain of the specimens: (1) the average strain over the whole height of the specimen (referred to as the nominal axial strain) which was based on readings from the four LVDTs covering the column height (i.e. LVDT-400 for specimens of batches 1-3; LVDT-600 for specimens of batches 4-6); (2) the average strain of the 100 mm mid-height region found from the corresponding strain gauge readings (referred to as the SG-100 axial strain); (3) the average strain of the 20 mm mid-height region found from the corresponding strain gauge readings (referred to as the SG-200 axial strain); (4) for specimens of batches 4-6, the average strain over the 320 mm mid-height region (referred to as the LVDT-320 axial strain). Most of the strain gauges functioned well during the test. When one or more strain gauges failed, the average strain was calculated by averaging readings from the surviving strain gauges of the same group.

Comparisons between these axial strains are shown in Figure 5.11. For hybrid DSTCs of batches 1-3 (Figure 5.11a), the SG-100 axial strain agrees very well with the SG-20 axial strain when the axial strain is lower than 0.01, which indicates that the axial deformation of the mid-height region was quite uniform; when the axial strain exceeds 0.01, the SG-100 axial strain and the SG-20 axial strain show some degree of deviation from each other. The nominal axial strain shows close agreement with the SG-100 and the SG-20 axial strains until a threshold strain value of around 0.005, beyond which the nominal axial strain becomes significantly larger than the SG-100 and the SG-20 axial strains. For hybrid DSTCs of batches 4-6 (Figure 5.11b), the nominal axial strain is in close agreement with the LVDT-320, SG-100 and SG-20 axial strains until a threshold

strain value (around 0.005), beyond which the nominal axial strain becomes significantly larger than the SG-100 and the SG-20 strains except for specimen D40-6FW-M. For specimen D40-6FW-M, the difference between strain values obtained by different methods is much smaller than that for the other specimens.

As the axial strain gauges were attached on the FRP, and significant slips may have existed between the FRP tube and the concrete especially after the development of significant localized deformation of concrete, the axial strain gauge readings cannot be assumed to closely reflect the strain state of the confined concrete. In the subsequent sections, the axial strain of the confined concrete is represented by the nominal axial strain, unless otherwise specified. It should be noted that the nominal axial strain represents the average deformation of the concrete over the column height, where the deformation near the ends may be different from that near the mid-height because of the lateral constraints from the two ends. The existence of such difference, as well as other possible deformation of the loading system, generally leads to slightly larger strains from the nominal axial strain, especially in the initial stage of loading. The effect of such differences, however, is believed to be minor, given the fact that the nominal axial strain agrees closely with the mid-height axial strain during the initial stage of loading.

It should also be noted that some specimens experienced a load fluctuation/sudden load drop during the test. Such a load fluctuation/drop was generally associated with a sudden change in the readings of the LVDTs and strain gauges: on the side where local damage occurred the LVDT/strain gauge readings suddenly became larger while those on the opposite side became smaller. Such differences in the readings of LVDTs/strain gauges became increasingly larger afterwards, indicating that the deformation was no longer uniform in these specimens. This

phenomenon is further discussed in Section 5.4.1.

5.3.3 Hoop Strains

Making use of readings from the three (for batches 1-3) or five (for batches 4-6) groups of hoop strain gauges located at different heights of the FRP tube, the hoop strain distributions at the ultimate state of all the specimens are shown in Figure 5.12. The maximum hoop strain and minimum hoop strain were generally found not at the mid-height of the specimens. Despite the larger scatter of these hoop strain readings, the average of all the hoop strain readings ($\epsilon_{h,rupt1}$) is very close to the average of hoop strain readings at the mid-height section ($\epsilon_{h,rupt2}$). It should also be noted that the hoop rupture strains (either $\epsilon_{h,rupt1}$ or $\epsilon_{h,rupt2}$) of hybrid DSTCs are much lower than those of the corresponding CFFTs (see Chapter 3, Table 3.4), which was mainly due to the fact that the concrete in hybrid DSTCs had more non-uniform dilation and more pronounced damage concentration than concrete in the corresponding CFFT specimens.

5.4 BEHAVIOR OF CONFINED CONCRETE

5.4.1 Axial Load-Axial Strain Curves of Hybrid DSTCs

The axial load-axial strain curves of all the specimens are shown in Figure 5.13. These specimens could be divided into three groups: (1) hybrid DSTCs with an approximately bilinear axial load-strain curve (i.e., specimens D54-2FW-M, D54-4FW-M and D40-6FW-M); (2) hybrid DSTCs with a load fluctuation in the axial load-strain curve (i.e., specimens D84-4FW-M1,2, D84-9FW-M, D104-9FW-M); (3) hybrid DSTCs with a sudden load drop in the axial load-strain curve (i.e., specimens D104-4FW-M, D66-6FW-M, D85-6FW-M and

D85-10FW-M). The axial load fluctuation/drop in the loading process was also reported by Ozbakkaloglu's research group (Ozbakkaloglu and Fanggi 2013a, 2013b; Fanggi and Ozbakkaloglu 2013) for their hybrid DSTC specimens with HSC. The peak axial loads F_{all} of all the specimens are summarized in Table 5.5.

Figures 5.14-5.16 further illustrate the development of axial and hoop strains during the tests of typical specimens. The hoop strain readings found from the mid-height section are shown in these figures. For specimens of the first group (e.g. specimens D54-4FW-M and D40-6FW-M, see Figure 5.14), the scatters of axial and hoop strains readings are quite small, indicating that the concrete dilated uniformly and the axial deformation was uniform over the cross-section during the loading process. For specimens D84-9FW-M and D104-9FW-M which had load fluctuations during the test (Figure 5.15), the readings of the four LVDTs agree with each other very well during the test (i.e., the top plate remained horizontal), but the hoop strains of the FRP tube deviate from each other, indicating non-uniform dilation in the circumferential direction. For specimens D66-6FW-M and D104-4FW-M which had a sudden load drop (Figure 5.16), it is clear that readings of the four LVDTs deviate from each other once the sudden load drop occurred, resulting in highly non-uniform axial deformation and dilation.

The testing frame used in the present study consisted of a ball joint connected to a top plate and a fixed flat plate at the bottom, where the load was applied to the specimen through the movement of the top plate driven by an actuator via the ball joint (Figures 5.8 and 5.9). The load from the top is thus always a concentric axial load in the vertical direction without any bending moment. As a consequence, the distribution of stresses on a circular specimen is expected to be axisymmetric over the cross-section. When the stiffness of the specimen is uniform in the

circumferential direction, the top plate remains in the horizontal direction; when one part of the specimen becomes weaker, the top plate tilts towards that particular part (i.e. the same load acting on that part leads to larger deformation).

For hybrid DSTCs with HSC (i.e. groups 2 and 3), local damage of concrete occurred after a certain axial strain. The local damage of concrete led to a load fluctuation/drop of the specimen despite that the displacement continued to increase. The resultant force of the whole section, however, still had to remain concentric to balance the applied load during this process, which means that: (1) the part of the cross-section, where severe local damage occurred, experienced larger deformation or possible compressive softening (i.e. stress reductions) because of a reduction in its stiffness; and (2) the other part of the cross-section, where no local damage occurred, was partially unloaded due to the tilting of the top plate (thus also stress reductions) although the displacement at the plate center continued to increase (e.g., specimen S104-4FW-M, Figure 5.17). However, as the load was still concentric, the distribution of axial stresses over the cross-section had to remain axisymmetric afterwards. Other consequences of this process are: (1) the part where local damage occurred expanded rapidly so that the FRP tube was rapidly strained locally, which consequently led to the recovery of stiffness of that part of concrete (see Figures 5.15 and 5.16); (2) the steel tube adjacent to the damaged concrete was more heavily loaded in order to maintain the balance of the system; the extent to which the steel tube could take up more stresses to compensate for the stiffness loss of the local concrete depends on the D_s/t_s ratio of the steel tube (which determines the stability of the steel tube itself), the void ratio (which determines the ratio between the load taken by the concrete and that taken by the steel), and the strength of concrete (which determines how severe the local damage of concrete is); and (3) some dynamic effects occurred, and the extent depends on the strength of HSC.

With the above explanations, it is clear that: (1) the deformation of concrete might be highly non-uniform over the cross-section for specimens with a load drop/fluctuation; (2) the axial stress of concrete was also non-uniform; (3) depending on the D_s/t_s ratio of the steel tube, the load taken by the steel tube might be below its yield load because of local buckling caused by excessive axial straining on part of the tube. All these issues mean that the accurate evaluation of the axial stress of concrete is a difficult, if not impossible, task. Therefore, in the subsequent subsections, certain assumptions are made in order to assess the behavior of the concrete section as a whole, based on the definition of average axial stresses.

5.4.2 Average Axial Stress of Confined Concrete in Hybrid DSTCs

The average axial stress of the concrete is defined to be the load carried by the concrete section divided by its cross-sectional area. The load carried by the concrete section is assumed to be equal to the load carried by the specimen subtracted by the load carried by the FRP tube and that carried by the inner steel tube at the same axial strain (see Figure 5.13). The load carried by the GFRP tube was found from the compression tests on hollow FRP tubes (see Figures 3.5 and 3.6); when the axial strain of a specimen exceeds the ultimate strain of the corresponding hollow FRP tube tests, it is assumed that the load resisted by the FRP tube is equal to its ultimate load because of the support from the concrete (see Section 3.3.5). The load carried by the inner steel tube was found from the compression tests on hollow steel tubes (Figure 5.6).

With these assumptions, the peak axial loads taken by the concrete F_c and the peak axial stresses of the confined concrete f'_{cc} are summarized in Table 5.5 for

all the specimens, while the axial stress-axial strain curves of hybrid DSTCs are shown in Figure 5.18. The ultimate axial strains ε_{cu} of the concrete at the rupture of FRP tube are also summarized in Table 5.5. The peak axial stress f'_{co} and the corresponding strain ε_{co} of unconfined concrete were used to normalize the ultimate axial stress and the ultimate axial strain, respectively (see Table 5.5).

5.4.3 Effect of Concrete Strength

The effect of concrete strength is illustrated in Figure 5.19. The curves in each subfigure of Figure 5.19 are for a group of specimens with the same FRP tube and steel tube. It is evident that the specimens with a relatively low concrete strength had a smooth stress-strain curve which consists of two ascending branches, but a fluctuation/drop in the axial stress generally occurred for specimens with HSC. Such stress fluctuations/drops appear to be more severe for concrete with a higher strength. The same observation can also be made for the test results presented in Ozbakkaloglu and Fanggi (2013a, 2013b) and Fanggi and Ozbakkaloglu. (2013). Figure 5.19 also shows that while specimens with a higher unconfined concrete strength typically have a higher ultimate axial stress, the ultimate axial strain of the confined concrete generally decreases with the unconfined concrete strength.

5.4.4 Effect of Thickness of FRP Tube

The effect of the thickness of FRP tube is illustrated in Figure 5.20. It has been well established that the behavior of FRP-confined concrete columns depends on the amount of confining FRP. When all the other parameters are the same, a thicker FRP tube leads to greater strength and ductility. The thickness of the FRP tube also affects significantly the stress-strain curve of confined concrete, especially its second portion of the stress-strain curve: a thicker the FRP tube

yields a stiffer the response of the second branch (Lam and Teng 2003; Teng et al. 2009). The thickness (stiffness) of FRP tube generally has similar effects on the confined concrete in hybrid DSTCs as is evident from Figure 5.20. Figure 5.20 also shows that the degree of stress drop in some specimens may be reduced (e.g. by comparing specimens D85-6FW-M and D85-10FW-M) or even converted to small stress fluctuations (e.g. by comparing specimens D104-4FW-M and D104-9FW-M) by using a thicker FRP tube. This is also consistent with the test observation made by Fanggi and Ozbakkaloglu (2013a, 2013b).

5.4.5 Effect of Void Ratio

The effect of void ratio can be examined by comparing the stress-strain curves of the confined concrete in specimens D84-4FW-M1 ($\varphi = 0.795$) and D84-4FW-MB ($\varphi = 0.600$) (Figure 5.21). Figure 5.21 shows that the void ratio does not have a significant effect on either the ultimate axial strain or the degree of stress drop. This is inconsistent with the test observation by Ozbakkaloglu and Fanggi (2013a) that the stress drop tends to be less severe for hybrid DSTCs with a smaller void ratio.

The curve of specimen D84-4FW-MB appears to have a stiffer second branch than its counterpart with a larger void ratio (i.e. specimen D84-4FW-M1) (Figure 5.21). This observation is consistent with that made by Wong *et al.* (2008) for hybrid DSTCs with NSC, although the difference shown in Figure 5.21 might also be partially due to the use of a steel tube which had a slightly smaller D_s/t_s ratio in specimen D84-4FW-MB.

5.4.6 Effect of Specimen Size

The effect of specimen size can be examined by comparing the stress-strain curves of the confined concrete between specimen D84-4FW-M1 (characteristic diameter = 200 mm) and specimen D85-6FW-M (characteristic diameter = 300mm), which had approximately the same confinement stiffness ($E_{frp}t_{frp}/D$) and the same concrete strength. Figure 5.22 shows that the concrete in the larger specimen (i.e. specimen D85-6FW-M) experienced a larger sudden drop than its smaller counterpart (i.e. specimen D84-4FW-M1), although this difference might also have been partially due to the use of a steel tube with a larger D_s/t_s ratio in specimen D85-6FW-M.

5.4.7 Comparison between CFFTs and Hybrid DSTCs

The behavior of confined concrete in hybrid DSTCs is compared with that in the corresponding CFFTs (presented in Chapter 3) in Figures 5.23, in terms of the axial stress-strain curves and axial strain-hoop strain curves respectively. Figure 5.23a shows that when the unconfined concrete strength is relatively low (i.e. 54 MPa), the axial stress-strain curves of the concrete in DSTCs agree well with those of the concrete in CFFTs, but the former generally end at a significantly lower ultimate axial strain because of the lower hoop rupture strain of FRP in these specimens (Figure 5.23a). The lower rupture strain of FRP is a consequence of the more non-uniform dilation of the concrete in hybrid DSTCs.

For specimens with a higher concrete strength (i.e. 84 MPa and 104 MPa), a fluctuation/drop in the axial stress generally occurred for DSTC specimens. Such a stress fluctuation/drop, however, did not occur or was much less pronounced for the corresponding CFFT specimens, leading to a higher second branch of the

stress-strain curves of concrete in CFFTs (Figures 5.23b and 5.23c). The ultimate axial strain of these hybrid DSTCs is also significantly smaller than that of the corresponding CFFTs due to a lower hoop rupture strain of FRP (Figures 5.23b and 5.23c) as explained earlier.

Initially, the axial strain-hoop strain curves of the concrete in DSTCs agree well with those of the concrete in CFFTs; once the axial strain exceeds around 0.005, the hoop strain of the concrete in DSTCs increased more slowly than that of concrete in CFFTs, indicating that the outward dilation of concrete in DSTCs is smaller. The curves of DSTCs, however, are generally much shorter than those of the corresponding CFFTs. This was caused mainly by the much more non-uniform hoop dilation of concrete in DSTCs, which led to a much smaller average hoop rupture strain of FRP tube.

5.5 COMPARISON WITH EXISTING MODEL

5.5.1 Yu *et al.*'s (2010) Model for Hybrid DSTCs

A simple stress-strain model for confined concrete in hybrid DSTCs was proposed by Yu *et al.* (2010), which was based on a design-oriented model proposed by Teng *et al.* (2009) for concrete in FRP-confined circular solid columns. Teng *et al.*'s (2009) model is a refined version of a well-recognized model developed by the same research group (Lam and Teng 2003). Compared with Lam and Teng's (2003) original model, Teng *et al.*'s (2009) model includes more accurate expressions for the ultimate axial strain and the compressive strength. Yu *et al.*'s (2010) model includes modifications to Teng *et al.*'s (2009) model to account for the effect of an inner void on the ultimate axial strain of concrete. Yu *et al.*'s (2010) model yields reasonably accurate but conservative predictions for hybrid DSTCs

with NSC (Yu 2007).

Yu *et al.*'s (2010) model consists of a parabolic first portion plus a linear second portion with a smooth transition at ε_t , and is described as follows:

$$\sigma_c = E_c \varepsilon_c - \frac{(E_c - E_{2c})^2}{4f_o} \varepsilon_c^2 \quad \text{for } 0 \leq \varepsilon_c \leq \varepsilon_t \quad (5.1)$$

and

$$\sigma_c = f_o + E_{2c} \varepsilon_c \quad \text{for } \varepsilon_t \leq \varepsilon_c \leq \varepsilon_{cu} \quad (5.2)$$

where σ_c and ε_c are the axial stress and the axial strain of confined concrete respectively; E_{2c} is the slope of the linear second portion of the stress-strain curve; f_o is the intercept of the stress axis by the linear second portion; E_c and ε_{cu} are the initial elastic modulus and the ultimate axial strain of confined concrete, respectively. The axial strain at the smooth transition point ε_t where the parabolic first portion meets the linear second portion is given by:

$$\varepsilon_t = \frac{2f_o}{E_c - E_{2c}} \quad (5.3)$$

The slope of the linear second portion E_{2c} is given by:

$$E_{2c} = \frac{f'_{cc} - f_o}{\varepsilon_{cu}} \quad (5.4)$$

where f'_{cc} is the compressive strength of confined concrete. f_o is taken to be the compressive strength of unconfined concrete f'_{co} . The compressive strength f'_{cc} and the ultimate axial strain ε_{cu} of confined concrete in hybrid DSTCs are given by:

$$\frac{f'_{cc}}{f'_{co}} = \begin{cases} 1 + 3.5(\rho_K - 0.01)\rho_\varepsilon & \rho_K \geq 0.01 \\ 1 & \rho_K < 0.01 \end{cases} \quad (5.5)$$

$$\frac{\varepsilon_{cu}}{\varepsilon_{co}} = 1.75 + 6.5\rho_K^{0.8}\rho_\varepsilon^{1.45}(1 - \varphi)^{-0.22} \quad (5.6)$$

$$\frac{f_l}{f'_{co}} = \frac{E_{frp}t_{frp}\varepsilon_{h,rupt}}{f'_{co}R} = \rho_K\rho_\varepsilon \quad (5.7)$$

$$\rho_K = \frac{E_{frp}t_{frp}}{E_{seco}R_o} \quad (5.8)$$

$$\rho_\varepsilon = \frac{\varepsilon_{h,rupt}}{\varepsilon_{co}} \quad (5.9)$$

where ρ_K is the confinement stiffness ratio and ρ_ε is the strain ratio. E_{frp} is the elastic modulus of FRP in the hoop direction; t_{frp} is the thickness of the FRP tube; $\varepsilon_{h,rupt}$ is the hoop strain of FRP at the rupture of the tube due to hoop tensile stresses; R_o is the outer radius of the annular concrete section (i.e. characteristic radius); E_{seco} and ε_{co} are the secant modulus and the axial strain at peak axial stress of unconfined concrete respectively, with $E_{seco} = f'_{co}/\varepsilon_{co}$; φ is the void ratio which is the ratio between the inner diameter and the outer diameter of the annular concrete section.

5.5.2 Comparison with Yu *et al.*'s (2010) Model

The test results from the present study are compared with Yu *et al.*'s (2010) model in Figure 5.24. The hoop rupture strain $\varepsilon_{h,rupt1}$ was used in all the predictions.

Figure 5.24a shows a comparison for hybrid DSTCs whose concrete had an approximately bilinear axial stress-strain curve until failure (i.e., specimens D54-2FW-M, D54-4FW-M and D40-6FW-M). It is evident that Yu *et al.*'s (2010) model provides reasonably accurate, yet conservative predictions for these test results.

Figure 5.24b shows a comparison for hybrid DSTCs with slight fluctuations in the axial stress-strain curve of concrete (i.e., specimens D84-4FW-BM, D84-4FW-M1,2, D84-9FW-M and D104-9FW-M). Although Yu *et al.*'s (2010) model fails to predict the stress fluctuations, it does provide predictions which are reasonably close to the test results.

Figure 5.24c shows a comparison for hybrid DSTCs with a sudden stress drop in the axial stress-strain curve of concrete (i.e., specimens D104-4FW-M, D66-6FW-M, D85-6FW-M and D85-10FW-M). For these specimens, Yu *et al.*'s (2010) model overestimates the test results after the occurrence of a sudden drop in the axial stress. As described above, the sudden stress drop was typically associated with the titling of the top loading plate of the testing machine, which led to quite non-uniform deformation in concrete over the cross-section. Yu *et al.*'s (2010) model, originally proposed to predict the average axial stress-axial strain curve of concrete in hybrid DSTCs, does not consider the complicated mechanism in such hybrid DSTCs. Further research is needed for the development of a stress-strain model for the concrete in such hybrid DSTCs when more test data is available. Such a stress-strain model should take due account of various factors, including the concrete strength, the void ratio, the D_s/t_s ratio of the inner steel tube, and the circumferential thickness of FRP tube, as discussed above.

5.6 CONCLUSIONS

This chapter has presented an experimental study on hybrid DSTCs under monotonic axial compression with a particular focus on the effect of three important issues (i.e., the use of HSC; the use of filament-wound tubes; the use of large-scale specimens). The results and discussions presented in the chapter allow the following conclusions to be drawn:

- (1) The experimental results demonstrated that hybrid DSTCs process excellent ductility even when high strength concrete is used;
- (2) The localization of damage (i.e. concrete crushing, steel buckling and/or FRP rupture), which occurred in all the specimens, appears to be more pronounced for specimens with a higher concrete strength and/or a thinner FRP tube;
- (3) Three types of axial stress-strain curves of concrete in hybrid DSTCs were found in the present study: (a) axial stress-strain curves with a bilinear ascending shape; (b) axial stress-strain curves with a stress fluctuation; (c) axial stress-strain curve with a sudden stress drop;
- (4) The sudden stress drop, appearing to be more significant for hybrid DSTCs with a higher concrete strength and/or a weaker FRP tube, was found to be initiated by the local damage of concrete, which led to highly non-uniform deformation over the cross-section of concrete;
- (5) Yu *et al.*'s (2010) model is capable of providing reasonably accurate predictions for specimens with a bilinear ascending stress-strain curve and specimens with slight fluctuations in the axial stress, but it overestimates the results of specimens with a sudden load drop.

5.7 REFERENCES

- ASTM C39/C39M. (2011). *Standard Test Method for Compressive Strength of Cylindrical Concrete Specimens*, American Society for Testing and Materials, Philadelphia, USA.
- ASTM D2290-08. (2008). *Standard Test Method for Apparent Hoop Tensile Strength of Plastic or Reinforced Plastic Pipe by Split Disk Method*, American Society for Testing and Materials, Philadelphia, USA.
- BS 18-1987. (1987). *Tensile Testing of Metals (including Aerospace Materials)*, British Standards Institution, London, UK.
- Fanggi, B.A.L. and Ozbakkaloglu. T. (2013). “Compressive behavior of aramid FRP-HSC-steel double-skin tubular columns”, *Construction and Building Materials*, 48(0), 554-565.
- GB-50608. (2010). *Technical Code for Infrastructure Application of FRP Composites*, China Planning Press, China.
- GB/T5350-2005. (2005). *Fiber-Reinforced Thermosetting Plastic Composites Pipe: Determination for Longitudinal Compressive Properties*, The Standards Press of China.
- Lam, L. and Teng, J.G. (2003). “Design-oriented stress-strain model for FRP-confined concrete in rectangular columns”, *Journal of Reinforced Plastics and Composites*, 22(13), 1149-1186.
- Ozbakkaloglu, T. and Fanggi, B.A.L. (2013a). “Axial compressive behavior of FRP-concrete-steel double-skin tubular columns made of normal-and high-strength concrete”, *Journal of Composites for Construction*, ASCE, 18(1).
- Ozbakkaloglu, T. and Fanggi, B.A.L. (2013b). “FRP-HSC-steel composite columns: behavior under monotonic and cyclic axial compression”, *Materials and Structures*, 1-19.

- Qian, J.R. and Liu, M.X. (2008). “Experimental investigation of FRP-concrete-steel double-skin tubular stubs under axial compressive loading”, *Journal of Building Structures*, 29(2), 104-113. (in Chinese).
- Teng, J.G., Yu, T. and Wong, Y.L. (2004). “Behaviour of hybrid FRP-concrete-steel double-skin tubular columns”, *Proceedings, Second International Conference on FRP Composites in Civil Engineering*, 8-10 December, Adelaide, Australia, 811-818.
- Teng, J.G., Yu, T., Wong, Y.L. and Dong, S.L. (2007). “Hybrid FRP-concrete-steel tubular columns: Concept and behavior”, *Construction and Building Materials*, 21(4), 846-854.
- Teng, J.G., Jiang, T., Lam, L. and Luo, Y.Z. (2009). “Refinement of a design-oriented stress-strain model for FRP-confined concrete”, *Journal of Composites for Construction*, ASCE, 13(4), 269-278.
- Wong, Y.L., Yu, T., Teng, J.G. and Dong, S.L. (2008). “Behavior of FRP confined concrete in annular section columns”, *Composites Part B: Engineering*, 39(3), 451-466.
- Xie, P., Yu, T., Wong, Y.L. and Teng, J.G. (2011). “Compressive behavior of large-scale hybrid FRP-concrete-steel double-skin tubular columns”, *Advanced Materials Research*, 243, 1138-1144.
- Yu, T. (2007). *Behavior of Hybrid FRP-Concrete-Steel Double-Skin Tubular Columns*, PhD Thesis, The Hong Kong Polytechnic University.
- Yu, T., Teng, J.G. and Wong, Y.L. (2010). “Stress-strain behavior of concrete in hybrid double-skin tubular columns”, *Journal of Structural Engineering*, ASCE, 136(4), 379-389.
- Zhang, B., Yu, T. and Teng, J.G. (2011). “Axial compression tests on hybrid double-skin tubular columns filled with high strength concrete”, *Proceedings, Third International Postgraduate Conference on Infrastructure and Environment*, 11-12 July, Hong Kong, China, 171-176.

Table 5.1: Details of specimens

Specimen	Specimen dimensions			Steel tube		FRP tube		Concrete batch
	D (mm)	h (mm)	ϕ	Type	D_s/t_s	Type	t_{frp} (mm)	
D54-2FW-M	200	400	0.795	A	31.8	2FW	2.2	1 (54.1MPa)
D54-4FW-M	200	400	0.795	A	31.8	4FW	4.7	
D84-4FW-M1	200	400	0.795	A	31.8	4FW	4.7	2 (84.6MPa)
D84-4FW-M2	200	400	0.795	A	31.8	4FW	4.7	
D84-4FW-MB	200	400	0.600	B	26.7	4FW	4.7	
D84-9FW-M	200	400	0.795	A	31.8	9FW	9.5	
D104-4FW-M	200	400	0.795	A	31.8	4FW	4.7	3 (104.6MPa)
D104-9FW-M	200	400	0.795	A	31.8	9FW	9.5	
D40-6FW-M	300	600	0.730	C	36.5	6FW	6.0	4 (40.9MPa)
D66-6FW-M	300	600	0.730	C	36.5	6FW	6.0	5 (66.1MPa)
D85-6FW-M	300	600	0.730	C	36.5	6FW	6.0	6 (85.8MPa)
D85-10FW-M	300	600	0.730	C	36.5	10FW	10.0	

Table 5.2: Dimension and properties of steel tubes

Type	D_s (mm)	t_s (mm)	D_s/t_s	Elastic modulus E_s (GPa)	Yielding stress f_y (MPa)	Ultimate strength f_u (MPa)
A	159.0	5.0	31.8	205.8	320.4	512.3
B	120.0	4.5	26.6	199.6	419.5	565.7
C	219.0	6.0	36.5	198.7	319.4	441.5

Table 5.3: Mix proportions of concrete

Specimen batch	Water cement ratio	Water	Cement	Fly ash	Silica fume	Super plasticizer*	Coarse aggregate	Sand
1	0.35	175	300	200	---	9	829	796
2	0.29	174	377	203	29	11	793	762
3	0.23	155	442	170	68	16	819	712
4	0.42	186	239	203	---	3	822	715
5	0.35	175	300	200	---	10	845	812
6	0.30	174	377	203	29	11	793	762

*The brand of the super plasticizer is "Grace HK", and the product model is "ADVA109".

Table 5.4: Properties of concrete

Batch No.	f_{co} (MPa)	E_c (GPa)	ε_{co} (%)
1	54.1	27.8	0.26
2	84.6	33.1	0.27
3	104.4	36.4	0.31
4	40.9	23.5	0.22
5	66.1	30.0	0.25
6	85.8	33.9	0.27

Table 5.5: Key test results

Specimen	F_{all} (kN)	F_c (kN)	f'_{cc} (MPa)	ε_{cu} (%)	$\frac{f'_{cc}}{f'_{co}}$	$\frac{\varepsilon_{cu}}{\varepsilon_{co}}$	$\varepsilon_{h,rup1}$ (%)	$\varepsilon_{h,rup2}$ (%)
D54-2FW-M	1965	1053	91.1	1.85	1.69	7.19	0.79	0.92
D54-4FW-M	2530	1401	121.2	2.79	2.25	10.7	0.80	0.78
D84-4FW-MB	4461	3410	169.7	2.47	2.01	8.98	0.94	0.91
D84-4FW-M1	2650	1567	135.6	2.20	1.60	8.15	0.80	0.60
D84-4FW-M2	2763	1683	145.7	2.30	1.72	8.52	0.73	0.79
D84-9FW-M	3413	2005	173.5	2.86	2.05	10.6	0.78	0.55
D104-4FW-M	2616	1550	134.2	1.95	1.29	6.26	0.53	0.64
D104-9FW-M	3512	2082	180.2	3.17	1.73	10.2	0.74	0.69
D40-6FW-M	6002	4079	123.6	3.74	3.02	16.9	1.23	1.20
D66-6FW-M	5284	3299	100.0	2.14	1.51	8.50	0.93	0.95
D85-6FW-M	5482	3771	114.3	1.79	1.33	6.68	0.83	0.91
D85-10FW-M	7089	4610	139.7	3.33	1.62	12.4	0.85	0.80

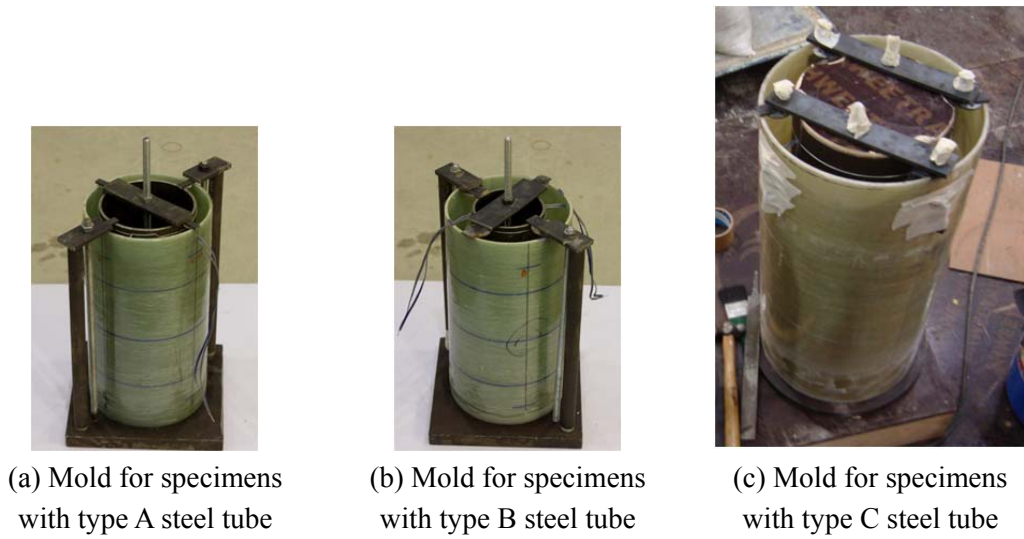


Figure 5.1: Molds of hybrid DSTCs

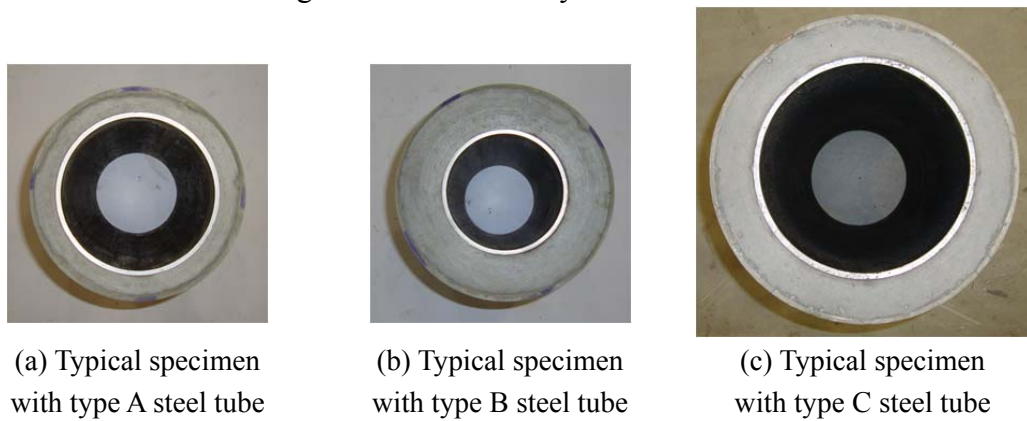


Figure 5.2: Cross-sections of different specimens

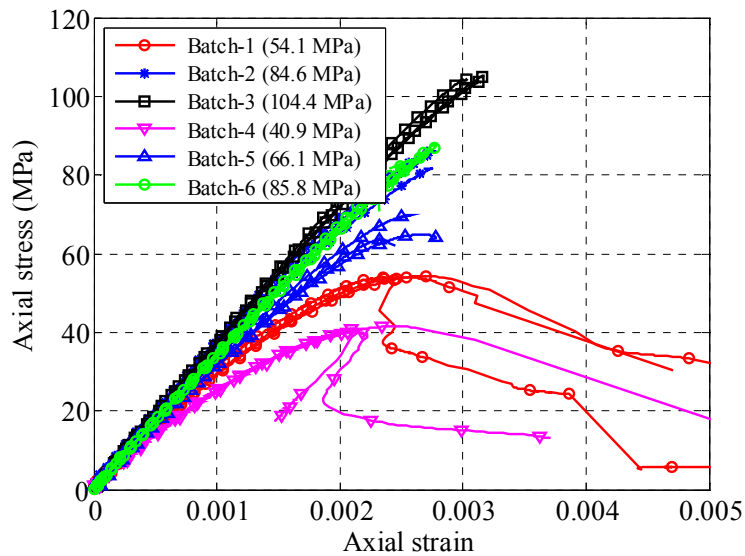


Figure 5.3: Axial stress-strain behavior of control cylinders

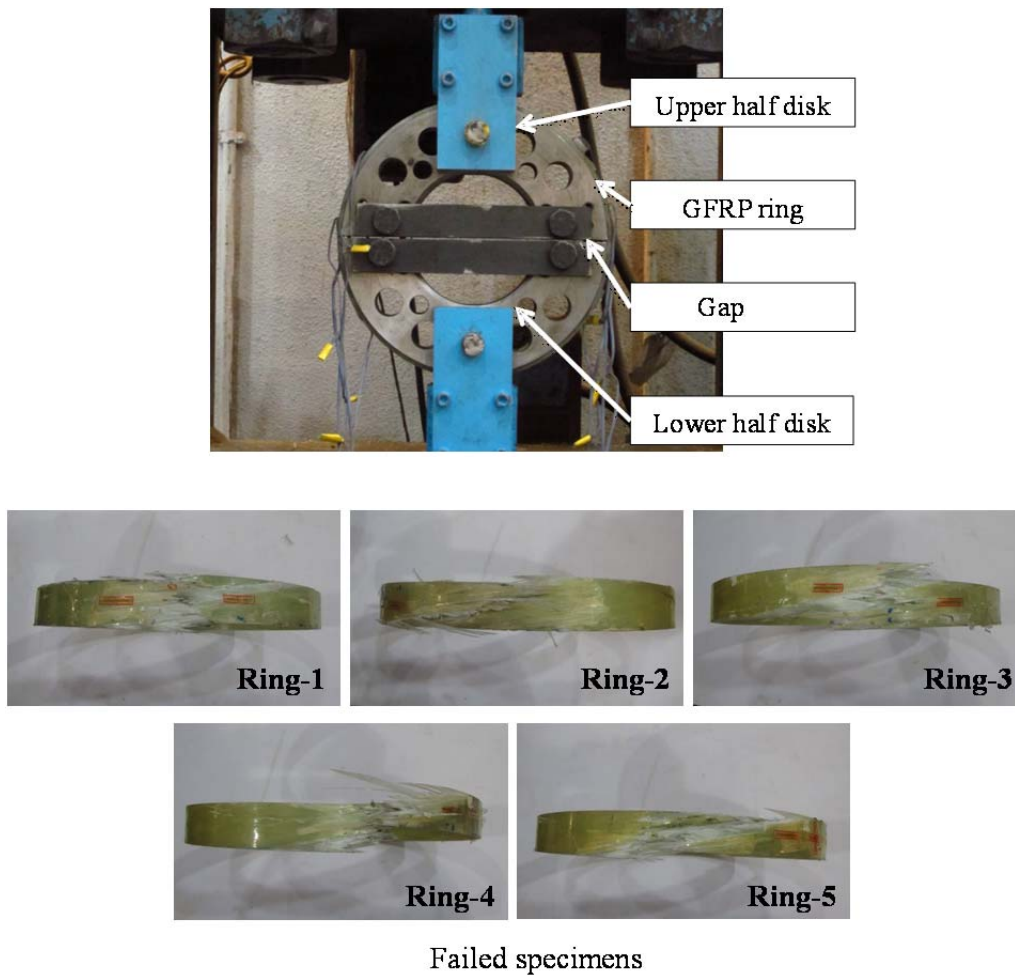


Figure 5.4: Tensile split-disk test of FRP tubes

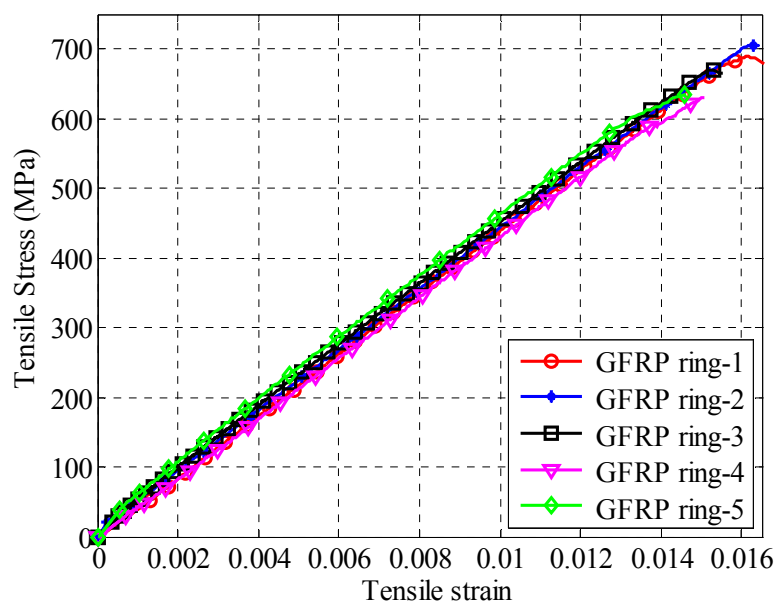


Figure 5.5: Tensile stress-strain curves of FRP tubes in the hoop direction



(a) Type A steel tube

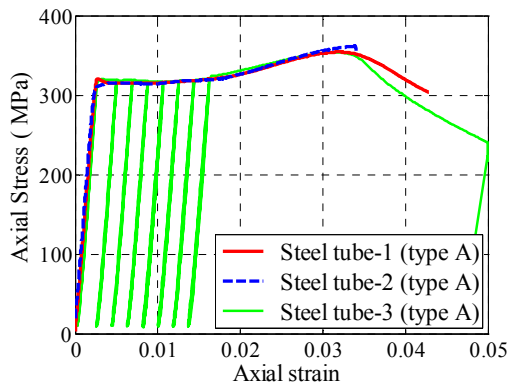


(b) Type B steel tube

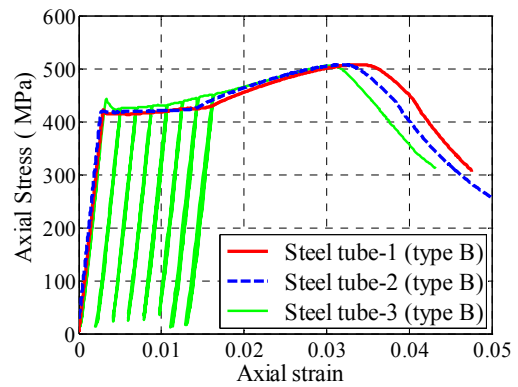


(c) Type C steel tube

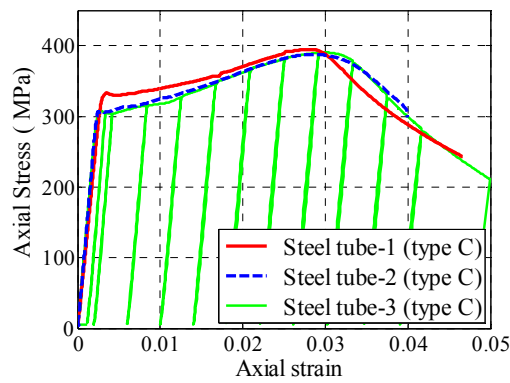
Figure 5.6: Steel tubes after axial compression



(a) Type A steel tube



(b) Type B steel tube



(c) Type C steel tube

Figure 5.7: Axial stress-axial strain curves of steel tubes

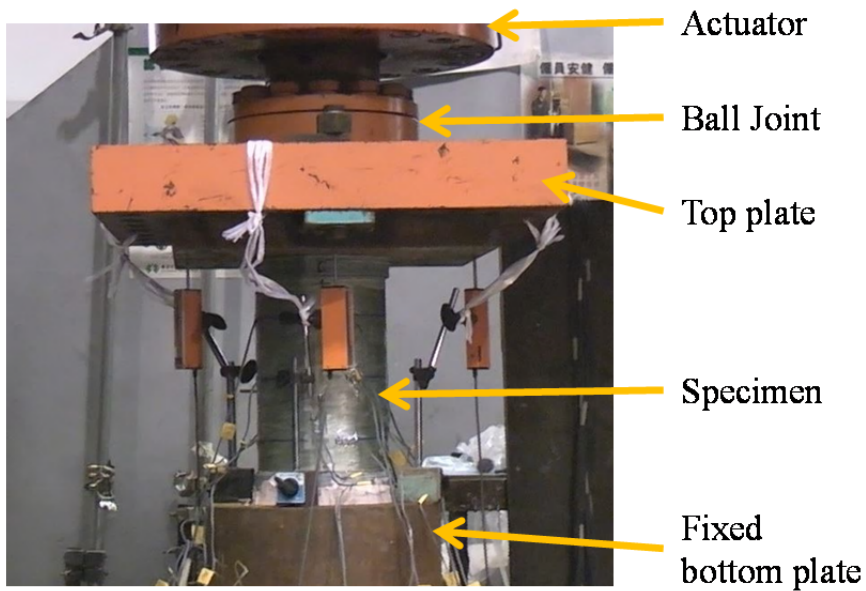
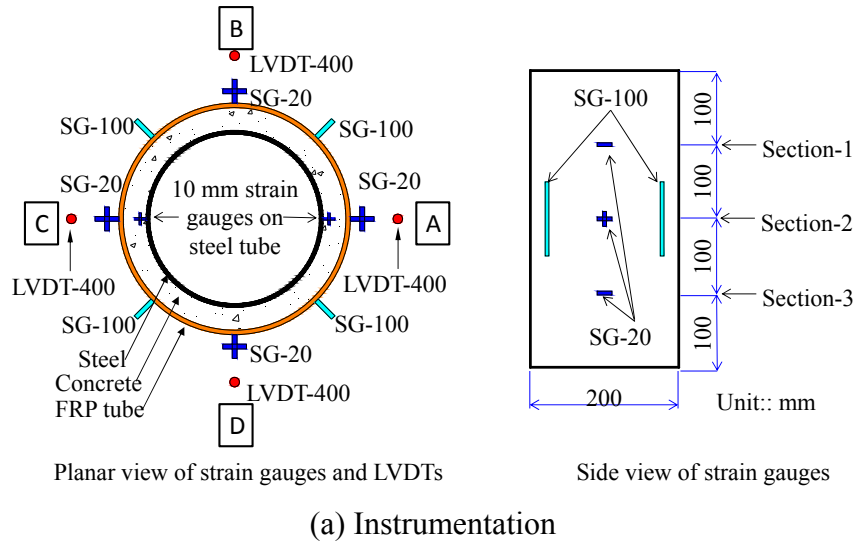
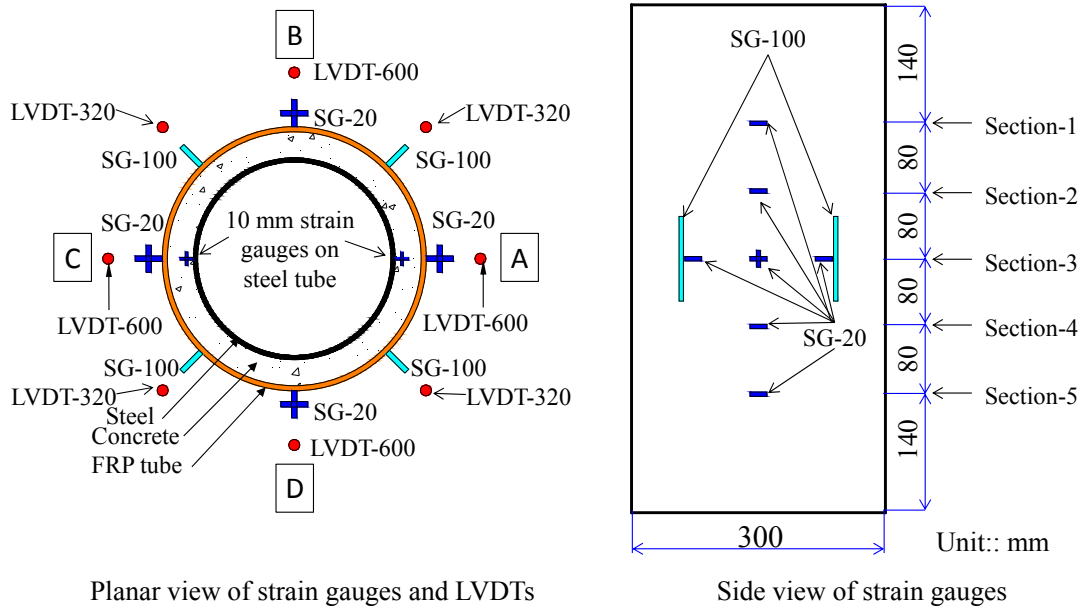
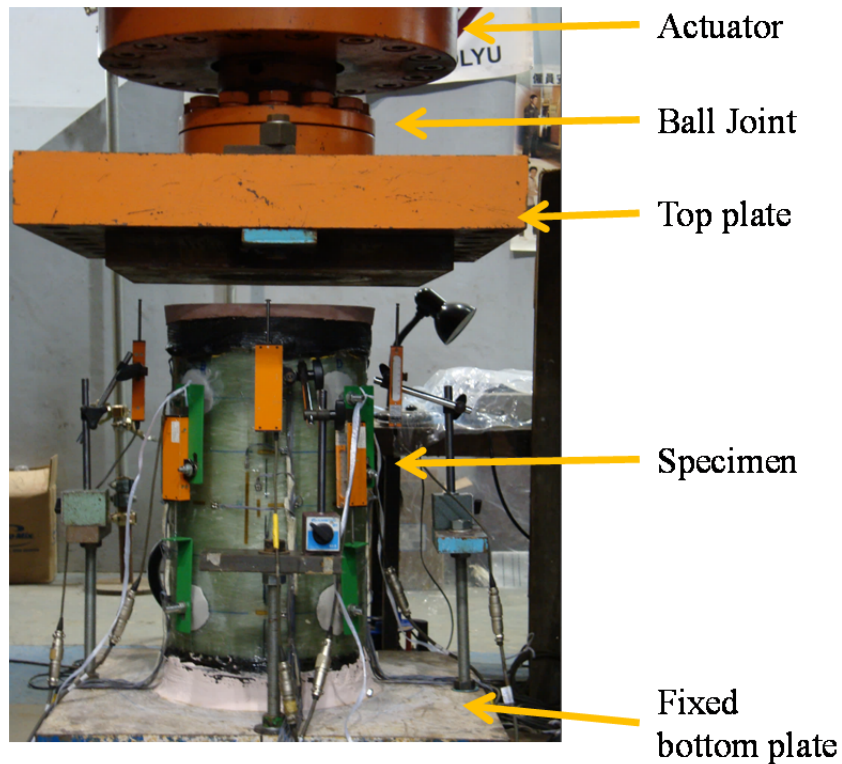


Figure 5.8: Experimental set-up and instrumentation for hybrid DSTCs of batches 1-3



(a) Instrumentation



(b) Experimental set-up

Figure 5.9: Experimental set-up and instrumentation for hybrid DSTCs of batches 4-6



(a) Failed specimens of batch 1



(b) Failed specimens of batch 2



(c) Failed specimens of batch 3



Figure 5.10: Specimens after test



D40-6FW-M

(d) Failed specimens of batch 4



D66-6FW-M

(e) Failed specimens of batch 5



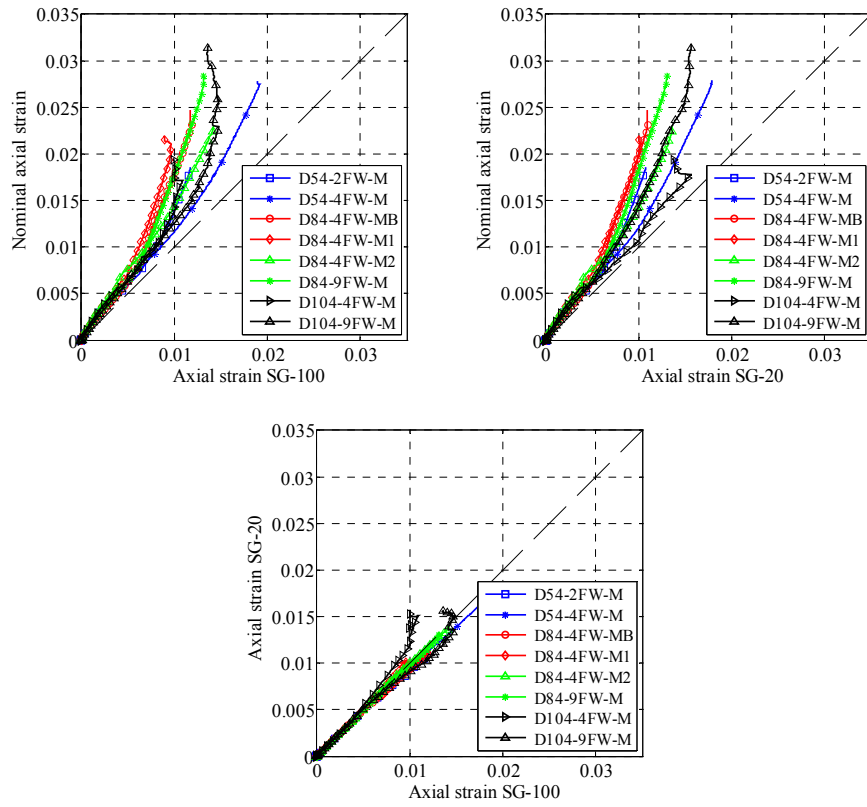
D85-6FW-M



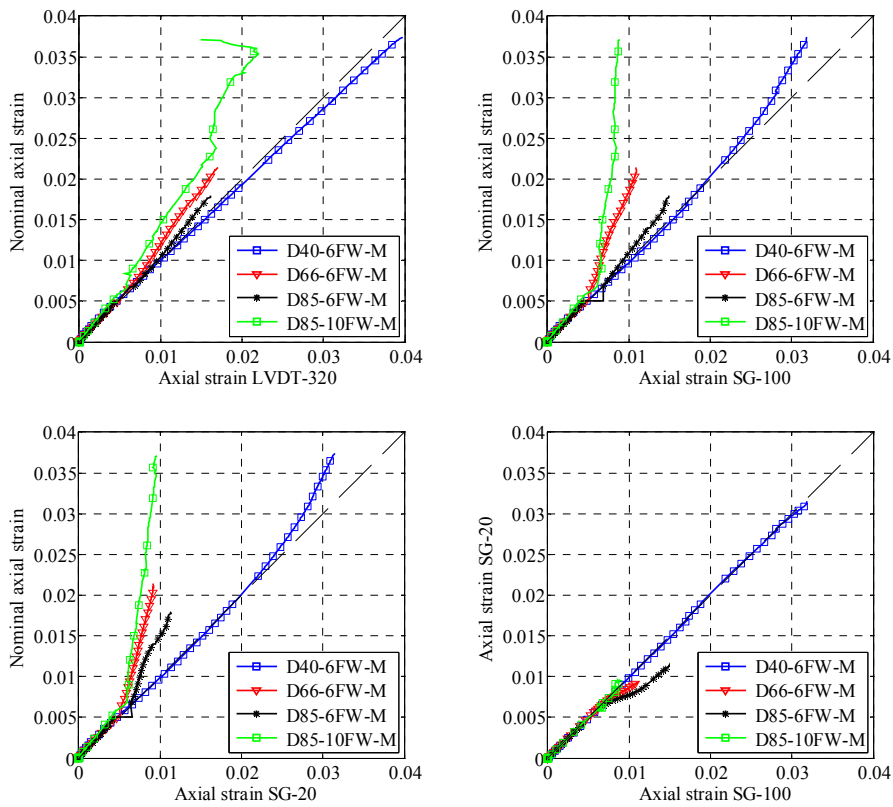
D85-10FW-M

(f) Failed specimens of batch 6

Figure 5.10: Specimens after test (continued)

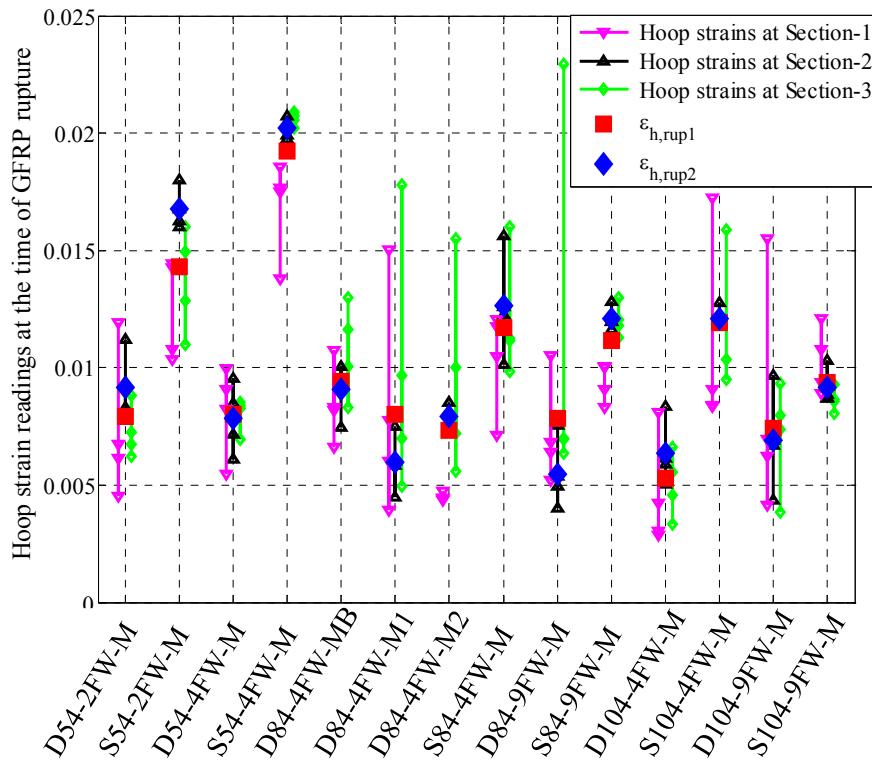


(a) Specimens of batches 1-3

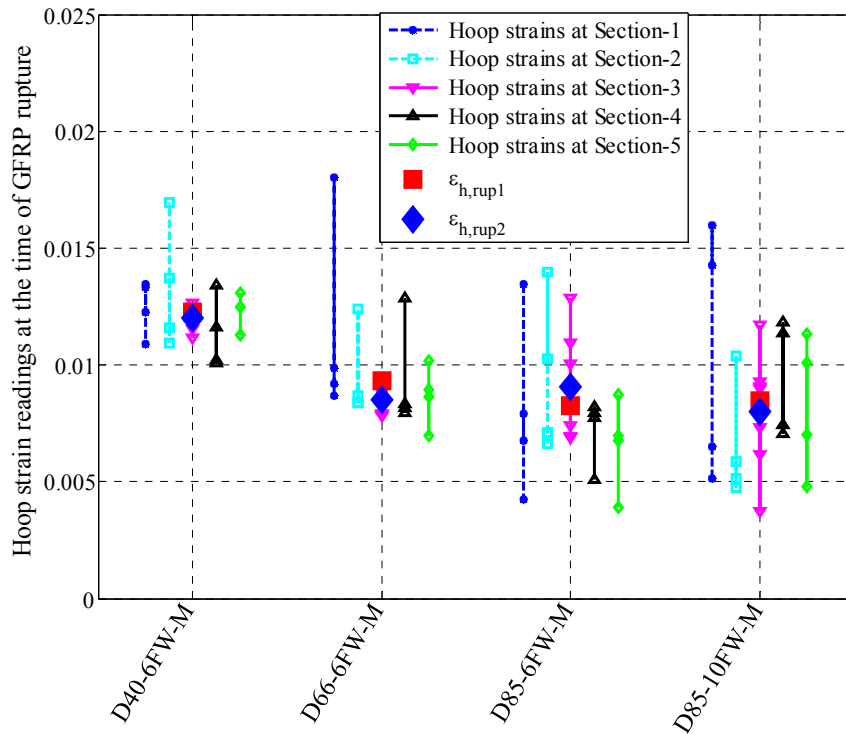


(b) Specimens of batches 4-6

Figure 5.11: Comparison of axial strains obtained using different methods



(a) Hybrid DSTCs of batches 1-3



(b) Hybrid DSTCs of batches 4-6

Figure 5.12: Hoop strain distributions

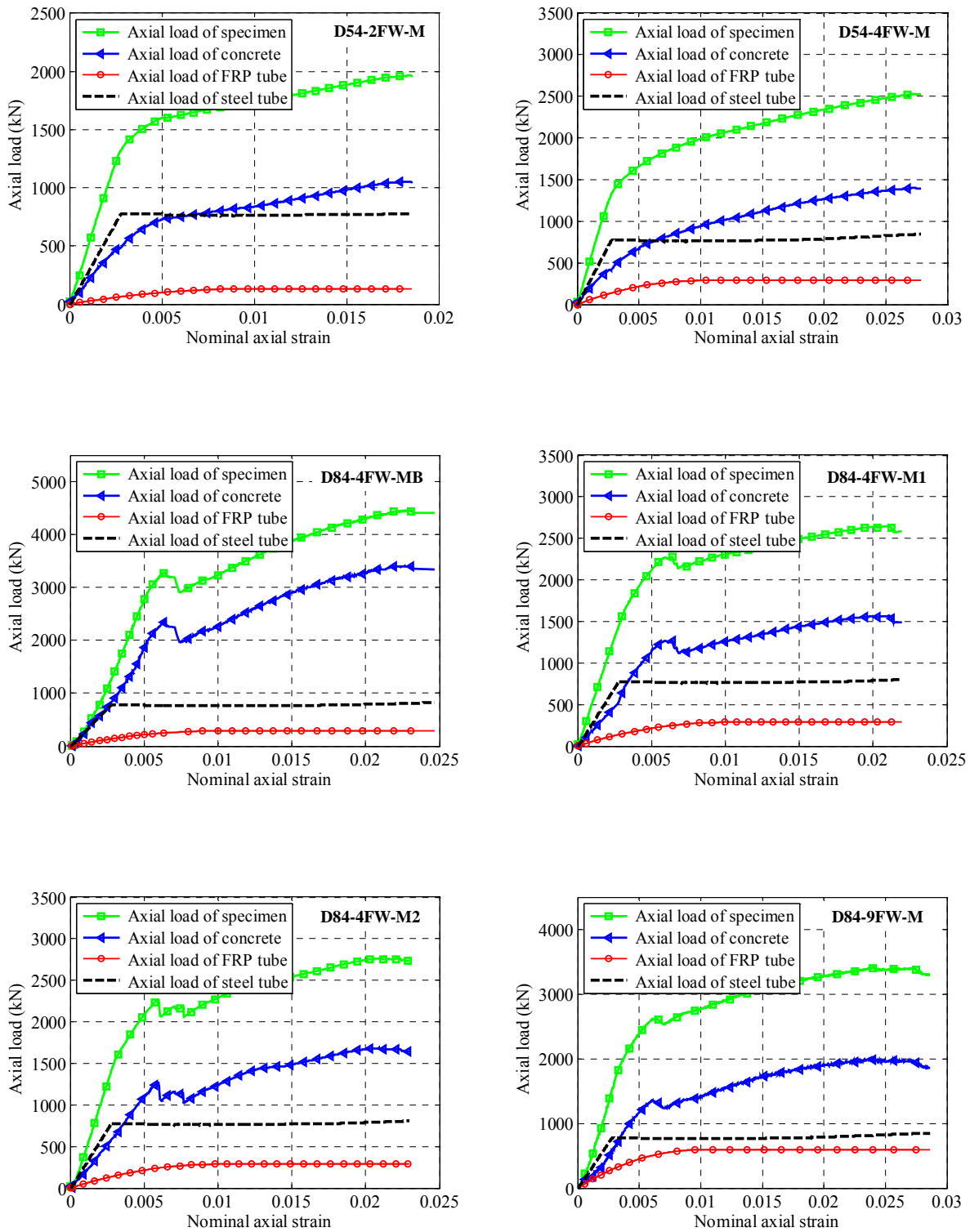


Figure 5.13: Axial load-axial strain curves of hybrid DSTCs

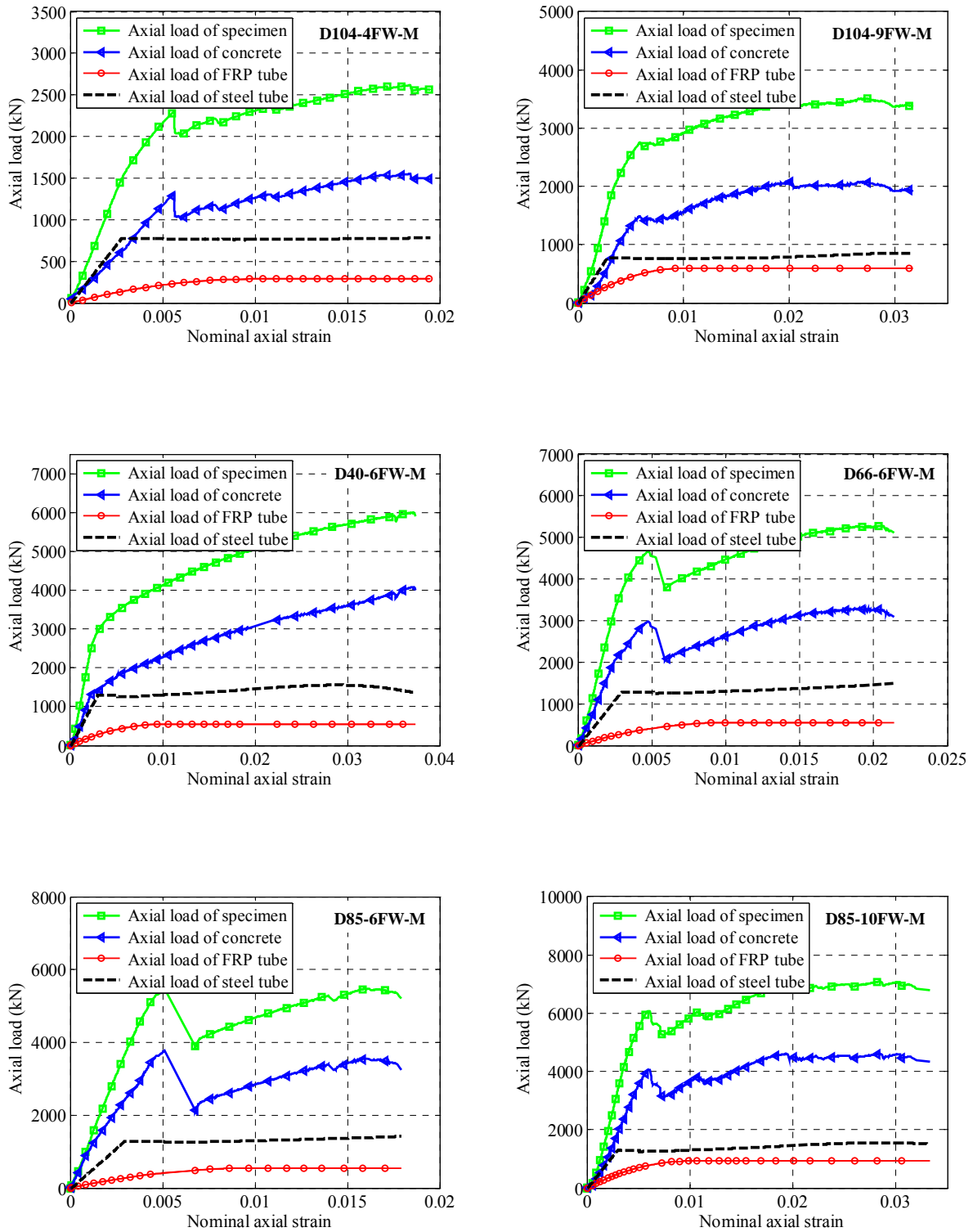
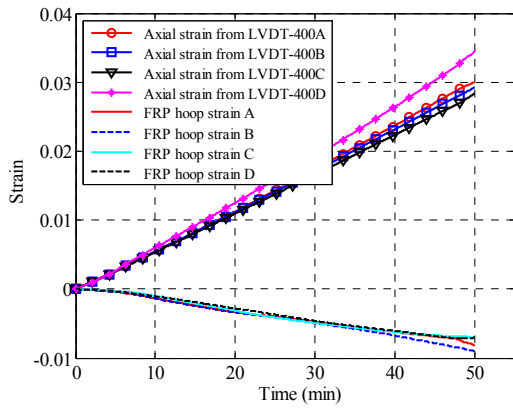
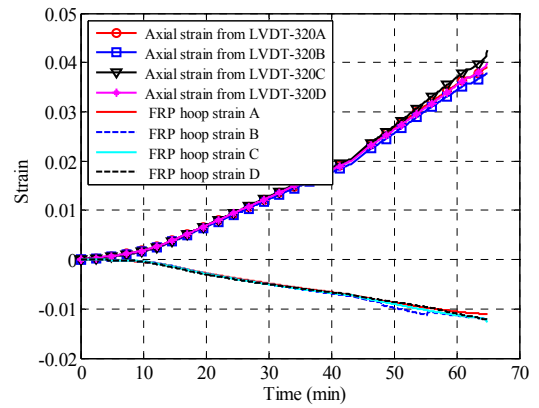


Figure 5.13: Axial load-axial strain curves of hybrid DSTCs (continued)

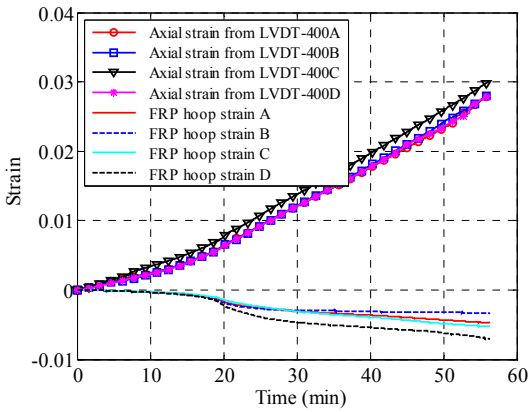


(a) Specimen D54-4FW-M

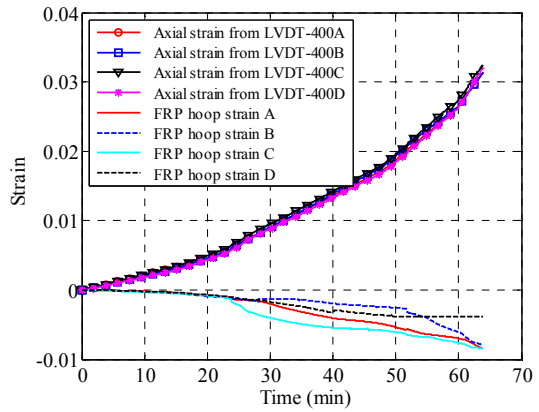


(b) Specimen D40-6FW-M

Figure 5.14: Development of strains during test: Specimens of Group 1

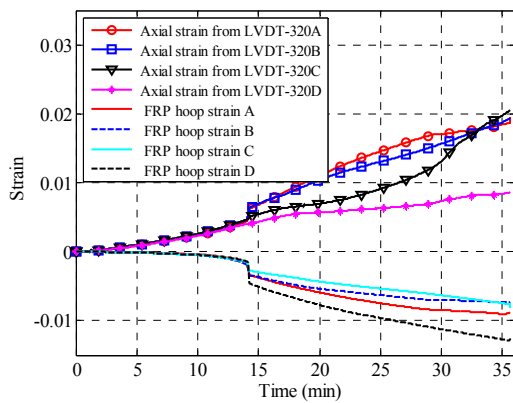


(a) Specimen D84-9FW-M

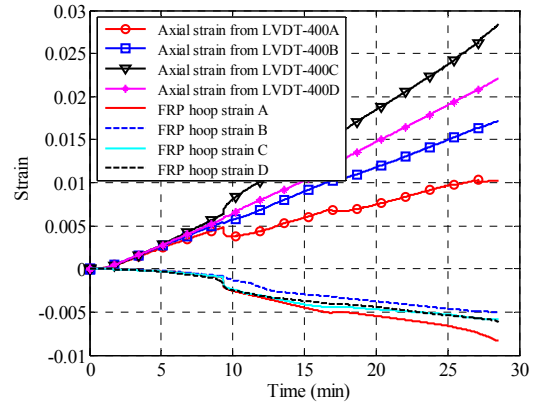


(a) Specimen D104-9FW-M

Figure 5.15: Development of strains during test: Specimens of Group 2



(a) Specimen D66-6FW-M



(b) Specimen D104-4FW-M

Figure 5.16: Development of strains during test: Specimens of Group 3

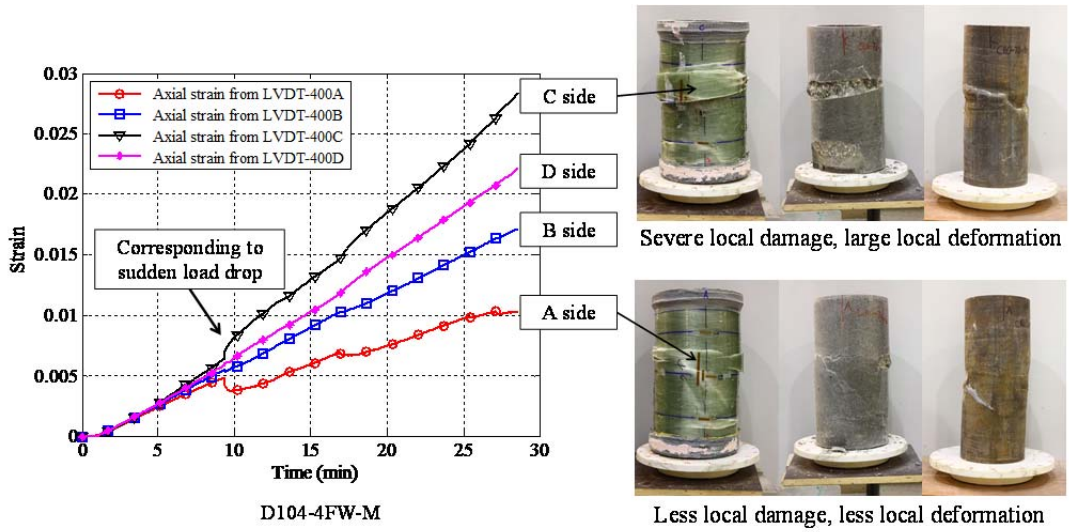
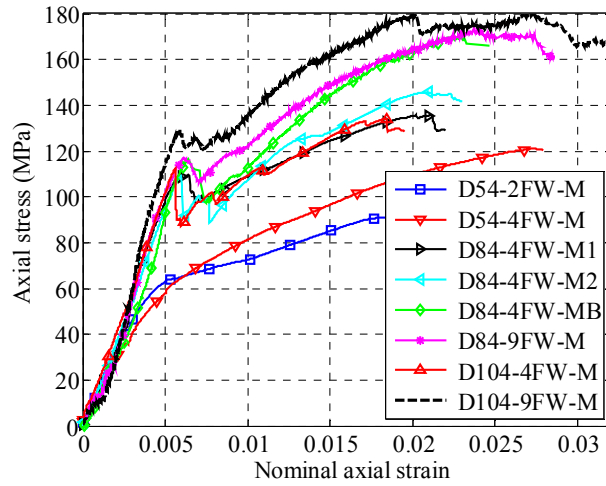
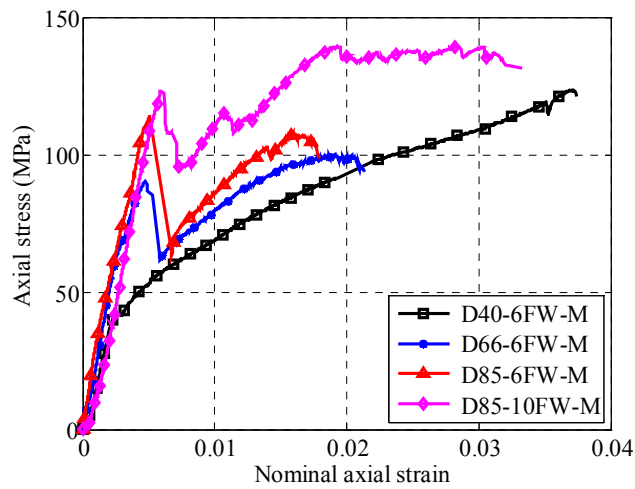


Figure 5.17: Damage localization over the cross section

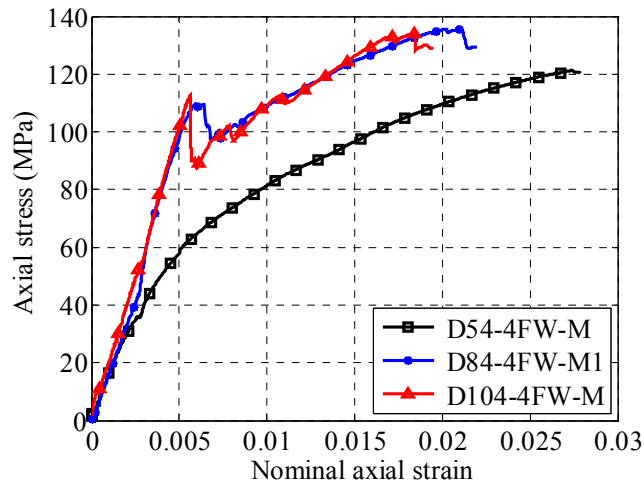


(a) Hybrid DSTCs of batches 1-3

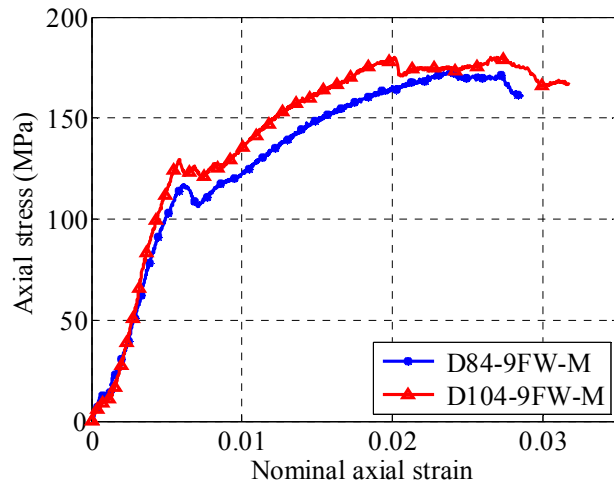


(b) Hybrid DSTCs of batches 4-6

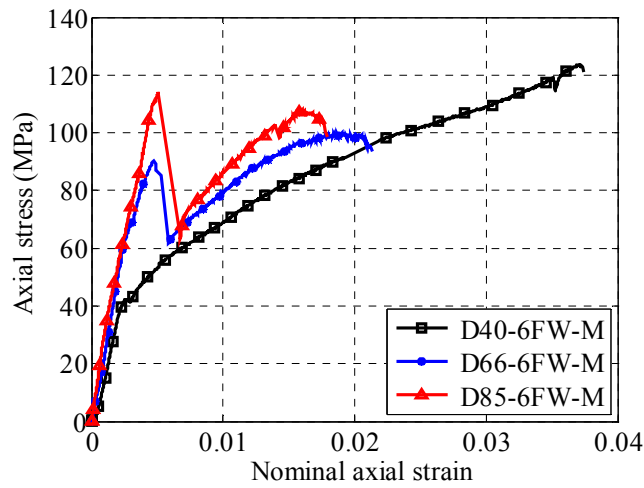
Figure 5.18: Axial stress-strain curves of concrete



(a)

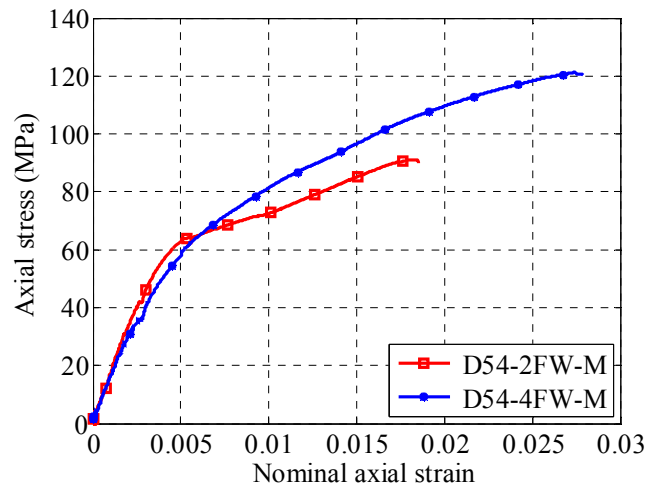


(b)

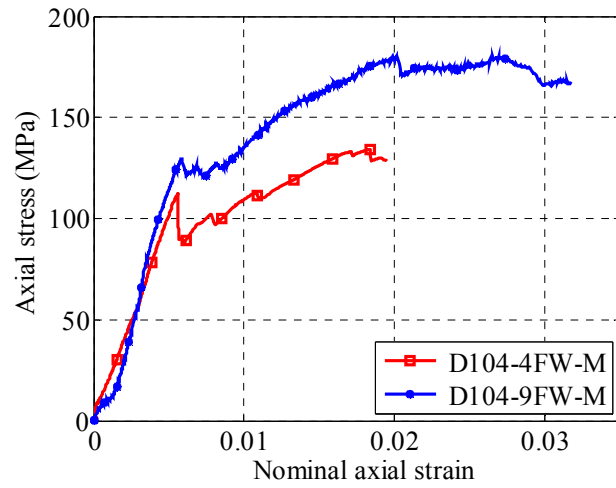


(c)

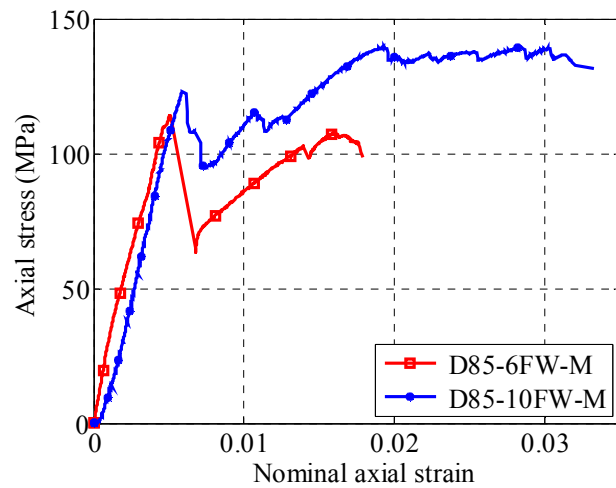
Figure 5.19 Effect of concrete strength on axial stress-strain curves of concrete



(a)



(b)



(c)

Figure 5.20: Effect of FRP tube thickness on axial stress- strain curves of concrete

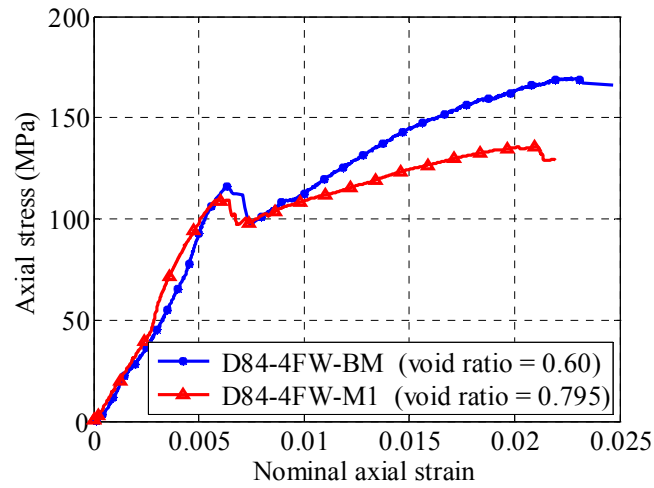


Figure 5.21: Effect of void ratio on axial stress-strain curves of concrete

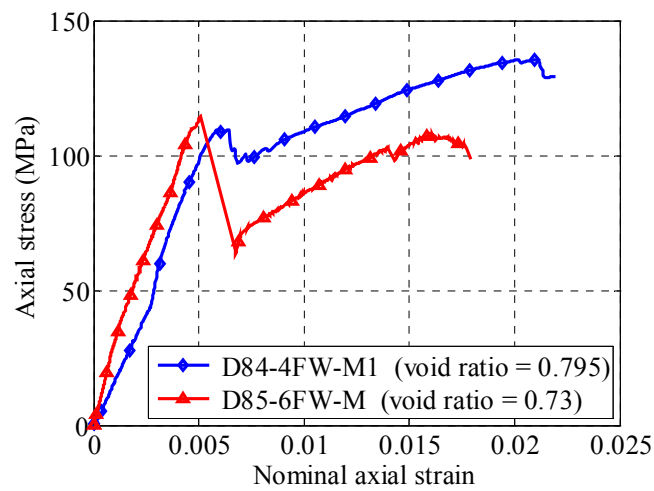
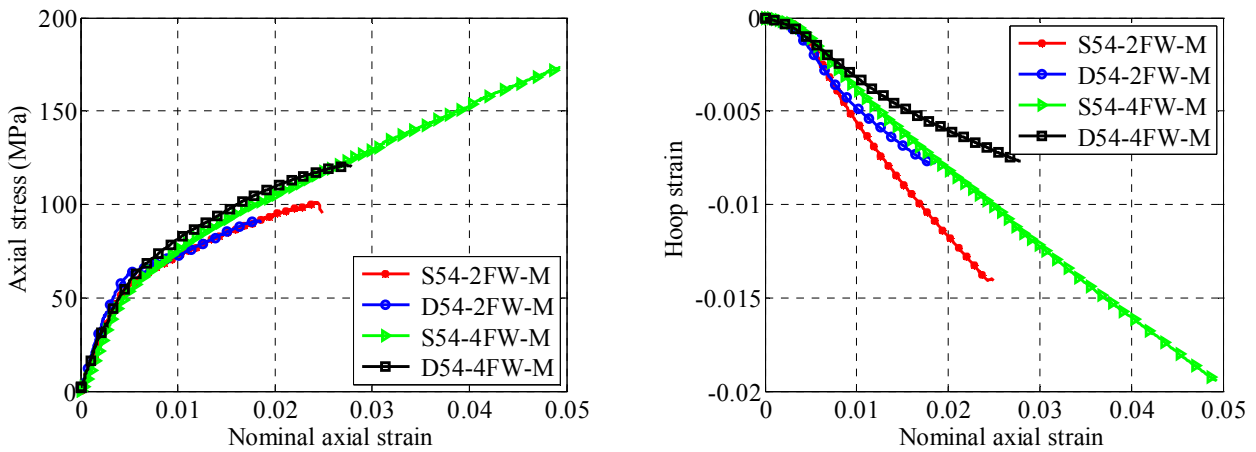
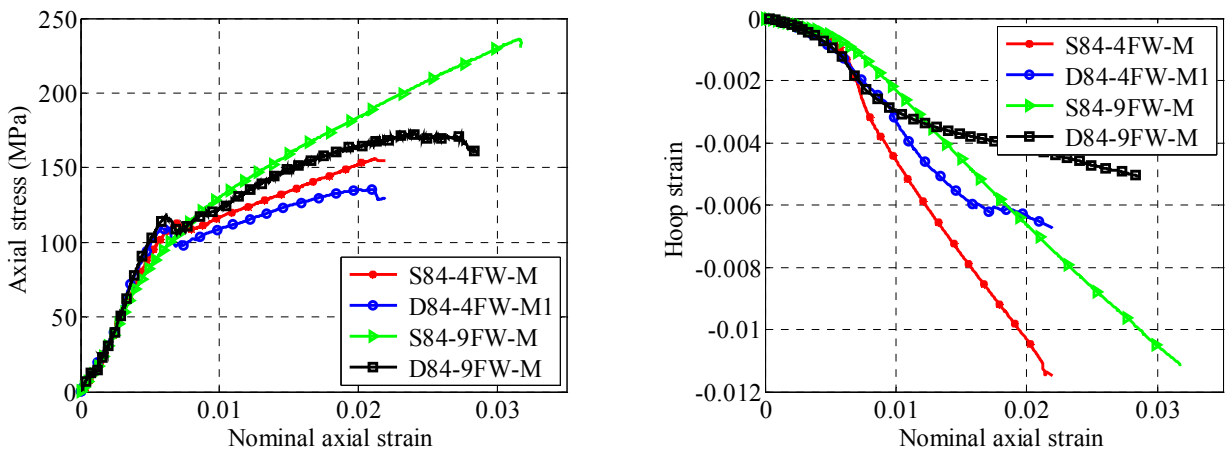


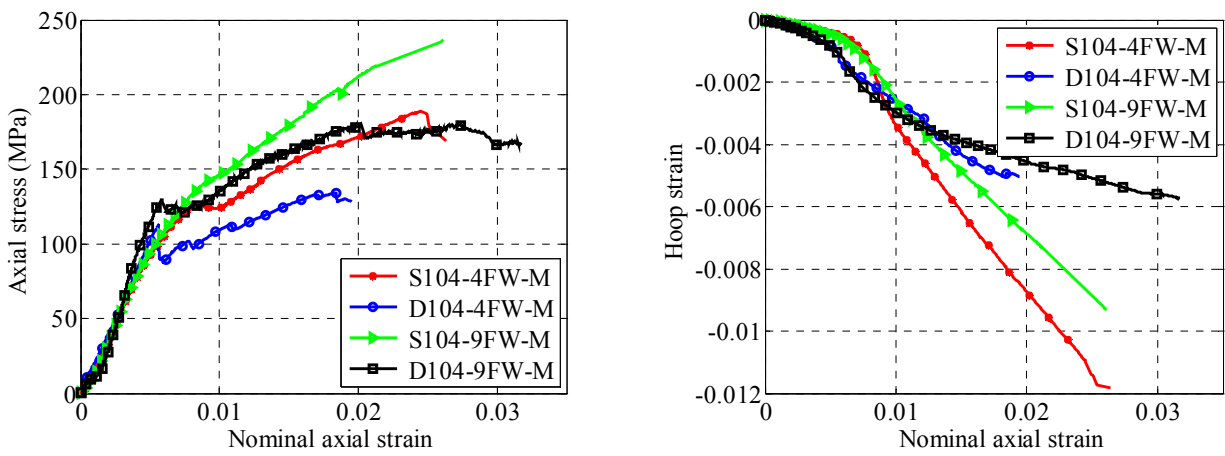
Figure 5.22: Effect of specimen size on axial stress- strain curves of concrete



(a) Specimens in batch 1

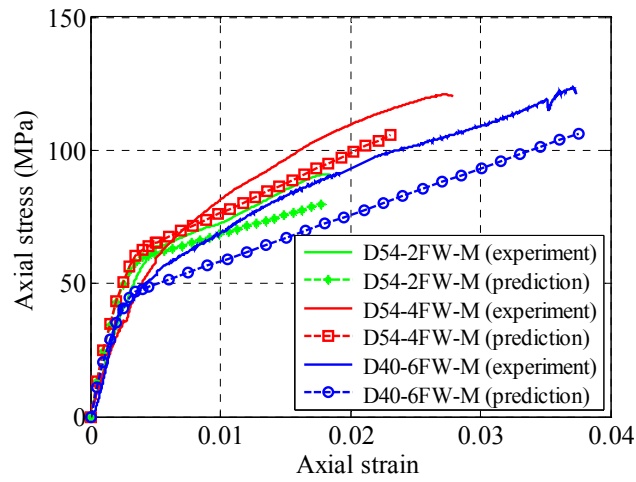


(b) Specimens in batch 2

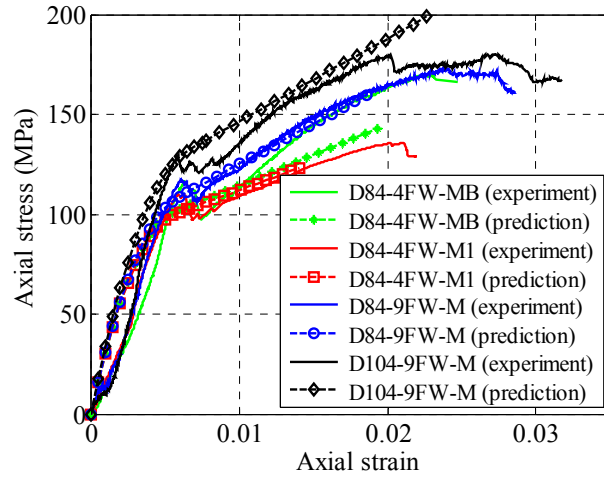


(c) Specimens in batch 3

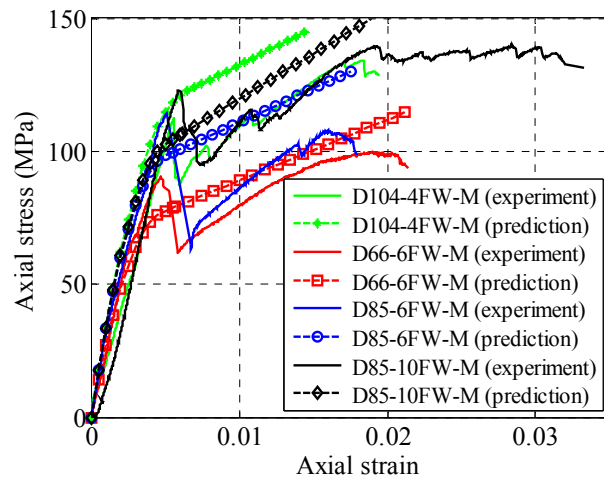
Figure 5.23: Comparison of concrete behavior between hybrid DSTCs and CFFTs



(a) Specimens with bi-linear ascending branch



(b) Specimens with axial load fluctuation



(c) Specimens with sudden load drop

Figure 5.24: Comparison of axial stress-strain curves of concrete with Yu *et al.*'s (2010) model

CHAPTER 6

BEHAVIOR OF HYBRID DSTCS UNDER CYCLIC AXIAL COMPRESSION

6.1 INTRODUCTION

The excellent ductility of hybrid FRP-concrete-steel double-skin tubular columns (hybrid DSTCs) means that they are particularly attractive for use in seismic regions. While a large amount of research has been conducted on the monotonic behavior of this novel form of columns (e.g. Teng *et al.* 2004; Teng *et al.* 2007; Yu 2007; Wong *et al.* 2008; Qian and Liu 2008; Yu *et al.* 2010; Zhang *et al.* 2011; Xie *et al.* 2011; Ozbakkaloglu and Fanggi 2013a, 2013b; Fanggi And Ozbakkaloglu 2013), only a limited amount of work has been conducted on the behavior of hybrid DSTCs under cyclic axial compression. The stress-strain behavior of the concrete in hybrid DSTCs subjected to cyclic axial compression is of particular importance in the modeling of their behavior under seismic loading.

To the best of the author's knowledge, only two studies have been conducted on hybrid DSTCs under cyclic axial compression (i.e. Yu *et al.* 2012; Ozbakkaloglu and Fanggi 2013b), and no cyclic stress-strain model has been developed for concrete in hybrid DSTCs. Yu *et al.* (2012) presented the first ever study into hybrid DSTCs subjected to cyclic axial compression, in which six specimens

(characteristic diameter: 205 mm; height: 400 mm; concrete strength: 43.9 MPa; wet-layup FRP tubes) were tested. The test results confirmed the ductile behavior of hybrid DSTCs under cyclic axial compression. Yu *et al.*'s (2010) monotonic stress-strain model was found to provide acceptable but conservative predictions of the experimental envelope curves of these hybrid DSTCs. Yu *et al.* (2012) also confirmed that Lam and Teng's (2009) cyclic stress-strain model provides reasonably accurate predictions of the experimental unloading/reloading cycles. Ozbakkaloglu and Fanggi (2013b) reported cyclic compression tests on six small-scale hybrid DSTCs with the steel inner tube filled with concrete (characteristic diameter: 150 mm; height: 300 mm; concrete strengths: 42.5 MPa and 82.4 MPa; prefabricated wet-layup FRP tubes). As Ozbakkaloglu and Fanggi's (2013b) study is only concerned with hybrid DSTCs with a concrete-filled inner void, it is not further discussed in this chapter.

Yu *et al.*'s (2012) study has generally been limited to normal strength concrete, small-scale specimens and wet-layup FRP tubes. There has been no experimental study on large-scale hybrid DSTCs with a filament-wound FRP tube and high strength concrete (HSC). Against this background, this chapter presents an experimental study of hybrid DSTCs under cyclic axial compression, with a particular focus on: (1) the use of HSC; (2) the use of filament-wound tubes; and (3) the use of large-scale specimens.

Chapter 4 has presented a unified cyclic stress-strain model for FRP-confined NSC/HSC which was developed on the basis of a critical assessment of Lam and Teng's (2009) model using a new test database. In this chapter, the applicability of this unified cyclic stress-strain model to concrete in hybrid DSTCs is also examined.

6.2 EXPERIMENTAL PROGRAM

6.2.1 Specimen Details

A total of 14 hybrid DSTCs were designed and tested as detailed in Table 6.1. These specimens were cast using 6 different batches of concrete. Hybrid DSTCs of batches 1-3 were cast together with the three batches of CFFTs presented in Chapter 3, respectively. For all 14 hybrid DSTCs, corresponding hybrid DSTCs were also fabricated and tested under monotonic axial compression, the results of which have been presented in Chapter 5.

As shown in Table 6.1, the specimens of batches 1-3 had a characteristic diameter of 200 mm and a height of 400 mm, while specimens of batches 4-6 were larger-scale specimens with a characteristic diameter of 300 mm and a height of 600 mm. The majority of hybrid DSTCs in the present study were designed with a large void ratio (i.e. 0.73 and 0.795), with only one exception (i.e. specimen D84-4FW-CB with a void ratio of 0.60). Three types of steel tubes were used, which are referred to as type A, type B and type C steel tubes respectively for ease of discussion (see Table 5.2). Filament-wound GFRP tubes with the fibers being at ± 80 degrees to the longitudinal axis were used.

The naming system for these specimens is similar to CFFTs in Chapter 3 and hybrid DSTCs in Chapter 5. Each specimen was given a name, which starts with the letter “D” to represent “hybrid DSTCs”, followed by a two- or three-digit number to represent the unconfined concrete strength, and then a number which defines the thickness (in mm) of the FRP tube, together with two letters “FW” indicating that the FRP tube is made through a filament-winding process. This is then followed by a letter “C” to represent cyclic axial loading; the last number “1”

or 2” in some of the specimens is to differentiate two nominally identical specimens. The information of the inner steel tube is again not given in the specimen name for brevity, except for the specimen with a type B steel tube and thus a smaller void ratio (i.e. D84-4FW-CB), for which a letter “B” is added to the end of its name.

6.2.2 Preparation of Specimens

The preparation of specimens was the same as that presented in Chapter 5, and is not repeated here. Each batch of specimens, including CFFTs (see Chapter 3), monotonically loaded DSTCs (see Chapter 5), and cyclically loaded DSTCs, were cast together (see Tables 3.1, 5.1 and 6.1). The batch numbers are consistent throughout this thesis. The mold used for casting concrete, the cross-sections of specimens, and the mix proportions of concrete used in the cyclic compression tests were all the same as those presented in Chapter 5 (see Figures 5.1 and 5.2 and Table 5.3 respectively).

6.2.3 Material Properties

6.2.3.1 Concrete

Three concrete control cylinders (152.5 mm x 305 mm) were prepared and tested for each batch of concrete to determine the concrete properties following ASTM C39/C39M (2011) (see Section 5.2.3.1). The average elastic modulus E_c , compressive strength f'_{co} and the corresponding strain ϵ_{co} obtained from these tests are given in Table 5.4. The stress-strain curves of all control cylinders are shown in Figure 5.3.

6.2.3.2 FRP Tubes

The FRP tubes used in the cyclic compression tests were exactly the same as those used in the monotonic compression tests presented in Chapter 5. Tensile split-disk tests on FRP rings were conducted following ASTM D2290-08 (2008), and compression tests on FRP rings were conducted following GB/T5350-2005 (2005). The results can be found in Section 3.2.3.2 and Section 5.2.3.2 respectively.

6.2.3.3 Steel Tubes

The steel tubes used in the cyclic compression tests were again exactly the same as those used in the monotonic compression tests presented in Chapter 5. Tensile coupon tests were conducted following BS 18 (1987), as well as compression tests on steel tubes. The results are available in Section 5.2.3.3.

6.2.4 Experimental Set-Up and Instrumentation

Readers may refer to Section 5.2.4 for the detailed information of experimental set-up and instrumentation. The information is available in Figures 5.8 and 5.9 for the specimens of batches 1-3 and those of batches 4-6, respectively.

6.2.5 Loading Schemes

A large testing facility with a maximum axial compression capacity of 10000 KN, was used to conduct axial compression tests with displacement control rates of 0.24 mm/min and 0.36 mm/min for the specimens of batches 1-3 and those of batches 4-6, respectively.

Two cyclic loading schemes were adopted for these hybrid DSTCs: (1) type C1: a single unloading/reloading cycle was applied at prescribed unloading displacement values; (2) type C2: several repeated unloading/reloading cycles were applied at prescribed unloading displacement values. Both the type C1 and type C2 loading schemes were designed for full unloading/reloading cycles where the unloading of each cycle was terminated at a zero load and the reloading of each cycle was terminated at the unloading displacement of the same cycle (i.e. where the unloading starts) or after reaching the envelope curve (Lam and Teng 2009).

For the specimens of batches 1-3, as there was only one cyclically loaded specimen for each sectional configuration, the specimen was subjected to a combination of type C1 and C2 loading: a single unloading/reloading cycle was applied at each of the first several prescribed unloading displacement values while 10 repeated cycles were applied at the last prescribed unloading displacement value. For specimen D84-4FW-CB, only 3 of the 10 intended repeated cycles were finished at the last prescribed unloading displacement value before the failure of the specimen. For the groups in batches 4-6 (i.e. D40-6FW, D66-6FW, D85-6FW) with two cyclically loaded specimens for each sectional configuration, one was subjected to type C1 loading while the other was subjected to type C2 loading. For specimen D85-10FW-C, type C1 loading was adopted. Details of the loading schemes are summarized in Table 6.2.

The loading schemes were executed manually with the use of the displacement readings averaged from 4 LVDTs (i.e. LVDT-400 for specimens of batches 1-3; LVDT-600 for specimens of batches 4-6) and the load readings from the column testing facility as the controlling parameters. All test data, including strains, loads, and displacements, were recorded simultaneously by a data logging system.

6.3 TEST OBSERVATIONS

6.3.1 General

As discussed in Section 5.3.1, the failure of filament-wound GFRP tubes was a progressive process. The failure processes of cyclically loaded hybrid DSTCs were similar to those of the corresponding monotonically loaded hybrid DSTCs, indicating that different loading schemes had little effect on this process. Progressive snapping of fibers was noticed in the final stage of test, until the explosive rupture of FRP tube associated with a big noise. Axial load fluctuations/a sudden load drop were also observed for cyclically loaded hybrid DSTCs with HSC. The mechanism for the axial load fluctuation/sudden load drop was discussed in Section 5.4.1.

After the test, the GFRP tube, the concrete and the inner steel tube were carefully examined (Figure 6.1). As expected, damage localization was found for all specimens. The rupture of FRP tube occurred at places where concentrated damage of the concrete infill occurred. Inward deformation/buckling of the inner steel tube was also observed at the same locations. The failure mode of cyclically loaded hybrid DSTCs (Figure 6.1) was similar to that of monotonically loaded hybrid DSTCs (see Figure 5.10), indicating that different loading schemes had little effect on the failure mode.

6.3.2 Axial Strains

As discussed in Section 5.3.2, both LVDTs and strain gauges were used to measure the axial deformation of the specimen during the test, which provided several ways to obtain the axial strain of the specimen. The average strain over the

whole height of the specimen, which was based on readings from four LVDTs (i.e. LVDT-400 for specimens of batches 1-3; LVDT-600 for specimens of batches 4-6), is referred as the nominal axial strain. Based on the discussions presented in Chapter 5, the nominal axial strain is used to represent the axial strain of the confined concrete, unless otherwise specified.

6.3.3 Hoop Strains

Making use of readings from the three (for batches 1-3) or five (for batches 4-6) groups of hoop strain gauges located at different heights of the FRP tube, the hoop strain distributions at the ultimate state of all the specimens are shown in Figure 6.2. The results from the tests of CFFTs (see Chapter 3) and monotonically loaded hybrid DSTCs (see Chapter 5) are also shown in Figure 6.2 for comparison.

The following observations can be made from Figure 6.2: (1) the maximum hoop strain and minimum hoop strain were generally found not at the mid-height of the specimens; (2) despite the larger scatter of these hoop strain readings, the average of all the hoop strain readings ($\varepsilon_{h,rup1}$) is very close to the average of hoop strain readings at the mid-height section ($\varepsilon_{h,rup2}$); (3) the hoop rupture strain (either $\varepsilon_{h,rup1}$ or $\varepsilon_{h,rup2}$) of hybrid DSTCs is much smaller than that of the corresponding CFFTs; (4) the hoop rupture strain (either $\varepsilon_{h,rup1}$ or $\varepsilon_{h,rup2}$) of monotonically loaded specimens is generally larger than the corresponding cyclically loaded specimens, which is believed to be due to the damage accumulation in the FRP tube caused by cyclic straining; (5) the average hoop rupture strain appears to be smaller for specimens with a higher concrete strength and/or a weaker tube.

6.4 BEHAVIOR OF CONFINED CONCRETE

6.4.1 Axial Load-Axial Strain Curves of Hybrid DSTCs

The axial load-axial strain curves of all hybrid DSTCs are shown in Figure 6.3, where those of cyclically loaded hybrid DSTCs are compared with the curves of the corresponding specimens under monotonic compression. It is evident from Figure 6.3 that the envelope curves of all the specimens subjected to cyclic axial compression are almost the same as the corresponding monotonic axial load-strain curves. This observation is similar to that presented in Chapter 3 for CFFTs as well as those reported by other researchers for concrete confined by an FRP wrap (e.g. Lam *et al.* 2006; Ozbakkaloglu and Akin 2012). This is also consistent with the observation for hybrid DSTCs with NSC (Yu *et al.* 2012).

6.4.2 Axial Stress-Axial Strain Behavior of Concrete

In hybrid DSTCs, the axial load is taken by the confined concrete, the inner steel tube as well as the FRP tube. In the present study, the average axial stress of the concrete is defined to be the load carried by the concrete section divided by its cross-sectional area. The load carried by the concrete section is assumed to be equal to the load carried by the specimen subtracted by the load resisted by the FRP tube and that by the inner steel tube at the same axial strain.

The load carried by the FRP tube under monotonic loading is found from compression tests on hollow FRP tubes (see Figures 3.5 and 3.6); when the axial strain of a specimen exceeds the ultimate strain of the corresponding hollow FRP tube, it is assumed that the load resisted by the FRP tube is equal to its ultimate load because of the support from the concrete (see section 3.3.5). For the load

taken by the FRP tube under the unloading/reloading cycles, the same assumption was adopted as that presented in Chapter 3 for CFFTs: in the unloading process, the load taken by the FRP tube reduces proportionally to the total axial load taken by the specimen, and reaches zero at the same time as the total load becomes zero; in the reloading process, the load taken by the FRP tube increases proportionally to the total axial load taken by the specimen, and reaches the previous load taken by the FRP tube again when the envelope curve is reached. As explained in Chapter 3, this assumption leads only to minor errors considering the small axial stiffness and small cross-sectional area of the FRP tube.

To find the load taken by the inner steel tube during cyclic loading is more involved. Yu *et al.* (2012) found that the axial strain at which the load carried by a hybrid DSTC is zero is generally larger than the plastic strain of the concrete, and smaller than the plastic strain of the steel tube. This means that tensile stresses may be developed in the steel tube during the unloading process of hybrid DSTCs, with equilibrating compressive stresses in the concrete. The bond/friction between the steel tube and the concrete ensures force equilibrium to be reached. In the present study, both monotonic and cyclic axial compression tests on hollow steel tubes were conducted (see Section 5.2.3.3 and Figures 5.6 & 5.7), but the behavior of steel tubes under reversed cyclic axial loading was not tested due to the limitation of testing facilities. When the unloading branch starts from a point beyond the initial compressive yield point, the unloading stress-strain curve of steel exhibits the Bauschinger effect in the tensile region, and vice versa. Many models have been developed for the reversed cyclic stress-strain relationship of steel, including mainly two types: (a) Ramberg-Osgood type model (Ramberg and Osgood 1943); (b) Guiffre-Menegotto-Pinto type model (Menegotto and Pinto 1973). In the present study, the Ramberg-Osgood type model proposed by Yokoo and Nakamura (1977), which was found to be quite accurate and yet simple

(Mansour *et al.* 2001), was adopted to find the load taken by the inner steel tube from the experimental axial strain readings. Yokoo and Nakamura's (1977) model can be expressed by the following equation:

$$\varepsilon_s - \varepsilon_i = \frac{f_s - f_i}{E_s} \left[1 + A^{-R} \left| \frac{f_s - f_i}{f_y} \right|^{R-1} \right] \quad (6.1)$$

where f_s and ε_s are the stress and strain of cyclically loaded steel, respectively; f_i and ε_i are the stress and strain of cyclically loaded steel at the load reversal point, respectively; E_s is the Young's modulus of steel; f_y is the yield stress of steel; $A = 1.9k_p^{-0.2}$ and $R = 10k_p^{-0.2}$; k_p is the plastic strain ratio, which is defined as $\varepsilon_p/\varepsilon_n = (\varepsilon_i - \varepsilon_n)/\varepsilon_n$. In this expression, ε_p is the plastic strain, and ε_n is the initial yield strain. Readers may refer to Yokoo and Nakamura (1977) and Mansour *et al.* (2001) for more detailed information of this model.

Figure 6.4 shows the cyclic stress-strain curves of confined concrete in two of the tested hybrid DSTCs (i.e. specimens D40-6FW-C2 and D85-10FW-C) by considering the Bauschinger effect using Eq. 6.1. The average axial strains obtained from the two axial strain gauges on the inner steel tube were used. Figure 6.4 shows that for the first two prescribed unloading strains which were smaller than 0.005, the concrete stress reached zero when the specimens were unloaded to zero load. However, for the larger unloading strains, compressive stresses in the concrete, and thus tensile stresses in the steel existed when the overall load taken by the specimens became zero. It is also interesting to note that the concrete stresses at the zero overall load points were almost identical for different unloading strains (all being larger than 0.005), which is probably partially due to the limit of bond strength between the steel tube and the concrete.

As explained above, readings from the axial strain gauges on the steel tube need

to be used to derive the axial stress-strain curves of concrete. However, in all the specimens except specimens D40-6FW-C2 and D85-10FW-C, the strain gauges stopped functioning before the end of the tests due to localized damage of concrete and steel; typically these strain readings were only available for the first 4-6 prescribed unloading/reloading cycles. For these specimens, the following methodology was adopted to obtain the load taken by the steel tube: (1) for unloading/reloading cycles where axial strain readings of the steel tube were available, Eq. 6.1 was used together with these strain readings; (2) for other cycles, based on the observation from Figure 6.4, it was assumed that the tensile stresses of steel at the zero overall load points were all equal to a constant value; this constant value was found following (1) using the averaging strain of steel at zero overall load from the few cycles at unloading strains larger than 0.005 of the same specimen; (3) it was further assumed that the load taken by the steel tube changed proportionally to the overall axial load taken by the specimen, with the steel reaching a tensile load corresponding to the tensile stress found from (2) when the overall load became zero.

Figure 6.4 shows a comparison between the stress-strain curves of concrete obtained using assumptions (2) and (3) listed above and those found using Eq. 6.1 for two hybrid DSTC specimens. A very good agreement is seen for both specimens in Figure 6.4, which demonstrates the validity of the proposed assumptions.

The axial stress-strain curves of the confined concrete in hybrid DSTCs obtained with the above assumptions are shown in Figure 6.5 for all the specimens, where those of cyclically loaded specimens are compared with the curves of the corresponding specimens under monotonic compression.

6.4.3 Key Results

The key test results of all hybrid DSTCs are summarized in Table 6.3. In this table, F_{all} is the peak axial load of the specimen from the test; F_c is the peak axial load taken by the concrete; f'_{cc} is the peak axial stress of the confined concrete; ε_{cu} is the ultimate axial strain of the concrete at the rupture of the FRP tube. The peak stress f'_{co} and the strain ε_{co} at peak stress of unconfined concrete are used to normalize the ultimate axial stress and the ultimate axial strain, respectively.

6.5 CYCLIC AXIAL STRESS-STRAIN MODEL

6.5.1 General

As discussed in Chapter 4, the key characteristics of FRP-confined concrete include: (1) the envelope curve is basically the same as the monotonic stress-strain curve; (2) the loading history has a cumulative effect on both the plastic strain and stress deterioration; (3) the unloading path is generally nonlinear with a continuously decreasing slope while the reloading path is approximately linear. Figure 6.5 shows that the confined concrete in hybrid DSTCs also has these key characteristics.

In Chapter 5, the stress-strain curves of the concrete in monotonically loaded hybrid DSTCs were compared with Yu *et al.*'s (2010) model. Because of the first characteristic above, the performance of Yu *et al.*'s (2010) model in predicting the envelope stress-strain curves of the concrete in cyclically loaded hybrid DSTCs can be expected to be similar to that revealed in Chapter 5. In this chapter, the present test results are compared with the predictions from the cyclic stress-strain model developed in Chapter 4 in terms of the envelope unloading/reloading

behavior. In making the predictions, the experimental envelope curves were used together with the model presented in Chapter 4, to eliminate any errors that may arise from the predicted envelope curve. Readers may refer to Chapter 4 for the cyclic stress-strain model and the terminology used in the model (see Section 4.3.3 and Figure 4.1).

6.5.2 Unloading Path

Lam and Teng (2009) developed Eqs. 4.11~4.16 for predicting the unloading path of FRP-confined concrete. In Chapter 4, the equation for a key parameter η (i.e. Eq. 4.15) has been revised to include the unconfined concrete strength f'_{co} as a parameter (see Section 4.3.5) so that these equations also work for HSC. The modified equations for the unloading path of FRP-confined concrete (i.e. Eqs. 4.11~4.14, 4.16~4.17) were used here. The predictions are compared with the experimental results in Figure 6.6. In making the predictions, the experimental ε_{un} , σ_{un} and ε_{pl} were used, so that the comparison in Figure 6.6 reflects only the performance of the equations for unloading path. As the concrete stresses at the termination points of unloading curves were not zero as shown in Figure 6.5, the plastic strain values ε_{pl} were estimated from the experimental stress-strain curves by extending the unloading stress-strain curve smoothly to the zero stress point, as suggested by Lam *et al.* (2006). Figure 6.6 shows that the equations proposed in Chapter 4 provide accurate predictions for the confined concrete in hybrid DSTCs, regardless of the unconfined strength of the concrete.

6.5.3 Plastic Strain of Envelope Cycles

Lam and Teng (2009) adopted Eqs. 4.18 for predicting the plastic strain of envelope unloading curves $\varepsilon_{pl,1}$ of FRP-confined concrete, where the unconfined

concrete strength f'_{co} and the envelope unloading strain $\varepsilon_{un,env}$ are the controlling parameters. Based on the test database assembled by the author, a new equation (i.e. Eq. 4.19) was proposed in Chapter 4 (see Section 4.3.6), where the unconfined concrete strength f'_{co} was excluded as a parameter.

For the hybrid DSTCs tested under cyclic compression, the plastic strains $\varepsilon_{pl,1}$ are shown against the corresponding envelope unloading strains $\varepsilon_{un,env}$ in Figure 6.7, where the trend lines for $\varepsilon_{un,env} > 0.0035$ are also shown. Table 6.4 summarizes the statistical characteristics of the trend lines for specimens in the present study. Figure 6.7 confirms the linear relationship between the plastic strain $\varepsilon_{pl,1}$ and the envelope unloading strain $\varepsilon_{un,env}$. Similar to FRP-confined concrete (see Chapter 4), this linear relationship is seen to be not significantly affected by the unconfined concrete strength f'_{co} . The coefficient a (i.e. the slope of the trend line) is further shown against the unconfined concrete strength in Figure 6.8, which clearly indicates that this coefficient is similar for most specimens covering a range of unconfined concrete strengths from 40.1 MPa to 104.4 MPa.

Based on the experimental results summarized in Table 6.4, the following equations are proposed for the plastic strain of envelope unloading curves, where the unconfined strength is not used as a parameter:

$$\varepsilon_{pl,1} = \begin{cases} 0 & 0 < \varepsilon_{un,env} \leq 0.001 \\ 0.292\varepsilon_{un,env} - 0.0003 & 0.001 < \varepsilon_{un,env} \leq 0.0035 \\ 0.781\varepsilon_{un,env} - 0.003 & 0.0035 < \varepsilon_{un,env} \leq \varepsilon_{cu} \end{cases} \quad (6.2)$$

In the development of Eq. 6.2, the two coefficients a and b were obtained by averaging the a and b values listed in Table 6.4 for all the specimens. Figure 6.9 shows that Eq. 6.2 can provide reasonably accurate predictions for the test results.

For comparison, the predictions from Eq. 4.19, which were developed based on a large test database of FRP-confined concrete, are shown against the results of hybrid DSTCs in Figure 6.9. It is interesting to note that Eq. 4.19 also provides reasonably accurate predictions for hybrid DSTCs, although its performance is slightly worse than Eq. 6.2. Considering the scatter of test results and the possible errors that may be caused by the methodology to obtain the experimental stress-strain curves of the concrete in hybrid DSTCs, it may be reasonable to suggest that Eq. 4.19 is also applicable to the concrete in hybrid DSTCs.

6.5.4 Stress Deterioration of Envelope Cycles

Lam and Teng (2009) adopted Eqs. 4.20~4.21 for predicting the new stress $\sigma_{new,1}$ on the first reloading path at the envelope unloading strain, where the stress deterioration ratio ϕ_1 of envelope cycles is an important parameter. In Chapter 4, a new equation (i.e. Eq. 4.22) was developed for predicting the stress deterioration ratio ϕ_1 of envelope cycles. A comparison shown in Figure 6.10 suggests that Eq. 4.22 can also yield accurate predictions for the confined concrete in hybrid DSTCs, so Eqs. 4.20~4.22 can be directly adopted for hybrid DSTCs.

6.5.5 Effect of Loading History

It is evident that the loading history has a cumulative effect on both the plastic strain and the stress deterioration of concrete in hybrid DSTCs (Figure 6.5). The cumulative effect of loading history is considered in Lam and Teng's (2009) model and modified in Chapter 4 using a larger test database.

6.5.5.1 Plastic Strain of Internal Cycles

For plastic strains of internal cycles, Lam and Teng (2009) proposed Eqs. 4.28~4.30, among which modifications were proposed to Eq. 4.30 in Chapter 4 based on a larger test database, leading to Eq. 4.31 (See Section 4.3.8.2). A comparison shown in Figure 6.11 suggests that Eq. 4.31 can also yield very accurate predictions for the plastic strains of internal cycles for the concrete in hybrid DSTCs. Therefore, Eqs. 4.28~4.29 and 3.31 can be adopted directly for hybrid DSTCs.

6.5.5.2 Stress Deterioration of Internal Cycles

Lam and Teng (2009) proposed Eqs. 4.32~4.34 for stress deterioration ratios of internal cycles. In Chapter 4, modifications were made to Eq. 4.34 based on a larger test database, leading to a new equation (i.e. Eq. 4.35, see Section 4.3.8.3). A comparison shown in Figure 6.12 suggests that Eq. 4.35 can also yield very accurate predictions for the plastic strains of internal cycles for the concrete in hybrid DSTCs. Therefore, Eqs. 4.32~4.33 and 4.35 can also adopted directly for hybrid DSTCs.

6.5.6 Overall Performance

The overall performance of the cyclic stress-strain model proposed in Chapter 4 is evaluated in Figures 6.13 and 6.14 in terms of the envelope unloading/reloading curves and the repeated unloading/reloading curves respectively.

In making the predictions in Figure 6.13, the experimental strain $\varepsilon_{un,env}$ and stress $\sigma_{un,env}$ on the envelope curve were used as the starting point of the

prediction. It is evident from Figure 6.13 that the proposed model in Chapter 4 can provide reasonably accurate predictions for the envelope unloading/reloading curves of the confined concrete in hybrid DSTCs.

In making the predictions in Figure 6.14, the experimental strain $\varepsilon_{un,env}$ and stress $\sigma_{un,env}$ on the envelope curve as well as the experimental plastic strain of envelope curve $\varepsilon_{pl,1}$ were used. For specimens of batches 1-3, each experimental cycle is shown against the prediction individually. Only comparisons for the 1st, 4th, 7th and 10th are shown in Figure 6.14a, as comparisons for other cycles are similar. For specimens of batches 4-6, there were only three repeated unloading/reloading cycles, so experimental curves are compared directly with predicted unloading/reloading curves in Figure 6.14b. Again, the model proposed in Chapter 4 is seen to provide reasonably accurate predictions for repeated unloading/reloading curves of the confined concrete in hybrid DSTCs.

6.7 CONCLUSIONS

This chapter has presented an experimental study on hybrid DSTCs under cyclic axial compression with a particular focus on the effect of three important issues (i.e. the use of HSC; the use of filament-wound tubes; the use of large-scale specimens). The experimental results and discussions allow the following conclusions to be drawn:

- (1) The envelope stress-strain curves of the concrete in cyclically loaded hybrid DSTCs is almost the same as the stress-strain curve of the concrete in the corresponding monotonically loaded specimen;
- (2) The hoop rupture strain (either $\varepsilon_{h,rup1}$ or $\varepsilon_{h,rup2}$) of monotonically loaded specimens is generally larger than that of the corresponding cyclically loaded

specimens;

- (3) The unloading/reloading behavior of concrete in cyclically loaded hybrid DSTCs is generally similar to that of the concrete in FRP-confined solid columns.

This chapter has also presented a comparison of the unloading/reloading paths between the test results and the predictions of the cyclic stress-strain model proposed in Chapter 4 for FRP-confined concrete. The comparison showed that the model proposed in Chapter 4 can also provide reasonably accurate predictions for the unloading/reloading paths of the concrete in hybrid DSTCs, provided that the envelope stress-strain curve is accurately defined.

The accurate prediction of the envelope stress-strain curve of the concrete in hybrid DSTCs requires an accurate monotonic stress-strain model for the concrete. The discussions in Chapter 5 revealed that Yu *et al.*'s (2010) monotonic stress-strain model is capable of providing reasonably accurate predictions for specimens with a bilinear ascending stress-strain curve and specimens with slight fluctuations in the axial stress, but overestimates the results of specimens with a sudden load drop. Further research is needed to correct the deficiency of Yu *et al.*'s (2010) model before it can be used in conjunction the equations for the unloading/reloading paths given in Chapter 4 to achieve accurate predictions of cyclic stress-strain curves for the concrete in hybrid DSTCs.

6.8 REFERENCES

- ASTM C39/C39M. (2011). *Standard Test Method for Compressive Strength of Cylindrical Concrete Specimens*, American Society for Testing and Materials, Philadelphia, USA.
- ASTM D2290-08. (2008). *Standard Test Method for Apparent Hoop Tensile Strength of Plastic or Reinforced Plastic Pipe by Split Disk Method*, American Society for Testing and Materials (ASTM), Philadelphia, USA.
- BS 18-1987. (1987). *Tensile Testing of Metals (including Aerospace Materials)*, British Standards Institution, London, UK.
- Fanggi, B.A.L. and Ozbakkaloglu, T. (2013). “Compressive behavior of aramid FRP–HSC–steel double-skin tubular columns”, *Construction and Building Materials*, 48(0), 554-565.
- GB/T5350-2005. (2005). *Fiber-Reinforced Thermosetting Plastic Composites Pipe: Determination for Longitudinal Compressive Properties*, The Standards Press of China.
- Gomes, A. and Appleton, J. (1997). “Nonlinear cyclic stress-strain relationship of reinforcing bars including buckling”, *Engineering Structures*, 19(10), 822-826.
- Lam, L., Teng, J.G., Cheung, C.H. and Xiao, Y. (2006). “FRP-confined concrete under axial cyclic compression”, *Cement and Concrete Composites*, 28, 949-958.
- Mansour, M., Lee, J.Y. and Hsu, T.T. (2001). “Cyclic stress-strain curves of concrete and steel bars in membrane elements”, *Journal of Structural Engineering*, ASCE, 127(12), 1402-1411.
- Menegotto, M. and Pinto, P.E. (1973). “Method of analysis for cyclically loaded RC frames including changes in geometry and non-elastic behaviour of elements under combined normal force and bending”, *IABSE Symposium on*

Resistance and Ultimate Deformability of Structures Acted on by Well-Defined Repeated Loads, Final Report, Lisbon.

Monti, G. and Nuti, C. (1992). “Nonlinear cyclic behavior of reinforcing bars including buckling”, *Journal of Structural Engineering*, ASCE, 18(12), 3268-3284.

Ozbakkaloglu, T. and Akin, E. (2012) “Behavior of FRP-confined normal-and high-strength concrete under cyclic axial compression”, *Journal of Composites for Construction*, ASCE, 16, 451-463.

Ozbakkaloglu, T. and Fanggi, B.A.L. (2013a). “Axial compressive behavior of FRP-concrete-steel double-skin tubular columns made of normal-and high-strength concrete”, *Journal of Composites for Construction*, ASCE, 18(1).

Ozbakkaloglu, T. and Fanggi, B.A.L. (2013b). “FRP–HSC–steel composite columns: behavior under monotonic and cyclic axial compression”, *Materials and Structures*, 1-19.

Qian, J.R. and Liu, M.X. (2008). “Experimental investigation of FRP-concrete-steel double-skin tubular stubs under axial compressive loading”, *Journal of Building Structures*, 29(2), 104-113. (in Chinese).

Ramberg, W. and Osgood, W.R. (1943). “Description of stress-strain curves by three parameters”, *Technical Note 902, National Advisory Committee for Aeronautics, Washington, DC.*

Teng, J.G., Yu, T. and Wong, Y.L. (2004). “Behaviour of hybrid FRP-concrete-steel double-skin tubular columns”, *Proceedings, Second International Conference on FRP Composites in Civil Engineering*, 8-10 December, Adelaide, Australia, 811-818.

Teng, J.G., Yu, T., Wong, Y.L. and Dong, S.L. (2007). “Hybrid FRP-concrete-steel tubular columns: Concept and behavior”, *Construction and Building Materials*, 21(4), 846-854.

- Teng, J.G., Jiang, T., Lam, L. and Luo, Y.Z. (2009). “Refinement of a design-oriented stress-strain model for FRP-confined concrete”, *Journal of Composites for Construction*, ASCE, 13(4), 269-278.
- Wong, Y.L., Yu, T., Teng, J.G. and Dong, S.L. (2008). “Behavior of FRP confined concrete in annular section columns”, *Composites Part B: Engineering*, 39(3), 451-466.
- Xie, P., Yu, T., Wong, Y.L. and Teng, J.G. (2011). “Compressive behavior of large-scale hybrid FRP-concrete-steel double-skin tubular columns”, *Advanced Materials Research*, 243, 1138-1144.
- Yu, T. (2007). *Behavior of Hybrid FRP-Concrete-Steel Double-Skin Tubular Columns*, PhD Thesis, The Hong Kong Polytechnic University.
- Yu, T., Teng, J.G. and Wong, Y.L. (2010). “Stress-strain behavior of concrete in hybrid double-skin tubular columns”, *Journal of Structural Engineering*, ASCE, 136(4), 379-389.
- Yu, T., Zhang, B., Cao, Y.B. and Teng, J.G. (2012). “Behavior of hybrid FRP-concrete-steel double-skin tubular columns subjected to cyclic axial compression”, *Thin-Walled Structures*, 61, 196-203.
- Yokoo, Y. and Nakamura, T. (1977). “Non-stationary hysteretic uniaxial stress-strain relations of a wide-flange steel”, *Transactions of Architectural Institute of Japan*, 260, 71-80.
- Zhang, B., Yu, T. and Teng, J.G. (2011). “Axial compression tests on hybrid double-skin tubular columns filled with high strength concrete”, *Proceedings, Third International Postgraduate Conference on Infrastructure and Environment*, 11-12 July, Hong Kong, China, 171-176.

Table 6.1: Details of specimens

Specimen	Specimen dimensions			Steel tube		FRP tube		Concrete batch
	D (mm)	h (mm)	ϕ	Type	D_s/t_s	Type	t_{frp} (mm)	
D54-2FW-C	200	400	0.795	A	31.8	2FW	2.2	1 (54.1MPa)
D54-4FW-C	200	400	0.795	A	31.8	4FW	4.7	
D84-4FW-C	200	400	0.795	A	31.8	4FW	4.7	2 (84.6MPa)
D84-4FW-CB	200	400	0.600	B	26.7	4FW	4.7	
D84-9FW-C	200	400	0.795	A	31.8	9FW	9.5	
D104-4FW-C	200	400	0.795	A	31.8	4FW	4.7	3 (104.6MPa)
D104-9FW-C	200	400	0.795	A	31.8	9FW	9.5	
D40-6FW-C1	300	600	0.730	C	36.5	6FW	6.0	4 (40.9MPa)
D40-6FW-C2	300	600	0.730	C	36.5	6FW	6.0	
D66-6FW-C1	300	600	0.730	C	36.5	6FW	6.0	5 (66.1MPa)
D66-6FW-C2	300	600	0.730	C	36.5	6FW	6.0	
D85-6FW-C1	300	600	0.730	C	36.5	6FW	6.0	6 (85.8MPa)
D85-6FW-C2	300	600	0.730	C	36.5	6FW	6.0	
D85-10FW-C	300	600	0.730	C	36.5	10FW	10.0	

Table 6.2: Cyclic loading schemes

Specimen	Unloading displacement (mm) found from the total axial shortening									
	Step	Step	Step	Step	Step	Step	Step	Step	Step	Step
	1	2	3	4	5	6	7	8	9	10
D54-2FW-C	0.92	1.90	2.90	3.93	4.94	5.94/10*	---	---	---	---
D54-4FW-C	0.91	1.89	3.87	5.90	7.90/10	---	---	---	---	---
D84-4FW-CB	1.00	2.04	4.13	6.15	8.13/3*	---	---	---	---	---
D84-4FW-C	0.89	1.92	2.91	3.98	5.00	6.03/10*	---	---	---	---
D84-9FW-C	0.94	1.92	3.91	5.92	7.96	9.86/10*	---	---	---	---
D104-4FW-C	0.95	1.94	2.85	3.90	4.92	5.91/10*	---	---	---	---
D104-9FW-C	0.92	1.91	3.90	5.94	8.01	10.0/10*	---	---	---	---
D40-6FW-C1	1.34/3*	2.36/3*	5.07/3*	10.1/3*	15.3/3*	---	---	---	---	---
D40-6FW-C2	1.26	2.56	5.03	6.71	8.48	10.14	11.7	13.5	15.2	16.9
D66-6FW-C1	1.08/3*	2.05/3*	3.34/3*	6.10/3*	9.13/3*	---	---	---	---	---
D66-6FW-C2	1.06	2.07	2.87	5.12	6.12	7.12	8.12	9.13	---	---
D85-6FW-C1	1.04/3*	2.05/3*	3.91/3*	6.23/3*	9.29/3*	---	---	---	---	---
D85-6FW-C2	1.05	2.05	3.05	4.10	5.14	6.20	7.14	8.20	9.07	10.1
D85-10FW-C	1.05	2.04	4.41	6.23	8.20	10.0	12.0	14.2	16.1	18.2

* The number after the back slash is the number of repeated cycles at that prescribed unloading displacement.

Table 6.3: Key test results

Specimen	F_{all} (kN)	F_c (kN)	f'_{cc} (MPa)	ε_{cu} (%)	$\frac{f'_{cc}}{f'_{co}}$	$\frac{\varepsilon_{cu}}{\varepsilon_{co}}$	$\varepsilon_{h,rup1}$ (%)	$\varepsilon_{h,rup2}$ (%)
D54-2FW-C	1885	982	85.0	1.73	1.57	6.73	0.68	0.69
D54-4FW-C	2509	1381	119.5	3.07	2.21	11.9	0.83	0.83
D84-4FW-CB	4106	3077	153.1	2.25	1.81	8.17	0.77	0.91
D84-4FW-C	2597	1533	132.7	2.08	1.57	7.58	0.62	0.62
D84-9FW-C	3260	1853	160.4	2.86	1.90	10.6	0.61	0.66
D104-4FW-C	2682	1605	138.9	2.15	1.33	6.90	0.57	0.59
D104-9FW-C	3400	1982	171.5	3.17	1.64	10.2	0.59	0.54
D40-6FW-C1	5059	2998	90.8	2.94	2.22	13.3	0.92	0.88
D40-6FW-C2	5290	3213	97.4	2.93	2.38	13.2	0.93	0.85
D66-6FW-C1	5304	3326	100.8	1.90	1.52	7.56	0.69	0.65
D66-6FW-C2	5045	3131	94.9	1.75	1.44	6.94	0.70	0.72
D85-6FW-C1	5846	4154	125.9	1.91	1.47	7.13	0.77	0.73
D85-6FW-C2	5651	3637	110.2	2.13	1.28	7.94	0.83	0.78
D85-10FW-C	6695	4360	132.1	3.71	1.53	13.8	0.85	0.80

Table 6.4: Linear relationships between unloading strains and plastic strains

Specimen	Unconfined concrete strength f'_{co} (MPa)	$\varepsilon_{pl,1} = a\varepsilon_{un,env} + b$		R^2
		a	b	
D54-2FW-C	54.1	0.766	-0.0032	0.970
D54-4FW-C	54.1	0.742	-0.0034	0.972
D84-4FW-CB	84.6	0.831	-0.0032	0.997
D84-4FW-C	84.6	0.762	-0.0034	0.997
D84-9FW-C	84.6	0.750	-0.0032	0.975
D104-4FW-C	104.4	0.763	-0.0032	0.993
D104-9FW-C	104.4	0.797	-0.0034	0.985
D40-6FW-C2	40.1	0.802	-0.0027	0.991
D66-6FW-C2	66.1	0.846	-0.0032	0.985
D85-6FW-C2	85.8	0.752	-0.0020	0.993
D85-10FW-C	85.8	0.782	-0.0025	0.995



(a) Failed specimens of batch 1



(b) Failed specimens of batch 2



(c) Failed specimens of batch 3

Figure 6.1: Specimens after test



D40-6FW-C1



D40-6FW-C2

(d) Failed specimens of batch 4



D66-6FW-C1



D66-6FW-C2

(e) Failed specimens of batch 5

Figure 6.1: Specimens after test (continued)



D85-6FW-C1



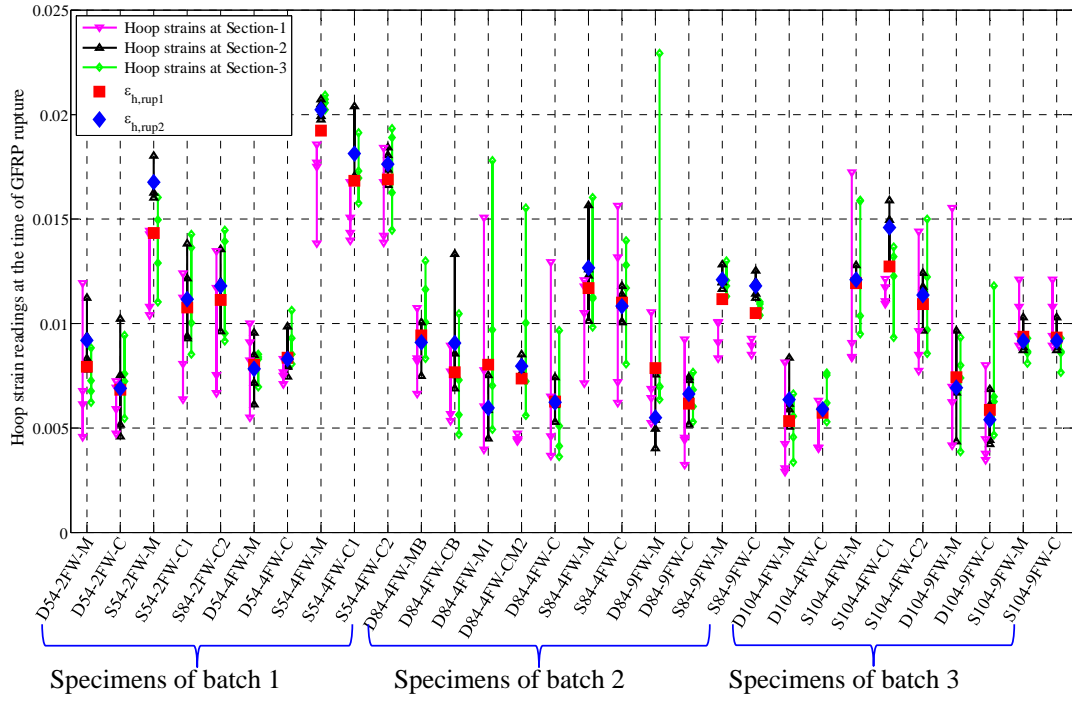
D85-6FW-C2



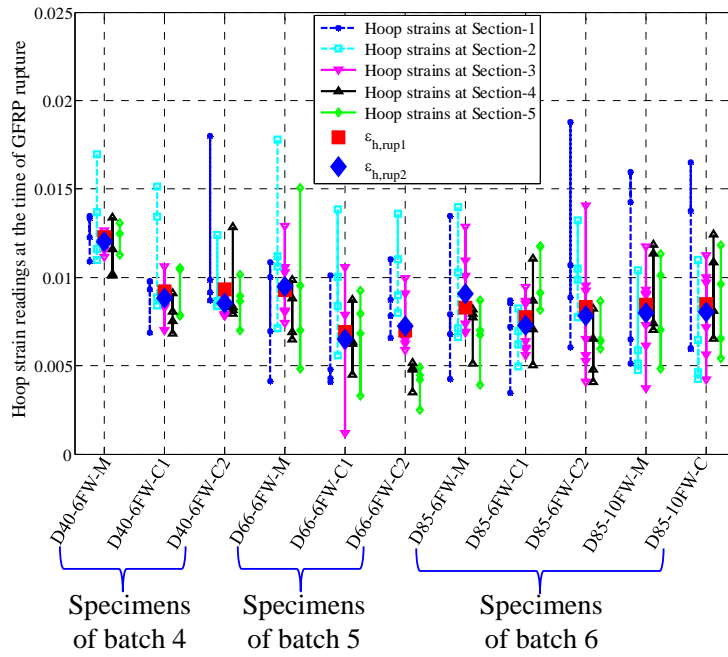
D85-10FW-C

(f) Failed specimens of batch 6

Figure 6.1: Specimens after test (continued)

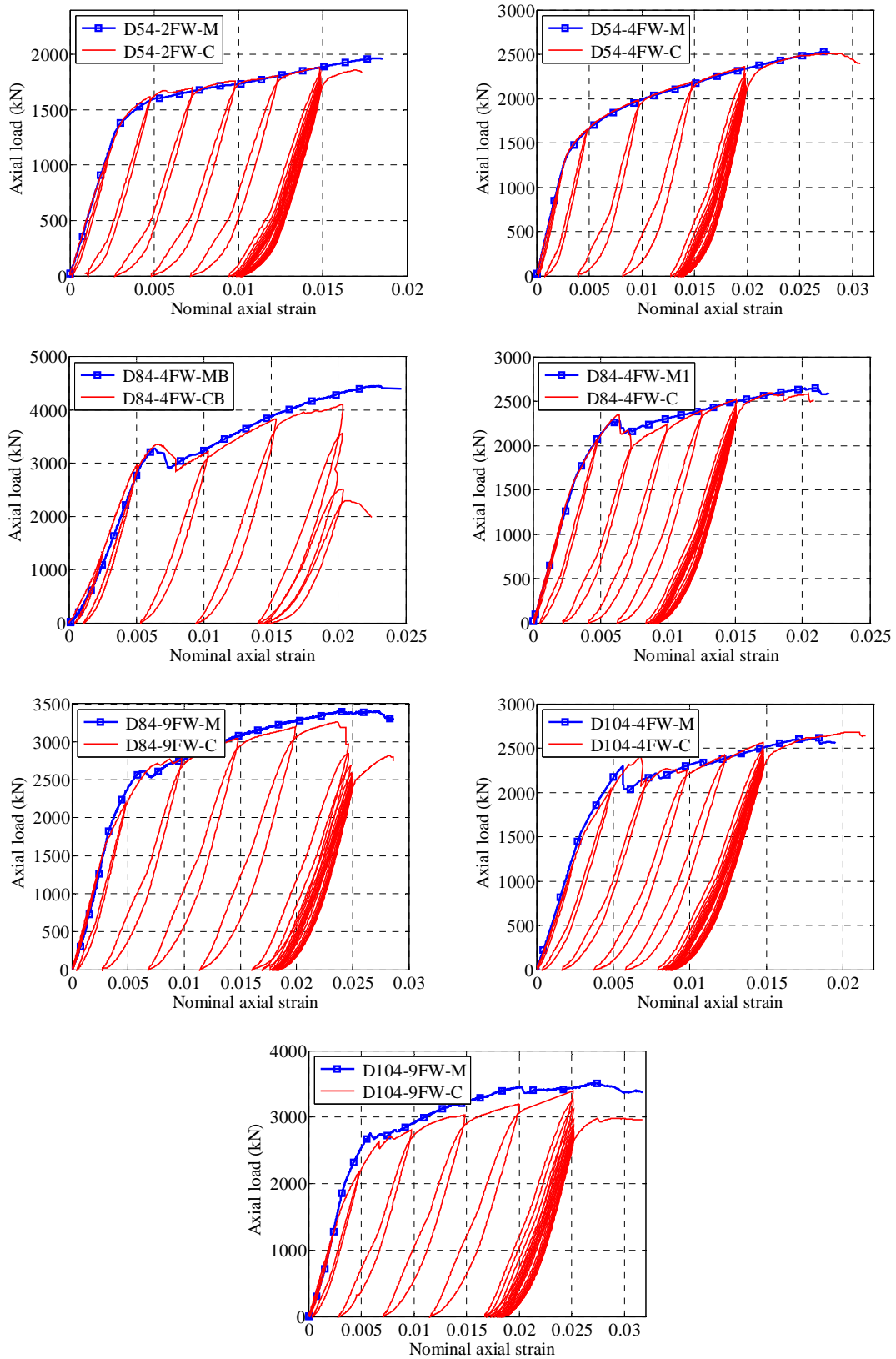


(a) Specimens of batches 1-3



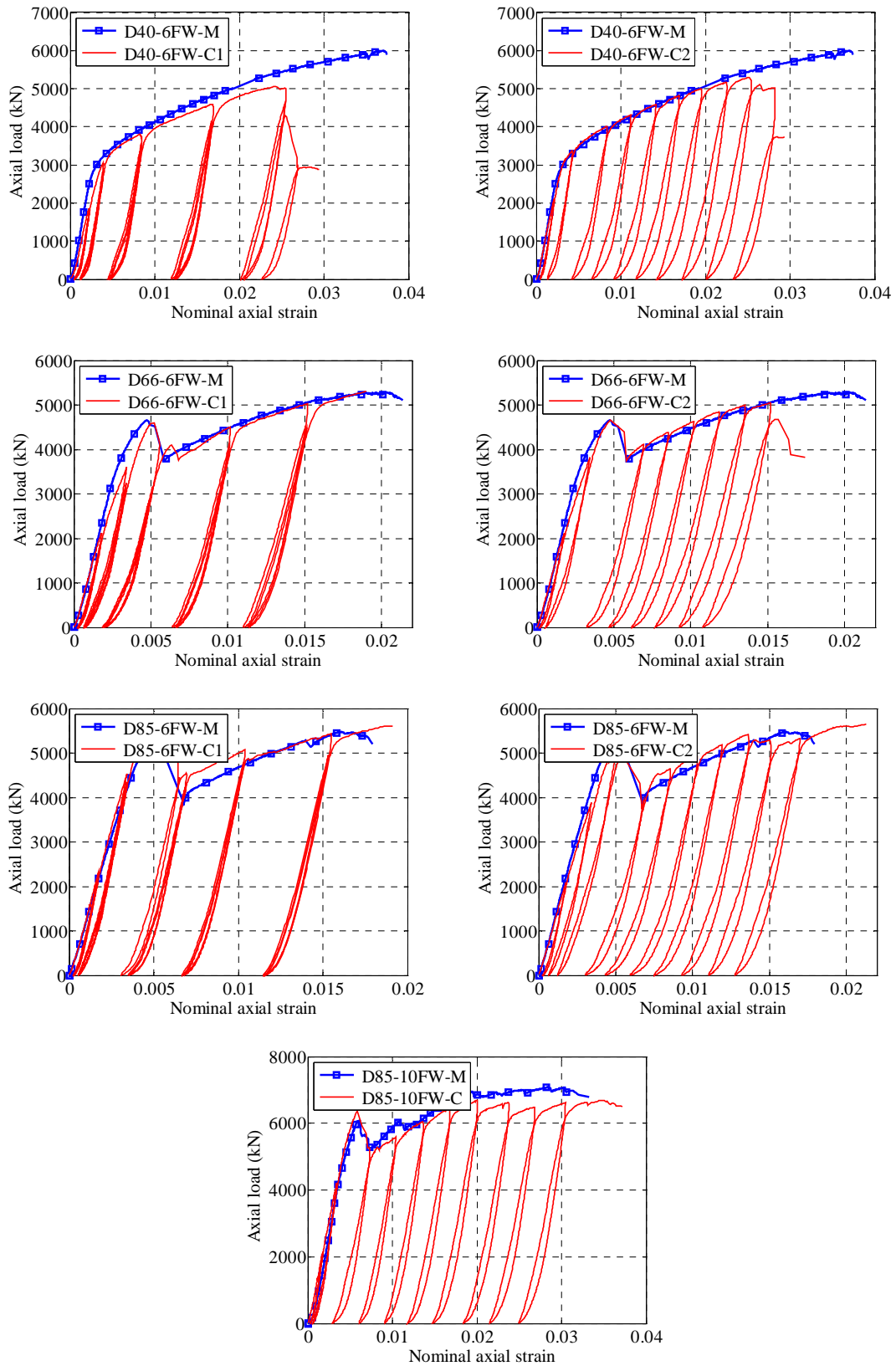
(b) Specimens of batches 4-6

Figure 6.2: Hoop strain distributions



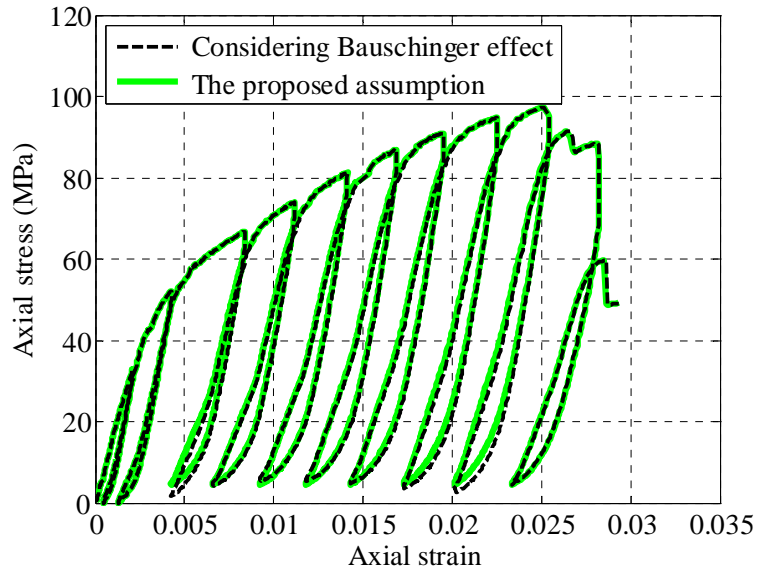
(a) Specimens of batches 1-3

Figure 6.3: Axial load-axial strain curves of hybrid DSTCs

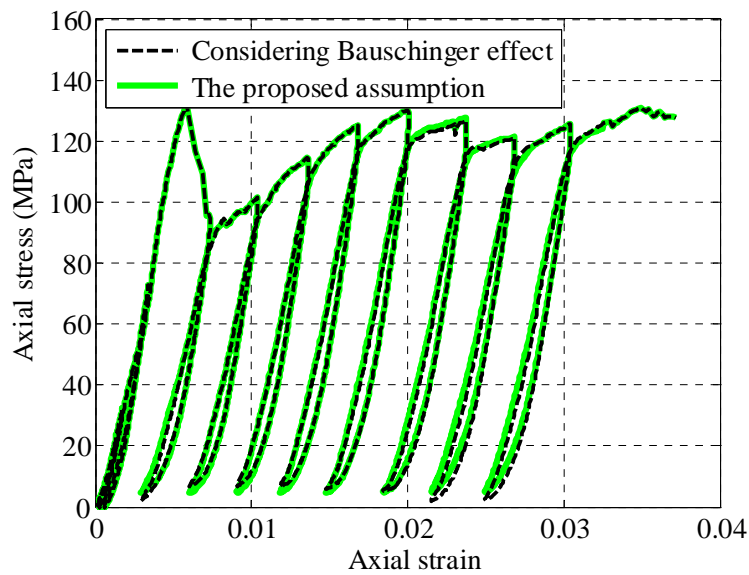


(a) Specimens of batches 4-6

Figure 6.3: Axial load-axial strain curves of hybrid DSTCs (continued)

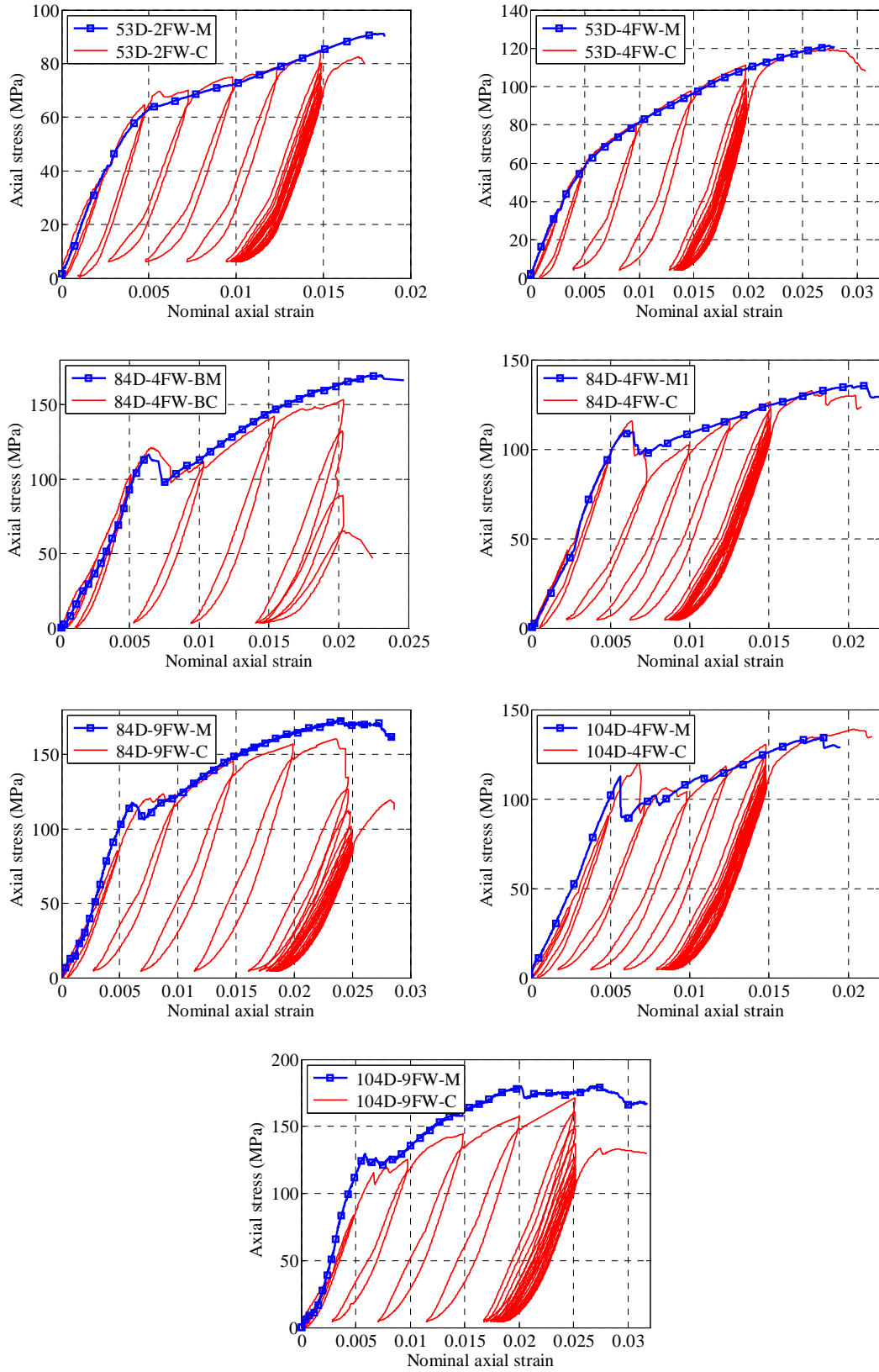


(a) Specimen D40-6FW-C2



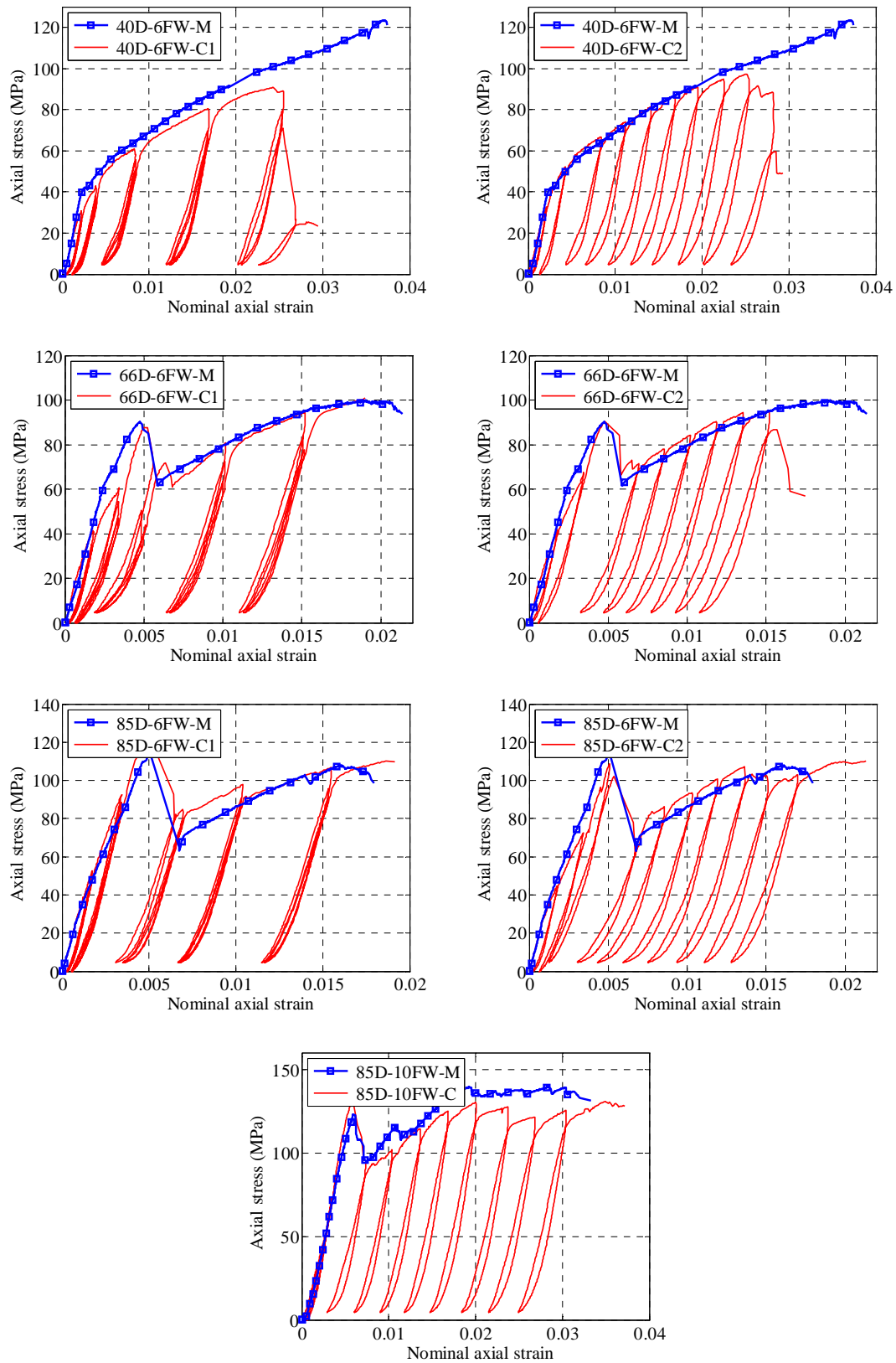
(d) Specimen D85-10FW-C

Figure 6.4: Cyclic axial stress-strain curves of concrete obtained using different methods



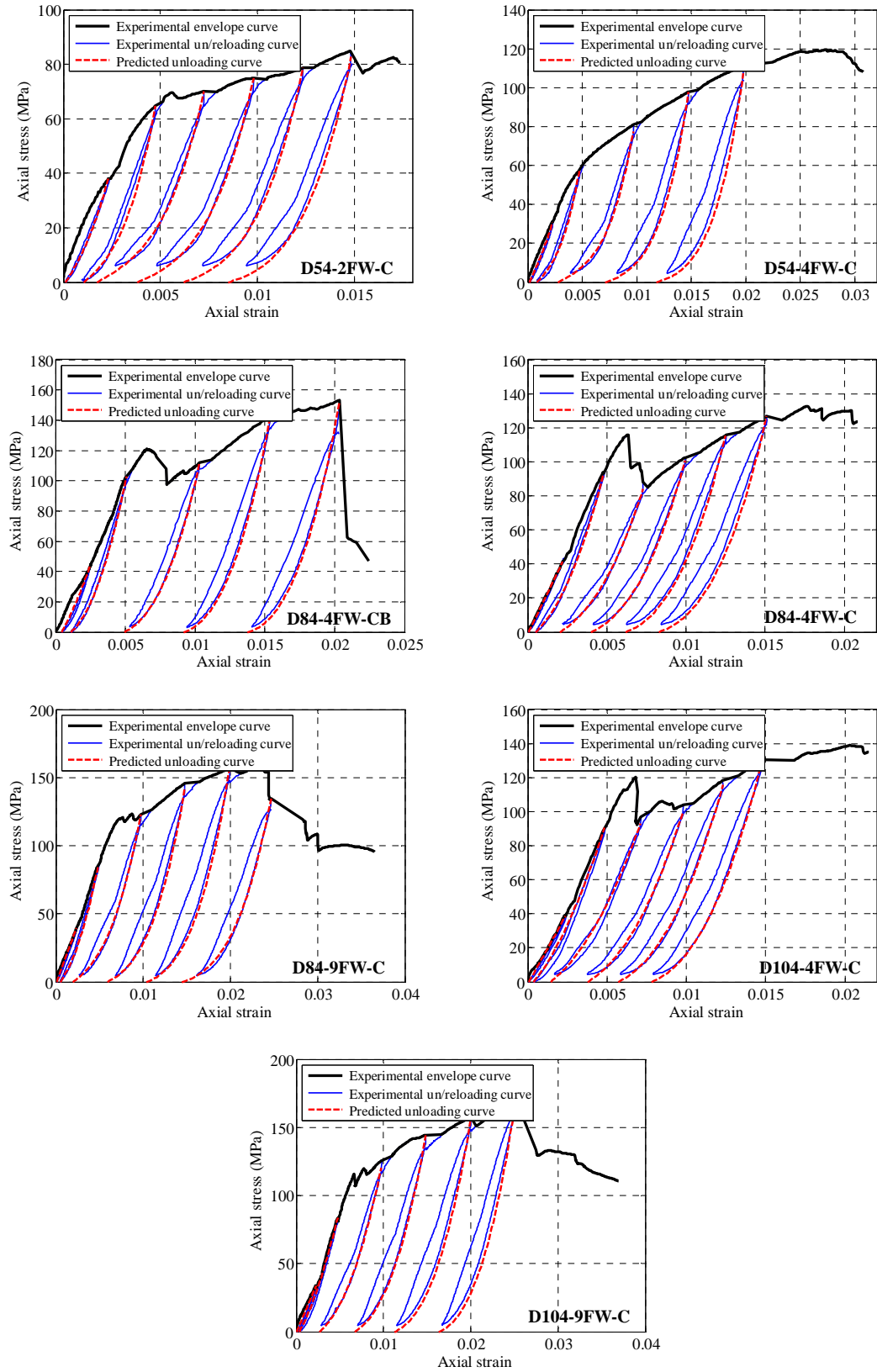
(a) Specimens of batches 1-3

Figure 6.5: Cyclic axial stress-strain curves of concrete

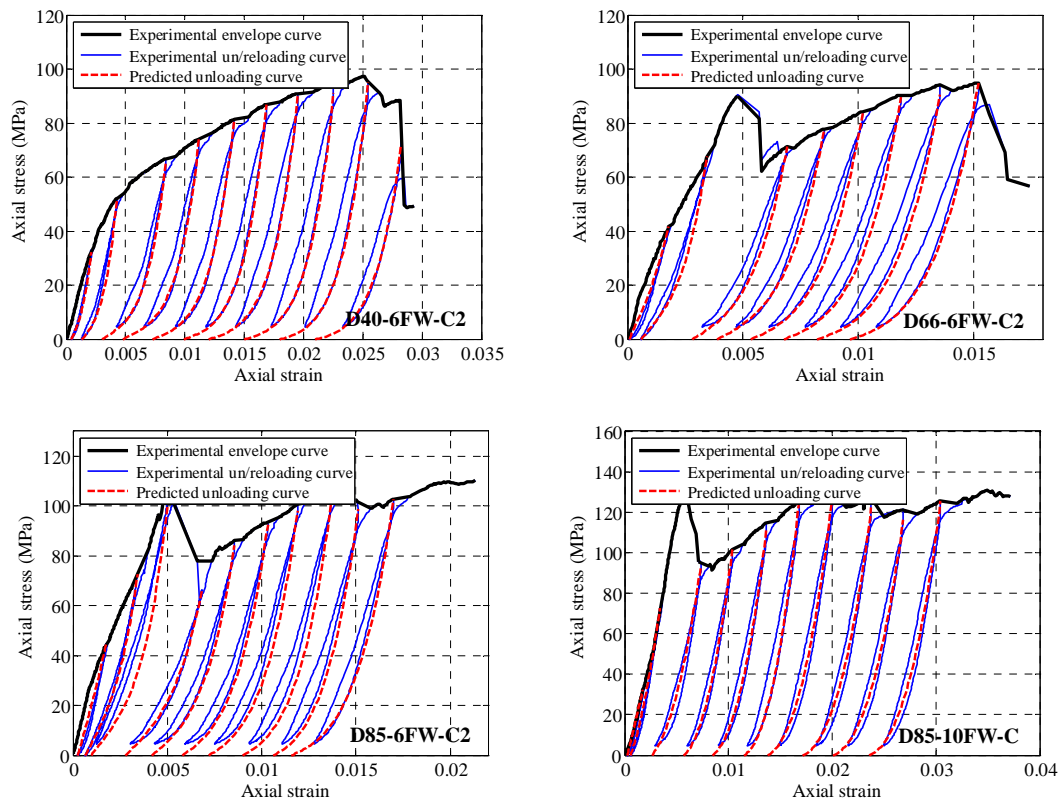


(a) Specimens of batches 4-6

Figure 6.5: Cyclic axial stress-strain curves of concrete (continued)



(a) Specimens of batches 1-3
 Figure 6.6: Prediction of unloading curves



(a) Specimens of batches 4-6

Figure 6.6: Prediction of unloading curves (continued)

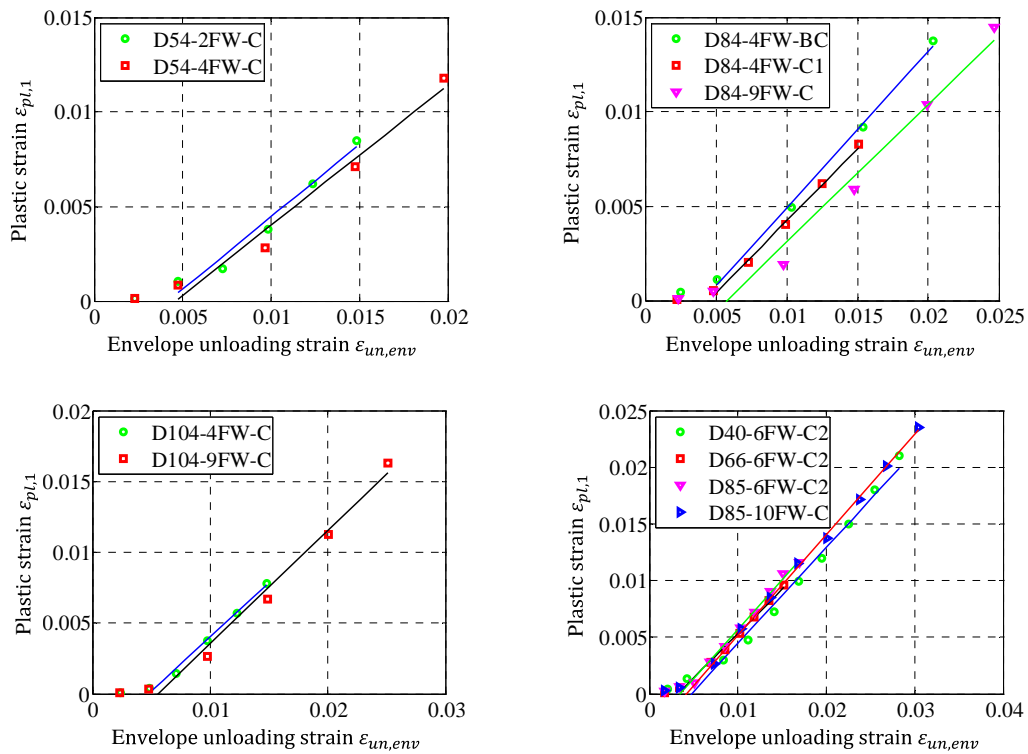


Figure 6.7: Relationship between plastic strains and envelope unloading strains

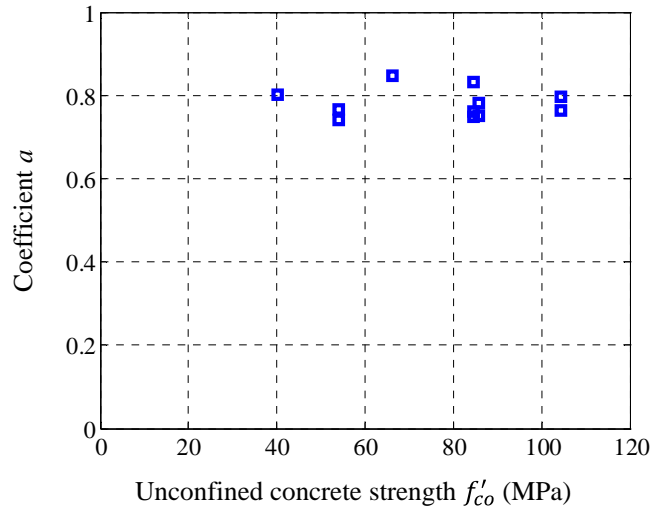


Figure 6.8: Effect of concrete strength on the plastic strain

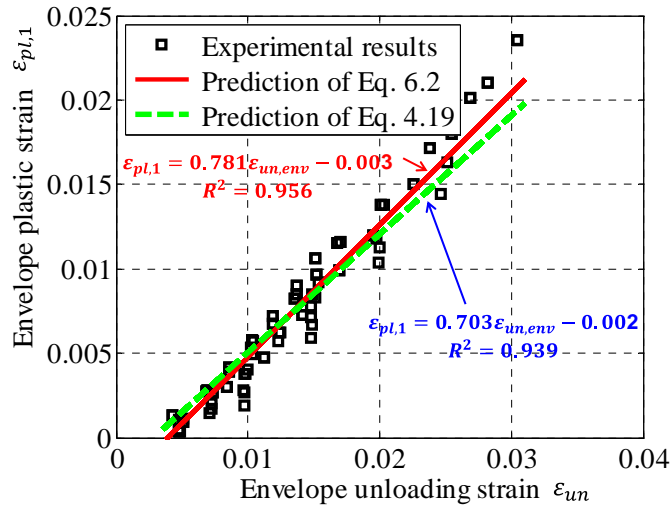


Figure 6.9: Performance of equations for the plastic strain of envelope cycles

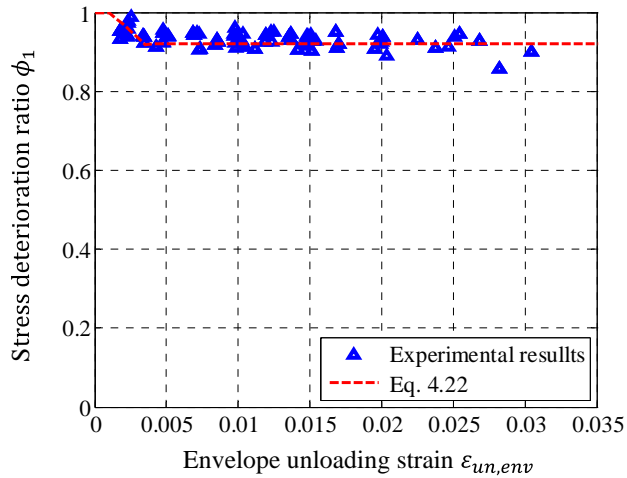


Figure 6.10: Performance of equations for the stress deterioration ratio of envelope cycles

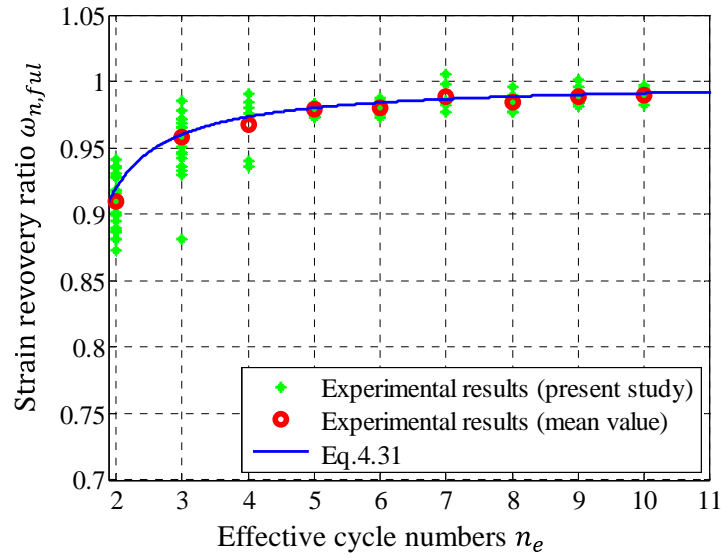


Figure 6.11: Performance of equations for the strain recovery ratio of internal cycles

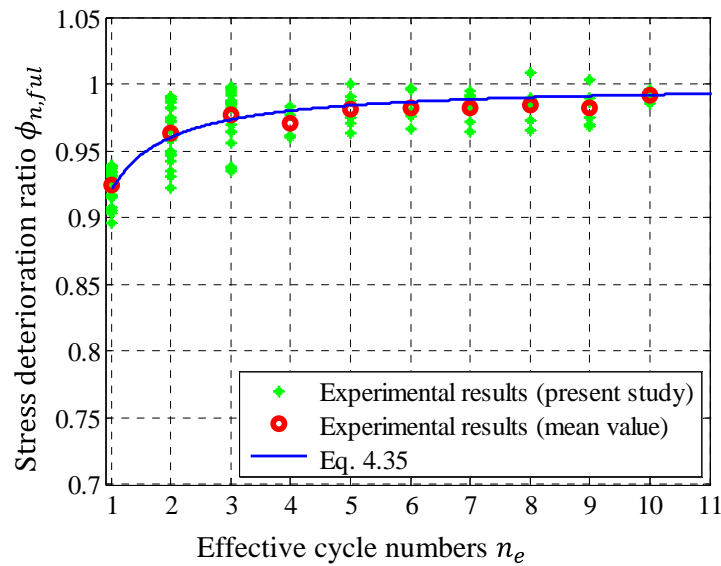


Figure 6.12: Performance of equations for the stress deterioration ratio of internal cycles

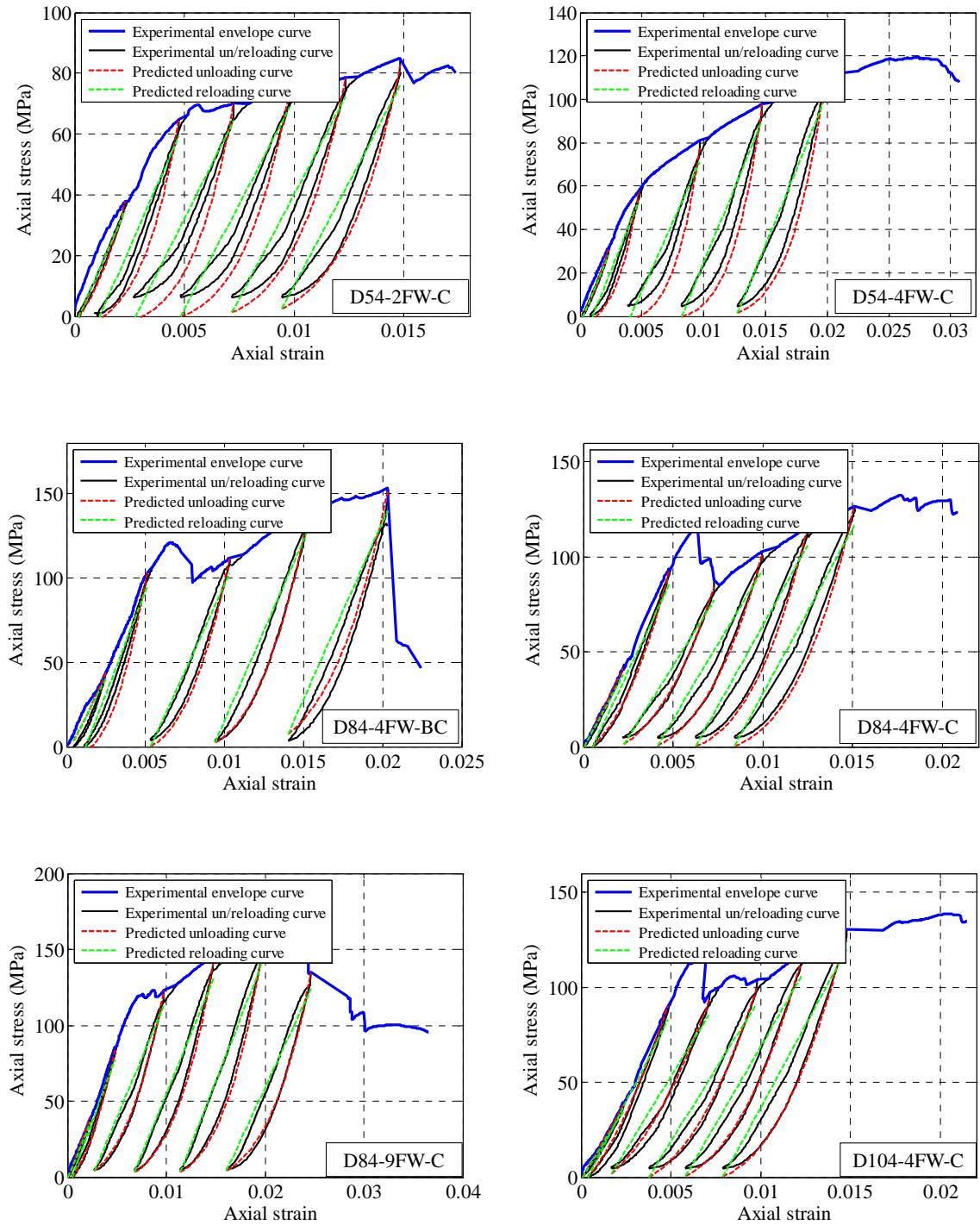


Figure 6.13: Performance of equations for envelope unloading/reloading curves

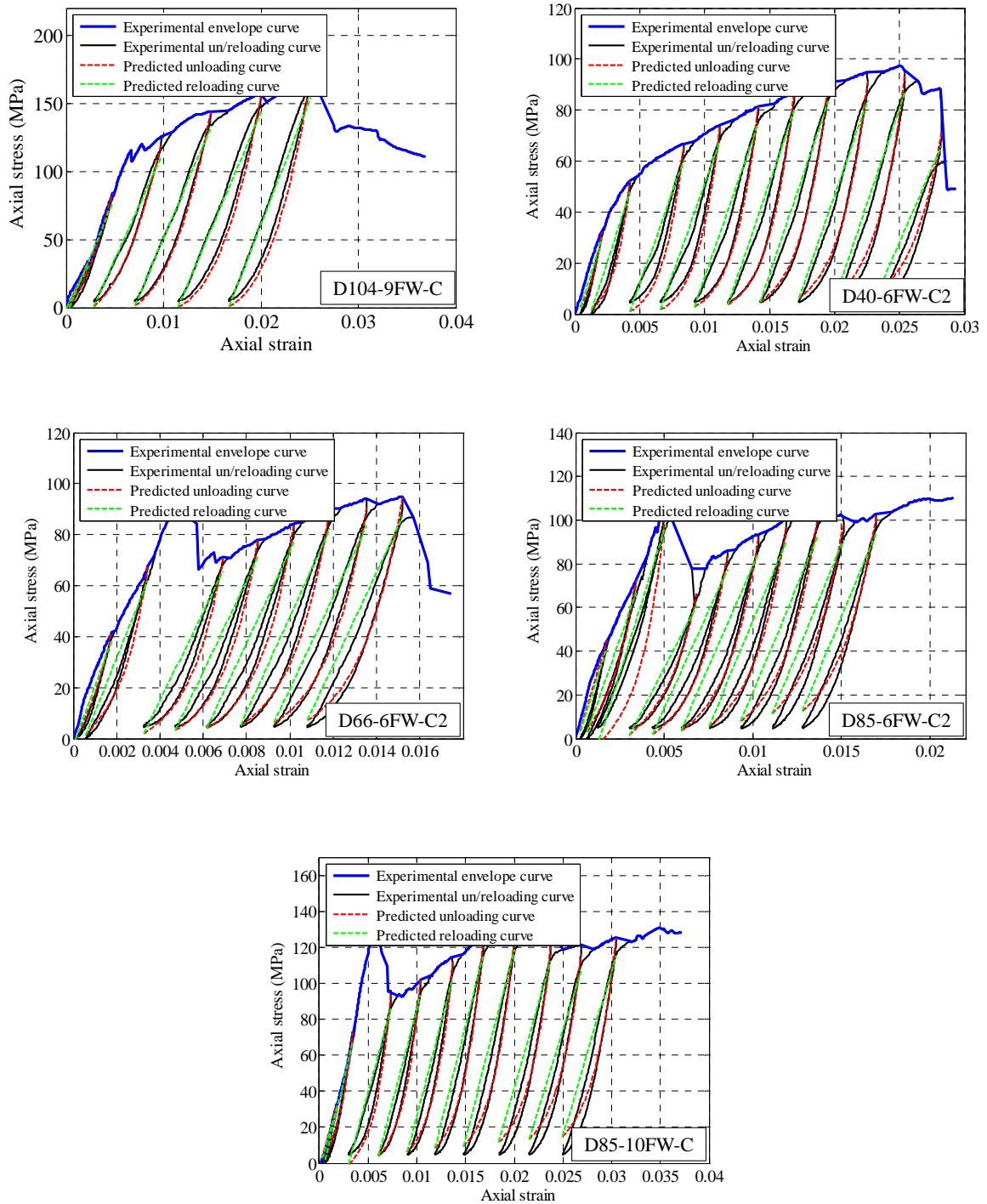
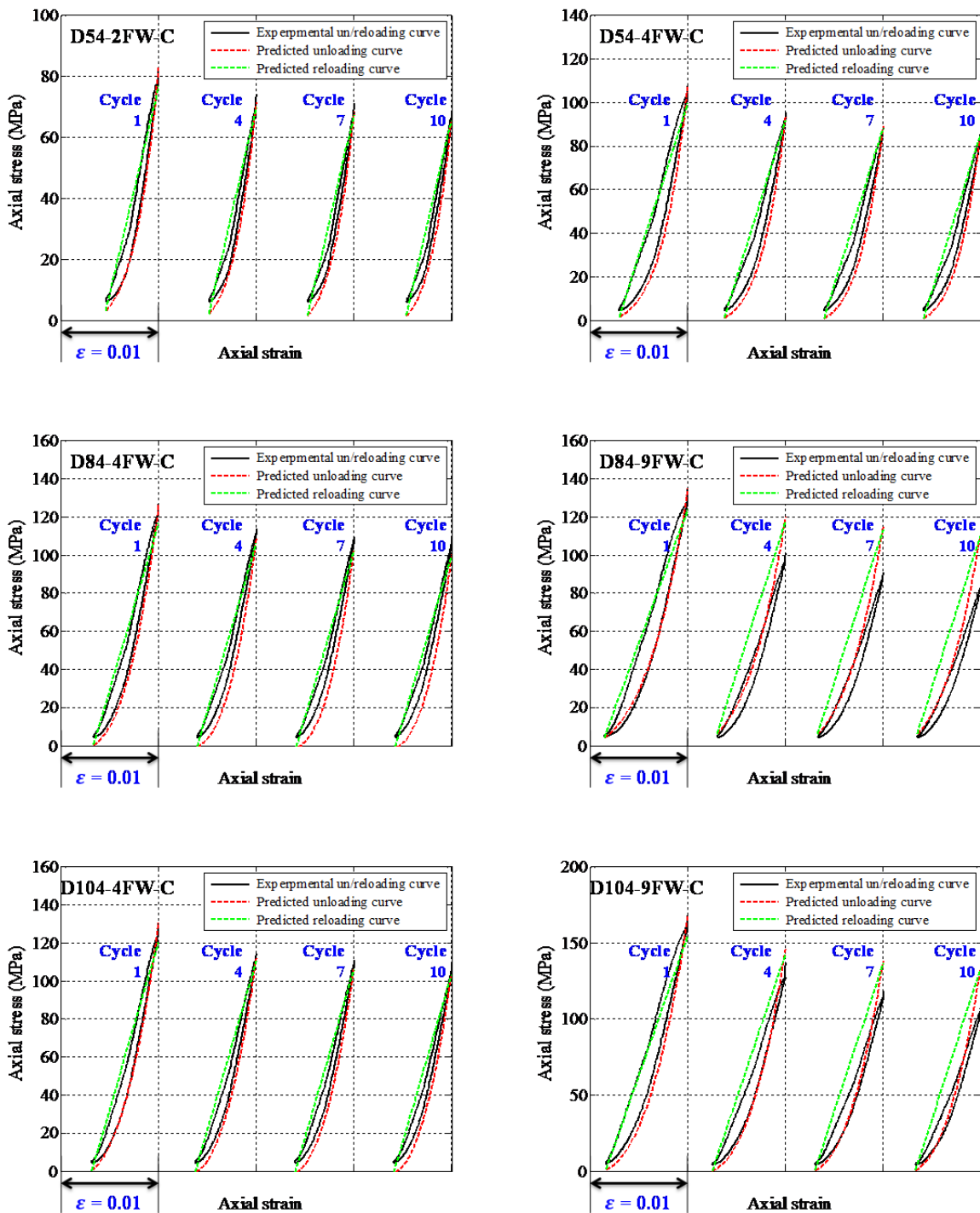
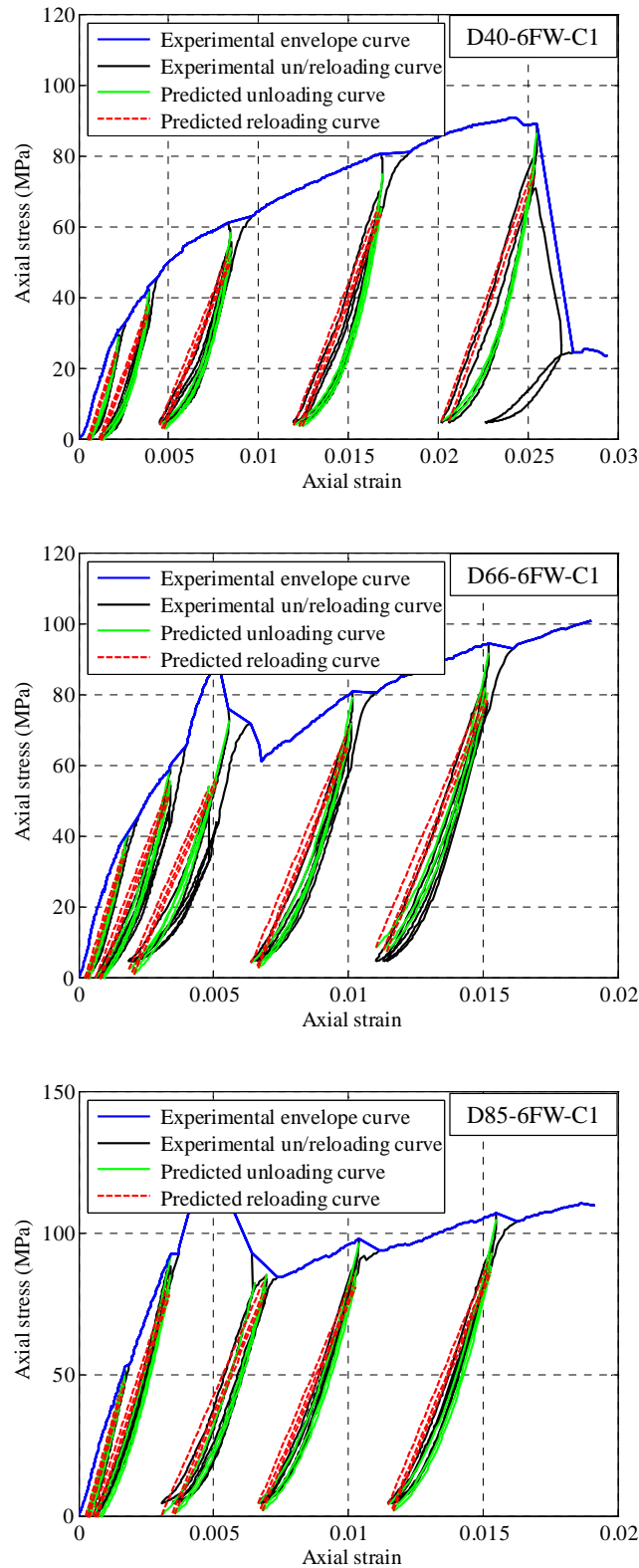


Figure 6.13: Performance of equations for envelope unloading/reloading curves (continued)



(a) Specimens of batches 1-3

Figure 6.14: Performance of equations for repeated unloading/reloading curves



(b) Specimens of batches 4-6

Figure 6.14: Performance of equations for repeated unloading/reloading curves (continued)

CHAPTER 7

BEHAVIOR OF HYBRID DSTCS UNDER COMBINED AXIAL COMPRESSION AND CYCLIC LATERAL LOADING

7.1 INTRODUCTION

Hybrid FRP-concrete-steel double-skin tubular columns (hybrid DSTCs) has been studied by the author's group for almost a decade (e.g. Teng *et al.* 2007; Yu *et al.* 2006; Yu 2007; Wong *et al.* 2008; Yu *et al.* 2010a, 2010b, 2010c, 2010d; Teng *et al.* 2010; Yu and Teng 2013). These studies showed that the concrete in the new column is effectively confined by the two tubes and the local buckling of the inner steel tube is either delayed or suppressed by the surrounding concrete, leading to a very ductile response. The excellent ductility of hybrid DSTCs means that they are particularly attractive for use in seismic regions. Therefore, their behavior under cyclic lateral loading is of significant interest. Existing work on the seismic behavior of hybrid DSTCs has been rather limited. To the best of the authors' knowledge, only Qian and Liu (2008) and Han *et al.* (2010) conducted cyclic lateral loading tests on small-scale hybrid DSTCs (i.e. with the outer diameter of the columns being smaller than 200 mm) constructed with normal strength concrete (NSC). The limitations of the studies conducted by Qian and Liu (2008) and Han *et al.* (2010) have been presented in Chapter 2 in detail. Since hybrid

DSTCs are highly ductile, and the absence of any steel bars ensures good-quality casting of high strength concrete (HSC), they offer a promising opportunity for the use of HSC which is more brittle than NSC. HSC also facilitates the use of a large void ratio for the column without compromising the contribution of concrete to its load-carrying capacity.

Against this background, this chapter presents the first experimental study on hybrid DSTCs with high strength concrete (HSC) subjected to axial compression in combination with cyclic lateral loading. A reasonably large section size (the outer diameter of annular concrete section is 300 mm) and a realistically large void ratio (i.e. 0.73) are chosen for these columns. The major parameters are concrete strength, axial load ratio and thickness of FRP tube.

7.2 EXPERIMENTAL PROGRAM

7.2.1 Specimen Details

The experimental program consisted of 8 large-scale hybrid DSTCs. All these specimens had a circular section with a characteristic diameter D (the outer diameter of the annular concrete section) of 300 mm and a void ratio of 0.73. The height was 1350 mm (4.5 times of the column diameter) from the point of lateral loading (referred to as “column head”) to the top of the stiff RC column footing (referred to as “column end”). The inner steel tube had a thickness t_s of 6 mm and an outer diameter D_s of 219 mm, leading to a D_s/t_s ratio of 36.5. The outer FRP tube had an inner diameter of 300 mm (Figure 7.1). Other details of the specimens are summarized in Table 7.1.

While a separate batch of concrete had to be mixed to cast each specimen

(excluding the footing which was casted with commercial concrete), the 8 DSTC specimens can be classified into four groups according to the target concrete strengths. The achieved concrete strengths of the four groups were around 37 MPa, 56 MPa, 80 MPa and 116 MPa respectively, with minor differences between individual specimens (see Table 7.1). Besides the concrete strength, the other test variables examined include the thickness of the FRP tube (6 mm or 10 mm), and the axial load ratio (0.2 or 0.4). The axial load ratio is defined by Eq. 7.1 and is further explained later. In addition, the inner steel tube of one of the specimens was partially filled with concrete near the column end to investigate that effect. Each specimen is given a name, which starts with a letter “D” to represent “DSTC”, followed by a two- or three-digit number to represent the concrete strength, and then a one- or two-digit number to represent the thickness of FRP tube together with a number “0.2” or “0.4” which defines the axial load ratio. The last letter “S” in one of the specimens indicates that it is the specimen with concrete filling of the lower part of the steel tube.

7.2.2 Preparation of Specimens

Each specimen consisted of a hybrid DSTC whose bottom portion was embedded in a stiff reinforced concrete (RC) footing. In the preparation process, the inner steel tube of the column was connected to the steel reinforcement embedded in the RC footing in the following way: (1) the steel tube was first welded to a square steel plate at the bottom of the concrete footing; (2) an annular steel plate was then welded to the steel tube to support the outer FRP tube; (3) six vertical stiffeners were then inserted between the square plate and the annular steel plate and welded to the two plates and the steel tube; (4) the steel reinforcement of the footing was then welded to these plates/stiffeners to form a rigid steel cage (Figure 7.2). Strain gauges were installed on the steel tube before the FRP outer

tube was placed directly on a pre-machined circular groove (5mm in depth) on the annular steel plate without additional connections (Figure 7.2). This means that tensile forces could not be transferred between the FRP tube and the footing. This design avoided excessive early tensile damage of the FRP tube in the longitudinal direction without significantly compromising the lateral loading capacity of the column because of the small axial stiffness of the FRP tube whose the fibers were oriented at ± 80 degrees to the longitudinal axis. Once the steel tube and the FRP tube were in place, the assembly was enclosed in a steel formwork for the casting of concrete to form the footing (Figure 7.2). After the curing of concrete in the footing, self-compacting concrete was cast into the annular space between the two tubes to form a hybrid DSTC. It should be noted that since part of the steel tube was embedded in the footing, the space inside the embedded part of the steel tube was also filled with concrete. For specimen D80-6-0.4-S, additional concrete was cast into the steel tube to fill the lower 320 mm of the column above the footing.

7.2.3 Material Properties

7.2.3.1 Concrete

Self-compacting concrete (SCC) was adopted to ensure the quality of concrete casting. The mix properties of SCC are shown in Table 7.2. Each column was cast with a separate batch of concrete, and for each batch of concrete, 3 plain concrete cylinders (152.5 mm in diameter and 305 mm in height) were prepared and tested following ASTM C39/C39M (2011). The test results are summarized in Table 7.1, where f'_{co} is the peak axial stress (i.e. the cylinder compressive strength); E_c is the elastic modulus of concrete; ϵ_{co} is the axial strain at peak axial stress. The axial stress-strain curves of these concrete cylinders are shown in Figure 7.3.

7.2.3.2 FRP Tubes

Two types of prefabricated filament-wound glass FRP (GFRP) tubes were used in the present study. The two types of FRP tubes differed only in the thickness: one type had a thickness of 6.0 mm and another type had a thickness of 10 mm. The volume ratio and the angles of the fibers in all these tubes were 0.559 and ± 80 degrees to the longitudinal axis of the tube respectively. As a consequence, the two types of tubes are assumed to have the same mechanical properties, with only a small longitudinal stiffness. These FRP tubes were also used in these large-scale hybrid DSTCs presented in Chapter 5 and Chapter 6. Tensile split-disk tests on FRP rings were conducted following ASTM D2290-08 (2008), and compression tests on FRP rings were conducted following GB/T5350-2005 (2005). The Young's modulus and the average rupture strain in the hoop direction are 43.6 GPa, 1.554%, respectively (Figure 5.4 and 5.5); the average ultimate axial stress, axial strain and secant elastic modulus at failure in compression were 95.1MPa, 0.95% and 10.0 GPa, respectively (Figure 3.5 and 3.6).

7.2.3.3 Steel Tubes

For the inner steel tubes which were cut from the same batch of two long steel tubes, tensile tests on three steel coupons were conducted following BS 18-1987 (1987) for each long tube. The elastic modulus, yield stress and tensile strength averaged from the six coupons are 200.0 GPa, 360.3 MPa and 490.6 MPa, respectively. The stress-strain curves of the steel coupons all showed a long yield plateau.

7.2.4 Testing Frame

All the tests were conducted using a large testing frame (Figures 7.4 and 7.5). The testing frame included a vertical actuator with a capacity of 10,000 kN connected to the upper loading plate (i.e. top plate) and a hinge joint connected to the lower loading plate (i.e. bottom plate); rollers were provided between the top plate and the bottom plate so that during the test the horizontal locations of the vertical actuator and the hinge could be aligned. In addition, a horizontal actuator with a capacity of 1,000 kN in tension and 1,500 kN in compression was provided to apply horizontal loading through a hinge joint. The column head was connected to the two hinges via a column head fixture particularly designed for such column tests. The two hinges were well lubricated before the test to minimize the frictional force between the top plate and the bottom plate. The column footing was fixed to a strong floor using high strength steel bolts (Figure 7.4).

During the test, significant frictional forces were induced between the top and the bottom plates because of the large axial load applied to the column and the relative movement between the two plates when the column was horizontally pulled or pushed. These forces need to be deducted from the load applied by the horizontal actuator to obtain the horizontal load actually resisted by the column. In the present study, a frictional coefficient of 0.527% was used which was obtained by Hu (2011) in his experimental study using the same testing frame.

7.2.5 Experimental Set-Up and Instrumentation

In order to monitor the behavior of the column, extensive strain gauging and many linear variable displacement transducers (LVDTs) were employed during the test as summarized below (Figure 7.5).

A number of strain gauges were used to measure the axial and the hoop strains of the column at each of six different column heights, namely, the circumferences at 30 mm (section 1), 150 mm (section 2), 300 mm (section 3), 450 mm (section 4), 600 mm (section 5) and 750 mm (section 6) from the column end, respectively. The gauge length of the strain gauges attached to the steel tubes was 10 mm while that of the strain gauges attached to the FRP tubes was 20 mm. The layout of strain gauges on each selected section is shown in Figure 7.6. The strain gauges are named as follows: the name starts with a letter (from A-H) to represent its circumferential location, followed by a number (from 1-6) to define its longitudinal location (i.e. sections 1 to 6), and then a letter “V” or “H” to indicate whether this is an vertical (axial) strain gauge or a hoop strain gauge. Upper-case letters are used in the names for strain gauges on the FRP tube, while lower-case letters are used for those on the steel tube. The layout of strain gauges is the same for all the specimens except for specimen D80-6-0.4-S where more strain gauges were installed at sections 4 to 6 to capture the more distributed damage of this specimen as a result of the partial filling of the steel tube. An underline is used in the names of these additional strain gauges for specimen D80-6-0.4-S.

Three pairs of LVDTs (i.e. LVDTs 1 to 6) were installed on the two sides of the loading plane (i.e. side A and side E, see Figure 7.5) of the column at intervals of 200 mm starting from the column end. These LVDTs were installed on the column surface through pre-fixed nuts (Figure 7.5). Two LVDTs (LVDTs 7 and 8) were installed at the column head (the point where the lateral load acts) to measure the lateral displacement. The rotation of the column head and the shortening of the column were also measured using LVDTs (i.e. LVDTs 9 to 12). LVDTs 13 and 14 were used to obtain the relative lateral movement of the top plate and the bottom plate for calculation of the frictional force in between (Figures 7.4 and 7.5). In addition, LVDTs 15 and 16 were installed on the footing to monitor the movement

it could experience during the test.

In addition, for ease of observation, a white grid was plotted on the surface of the FRP tube (Figure 7.4). Initially, a 20 mm x 20 mm white grid was drawn on specimen D56-6-0.2, which was found to be too small for effective photographing. A 40 mm x 40 mm grid was adopted for all the rest specimens.

7.2.6 Loading Schemes

A constant axial load N was first applied to each column with a loading rate of 50 kN/min. The axial load was applied on the FRP tube, the steel tube and the concrete simultaneously. The magnitude of N was calculated from the following equation using a pre-defined axial load ratio n (Table 7.1) and the nominal squash load N_{sq} of the column:

$$N = nN_{sq} = n(f_y A_s + f_{co} A_c) \quad (7.1)$$

where f_y and A_s are the yield stress and the cross-section area of the inner steel tube respectively; f_{co} and A_c are the cylinder compressive strength and the area of the concrete annular section respectively.

Following the practice of many existing studies (e.g. Priestly and Park 1987; Hsu and Chang 2001; Bae and Bayrak 2008; Hu 2011), the lateral loading was applied step by step based on the yield displacement of the column. The yield displacement of the column was defined in accordance with the following procedure as recommended by Priestly and Park (1987): (1) the column is loaded to a level which is 0.75 times the maximum lateral load H_{peak} ; H_{peak} was estimated in the present study with the effect of confinement for the concrete

ignored and with the P- Δ effect considered (Chen and Atsuta 1976); (2) the yield displacement δ_y is defined as the elastic limit of an equivalent elastic-perfectly plastic curve with a reduced stiffness being equal to the secant stiffness at 75% of the peak lateral load (i.e. $0.75H_{peak}$; see Figure 7.7); and this secant stiffness is averaged from the two test values found for the pull direction and the push direction respectively. The yield displacements obtained following this procedure for the present test columns are summarized in Table 7.3. The cyclic loading scheme for each column was then based on the yield displacement determined in-situ and consisted of two cycles at displacement levels of $\pm\delta_y$, $\pm 2\delta_y$, $\pm 3\delta_y$, $\pm 5\delta_y$, $\pm 7\delta_y$ respectively, and one cycle at displacement levels of $\pm 9\delta_y$, $\pm 11\delta_y$ and $\pm 13\delta_y$ respectively (Figure 7.8). For all the columns, the loading rate was initially 5.0 kN/min until the lateral load reached 75% of the estimated value of H_{peak} ; afterwards, loading continued with displacement control at a gradually increasing rate until it reached a maximum value of 9 mm/min. Different column specimens failed at different displacement levels, so for most columns, not all the intended loading cycles were completed. The testing procedure was stopped when the lateral load resistance dropped substantially from the peak value. It should be noted that in the above description, the term “displacement” or “lateral displacement” refers to the lateral displacement at the column head. This simplification in terminology is also used elsewhere in this chapter unless otherwise specified.

After the completion of lateral loading cycles, specimens D56-6-0.2, D116-6-0.2 and D80-6-0.4 were further tested under monotonic axial compression to examine the residual axial load capacities of these columns.

7.3 EXPERIMENTAL RESULTS AND DISCUSSIONS

7.3.1 General

The experimental observations and results are presented and discussed in this section. For clarity of presentation, the push direction is defined to be the positive direction while the pull direction the negative direction (Figure 7.5); compressive stresses/strains are defined to be positive while tensile strains/stresses are defined to be negative. These definitions are adopted throughout this chapter unless otherwise specified. Therefore, for example, side “A” of the column is in compression and side “E” is in tension when a column is loaded in the push (positive) direction (see Figure 7.5).

7.3.2 Test Observations

Upon the imposition of the constant axial load, none of the column specimens showed any sign of distress. The axial strain gauge readings showed that the vertical alignment of the column was generally very good. The hoop strain gauge readings indicated that at sections 2 and 3, the steel tube experienced a larger dilation than the FRP tube, due to the larger Poisson’s ratio of steel. As a result, radial interfacial compressive stresses developed between the steel tube and the concrete, leading to some confinement of the concrete by the steel tube. However, at section 1, the hoop strains of the steel tube were generally very small because of the constraint from the concrete footing.

The process of damage was generally similar for all the column specimens except specimen D80-6-0.4-S. At the first two lateral displacement levels ($\pm 0.75\delta_y, \pm\delta_y$), no obvious damage was observed on the FRP tube, and the strain gauge readings

confirmed that plane sections remained plane at all the monitored sections (see Figure 7.9 which shows typical distributions of longitudinal strains over sections; in Figure 7.9, the strain readings at the x-coordinates of 156 and -156 were from strain gauges on the FRP tube while the other strain readings were from strain gauges on the steel tube). The first sign of damage was indicated by resin cracking along one of the fiber directions on the tension side of the FRP tube (Figure 7.10a). Resin cracking of the FRP tube was limited mainly to the lowest 240 mm of the column height due to the high moments there. As the lateral displacement level increased ($\pm 5\delta_y, \pm 7\delta_y, \pm 9\delta_y$), severe damage was developed in the lowest 120 mm region of the FRP tube due to alternating tensile and compressive straining (Figures 7.10b and 7.10c). The axial shortening of the column then increased rapidly due to the severe damage at the bottom of the column, which caused a sudden increase in the hoop strain readings on the FRP tube. After that, the axial strain readings indicated that the plane section assumption was no longer correct for sections within the bottom 300 mm region, but was still valid for higher sections (i.e. above 300 mm) (Figure 7.9). Rupture of the FRP tube, which was due to concrete dilation combined with tension-compression cycling, finally occurred within the lowest 80 mm from the footing on the compression side of the column (Figure 7.10d). These eight specimens after test are shown in Figure 7.11. Damage to the concrete was concentrated within the bottom 100 mm region due to cyclic loading (Figure 7.12). Severe local buckling deformations were found on the inner steel tube in the bottom region (Figure 7.12). Local fracture of the steel tube was also found in some of the specimens (i.e. specimens D37-6-0.2, D80-10-0.4, D116-10-0.4).

The steel tube of specimen D80-6-0.4-S was partially filled with concrete in the bottom portion, which led to significant differences in its experimental behavior. A direct comparison between specimens D80-6-0.4-S and D80-6-0.4 after testing

(Figure 7.12d) suggests that the deformation of the former was much more distributed. Further examination showed that noticeable damage of the FRP tube and the inner concrete occurred at three different heights of specimen D80-6-0.4-S, namely, around 120 mm, 240 mm and 300 mm from the column end respectively; the locations of final rupture of the FRP tube, being at the latter two places, are considerably higher than those of the other seven specimens (Figure 7.12). No apparent buckling deformation was found in the steel tube of this specimen because of the additional support from the concrete inside (Figure 7.12d).

7.3.3 Lateral Load-Lateral Displacement Curves

The lateral load-lateral displacement curves of all the specimens are presented in Figure 7.13, where envelope curves are shown together with the cyclic curves. The lateral displacement was averaged from the readings of the two LVDTs installed at the column head (i.e. LVDTs 7 and 8). All the sub-figures in Figure 7.13 are plotted to the same scale for ease of comparison. The point corresponding to the rupture of FRP tube is also marked on each curve. The rounded hysteresis loops shown in Figure 7.13 clearly demonstrate the excellent ductility and seismic resistance of hybrid DSTCs, even when concrete with a very high strength was used. The envelope curve of each specimen includes an ascending branch until the peak lateral load, a short horizontal portion over which the lateral load fluctuates within a small range, and a long descending branch in which the lateral load decreases as the lateral displacement increases. The descending branch is affected significantly by the P- Δ effect. The lateral deformation capacity of the column is seen to decrease as the concrete strength and the axial load ratio increase, but increase as the thickness of the FRP tube increases.

7.3.4 Envelope Moment-Curvature Curves

The effects of concrete strength, thickness of the FRP tube and axial load ratio are further examined in Figures 7.14-7.17 which shows the envelope moment-curvature curves. In Figures 7.14-7.17, the moment is that of the section at 100 mm from the column end with the P- Δ effect taken into account; the curvature is the average value over the lowest 200 mm of the column calculated from the readings of LVDTs (i.e. LVDTs 1 and 2) using the following equation:

$$\varphi_{\Delta} = (\Delta_1 - \Delta_2)/D'l_{seg} \quad (7.2)$$

where φ_{Δ} is the average curvature of the chosen segment based on LVDT readings; l_{seg} is the length of the segment; Δ_1 and Δ_2 are the LVDT readings on side A and side E of the segment respectively; and D' is the horizontal distance between the tips of the two LVDTs, which is slightly larger than the diameter of the column.

In Figures 7.14-7.17, the positive direction refers to the positive lateral load direction, and the envelope curves for the two directions are in close agreement. These envelope curves generally consist of three portions: (1) an initial steep ascending branch; (2) a second gradual ascending branch (for specimen D80-6-0.4-S) or a long plateau (for the other 7 specimens); and (3) a short steep descending branch. The long second portion means that the moment at the chosen column section changes little over a wide range of curvature values, which indicates that hybrid DSTCs exhibit very ductile sectional behavior under combined axial compression and cyclic bending.

The effect of concrete strength can be examined using Figure 7.14, where the curves are grouped in three subfigures. It is evident that the specimen with a

higher concrete strength has a higher moment capacity and is likely to have a smaller deformation capacity. The comparisons shown in Figure 7.15 indicate that a thicker FRP tube leads to a slightly larger moment capacity and better ductility for the column. Figure 7.16 shows that the specimen with a higher axial load ratio ($n=0.4$) fails at a much smaller curvature than its counterpart with a lower axial load ratio ($n=0.2$), illustrating the important influence of axial load ratio. The curve of specimen D80-6-0.4-S whose inner steel tube was partially filled with concrete is compared with that of its counterpart (i.e. D80-6-0.4) in Figure 7.17. It is evident that the additional concrete infill increased the slope of the second portion of the curve substantially, leading to a considerably larger moment capacity as well as much better ductility.

The points corresponding to the rupture of FRP tube are also marked on the curves shown in Figures 7.14-7.17. These points are generally at or very close to the end of the second portion of the curve, suggesting that the moment capacity of the column decreased rapidly only after the rupture of FRP tube. Considering that the lateral load already decreased significantly when the rupture of FRP tube occurred (Figure 7.13), it is clear that the member behavior of the column was significantly affected by the $P-\Delta$ effect of the large axial load.

7.3.5 Curvature Distributions over the Column Height

With the 6 LVDTs installed near the column end (i.e. LVDTs 1-6), the average curvatures of the three monitored segments, covering the regions of 0-200 mm (segment 1), 200-400 mm (segment 2) and 400-600 mm (segment 3) from the column end respectively, can be calculated using Eq. 7.2. Figure 7.18 shows the curvature distributions over the column height for specimens D80-6-0.4 and D80-6-0.4-S. The curvature distributions for the other 6 specimens are similar to

those for specimen D80-6-0.4, and are not discussed here. It is evident from Figure 7.18 that for specimens with a uniform hollow section, the deformation was localized in segment 1, but for specimen D80-6-0.4-S with an additional concrete infill, the deformation was much more distributed, with the curvature of segment 2 becoming even larger than that of segment 1 during the final stage of loading. This is consistent with the experimental observation described above.

7.3.6 Axial Displacement

Figure 7.19 shows the development of axial displacement with the loading process for typical specimens. The axial displacement was obtained by averaging the readings from LVDTs 11 and 12, so it represents the vertical movement of the lower loading plate (see Figure 7.5), which included the axial shortening of the column, the axial displacement due to the tilting of the column as well as other possible deformation of the loading system (e.g. the hinge). The initial leap in the axial displacement was mainly caused by the imposition of the constant axial load at the beginning of the test. As expected, the axial displacement increased with the lateral displacement because of the tilting of the column. By examining the values of axial displacement when the lateral displacement is zero, it is seen that the axial displacement increases cumulatively with the cyclic loading process, as a result of the cumulative damage and/or plastic deformation of the constituent materials (i.e. concrete, steel and FRP). Such increases of axial displacement are seen to be relatively small for the first few cycles, become more significant afterwards, and increase much more rapidly during the last one or two cycles before failure. By comparing Figure 7.19a with Figure 7.19b, it is evident that the cumulative axial shortening of the column was significantly reduced by the additional concrete infill. The axial load ratio is also seen to have a significant effect on the cumulative axial shortening (Figures 7.19c and 7.19d).

7.3.7 Hoop Strain Distributions

Hoop strain gauges were installed on the FRP tube (see Figures 7.5 and 7.6) to measure the hoop strains of the FRP tube as a result of the lateral expansion (or dilation) of concrete. It is easy to understand that the expansion of concrete is generally non-uniform in such columns because of the moment gradient over the height and the strain gradient over the cross-section.

Figure 7.20a shows the development of hoop strains with the lateral displacement for section 1 of a typical specimen. When the lateral displacement was positive, side A of the column was under compression while side E was under tension; it is thus not surprising to find that the hoop strain gauge located at side A recorded the highest tensile strain. On the contrary, on the left side of the figure (i.e. where the lateral displacement is negative), the hoop strain corresponding to side E reached the highest absolute value. Despite the highly non-uniform hoop strain distribution, it is interesting to note that all the hoop strains are negative (i.e. tensile), suggesting that the concrete was significantly confined in both the compression and the tension zones of the column section.

Figure 7.20b shows the development of hoop strains at different sections over the column for side A of specimen D56-6-0.2, which is typical of the specimens without a concrete infill in the steel tube. It is not surprising to see that the hoop strains are generally larger at a lower section as the moment increases towards the column end.

The hoop strain results of specimen D80-6-0.4-S are shown in Figure 7.20c. When the lateral displacement is relatively small (i.e. smaller than 50 mm), the variations of hoop strains with the lateral displacement are similar to those of the

other 7 specimens, with the maximum hoop strain being at the lowest section. However, when the lateral displacement is larger than 50 mm, the hoop strain at section 3 (i.e. A3H) becomes even larger than those at sections 1 and 2. Indeed, the rupture of FRP occurred near section 3 in this specimen (Figure 7.12d). This is believed to be due to the fact that the lower 320 mm of the inner steel tube of this specimen was filled with concrete, which shifted the location of FRP tube rupture to the weaker part above the concrete infill in the steel tube.

Table 7.4 summarizes the maximum readings of the hoop strain gauges installed at different heights of the FRP tube. The maximum hoop strain reading recorded on each specimen is highlighted in this table. It is clear that the maximum hoop strain occurred at the lowest section (i.e. section 1), except for specimen D80-6-0.4-S where the maximum hoop strain occurred at section 3. The average maximum hoop strain of all the specimens is 1.35%, which is only slightly lower than the value (i.e. 1.55%) found from split disk tests, suggesting that the effect of axial stress of the FRP tube on its ultimate hoop strain is limited.

7.3.8 Ductility of Hybrid DSTCs

The ductility of a structural member is generally defined as its ability to sustain inelastic deformations prior to collapse, without a substantial loss of strength. The ductility of a column is generally evaluated as its deformation capacity or energy dissipation capacity (Priestley and Park 1987; Park 1989; Usami and Ge 1994; Williams and Sexsmith 1995; Mirmiran *et al.* 1999; Wu *et al.* 2006; Hu 2011). The most commonly used parameter appears to be the ductility index μ_δ defined by the following equation (Priestley and Park 1987; Usami and Ge 1994; Williams and Sexsmith 1995; Mirmiran *et al.* 1999; Wu *et al.* 2006):

$$\mu_{\delta} = \delta_u / \delta_y \quad (7.3)$$

where δ_y and δ_u are the yield displacement and the ultimate displacement respectively. Various definitions of yield and ultimate displacements have been used by previous researchers. In the present study, the yield displacement is defined as the displacement corresponding to the elastic limit of an equivalent elastic-perfectly plastic lateral load-displacement curve with a reduced stiffness being equal to the secant stiffness at 75% of the peak load (Figure 7.21), following Park (1989), Boyd *et al.* (1995), Elremaily and Azizinamini (2002) and Hu (2011). The ultimate displacement is defined as the displacement when the load carried by the column has undergone a 20% reduction, following Priestley and Park (1987), Iacobucci *et al.* (2003) and Hu (2011). The values of the ductility index based on the above definitions are summarized in Table 7.5. It may also be noted that the value of the ductility index for the same column depends significantly on whether it is calculated based on the envelope load-displacement curve in the positive or the negative direction due to the asymmetric nature of lateral load-displacement curves (Figure 7.13).

Table 7.5 demonstrates again the excellent ductility of hybrid DSTCs. As expected, the ductility index decreases as the concrete strength or the axial load ratio increases. However, the thickness of FRP tube and the additional concrete infill in the steel tube do not seem to have a significant effect on the ductility index. The ductility index of specimen D80-6-0.4-S is only slightly larger than that of specimen D80-6-0.4. The two specimens with a 10 mm FRP tube even have slightly lower values for the ductility index than their respective counterparts with a 6 mm FRP tube. A further examination of the test data revealed that this is due to the higher peak load and the larger yield displacement of the specimens with a thicker FRP tube or with an addition concrete infill.

It is also worth noting that the conditions of different columns can be quite different when the load carried by the column reduces by 20% from its peak value (e.g. the 6 mm FRP tube in some specimens was close to final failure while the two specimens D80-10-0.4 and D116-10-0.4 with a 10 mm FRP tube was still in a good state). The present tests indicated that the structural integrity of hybrid DSTCs is generally very good until the hoop rupture of the FRP tube. Therefore, it may be more reasonable to take the rupture of the FRP tube as the ultimate state of hybrid DSTCs. If this new definition is adopted, the values of the ductility index as summarized in Table 7.5 indicate that specimens with a thicker FRP tube or additional concrete infill in the steel tube have better ductility (Table 7.5).

7.3.9 Length of Equivalent Plastic Hinge

Priestly and Park. (1987) proposed that the lateral displacement at the ultimate condition Δ_u can be calculated using the following equation:

$$\begin{aligned}\Delta_u &= \Delta_y + \theta_p(L - 0.5L_p) \\ \theta_p &= \theta_u - \theta_y\end{aligned}\tag{7.4}$$

where Δ_y is the yield displacement; θ_p is the rotation of the plastic hinge after the column yields; L is the column length; L_p is the length of the equivalent plastic hinge region; θ_y and θ_u are the rotations of the plastic hinge at the yield displacement and the ultimate displacement respectively. Eq. 7.4 is based on the assumption that post-yielding lateral displacement of the column head is due purely to the rotations of the column as a rigid body at the center of the equivalent plastic hinge region. The length of the equivalent plastic hinge can be calculated using Eq. 7.4 once the rotations at the column end at the yield and the ultimate

displacements are known. In the present study, the rotation at the column end can be calculated from the readings of LVDTs 9 and 10 (Figure 7.5) using the following equation:

$$\theta = \tan^{-1}((\Delta_{LVDT-09} - \Delta_{LVDT-10})/L_b) \quad (7.5)$$

where $\Delta_{LVDT-09}$ and $\Delta_{LVDT-10}$ are the readings of LVDTs 9 and 10 respectively; and L_b is the horizontal distance between LVDTs 9 and 10, which is 350 mm. The lengths of equivalent plastic hinge so obtained are listed in Table 7.5. It is interesting to note that the values are very similar for all the specimens, and are very close to the effective height of the cross-section for pure bending (i.e. the diameter of the column minus the thickness of the annular concrete section, which is 260 mm).

It should also be noted that while Eq. 7.4 and the above assumptions reflect closely the real situation of the other 7 specimens, they may not be applicable to specimen D80-6-0.4-S in which the deformation was distributed over a larger length of the column. The concept of equivalent plastic hinge region needs to be re-examined for such columns with a variable cross-section.

7.3.10 Residual Strength of Hybrid DSTCs

Specimens D56-6-0.2, D116-6-0.2 and D80-6-0.4 were tested under axial compression following the cyclic lateral loading test. Figure 7.22 shows the axial load-axial shortening curves of these three specimens. Specimen D56-6-0.2 is seen to have a much higher residual axial load capacity than the other two specimens, due to the less severe damage to the FRP tube and the concrete by cyclic lateral loading. At the peak residual strength of specimen D56-6-0.2, a

large noise was heard because of the explosive rupture of the remaining part of the FRP tube, which led to a sudden drop in the axial load. By contrast, specimens D116-6-0.2 and D80-6-0.4 had an approximately elastic-plastic curve, with the residual axial load capacity being around 2000 kN, which came mainly from the steel inner tube.

7.4. CONCLUSIONS

This chapter has presented the first experimental study on hybrid DSTCs filled with HSC subjected to axial compression in combination with cyclic lateral loading. A relatively large column section was employed to allow reliable experimental modeling of real columns. The test results provide valuable data needed for the formulation and verification of a theoretical model for the hysteric behavior of hybrid DSTCs, particularly when they are filled with HSC. The test results and discussions presented also allow the following conclusions to be drawn:

- (1) Hybrid DSTCs possess excellent ductility and seismic resistance even when high strength concrete with a cylinder compressive strength of around 120 MPa is used;
- (2) Hybrid DSTCs with a higher concrete strength generally have a higher moment capacity but a smaller deformation capacity;
- (3) A thicker FRP tube leads to a slightly larger moment capacity and better ductility for hybrid DSTCs;
- (4) The axial load ratio has a significant effect on both the lateral load capacity and the ductility of hybrid DSTCs;
- (5) Column damage is concentrated in a small plastic hinge region near the column end, and the height of this region is similar to the column diameter;

- (6) The performance of hybrid DSTCs can be enhanced by partially filling the inner steel tube with concrete near the column end.

7.5 REFERENCES

- ASTM C39/C39M. (2011). *Standard Test Method for Compressive Strength of Cylindrical Concrete Specimens*, American Society for Testing and Materials, Philadelphia, USA.
- ASTM D2290-08. (2008). *Standard Test Method for Apparent Hoop Tensile Strength of Plastic or Reinforced Plastic Pipe by Split Disk Method*, American Society for Testing and Materials (ASTM), Philadelphia, USA.
- Bae, S. and Bayrak, O. (2008). “Seismic performance of full-scale reinforced concrete columns”, *ACI Structural Journal*, 105(2), 123-133.
- BS 18-1987. (1987). *Tensile Testing of Metals (including Aerospace Materials)*, British Standards Institution, London, UK.
- Chen, W.F. and Atsuta, T. (1976). *Theory of Beam Columns*, McGraw-Hill, New York.
- GB-50608. (2011). *Technical Code for Infrastructure Application of FRP Composites*, China Planning Press, China.
- Han, L.H., Tao, Z., Liao, F.Y. and Xu, Y. (2010). “Tests on cyclic performance of FRP-concrete-steel double-skin tubular columns”, *Thin-Walled Structures*, 48(6), 430-493.
- Hu, Y.M. (2011). *Behaviour and Modelling of FRP-Confined Hollow and Concrete-Filled Steel Tubular Columns*, PhD Thesis, The Hong Kong Polytechnic University.
- Hsu, H.L. and Chang, D.L. (2001). “Upgrading the performance of steel box piers subjected to earthquakes”, *Journal of Constructional Steel Research*, 57(9), 945-958.

- Iacobucci, R.D., Sheikh, S.A. and Bayrak, O. (2003). "Retrofit of square concrete columns with carbon fiber-reinforced polymer for seismic resistance", *ACI Structural Journal*, 100(6), 785-794.
- Mirmiran, A., Shahawy, M. and Samaan, M. (1999). "Strength and ductility of hybrid FRP-concrete beam-columns", *Journal of Structural Engineering*, ASCE, 125(10), 1085-1093.
- Nordin, H. and Täljsten, B. (2004). "Testing of hybrid FRP composite beams in bending", *Composites Part B: Engineering*, 35(1), 27-33.
- Park, R. (1989). "Evaluation of ductility of structures and structural assemblages for laboratory testing", *Bulletin of the New Zealand National Society for Earthquake Engineering*, 22(3), 155-166.
- Priestley, M.J.N. and Park, R. (1987). "Strength and ductility of concrete bridge columns under seismic loading", *ACI Structural Journal*, 84(1), 61-76.
- Qian, J.R. and Liu, M.X. (2008). "Test of seismic behaviour of FRP-concrete-steel double-skin tubular columns", *China Civil Engineering Journal*, 41(3), 29-36. (in Chinese).
- Teng, J.G., Yu, T. and Wong, Y.L. (2004). "Behaviour of hybrid FRP-concrete-steel double-skin tubular columns", *Proceedings, Second International Conference on FRP Composites in Civil Engineering*, 8-10 December, Adelaide, Australia, 811-818.
- Teng, J.G., Yu, T., Wong, Y.L. and Dong, S.L. (2007). "Hybrid FRP-concrete-steel tubular columns: Concept and behavior", *Construction and Building Materials*, 21(4), 846-854.
- Teng, J.G., Yu, T. and Wong, Y.L. (2010). "Hybrid FRP-concrete-steel double-skin tubular structural members", *Proceedings, Fifth International Conference on FRP Composites in Civil Engineering*, 27-29 September, Beijing, China,

26-32.

Usami, T. and Ge, H.B. (1994). "Ductility of concrete-filled steel box columns under cyclic loading", *Journal of Structural Engineering*, ASCE, 120(7), 2021-2040.

Williams, M. and Sexsmith, R.G. (1995). "Seismic damage indices for concrete structures: a state-of-art review", *Earthquake Spectra*, 11(2), 319-349.

Wu, Y.F., Liu, T. and Oehlers, D.J. (2006). "Fundamental principles that govern retrofitting of reinforced concrete columns by steel and FRP jacketing", *Advances in Structural Engineering*, 9(4), 507-533.

Wong, Y.L., Yu, T., Teng, J.G. and Dong, S.L. (2008). "Behavior of FRP confined concrete in annular section columns", *Composites Part B: Engineering*, 39(3), 451-466.

Yu, T., Wong, Y.L., Teng, J.G. and Dong, S.L. (2006). "Flexural behaviour of hybrid FRP-concrete-steel double-skin tubular members", *Journal of Composites for Construction*, ASCE, 10(5), 443-452.

Yu, T. (2007). *Behavior of Hybrid FRP-Concrete-Steel Double-Skin Tubular Columns*, PhD Thesis, The Hong Kong Polytechnic University.

Yu, T., Teng, J.G., Wong, Y.L. and Dong, S.L. (2010a). "Finite element modelling of confined concrete-I: Drucker-Prager type plasticity model", *Engineering Structures*, 32(3), 665-679.

Yu, T., Teng, J.G., Wong, Y.L. and Dong, S.L. (2010b). "Finite element modelling of confined concrete-II: Plastic-damage model", *Engineering Structures*, 32(3), 680-691.

Yu, T., Teng, J.G. and Wong, Y.L. (2010c). "Stress-strain behavior of concrete in hybrid double-skin tubular columns", *Journal of Structural Engineering*, ASCE, 136(4), 379-389.

- Yu, T., Wong, Y.L. and Teng, J.G. (2010d). “Behaviour of hybrid FRP-concrete-steel double-skin tubular columns subjected to eccentric compression”, *Advances in Structural Engineering*, 13(5), 961-974.
- Yu, T. and Teng, J.G. (2013). “Behavior of Hybrid FRP-Concrete-Steel Double-Skin Tubular Columns with a Square Outer Tube and a Circular Inner Tube Subjected to Axial Compression”, *Journal of Composites for Construction*, ASCE, 17(2), 271-279.

Table 7.1: Specimen details

Specimen	Concrete properties			FRP tube	Axial load ratio
	f'_{co} (MPa)	E_c (GPa)	ε_{co} (%)	t_{frp} (mm)	n
D37-6-0.2	37.4	28.9	0.26	6.0	0.2
D56-6-0.2	56.0	35.4	0.30	6.0	0.2
D80-6-0.4	80.0	42.3	0.30	6.0	0.4
D80-6-0.4-S	80.0	42.3	0.32	6.0	0.4
D80-10-0.4	82.7	43.0	0.28	10.0	0.4
D116-6-0.2	116.4	51.0	0.36	6.0	0.2
D116-6-0.4	117.3	51.2	0.31	6.0	0.4
D116-10-0.4	114.8	50.7	0.31	10.0	0.4

Table 7.2: Mix properties of concrete

Specimen	Water cement ratio	Water	Cement	Fly ash	Silica fume	Super plasticizer	Coarse aggregate	Sand
D37-6-0.2	0.42	186	239	203	---	3	863	829
D56-6-0.2	0.35	175	300	200	---	10	845	812
D80-6-0.4	0.33	175	300	230	---	10	828	795
D80-6-0.4-S	0.33	175	300	230	---	10	828	795
D80-10-0.4	0.33	175	300	230	---	10	828	795
D116-6-0.2	0.25	165	429	165	66	17	837	685
D116-6-0.4	0.23	155	442	170	68	14	822	715
D116-10-0.4	0.23	155	442	170	68	14	822	715

*The brand of the super plasticizer is "Grace HK", the product model is "ADVA109".

Table 7.3: Details of loading schemes

Specimen name	Axial load ratio n	Applied axial load N (kN)	Estimated yield moment (kN.m)	Estimated maximum lateral load (kN)	Estimated yield displacement (mm)
D37-6-0.2	0.2	530.8	140.0	103.7	10.2
D56-6-0.2	0.2	668.3	164.3	121.7	12.0
D80-6-0.4	0.4	1546.2	171.8	127.3	7.20
D80-6-0.4-S	0.4	1623.9	178.4	132.1	7.50
D80-10-0.4	0.4	1478.7	167.5	124.1	8.50
D116-6-0.2	0.2	1060.4	233.6	173.0	16.4
D116-6-0.4	0.4	2115.9	235.1	174.1	8.10
D116-10-0.4	0.4	2103.1	233.7	173.1	10.0

Table 7.4: Maximum readings of hoop strain gauges on FRP tubes

Specimen	Loading direction	$\epsilon_{h,max}$	$\epsilon_{h,max}$	$\epsilon_{h,max}$	$\epsilon_{h,max}$	$\epsilon_{h,max}$	$\epsilon_{h,max}$
		(%)	(%)	(%)	(%)	(%)	(%)
		at Section-1	at Section-2	at Section-3	at Section-4	at Section-5	at Section-6
D37-6-0.2	Positive	0.98 (A1H)	0.86 (A2H)	0.34 (A3H)	0.12 (A4H)	---	---
	Negative	<u>1.25</u> (E1H)	0.42 (G2H)	0.32 (F3H)	0.12 (E4H)	---	---
D56-6-0.2	Positive	<u>1.46</u> (A1H)	0.33 (B2H)	0.14 (A3H)	0.11 (A4H)	---	---
	Negative	1.44 (E1H)	0.41 (D2H)	0.11 (E3H)	0.10 (E4H)	---	---
D80-6-0.4	Positive	1.24 (B1H)	0.55 (H2H)	0.28 (B3H)	0.07 (A4H)	---	---
	Negative	<u>1.43</u> (E1H)	0.69 (D2H)	0.21 (D3H)	0.09 (E4H)	---	---
D80-6-0.4-S	Positive	1.08 (A1H)	0.85 (H2H)	<u>1.32</u> (B3H)	0.47 (H4H)	0.19 (A5H)	0.06 (A6H)
	Negative	1.06 (F1H)	0.97 (F2H)	0.73 (E3H)	1.03 (F4H)	0.38 (E5H)	0.10 (E6H)
D80-10-0.4	Positive	0.95 (A1H)	0.47 (B2H)	0.18 (A3H)	0.14 (A4H)	---	---
	Negative	<u>1.39</u> (E1H)	0.59 (F2H)	0.16 (F3H)	0.12 (E4H)	---	---
D116-6-0.2	Positive	0.95 (B1H)	0.46 (H2H)	0.14 (H3H)	0.11 (A4H)	---	---
	Negative	<u>1.37</u> (E1H)	0.26 (F2H)	0.13 (E3H)	0.10 (E4H)	---	---
D116-6-0.4	Positive	1.03 (H1H)	0.80 (H2H)	0.26 (H3H)	0.11 (A4H)	---	---
	Negative	<u>1.16</u> (F1H)	1.00 (E2H)	0.24 (F3H)	0.08 (E4H)	---	---
D116-10-0.4	Positive	<u>1.42</u> (H1H)	0.70 (A2H)	0.14 (B3H)	0.06 (A4H)	---	---
	Negative	0.86 (E1H)	0.73 (D2H)	0.18 (D3H)	0.06 (E4H)	---	---

The underlined numbers are the maximum readings of hoop strain gauges installed on the FRP tube for each specimen.

The name of the corresponding strain gauge is provided in the bracket.

Table 7.5: Ductility indices of hybrid DSTCs

Specimen		δ_y (mm)	δ_u^a (mm)	μ_δ^a	L_p^a (mm)	δ_u^b (mm)	μ_δ^b	L_p^b (mm)
D37-6-0.2	Positive direction	12.7	101.9	8.0	248	134.1	10.6	241
	Negative direction	13.8	111.5	8.1	248	124.6	9.0	245
	Average	13.2	106.7	8.1	248	129.4	9.8	243
D56-6-0.2	Positive direction	14.0	92.5	6.6	255	117.7	8.4	247
	Negative direction	14.4	126.8	8.8	245	144.5	10.0	242
	Average	14.2	109.6	7.7	250	131.1	9.2	244
D80-6-0.4	Positive direction	10.2	55.6	5.4	264	62.3	6.1	259
	Negative direction	8.6	64.1	7.5	251	64.5	7.5	250
	Average	9.4	59.8	6.5	258	63.4	6.8	254
D80-6-0.4-S	Positive direction	9.2	70.7	7.7	250	111.4	12.1	238
	Negative direction	12.3	69.0	5.6	263	112.0	9.1	244
	Average	10.8	69.8	6.6	256	111.7	10.6	241
D80-10-0.4	Positive direction	10.4	67.1	6.4	256	95.2	9.1	244
	Negative direction	11.8	69.0	5.8	261	93.3	7.9	249
	Average	11.1	68.0	6.1	258	94.3	8.5	246
D116-6-0.2	Positive direction	14.9	67.9	4.6	275	111.1	7.5	250
	Negative direction	12.1	81.4	6.7	254	110.8	9.1	244
	Average	13.5	74.7	5.6	265	111.0	8.3	247
D116-6-0.4	Positive direction	9.2	45.5	4.9	270	42.0	4.5	275
	Negative direction	9.3	37.2	4.0	285	43.1	4.6	274
	Average	9.3	41.4	4.5	278	42.5	4.6	275
D116-10-0.4	Positive direction	10.8	46.6	4.3	279	70.4	6.5	256
	Negative direction	12.8	48.9	3.8	289	69.2	5.4	265
	Average	11.8	47.7	4.1	284	69.8	6.0	260

^a the values when the ultimate displacement was defined to be the displacement corresponding to 20% reduction of the peak lateral load;

^b the values when the ultimate displacement was defined to be the displacement corresponding to the FRP tube rupture.

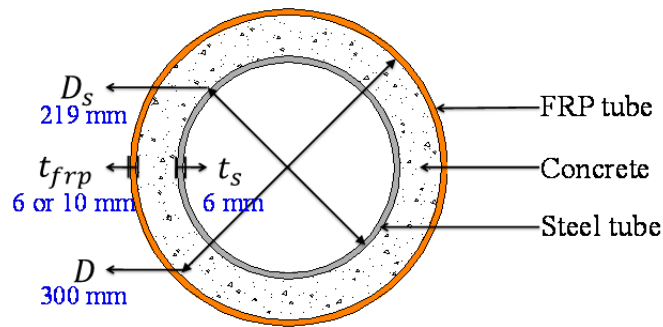


Figure 7.1: Cross-section of hybrid DSTCs

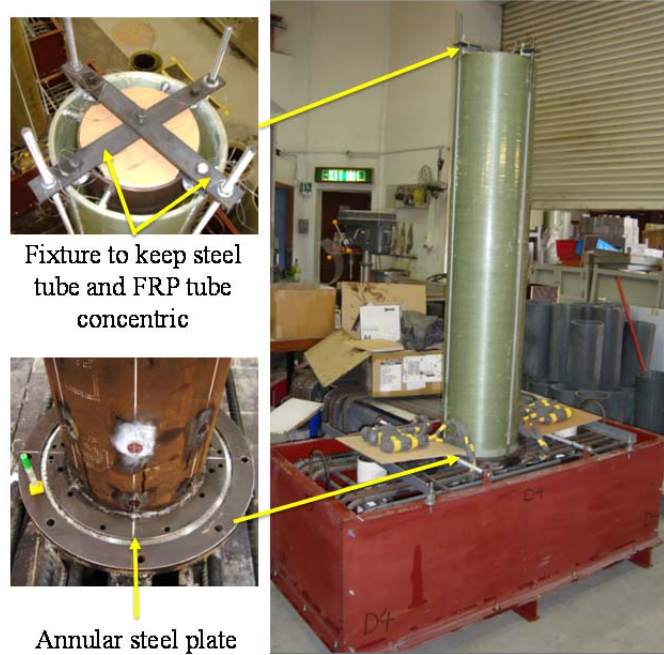
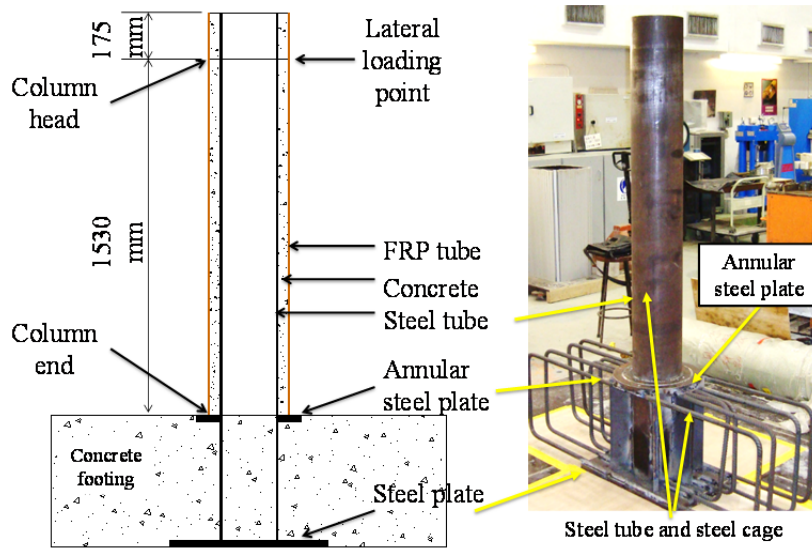


Figure 7.2: Preparation of hybrid DSTCs before concrete casting

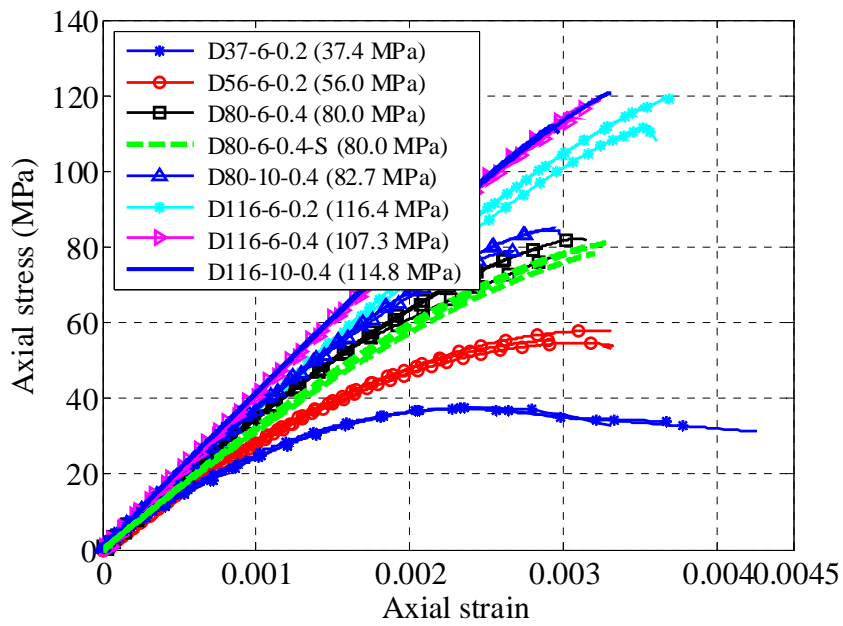


Figure 7.3: Axial stress-strain behavior of control cylinders

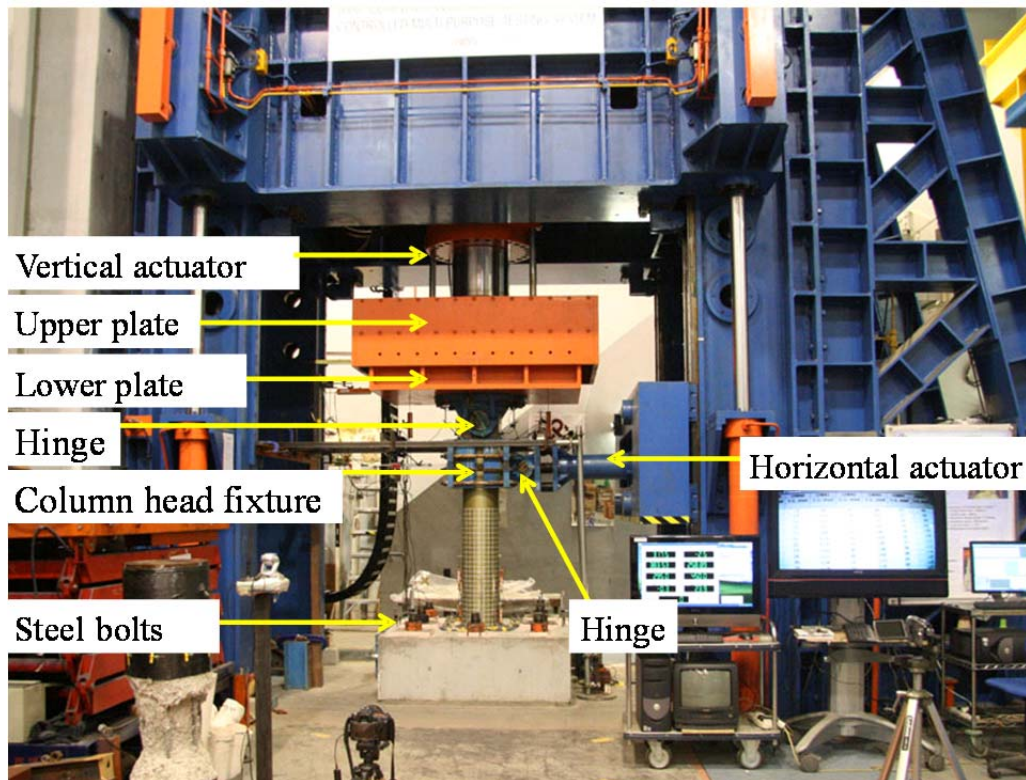


Figure 7.4: Experimental set-up

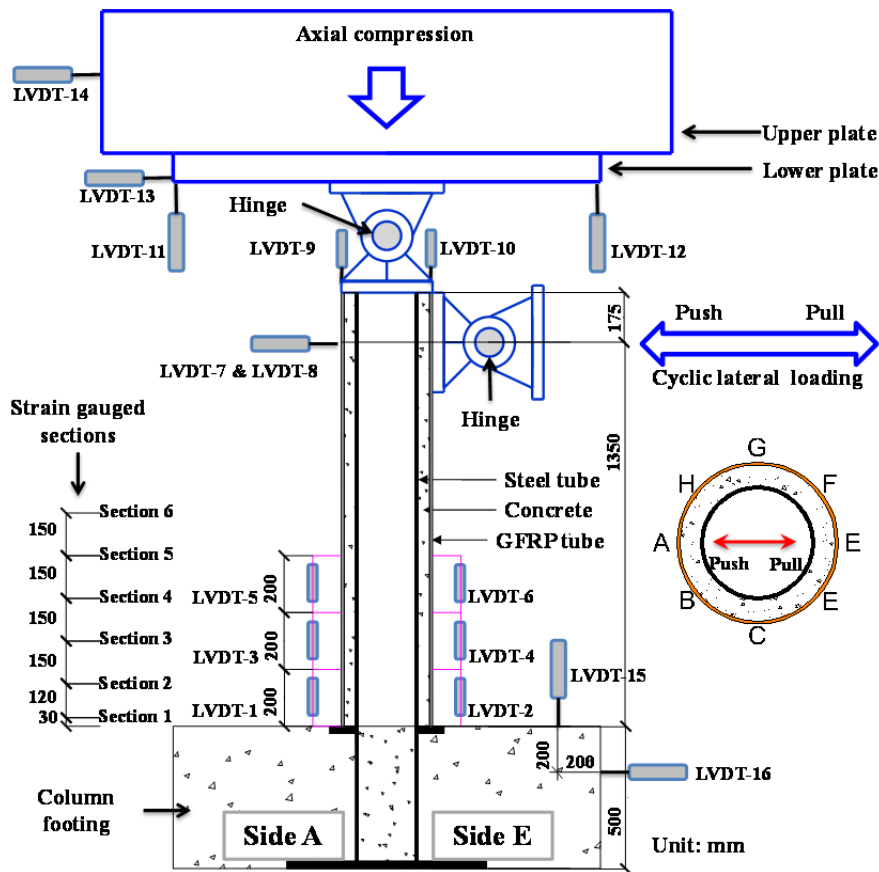


Figure 7.5: Layout of LVDTs and strain gauges

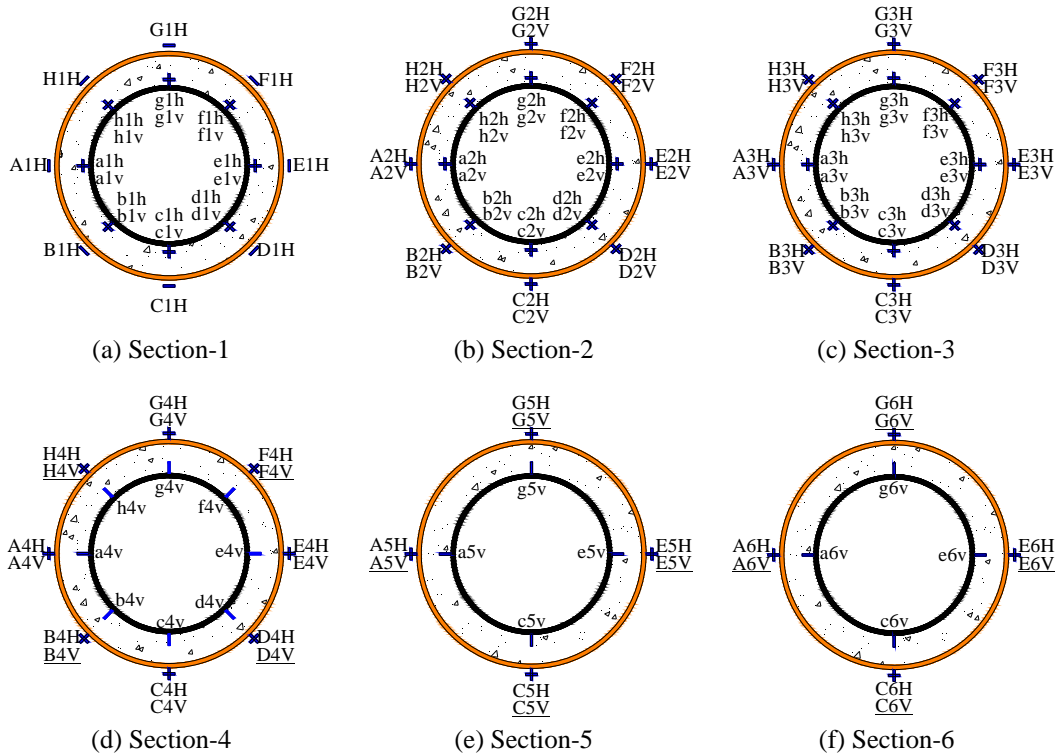


Figure 7.6: Planar layout of strain gauges on cross-section

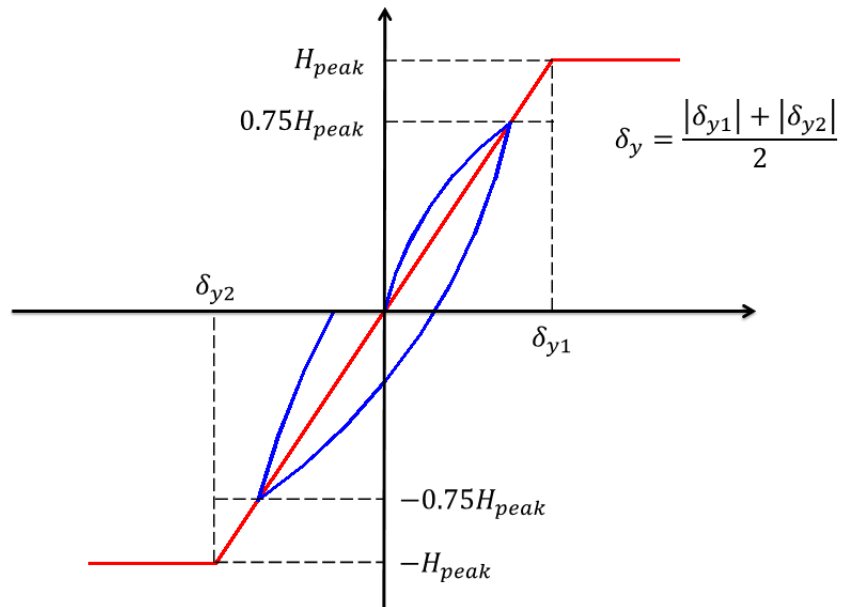


Figure 7.7: Experimental definition of yield displacement

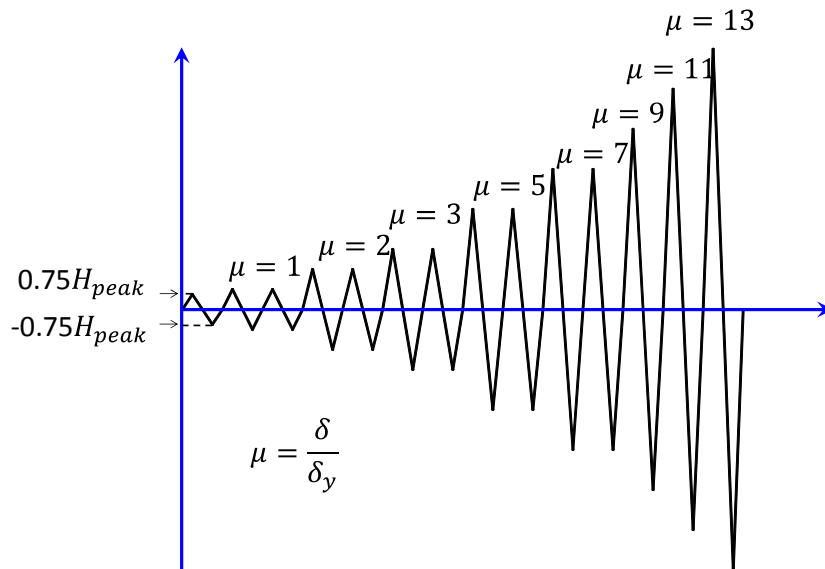


Figure 7.8: Cyclic loading schemes

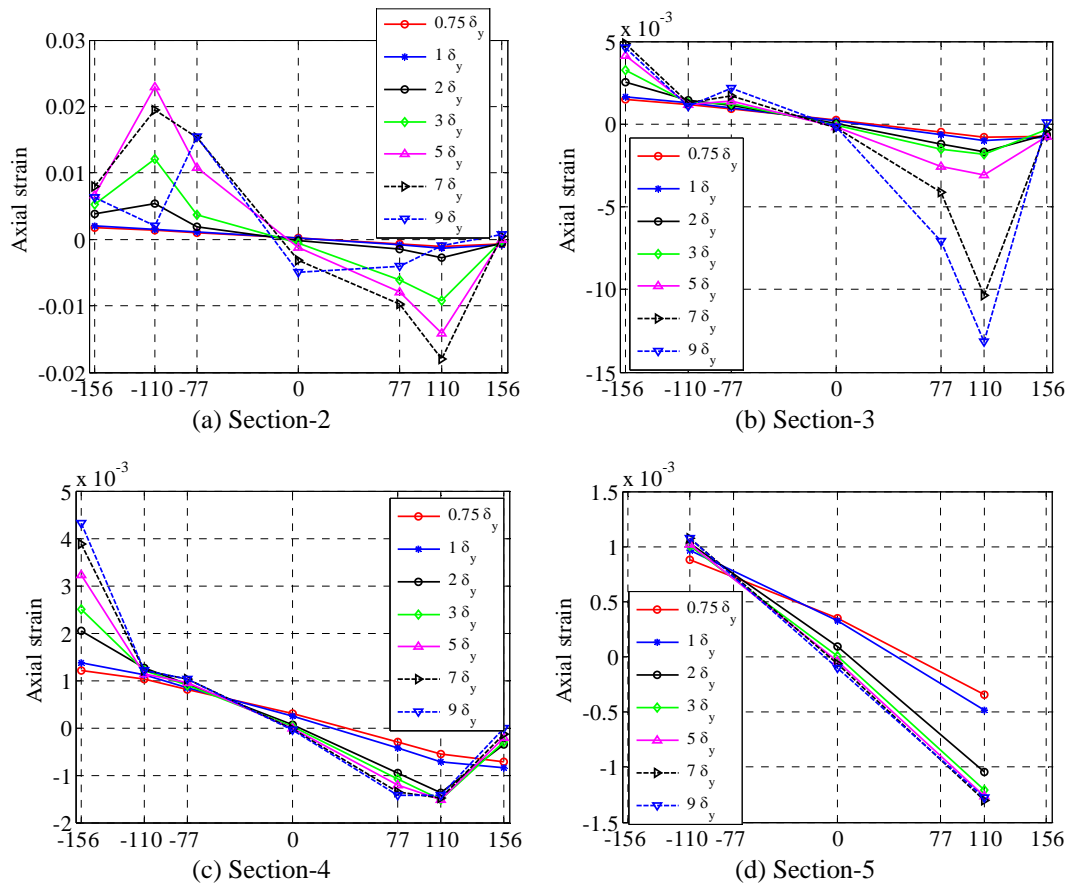


Figure 7.9: Distributions of axial strains on cross-section in specimen D37-6-0.2

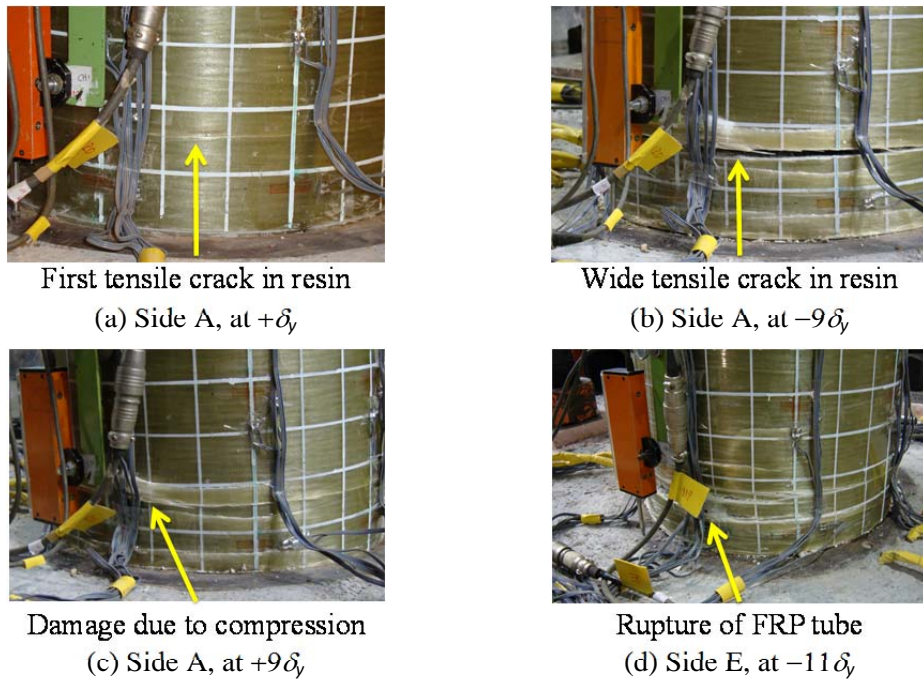
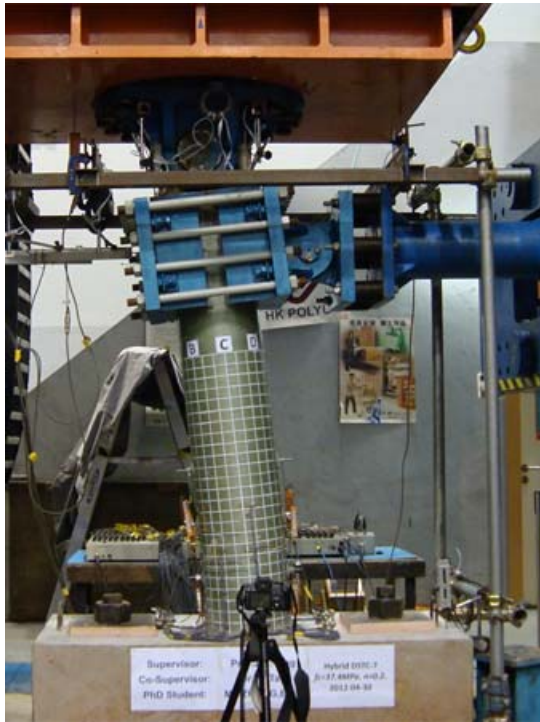


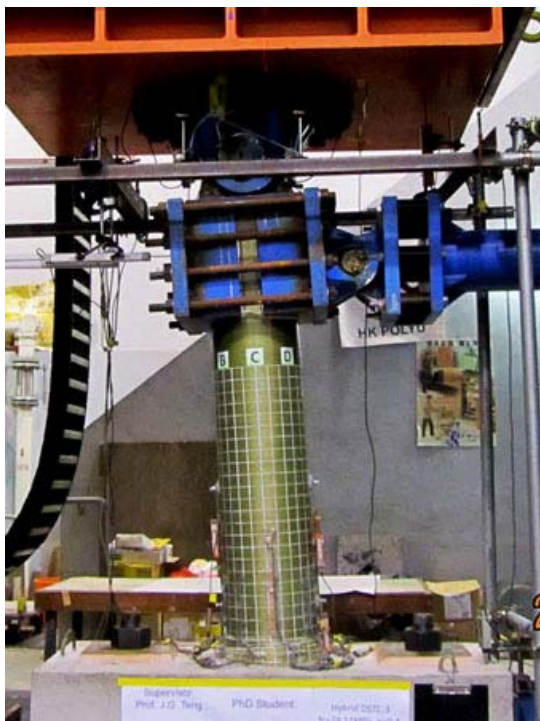
Figure 7.10: Progress of damage in specimen D37-6-0.2



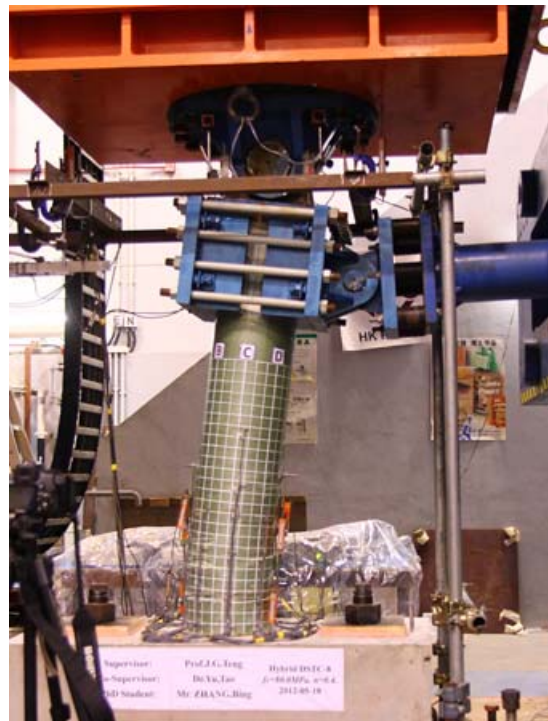
(a) Specimen D37-6-0.2



(b) Specimen D56-6-0.2

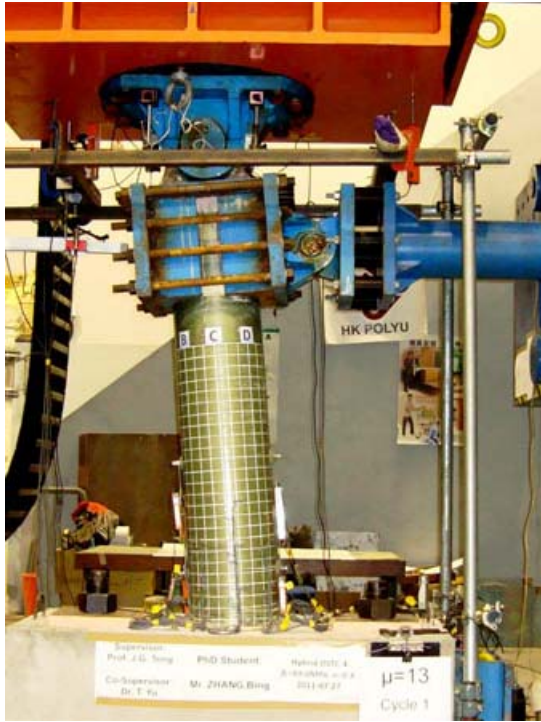


(c) Specimen D80-6-0.4

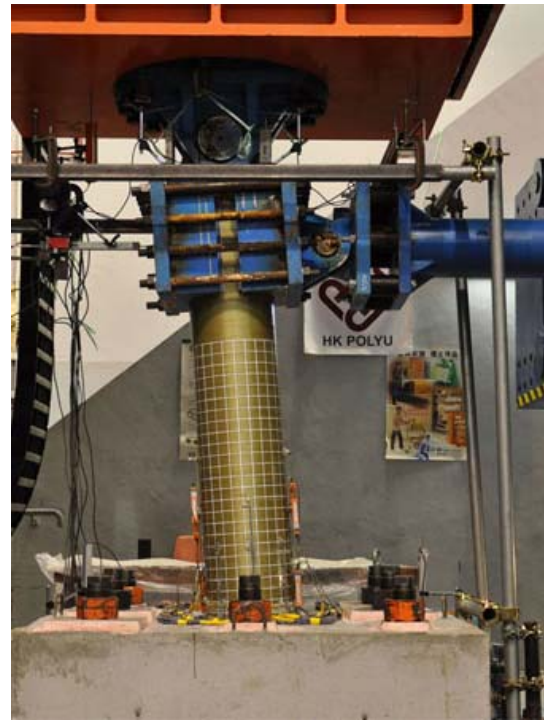


(d) Specimen D80-6-0.4-S

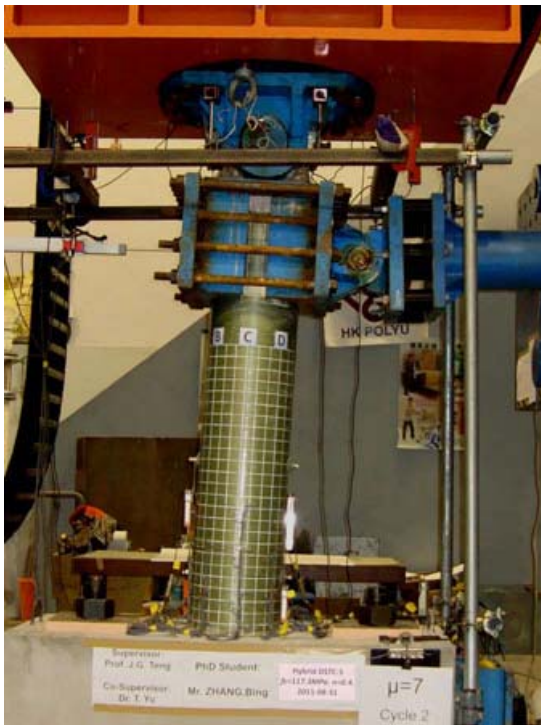
Figure 7.11: Specimens after test



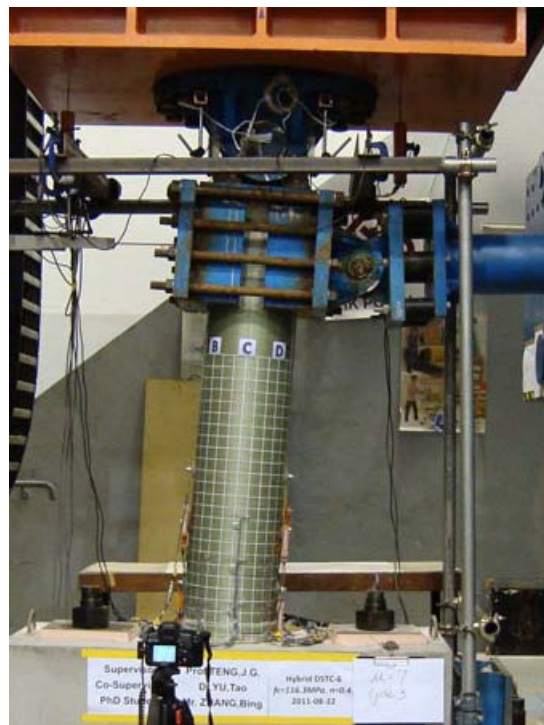
(e) Specimen D80-10-0.4



(f) Specimen D116-6-0.2

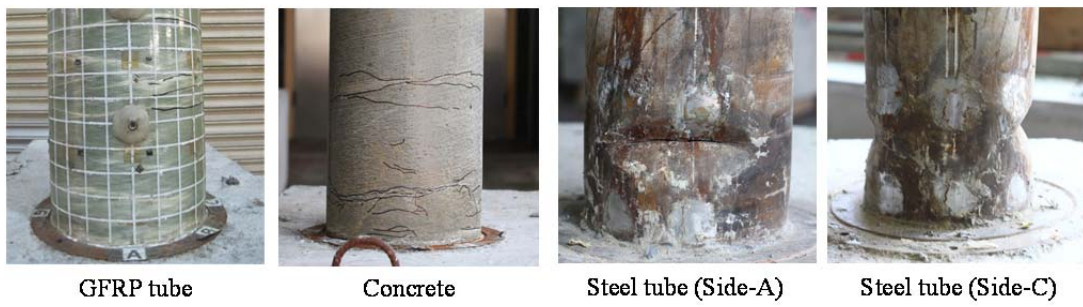


(g) Specimen D116-6-0.4



(h) Specimen D116-10-0.4

Figure 7.11: Specimens after test (continued)



(a) Specimen D37-6-0.2



(b) Specimen D56-6-0.2



(c) Specimen D80-6-0.4



(d) Specimen D80-6-0.4-S

Figure 7.12: Damage to FRP tube, concrete and steel tube



GFRP tube

Concrete

Steel tube (Side-A)

Steel tube (Side-C)

(e) Specimen D80-10-0.4



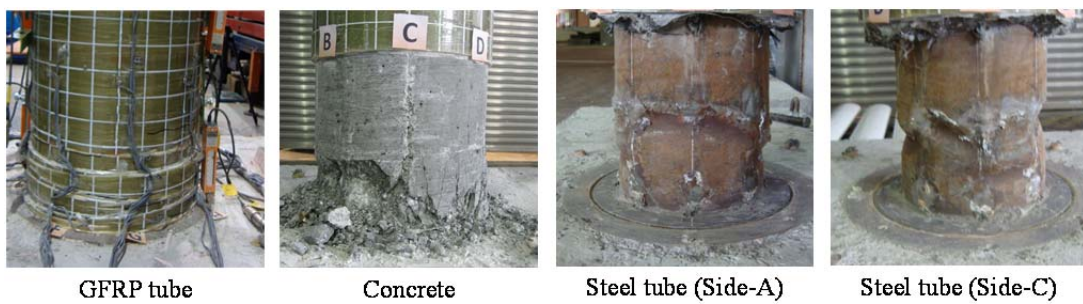
GFRP tube

Concrete

Steel tube (Side-A)

Steel tube (Side-C)

(f) Specimen D116-6-0.2



GFRP tube

Concrete

Steel tube (Side-A)

Steel tube (Side-C)

(g) Specimen D116-6-0.4



GFRP tube

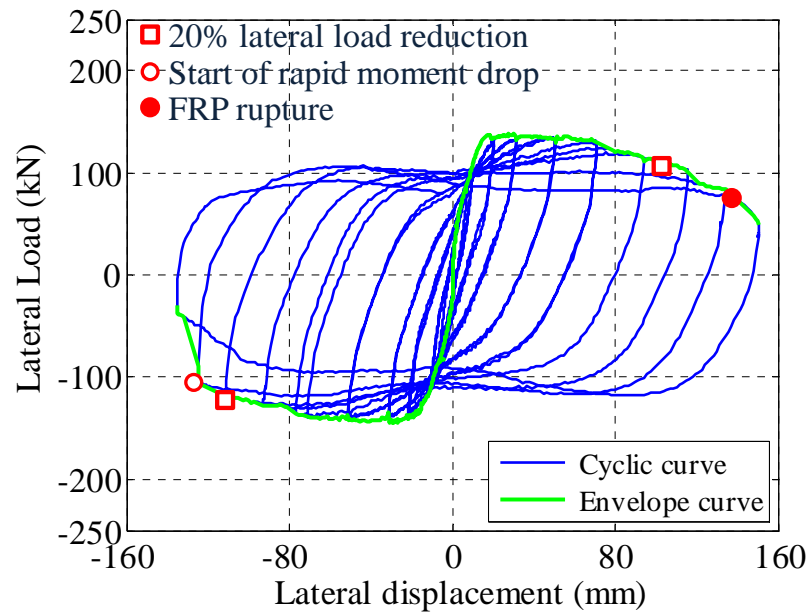
Concrete

Steel tube (Side-A)

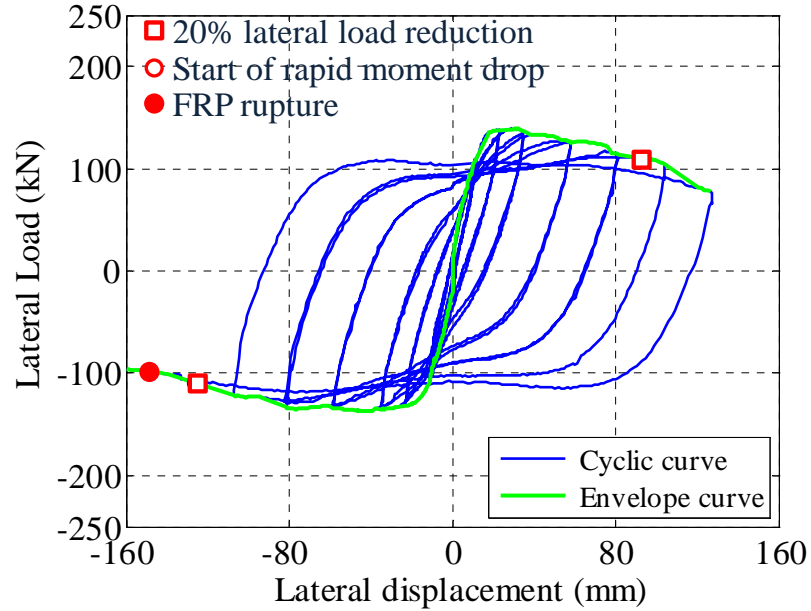
Steel tube (Side-C)

(h) Specimen D116-10-0.4

Figure 7.12: Damage to FRP tube, concrete and steel tube (continued)

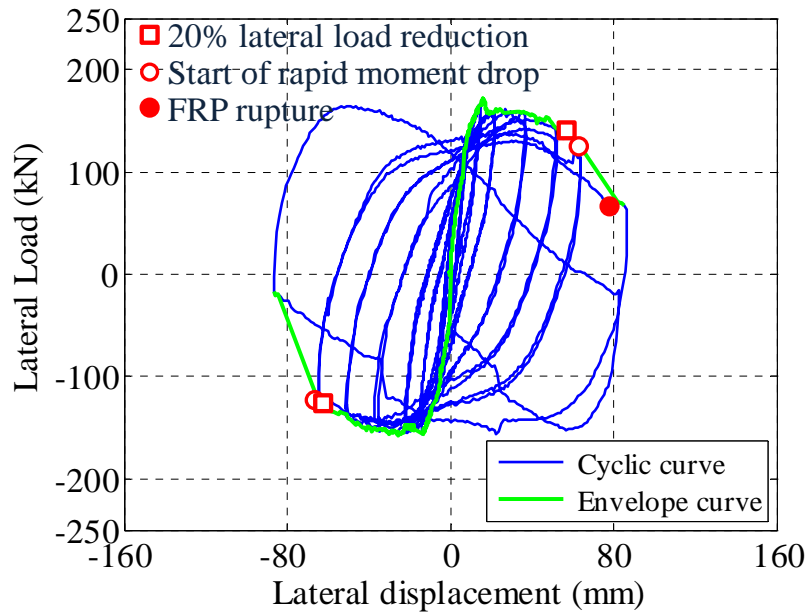


(a) Specimen D37-6-0.2

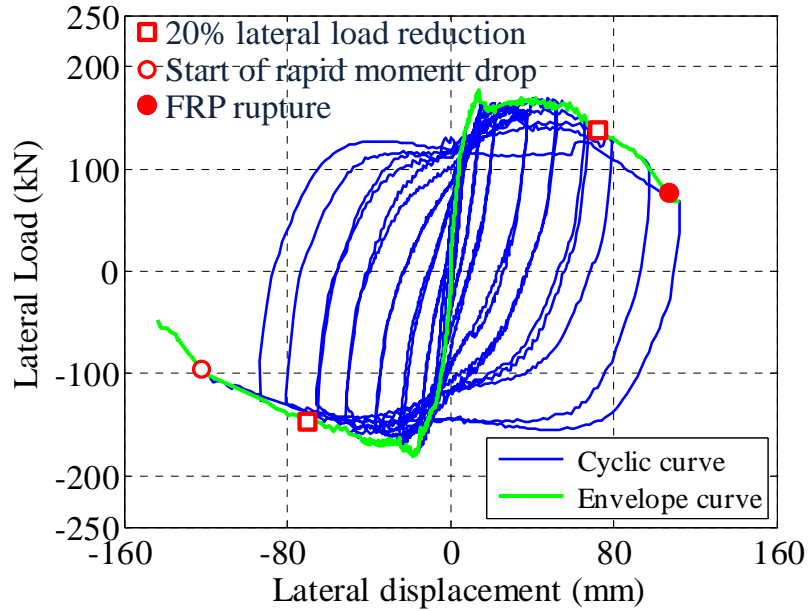


(b) Specimen D56-6-0.2

Figure 7.13: Hysteresis curves under cyclic lateral loading

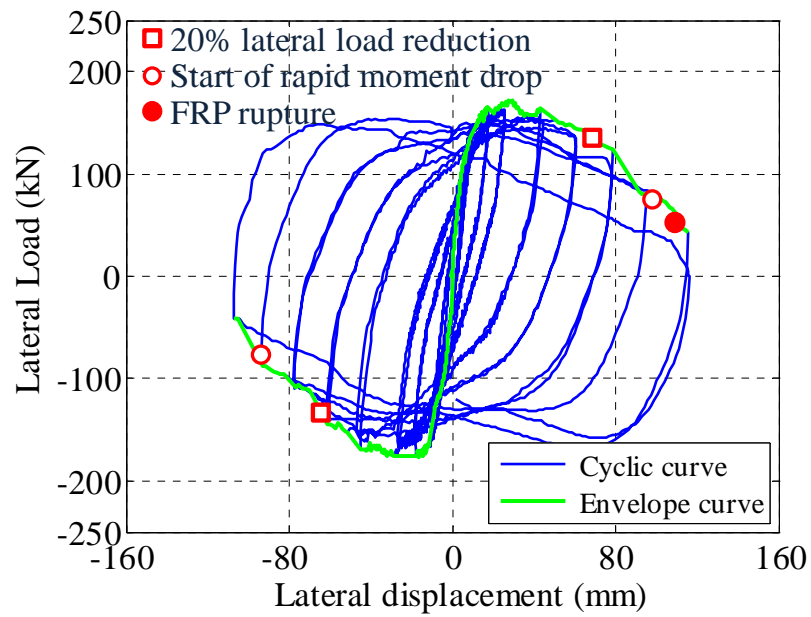


(c) Specimen D80-6-0.4

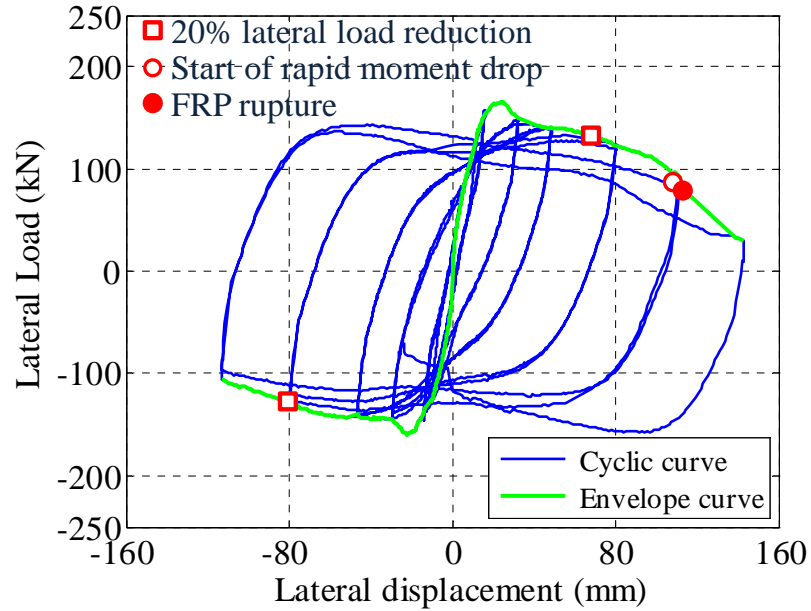


(d) Specimen D80-6-0.4-S

Figure 7.13: Hysteresis curves under cyclic lateral loading (continued)

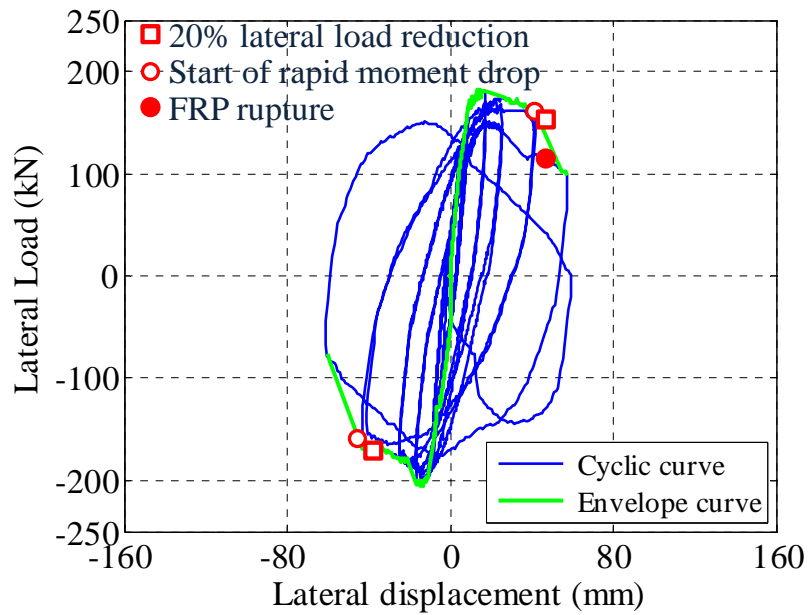


(e) Specimen D80-10-0.4

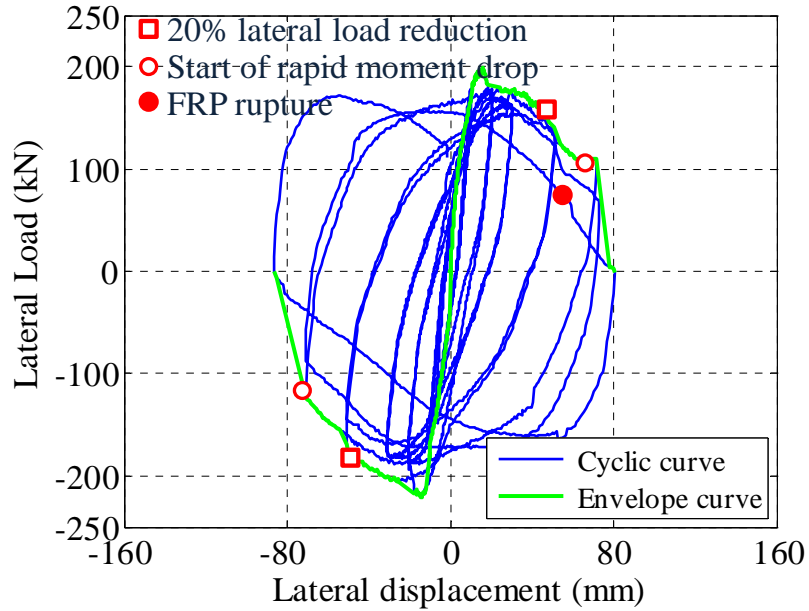


(f) Specimen D116-6-0.2

Figure 7.13: Hysteresis curves under cyclic lateral loading (continued)



(g) Specimen D116-6-0.4



(h) Specimen D116-10-0.4

Figure 7.13: Hysteresis curves under cyclic lateral loading (continued)

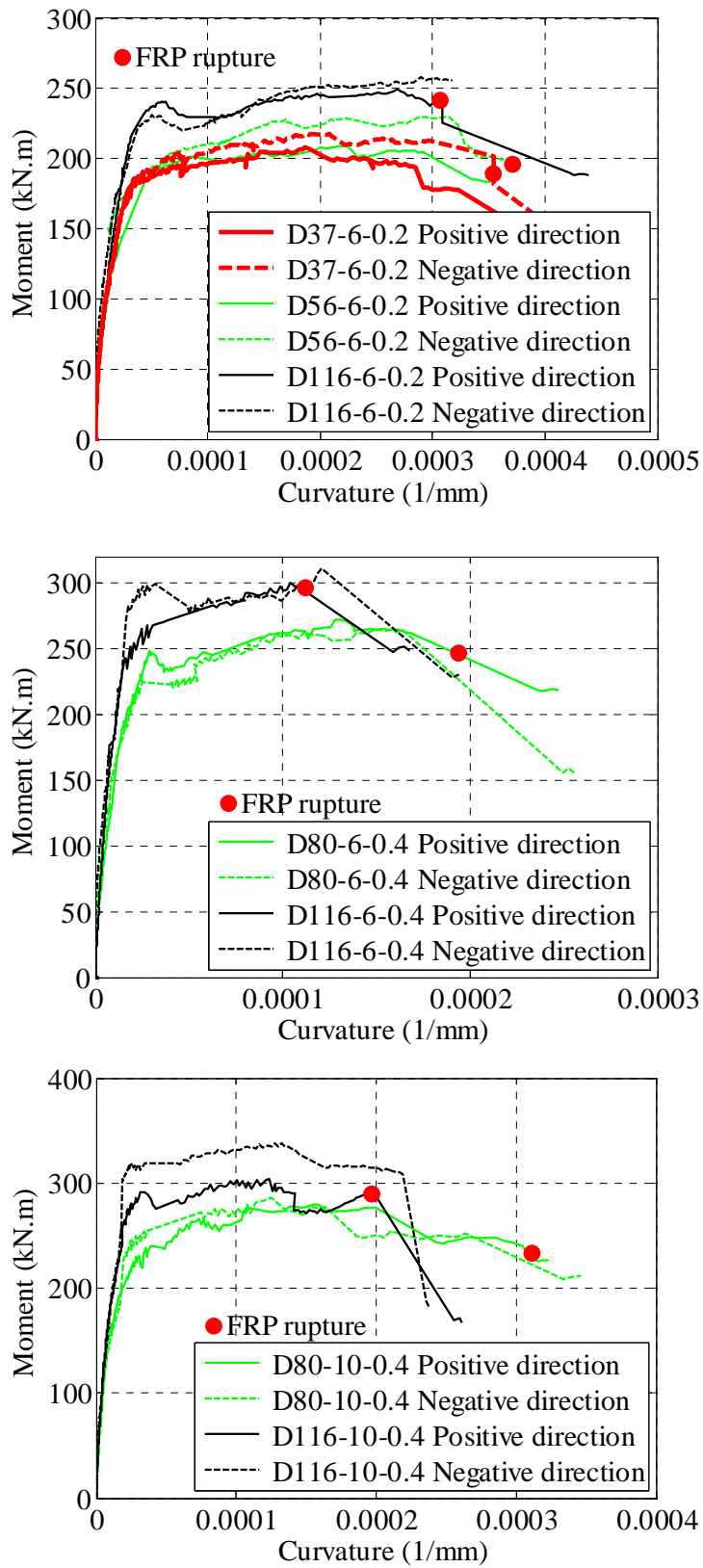


Figure 7.14: Effect of concrete strength on envelope moment-curvature curves

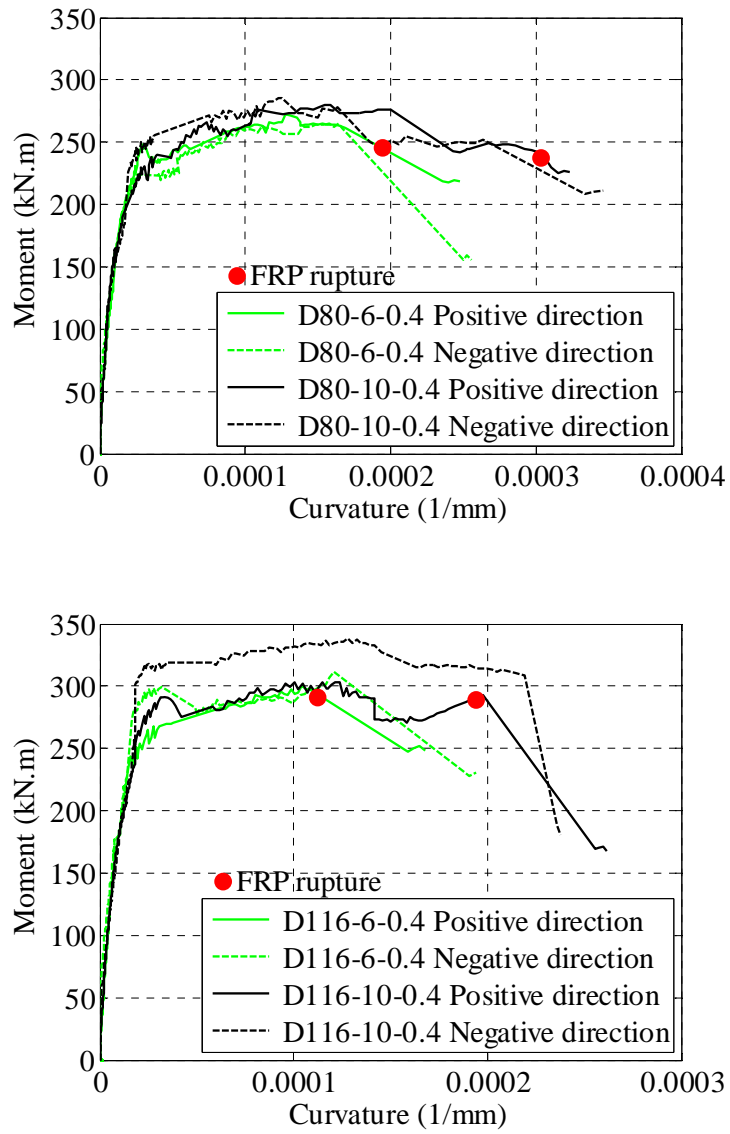


Figure 7.15: Effect of FRP tube thickness on envelope moment-curvature curves

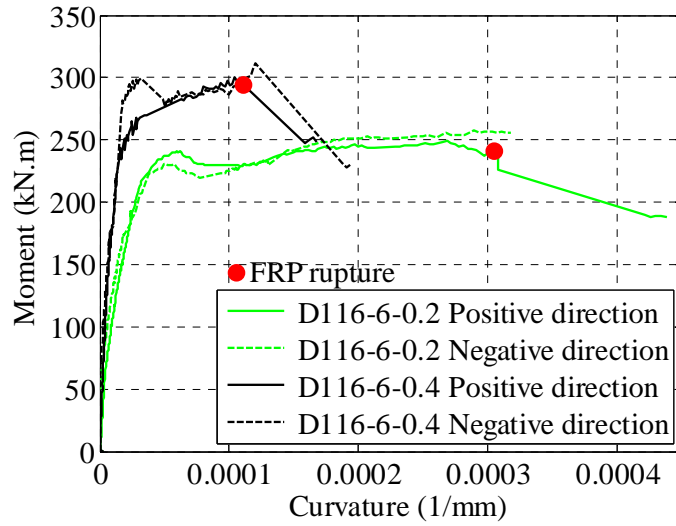


Figure 7.16: Effect of axial load ratio on envelope moment-curvature curves

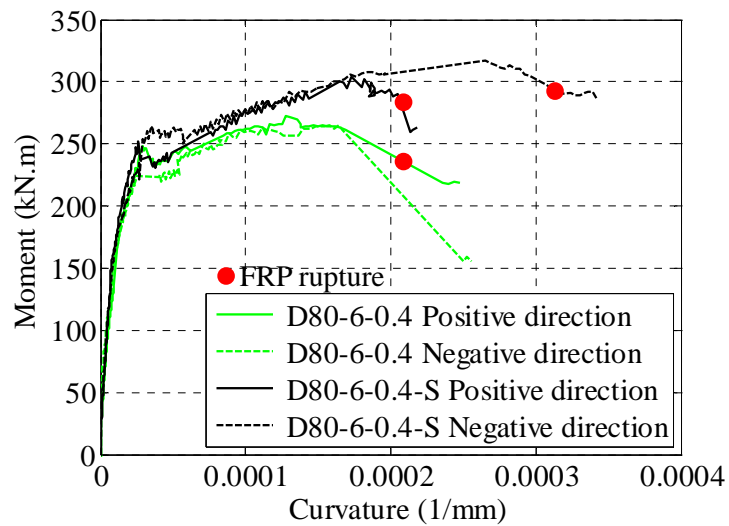
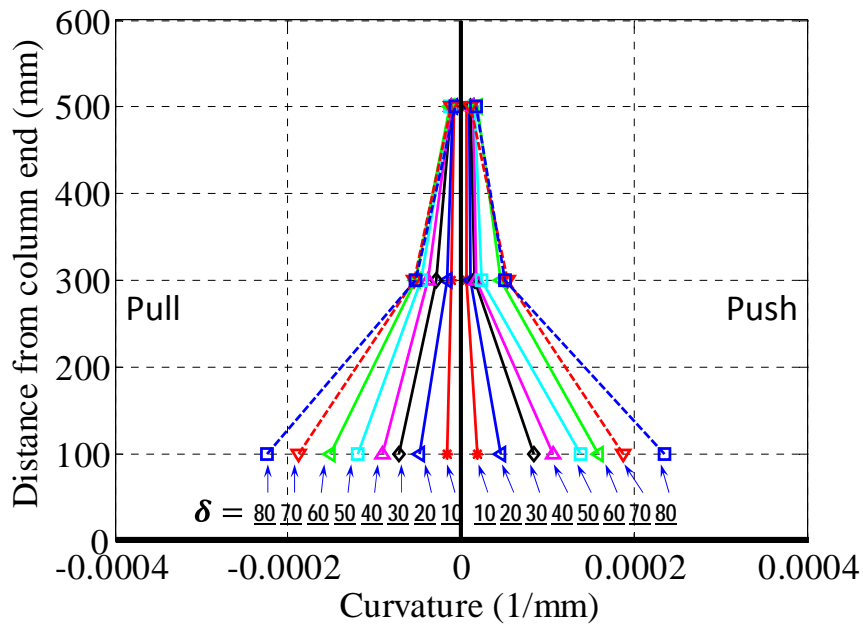
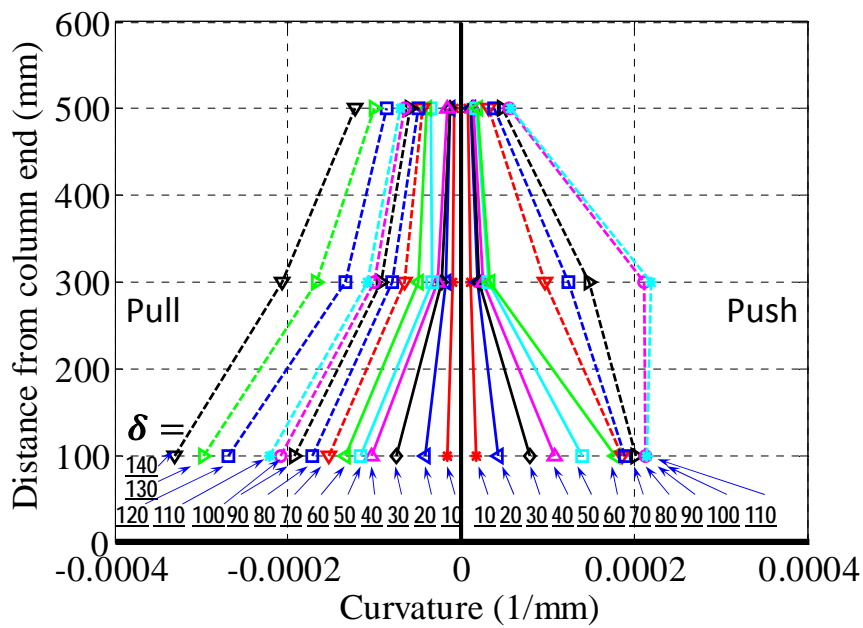


Figure 7.17: Effect of additional concrete infill in the steel tube on envelope moment-curvature curves

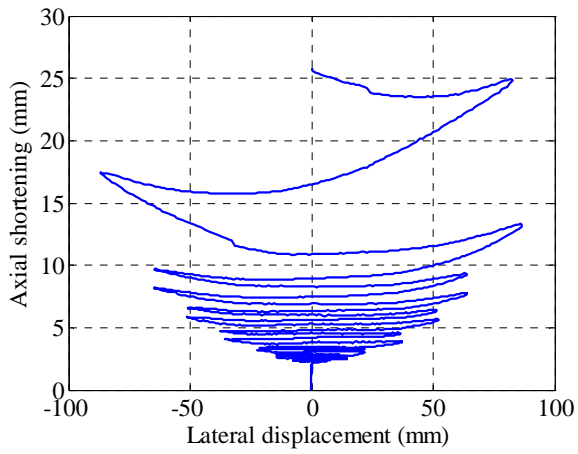


(a) Specimen D80-6-0.4

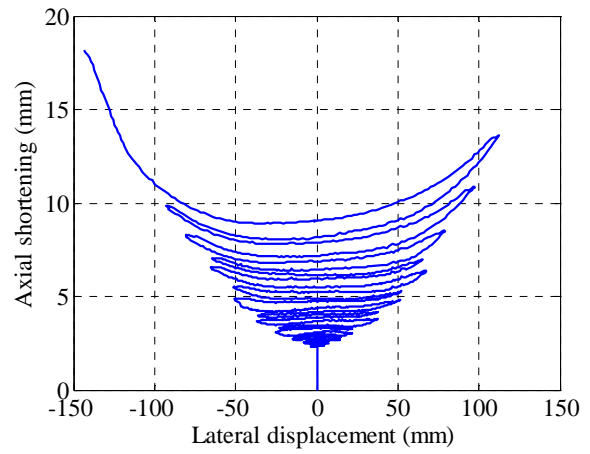


(b) Specimen D80-6-0.4-S

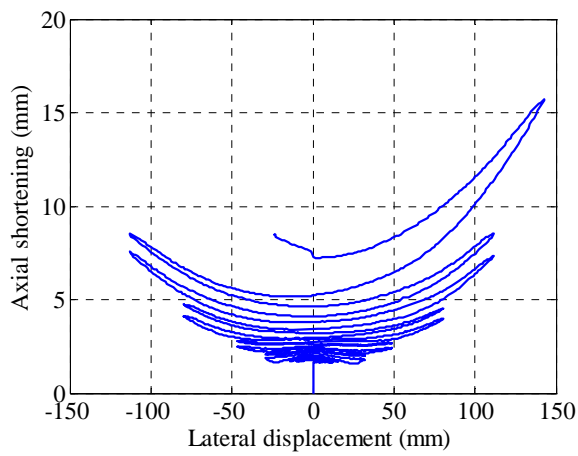
Figure 7.18: Distributions of curvature over the column height



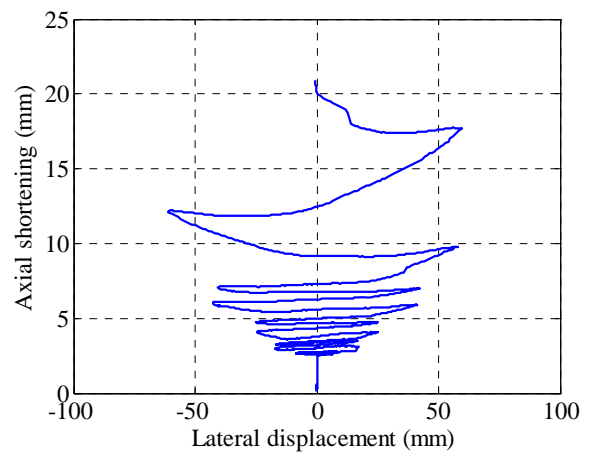
(a) Specimen D80-6-0.4



(b) Specimen D80-6-0.4-S

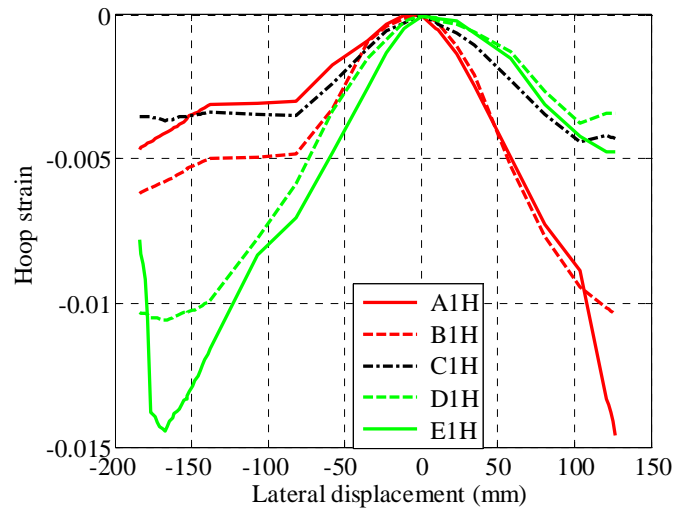


(c) Specimen D116-6-0.2

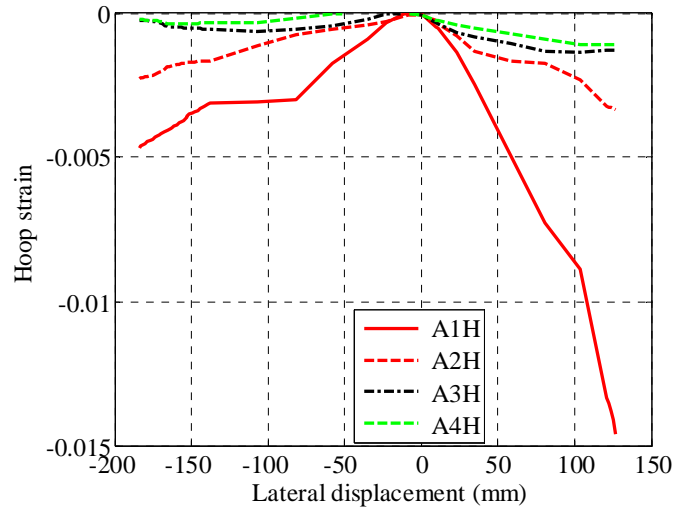


(d) Specimen D116-6-0.4

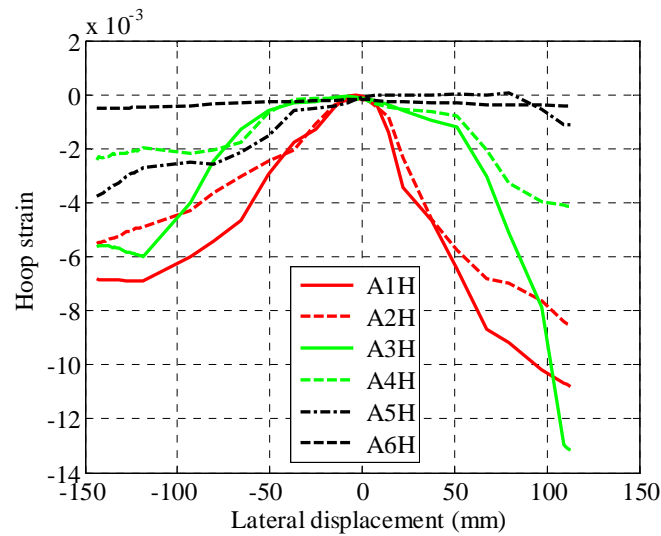
Figure 7.19: Axial shortening versus lateral displacement during the loading process



(a) Hoop strains at different circumferential positions in specimen D56-6-0.2



(b) Hoop strains at different heights in specimen D56-6-0.2



(c) Hoop strains at different heights in specimen D80-6-0.4-S

Figure 7.20: Variations of hoop strain with lateral displacement

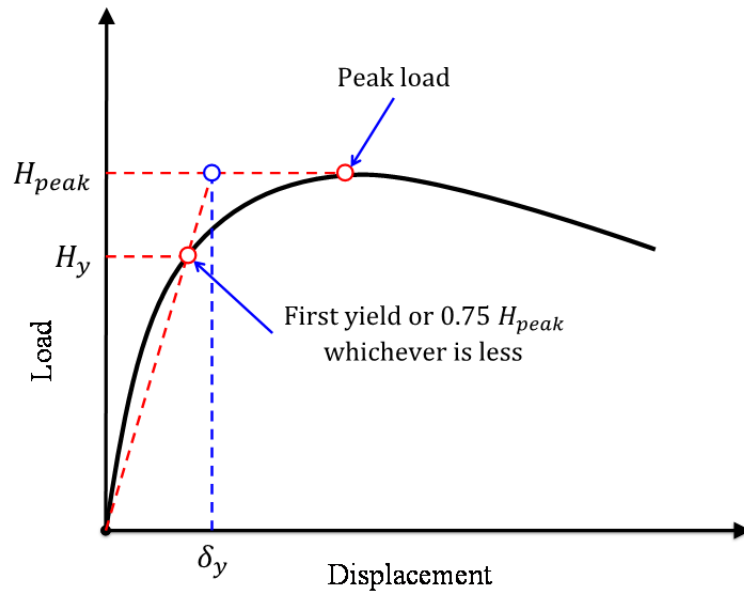


Figure 7.21: Definition of the yield displacement

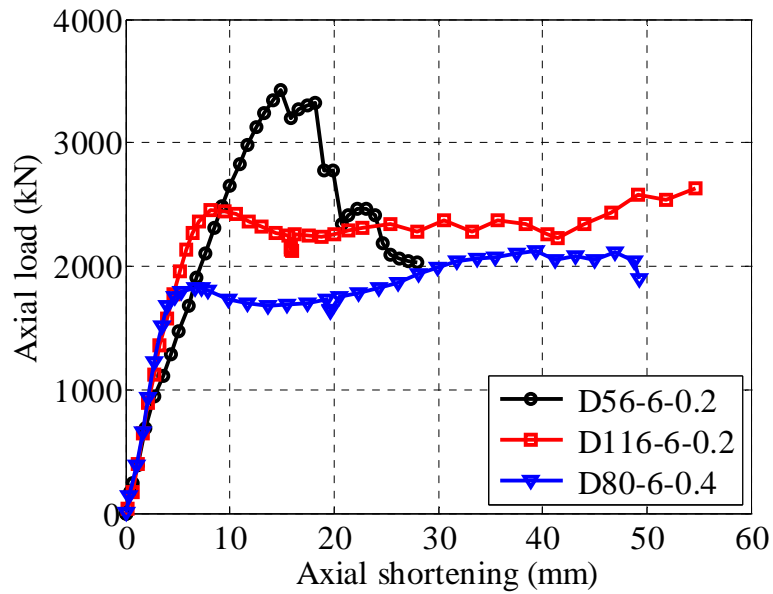


Figure 7.22: Residual axial strength after cyclic lateral loading

CHAPTER 8

NUMERICAL SIMULATION OF HYSTERETIC BEHAVIOR OF HYBRID DSTCS

8.1 INTRODUCTION

For the seismic assessment or retrofit design of existing structures, the performance-based seismic design approach has been widely accepted in structural engineering practice, in which the performance of a structure or a structural member is estimated through the performance point (ATC-40 1996) or the target displacement (FEMA-356 2000). Within this context, the open-source program “Open System for Earthquake Engineering Simulation” (OpenSees 2009), developed at the University of California, Berkeley, has drawn extensive attention as it offers a good programming platform for the numerical simulation of structures under seismic loading. As an open-source program, OpenSees allows researchers to introduce new materials, new elements and new material constitutive models based on the latest research results.

In order to investigate the seismic performance of hybrid DSTCs, an experimental study of hybrid DSTCs under combined axial compression and cyclic lateral loading was undertaken in Chapter 7. All the test specimens had a circular section with a characteristic diameter (the outer diameter of the concrete core) of 300 mm

and a height of 1350 mm. The effects of concrete strength, axial load ratio as well as FRP tube thickness were examined. The hybrid DSTC column specimens were found to possess excellent seismic resistance even when high strength concrete with a cylinder compressive strength of around 120 MPa was used. For the performance-based seismic design approach to be used in practice, a numerical column model for hybrid DSTCs under such cyclic/seismic loading is needed.

A numerical model for the seismic behavior of hybrid DSTCs is presented in this chapter. In this model, the cyclic stress-strain model for confined concrete in hybrid DSTCs (see Chapters 4 and 6) was first extended to include the tensile behavior of confined concrete. This constitutive model was then implemented into OpenSees for use in moment-curvature analysis, pushover analysis as well as hysteretic response analysis of hybrid DSTCs.

8.2 STRESS-STRAIN MODELS

8.2.1 Confined Concrete in Hybrid DSTCs

8.2.1.1 Concrete under Cyclic Compression

Yu *et al.* (2010) proposed a monotonic stress-strain model for confined concrete in hybrid DSTCs based on both experiment and finite-element results, with the important parameters (i.e. the confinement stiffness and the strain capacity of the FRP tube as well as the void ratio) duly accounted for. Readers are referred to Section 5.5 of Chapter 5 for more details of Yu *et al.*'s (2010) model. As shown in Chapters 5 and 6, the envelope curve of confined concrete in hybrid DSTCs under cyclic compression can be represented using Yu *et al.*'s (2010) stress-strain model.

Lam and Teng (2009) developed a complete set of formulas to describe the stress-strain hysteresis of FRP-confined concrete within the compressive stress-strain domain (i.e., $\varepsilon_c \geq 0$ and $\sigma_c \geq 0$). An improved cyclic stress-strain model for FRP-confined concrete, modified from Lam and Teng's (2009) model, was presented in Chapter 4. The development of this improved model was based on a critical assessment of Lam and Teng's (2009) model by making use of a large test database containing new test results on both concrete in filament-wound FRP tubes and concrete confined with an FRP wrap that have been published after Lam and Teng's (2009) study. The improved cyclic stress-strain model corrects the deficiencies of Lam and Teng's (2009) model, and can provide reasonably accurate predictions for both NSC and HSC confined with either an FRP wrap or an FRP filament-wound tube. The applicability of the cyclic stress-strain model to concrete in hybrid DSTCs was also examined in Chapter 6. The comparisons there showed that the model proposed in Chapter 4 can also provide reasonably predictions of the unloading/reloading paths of concrete in hybrid DSTCs, and was used there to predict the behavior of confined concrete in hybrid DSTCs under cyclic axial compression.

The unloading path of a cyclic axial stress-strain curve is the stress-strain path traced by the concrete as its strain reduces (Figure 8.1a). In Lam and Teng's (2009) model, this path is represented by a polynomial given by Eqs. 4.11-4.16. In these equations, two parameters are used to control the shape of the unloading path: (1) parameter η which controls the rate of change in the degree of non-linearity (or the curvature) of an unloading path with the unloading strain; (2) parameter $E_{un,0}$ which controls the slope of the unloading path at zero stress. The reloading path, which is the stress-strain path traced by the concrete as its strain increases from a starting point on an unloading path (Figure 8.1a), is represented, in typical cases, by a linear portion from the onset of reloading to a reference strain point, and a

parabolic portion from the reference strain point to the envelope returning point where the reloading path meets the envelope curve. The linear portion is described by Eqs. 4.36 and 4.37, and the parabolic portion is given by Eqs. 4.38-4.42. For more details of the unloading and reloading paths, readers are referred to Chapter 4 as well as Lam and Teng (2009).

It is important to note that the plastic strain ε_{pl} and the degree of stress deterioration after unloading/reloading cycles, which is characterised by the new stress at the reference strain point σ_{new} in Lam and Teng's (2009) model, are the two key parameters controlling the hysteretic response of confined concrete under cyclic compression. A set of equations for predicting the plastic strain and stress deterioration ratio (ratio between the new stress and the reference stress) is given in Lam and Teng (2009). These equations have been modified in Chapter 4 for applicability to both FRP-confined NSC and HSC, and have then been used in Chapter 6 for confined NSC and HSC in hybrid DSTCs. The revised equations for the plastic strain and the stress deterioration ratio (i.e., Eqs. 4.19 and 4.22 for the plastic strain and the stress deterioration ratio of envelope cycles, respectively; Eqs. 4.28 and 4.29 for the plastic strain of internal cycles, with Eq. 4.31 proposed in the present study for $\omega_{n,ful}$; Eqs. 4.32 and 4.33 for the stress deterioration ratios of internal cycles, with Eq. 4.35 proposed in the present study for $\phi_{n,ful}$) accurately predict the complete cyclic stress-strain history of confined concrete in hybrid DSTCs under axial compression. In particular, the revised set of equations allows the prediction of local unloading/reloading cycles at low amplitudes in a random event at an arbitrary point within the compressive stress-strain domain covered by the envelope curve (i.e., Eqs. 4.23-4.27 for partial unloading/reloading conditions).

8.2.1.2 Concrete under Cyclic Tension

The material model Concrete02 in OpenSees, which was proposed by Yassin (1994) for unconfined concrete, was adopted to describe the tensile behavior of confined concrete by Teng *et al.* (2010). In Yassin's (1994) model, the monotonic tensile stress-strain curve of concrete consists of a linear ascending part with the slope being equal to the modulus of elasticity of concrete in compression E_c and a linear descending part from the tensile strength point to the ultimate tensile strain point at zero stress (Figure 8.1b). The tensile strength of concrete is taken as $f_t = 0.632\sqrt{f'_{co}}$ (MPa) and the ultimate tensile strain is given by $\varepsilon_{tu} = f_t(1/E_{ts} + 1/E_c)$, where E_{ts} is the stiffness of tensile softening (taken as $0.05E_c$). In Yassin's (1994) model, unloading from any point of the monotonic tensile stress-strain curve follows a linear path toward the starting point of the tensile loading, and reloading from any point of an unloading path follows the same path back to the monotonic tensile stress-strain curve.

As pointed out by Teng *et al.* (2010), the effect of compressive deterioration on the tensile modulus of concrete was neglected in Yassin's (1994) model. As a result, the initial modulus of concrete under tension is the same as the initial compressive elastic modulus E_c (Figure 8.1b), in which the effect of compressive deterioration caused by prior loading history is not accounted for. Yassin's (1994) model was thus modified by Teng *et al.* (2010) to overcome this deficiency; the modified version has the following features: (1) the tensile modulus of concrete is assumed to be equal to E_c only when it is loaded from the origin; (2) the tensile modulus of concrete is taken to be the compressive modulus of concrete at zero stress $E_{un,0}$ as defined by Eq. 4.16 when entering the tension zone along an unloading path at a point with $\sigma_c = 0$ and $\varepsilon_c > 0$. This modification ensures the continuity of the stress-strain response across the dividing line between

compression and tension for FRP-confined concrete.

As explained in Chapter 5, the confined concrete in hybrid DSTCs has similar cyclic stress-strain behavior to that of FRP-confined concrete in solid circular sections. The equation for defining $E_{un,0}$ for FRP-confined concrete (Eq. 4.16) was also found to be accurate for confined concrete in hybrid DSTCs. Therefore, Yassin's (1994) model with the modifications introduced by Teng *et al.* (2010) is employed to describe the tensile behavior of confined concrete in the present study.

8.2.1.3 Cyclic Stress-Strain Model for Concrete

The cyclic stress-strain model for confined concrete in hybrid DSTCs, covering uniaxial cyclic behavior in both compression and tension as described above, was implemented using the “Microsoft Visual Studio” platform to produce a dynamic-link library (DLL) file. This DLL file was then implemented into OpenSees (Version 2.2.0) as a new material model named “DSTCconcrete”, which can be invoked in numerical simulations.

8.2.2 Stress-Strain Model for Steel

8.2.2.1 Strain Penetration

For a concrete column, strain penetration of longitudinal steel bars is a phenomenon associated with the gradual transfer of longitudinal bar forces to the surrounding concrete in the footing. The loaded end of an anchored bar exhibit slips at the connection interface, which is caused by the accumulative strain difference between the reinforcing bar and the concrete in the footing. It has been

well established that strain penetration occurs in the longitudinal bars of reinforced concrete columns under flexural loading (e.g. Sritharan *et al.* 2000; Zhao and Sritharan 2007). The slips of longitudinal bars caused by strain penetration lead to significant rotations at the fixed-ends of a column. Ignoring the effect of strain penetration in linear and nonlinear analyses of concrete structures leads to underestimations of deflections and member elongations, and overestimations of the stiffness, hysteretic energy dissipation capacity, strains as well as section curvature. OpenSees includes a strain penetration model named “Bond_SP01” which was originally developed by Zhao and Sritharan (2007) for the simulation of fixed-end rotation of conventional RC columns and beam-column joints. In Zhao and Sritharan’s (2007) approach, the fixed-end rotation of a column or a beam-column joint is computed from the responses of zero-length bond-slip elements added to individual longitudinal steel bars at each fixed end.

As presented in Chapter 7, the inner steel tube of the hybrid DSTC specimens was fully anchored into the column footing. The detailing of the connection was as follows (Figure 8.2): (1) the steel tube was first welded to a square steel plate (600mm long, 400mm wide and 25mm thick) at the bottom of the concrete footing; (2) an annular steel plate (with an outer diameter of 400mm, an inner diameter of 219 mm and a thickness of 25 mm) was then welded to the steel tube to support the outer FRP tube; (3) six vertical stiffeners (450mm in height, 120mm in width and 20mm in thickness) were then inserted between the square plate and the annular steel plate and welded to the two plates and the steel tube; (4) the steel reinforcement of the footing was then welded to these plates/stiffeners to form a rigid steel cage. With such a strong anchorage arrangement, it is believed that the longitudinal forces of longitudinal steel tube were transferred to the surrounding concrete in the column footing not only by the inner steel tube but also through

the six vertical stiffeners and the bottom steel plate. Due to the existence of the bottom plate and the six vertical stiffeners, the interfacial slips between the steel tube and the surrounding concrete in the footing were prohibited. It is thus believed that strain penetration was prevented in these column tests, and thus needs not be considered in numerical simulations.

8.2.2.2 Steel under Cyclic Tension and Compression

The model “ReinforcingSteel”, which is available in OpenSees, is based on the model of Chang and Mander (1994) and includes a strain hardening branch in the monotonic stress-strain curve (the backbone curve) (Figure 8.3). Heo and Kunnath (2009) suggested that the “ReinforcingSteel” model is more suitable for use in the nonlinear analysis of RC members using a fiber-based cross-section discretization. The backbone curve of the “ReinforcingSteel” model consists of a linear initial branch, a yield plateau, and a strain hardening branch. In the “ReinforcingSteel” model, modifications have been made to the original Chang and Mander (1994) model, such as the conversion from the engineering coordinate system to the natural coordinate system to allow the use of a single backbone curve for both the tensile and the compressive stress-strain responses.

The “ReinforcingSteel” model was used in the present study to simulate the inner steel tube in hybrid DSTCs. As presented in Chapter 7, the elastic modulus, yield stress and tensile strength of the inner steel tube are 200.0 GPa, 360.3 MPa and 490.6 MPa, respectively.

8.2.3 Stress-Strain Model for FRP

8.2.3.1 Properties of FRP Tubes

As mentioned in Chapter 7, the GFRP tubes were manufactured using the filament-winding process. The volume ratio and the angles of the fibers in all these tubes were 0.559 and ± 80 degrees to the longitudinal axis of the tube, respectively. Tensile split-disk tests on FRP rings were conducted following ASTM D2290-08 (2008), and compression tests on FRP rings were conducted following GB/T5350-2005 (2005). The Young's modulus and the average rupture strain in the hoop direction are 43.6 GPa, 1.55%, respectively (Figures 5.4 and 5.5); the average ultimate axial stress, axial strain and secant elastic modulus at failure in compression are 95.1MPa, 0.95% and 10.0 GPa, respectively (Figures 3.5 and 3.6).

8.2.3.2 FRP Tubes under Cyclic Tension and Compression

When the outer GFRP tube is under axial compression, the axial load carried by the outer FRP tube should not be neglected. The axial load contributed by the FRP tube may be found from the compression tests on hollow FRP tubes as mentioned above. When the axial compressive strain of an FRP tube exceeds the ultimate axial strain from the corresponding hollow FRP tube tests, it is assumed that the load resisted by the FRP tube is equal to its ultimate load due to the support from the concrete core. As the FRP tube of the hybrid DSTC specimens was placed directly on the annular steel plate (Chapter 7) and had fibers only oriented ± 80 degrees to the longitudinal axis of the tube, the GFRP tube is not expected to transfer tensile forces to the column footing. As a result, the longitudinal tensile resistance of the GFRP tube can be ignored in numerical simulations.

Based on the above considerations, the “Elastic-Perfectly Plastic Material” option as provided in OpenSees was used to represent the outer GFRP tube. The relevant material parameters are as follows: (1) the elastic modulus for the elastic–perfectly plastic material was taken to be the secant modulus for the material at peak stress obtained from axial compression tests on hollow GFRP tubes, and the value is 10.0 GPa (Figure 3.6); (2) the strain at which the material reaches the plastic state in compression is 0.95% based on axial compression tests on hollow GFRP tubes; (3) the strain at which the material reaches the plastic state in tension is 0.0 as the GFRP tube is assumed to resist no longitudinal tension.

8.3 NUMERICAL SIMULATIONS

8.3.1 Remarks on the Experimental Study

As presented in Chapter 7, a systematic experimental study on hybrid DSTCs subjected to cyclic lateral loading in combination with a constant axial compressive force was undertaken as part of the present PhD research program. Details the column specimens can be found in Tables 7.1 and 7.3. All these columns were tested in single-curvature bending (Figure 7.6).

A large loading frame (i.e. the Computer-Electro-Hydraulic Servo-Controlled Multi-Purpose Testing System) was used to test all the column specimens. It should be noted that the vertical actuator could move synchronously with the column head during the lateral cyclic loading, which ensured that the axial load was always applied vertically to the column head. In some other similar experimental studies (e.g. Haroun *et al.* 2003; Saadatmanesh *et al.* 1996), the axial compression load was applied by pre-tensioned steel bars, in which case the axial

compression load would be at an angle of inclination from the vertical direction due to the lateral displacement of the column head. This inclination leads to a horizontal component of the axial load in the opposite direction of the lateral load. The present test framework is more advantageous than these other systems, and makes subsequent numerical simulations simpler.

In the numerical simulations, the columns were subjected to lateral displacements under a constant axial compression load which was always in the vertical direction. The horizontal friction force of the testing system was excluded from the lateral load as explained in Chapter 7.

8.3.2 Moment-Curvature Analysis

Moment-curvature analysis was first conducted for all hybrid DSTCs tested under cyclic lateral loading using a “ZeroLength” element available in OpenSees with the fiber discretization of cross section. The “ZeroLength” element is defined by two nodes at the same location. These two nodes are connected by uniaxial materials (i.e., concrete, steel and FRP in the present study) to represent the force-deformation relationship for the element. The way of discretization of the column section is shown in Figure 8.4. For all column specimens except D80-6-0.4-S, eight radial and eighteen tangential divisions were employed for the annular concrete section; two radial and eighteen tangential divisions were employed for the GFRP tube and the inner steel tube (Figure 8.4a). For specimen D80-6-0.4-S, as the inner steel tube was filled with concrete for the lower 320 mm of the column height, the concrete in the steel tube was discretized into eight radial and eighteen tangential divisions (Figure 8.4b). This level of discretization was found to lead to sufficiently accurate results based on a convergence study. The “DSTCconcrete” model for the confined concrete in hybrid DSTCs, the

“Reinforcing Steel” model for the inner steel tube and the “Elastic-Perfectly Plastic Material” model for the FRP tube were used to predict the moment curvature relationship of these hybrid DSTCs.

The experimental moment-curvature curves are presented in Chapter 7. The moment is that of the section at 100 mm from the column end with the $P-\Delta$ effect taken into account; the curvature is the average value over the lowest 200 mm of the column calculated from the readings of LVDTs (see section 7.3.4). The positive direction refers to the positive lateral load direction as defined in Chapter 7. The moment-curvature envelope curves for both directions are shown in Figure 8.5. Only the data points corresponding to the envelope curves are shown in the figure.

The predicted moment-curvature curves are compared with corresponding experimental moment-curvature curves in Figure 8.5. The numerical model can generally capture the shape of the experimental moment-curvature curves, providing reasonably accurate but somewhat conservative predictions. The conservativeness of the numerical model is inherently due to Yu *et al.*'s (2010) monotonic stress-strain model for hybrid DSTCs (see Chapter 6), which was employed to predict the envelope curve of confined concrete in hybrid DSTCs under cyclic axial compression. Nevertheless, the numerical model can capture the moment-curvature relationship of hybrid DSTCs with reasonable accuracy, indicating that the material model “DSTCconcrete” is sufficiently accurate and safe for practical purposes.

8.3.3 Pushover Analysis

The “NonlinearBeamColumn” element available in OpenSees, which is a

force-based nonlinear beam-column element and considers both geometrical nonlinearity and the spread of plasticity, was used in the present numerical simulations. All the test columns were modelled longitudinally with four elements as shown in Figure 8.6. Five Gauss-Lobatto integration points are defined along each element. For all specimens except for D80-6-0.4-S, the fiber discretization of cross section is the same for all elements as shown in Figure 8.6a: eight radial and eighteen tangential divisions were employed for the annular concrete section; two radial and eighteen tangential divisions were employed for both the GFRP tube and the inner steel tube. For specimens D80-6-0.4-S, the inner steel tube was filled with concrete for the lower 320 mm of the column height; so for the first beam-column element (i.e. near the footing), the concrete in the steel tube was also discretized into eight radial and eighteen tangential divisions (Figure 8.6b). The number of elements, the number of integration points and the level of discretization were found to lead to sufficiently accurate results based on a convergence study. Similar to the moment-curvature as discussed above, the “DSTCconcrete” material for concrete, the “Reinforcing Steel” material for steel and the “Elastic-Perfectly Plastic Material” for FRP tube were used in the numerical simulations.

Monotonic pushover analysis was conducted in a displacement control mode. As presented in Chapter 7, the tests of the hybrid DSTC specimens were stopped when the lateral load resistance dropped substantially (i.e., the lateral load capacity of the last loading cycle was substantially smaller than the previous loading cycle). As observed in the tests, for the final stage of cyclic loading, both the GFRP tube and the concrete suffered severe damage that was concentrated near the column end; severe buckling of the inner steel tube was also observed after the removal of the FRP tube and the concrete; the plain section assumption is believed to be no longer valid in the severely damaged zone. Given this

consideration, the monotonic pushover analysis was terminated at the displacement of the penultimate loading cycle for each column.

The lateral load-lateral displacement envelope curves from tests are shown in Figure 8.7 together with the curves from numerical simulation. It is clear that the proposed numerical model can yield reasonably accurate results for all hybrid DSTCs, regardless of the type of concrete used (i.e. NSC or HSC).

8.3.4 Hysteretic Behavior Analysis

This numerical model was also used to simulate the hysteretic behavior of the hybrid DSTC specimens. The numerical simulation of a given column was terminated at the same lateral displacement as the monotonic pushover analysis (i.e., terminated at the penultimate cyclic loading cycle for each column). In Figure 8.8, the lateral load-lateral displacement curves of all specimens are shown together with the curves from numerical simulation. Again, it is clear that the proposed numerical model can yield reasonably accurate results for all hybrid DSTCs regardless of the type of concrete used (i.e. NSC or HSC).

8.4 CONCLUSIONS

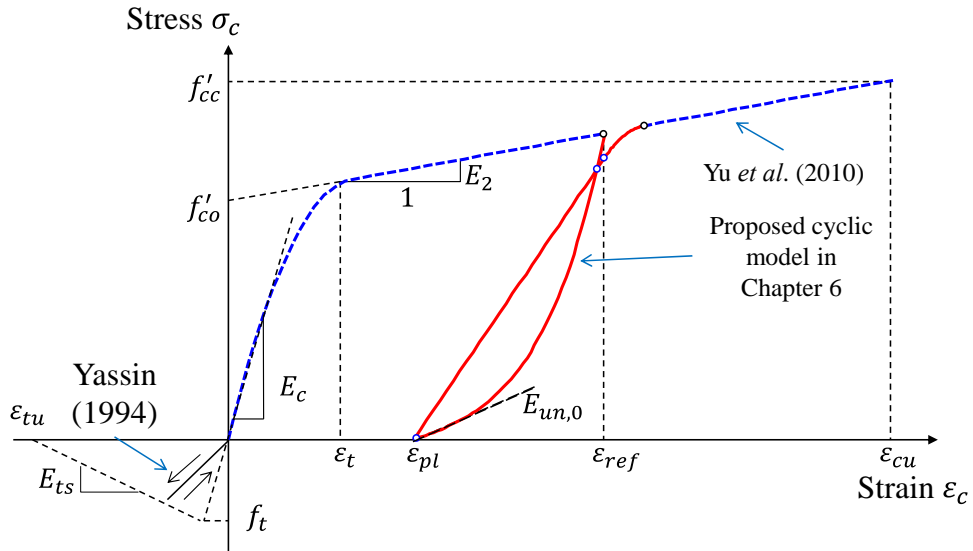
A numerical column model was developed for simulating the seismic behavior of hybrid DSTCs. This numerical model was implemented into OpenSees using its force-based “NonLinearBeamColumn” element that considers both geometric nonlinearity and material nonlinearity. The key to this numerical column model is an accurate stress-strain model for the confined concrete in hybrid DSTCs subjected to cyclic axial compression. For this purpose, the cyclic stress-strain model for confined concrete in compression in hybrid DSTCs developed in the

earlier parts of the present PhD research program was extended to include cyclic tensile behavior. The resulting stress-strain model was implemented into OpenSees as the “DSTCconcrete” material model. Comparisons between test results and predictions of the proposed numerical model showed that the numerical model can generally yield reasonably accurate but conservative predictions. The numerical column model is thus sufficiently accurate for use in the seismic performance prediction of hybrid DSTCs.

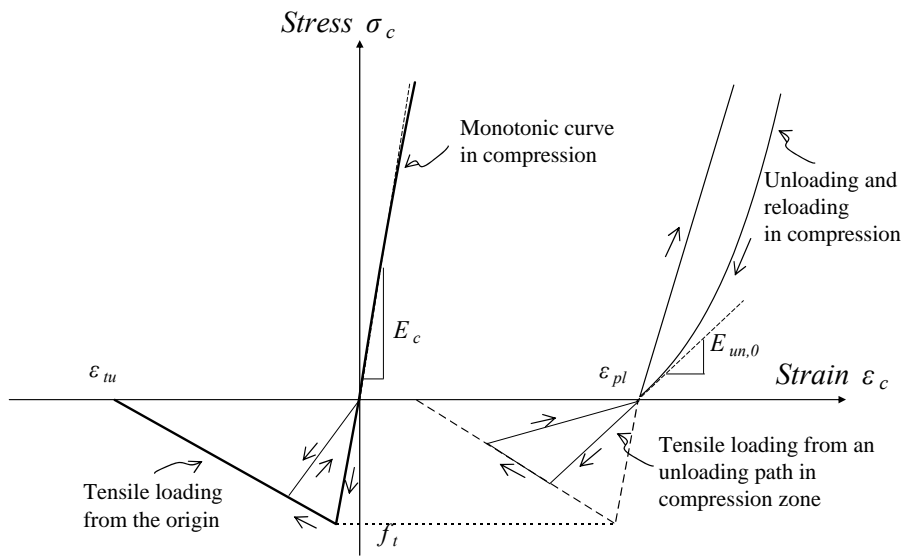
8.5 REFERENCES

- ASTM D2290-08. (2008). *Standard Test Method for Apparent Hoop Tensile Strength of Plastic or Reinforced Plastic Pipe by Split Disk Method*, American Society for Testing and Materials (ASTM), Philadelphia, USA.
- ATC-40. (1996). *Seismic Evaluation and Retrofit of Concrete Buildings, Volume 1*, Report No. SSC 96-01, Seismic Safety Commission, State of California, USA.
- Chang, G. and Mander, J. (1994). *Seismic Energy Based Fatigue Damage Analysis of Bridge Columns: Part I – Evaluation of Seismic Capacity*, NCEER Technical Report 94-0006.
- FEMA 440. (2005). *Improvement of Nonlinear Static Seismic Analysis Procedures*, Report No. FEMA 440, Federal Emergency Management Agency, Washington, DC, USA.
- GB/T5350-2005. (2005). *Fiber-Reinforced Thermosetting Plastic Composites Pipe: Determination for Longitudinal Compressive Properties*, The Standards Press of China.
- Heo, Y.A. and Kunnath, S.K. (2009). “Sensitivity to constitutive modeling in fiber-based discretization of reinforced concrete members for performance-based seismic evaluation”, *Advances in Structural Engineering*, 12(1), 37-51.
- Lam, L. and Teng, J. G. (2009). “Stress-strain model for FRP-confined concrete under cyclic axial compression”, *Engineering Structures*, 31(2), 308-321.
- OpenSees. (2009). *Open System for Earthquake Engineering Simulation*. Pacific Earthquake Engineering Research Center, University of California, Berkeley, <http://opensees.berkeley.edu>.
- Sritharan, S., Priestley, N. and Seible, F. (2000). “Nonlinear finite element analyses of concrete bridge joint systems subjected to seismic actions”, *Finite Elements in Analysis and Design*, 36, 215-233.

- Teng, J. G., Lu, J. Y., Lam, L. and Xiao, Q. G. (2011). “Numerical simulation of FRP-jacketed RC columns subjected to cyclic loading”, *Advances in FRP Composites in Civil Engineering*, Springer Berlin Heidelberg, 820-823.
- Yassin, M.H.M. (1994). *Nonlinear Analysis of Prestressed Concrete Structures under Monotonic and Cyclic Loads*, PhD thesis, University of California, Berkeley, CA, USA.
- Yu, T., Teng, J.G. and Wong, Y.L. (2010c). “Stress-strain behavior of concrete in hybrid double-skin tubular columns”, *Journal of Structural Engineering*, ASCE, 136(4), 379-389.
- Zhao, J. and Sritharan, S. (2007). “Modeling of strain penetration effects in fiber-based analysis of reinforced concrete structures”, *ACI Structural Journal*, 104(2), 133-141.



(a) Stress-strain model for confined concrete in hybrid DSTCs



(b) Stress-strain model for FRP-confined concrete in tension

(from Teng *et al.* 2010)

Figure 8.1: Stress-strain model for confined concrete in hybrid DSTCs

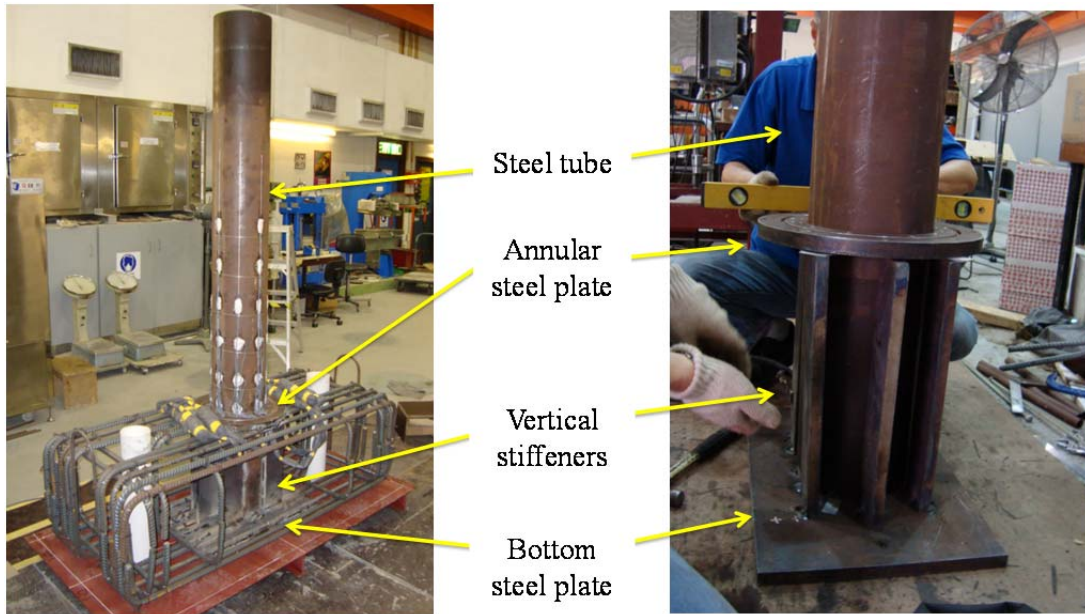


Figure 8.2: The connection detailing of the inner steel tube

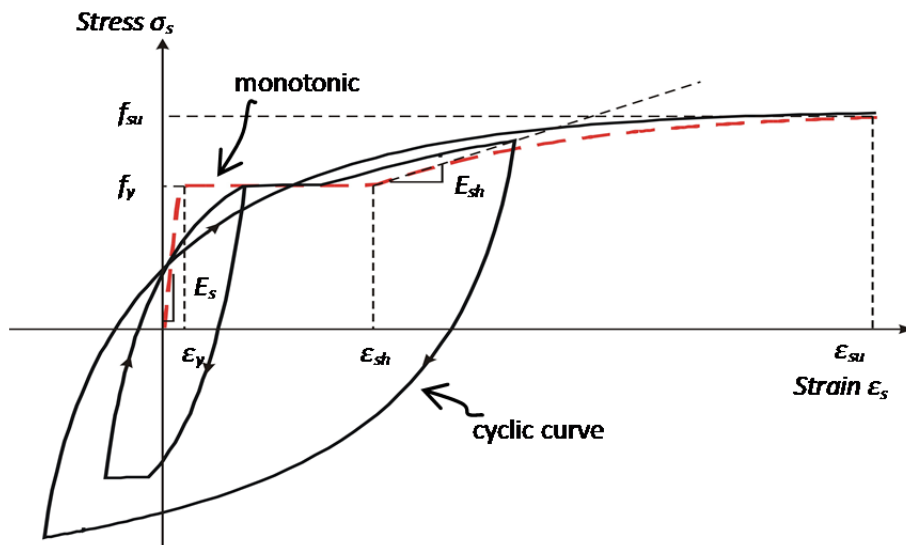
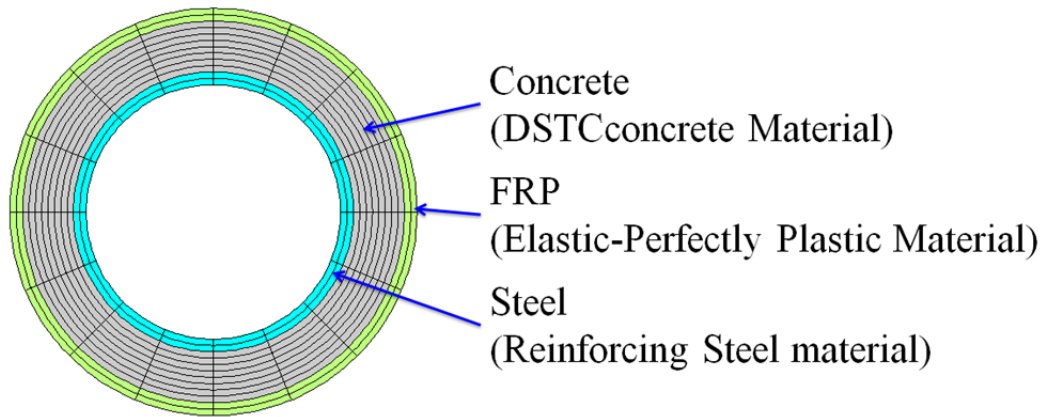
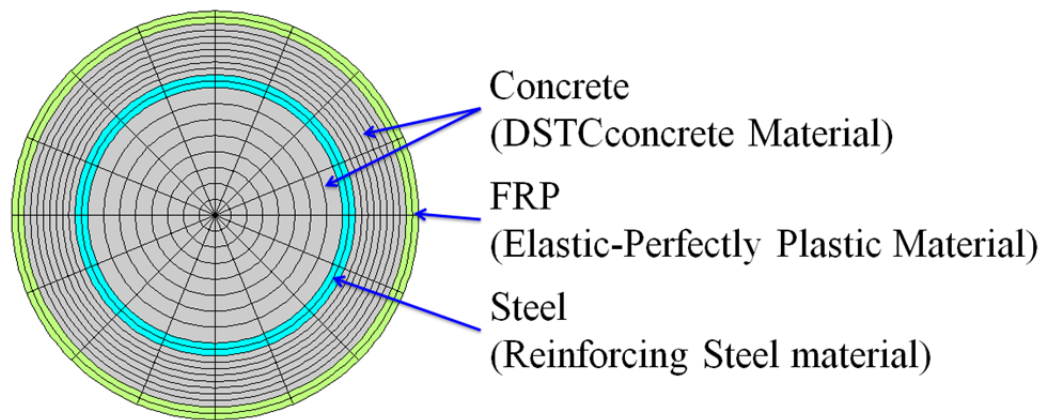


Figure 8.3: Stress-strain model for reinforcing steel

(from Teng *et al.* 2010)



(a) All specimens except of specimen D80-6-0.4-S



(b) Specimen D80-6-0.4-S

Figure 8.4: The discretization of the column section

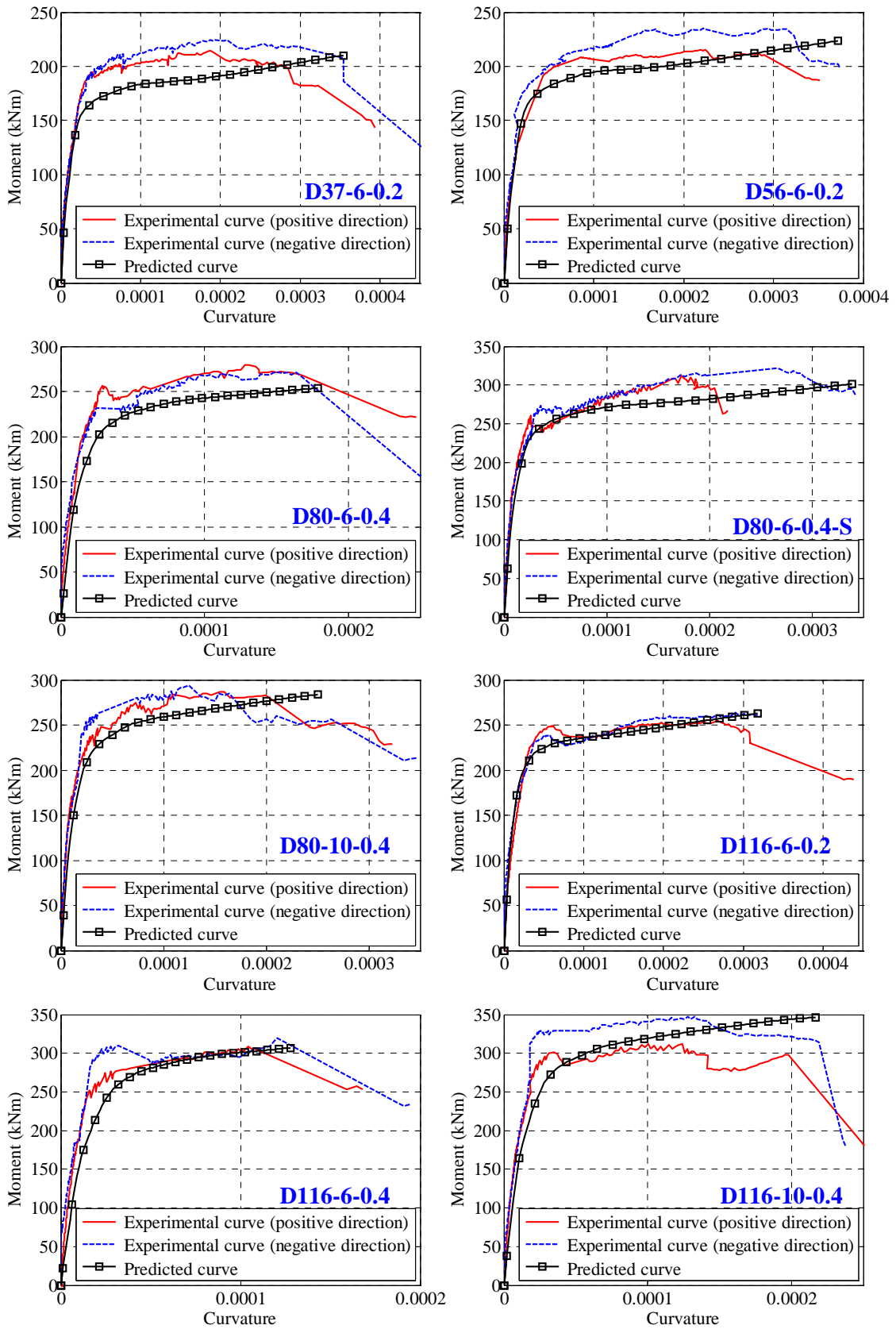
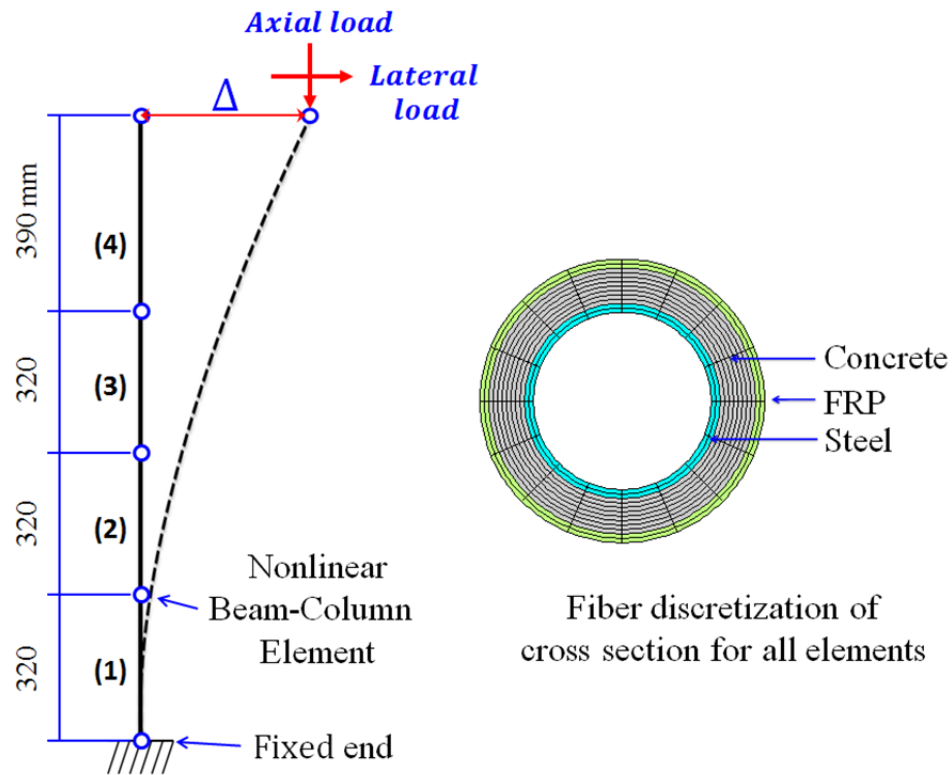
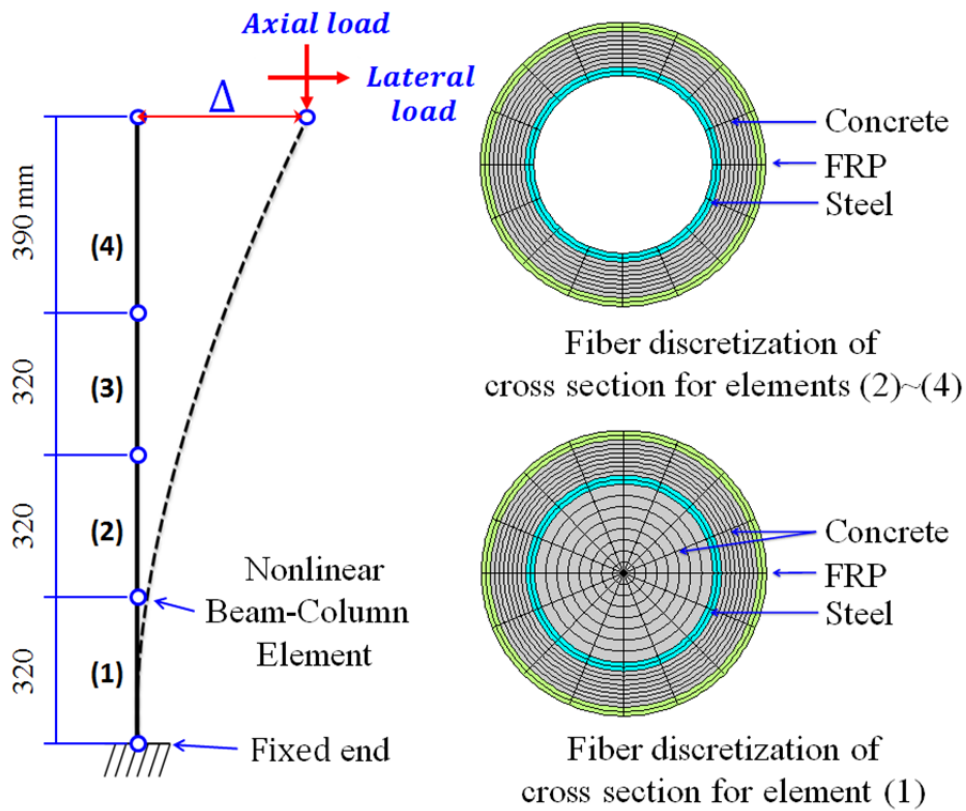


Figure 8.5: Moment-curvature analysis



(a) Specimens except of specimen D80-6-0.4-S



(b) Specimen D80-6-0.4-S

Figure 8.6: Numerical models for hybrid DSTCs

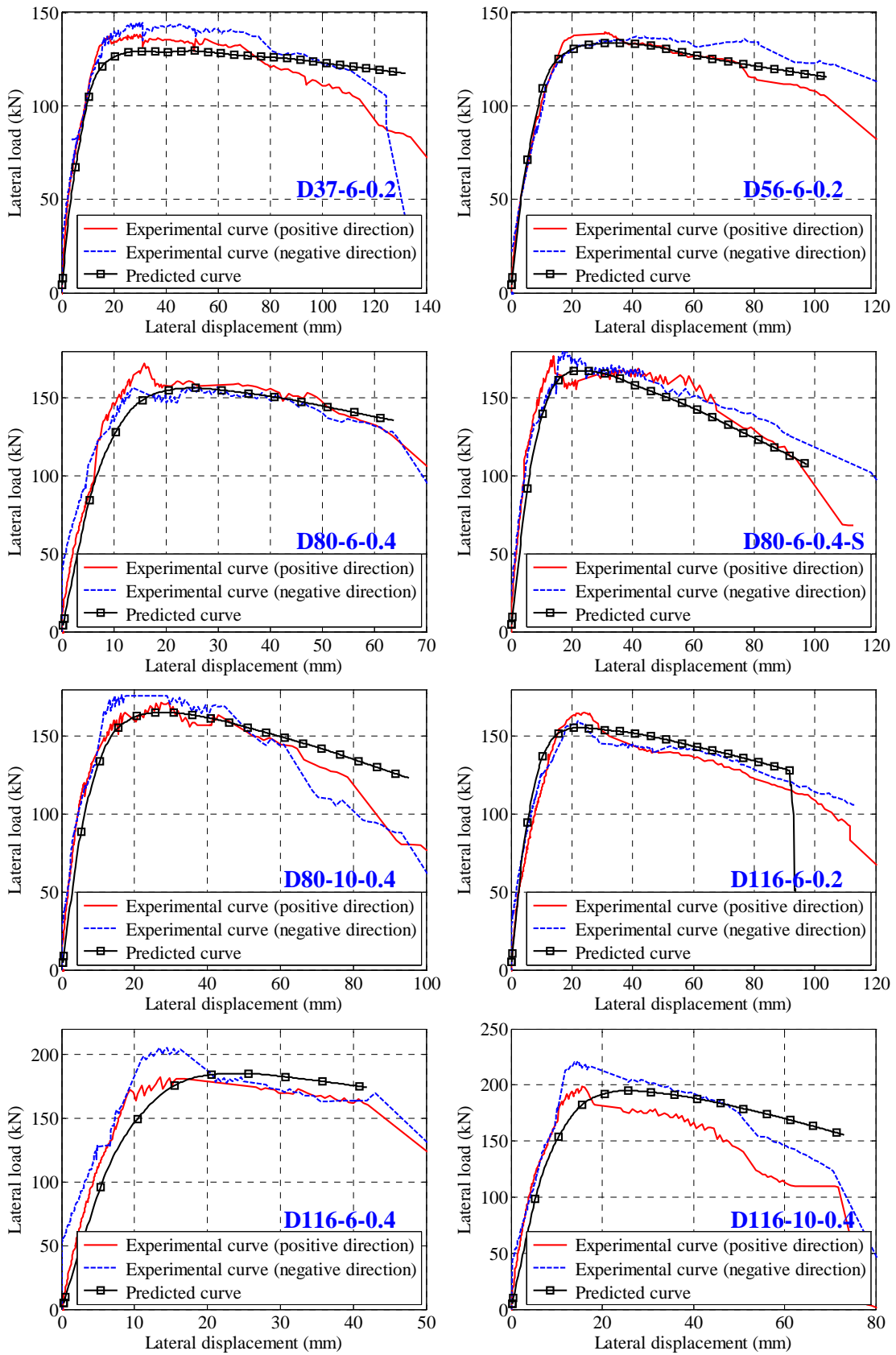
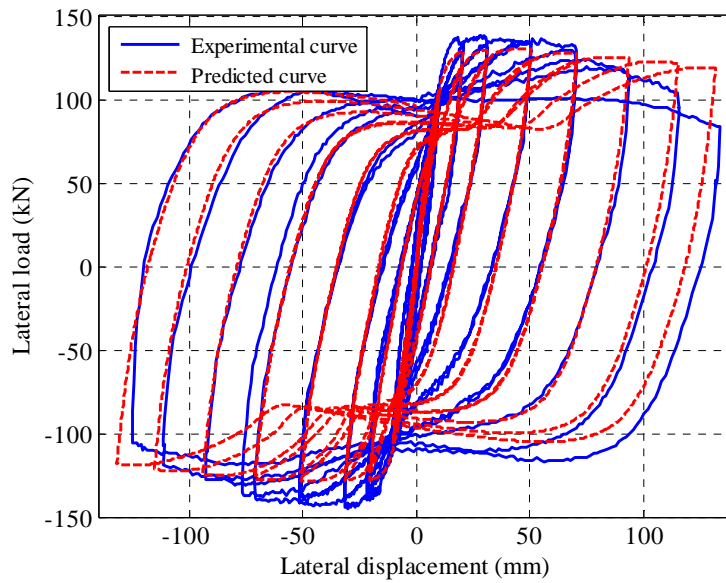
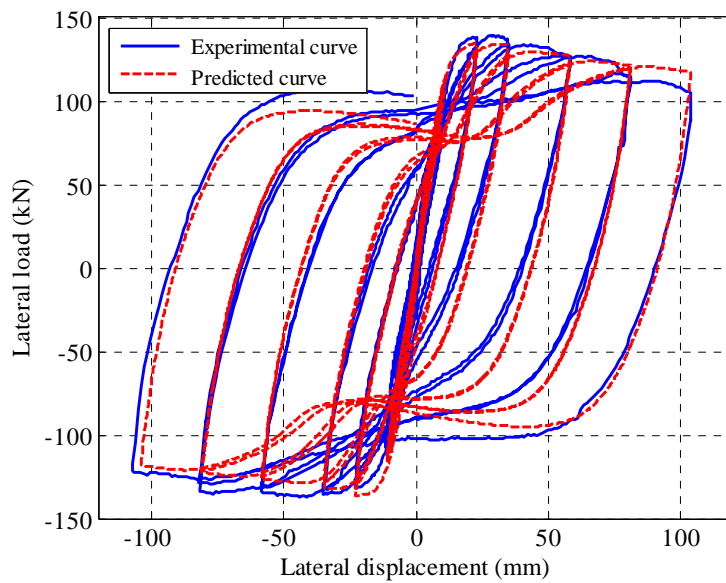


Figure 8.5: Pushover analysis

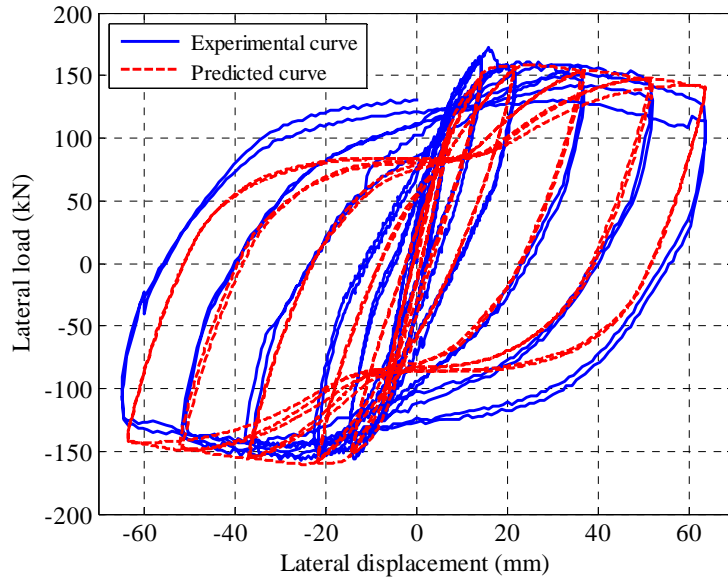


(a) D37-6-0.2

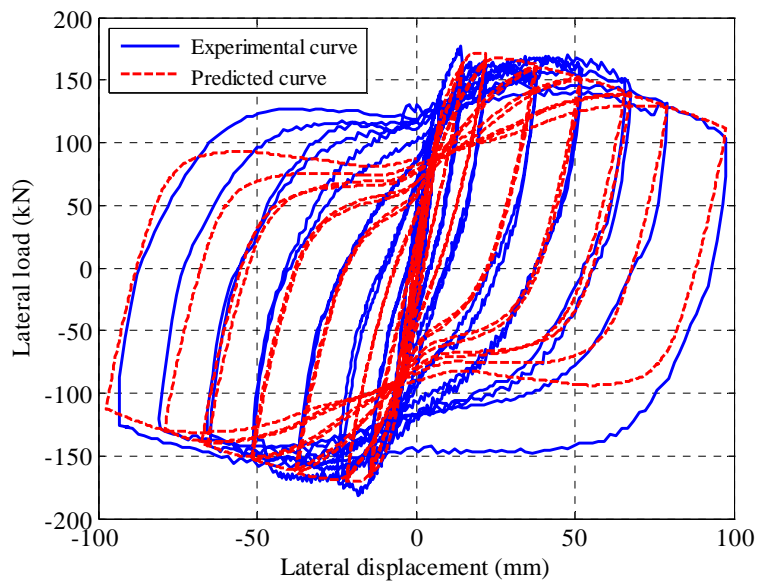


(b) D56-6-0.2

Figure 8.8: Hysteretic behavior analysis

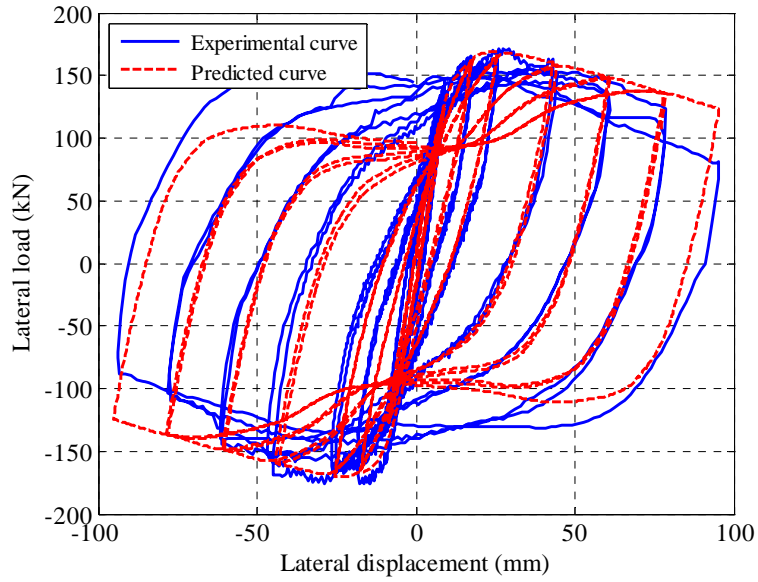


(c) D80-6-0.4

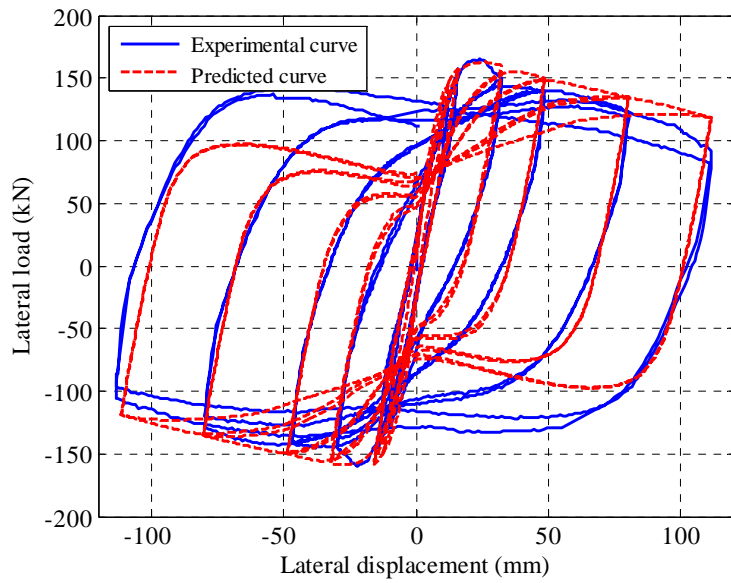


(d) D80-6-0.4-S

Figure 8.8: Hysteretic behavior analysis (continued)

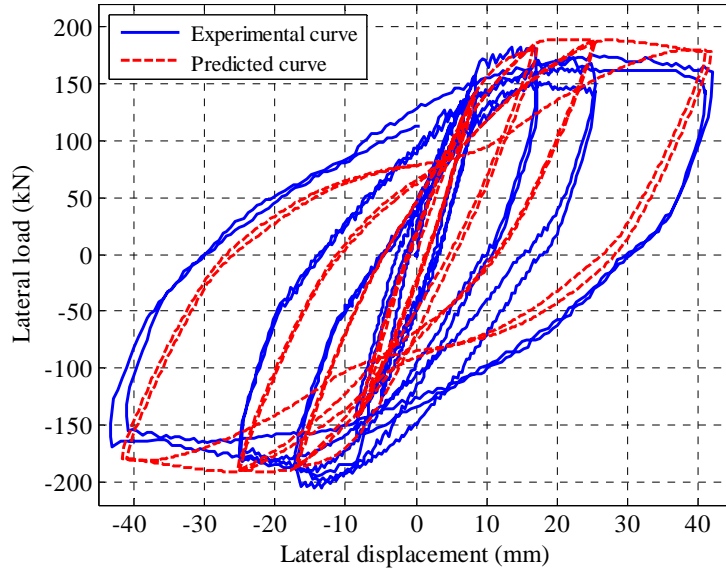


(e) D80-10-0.4

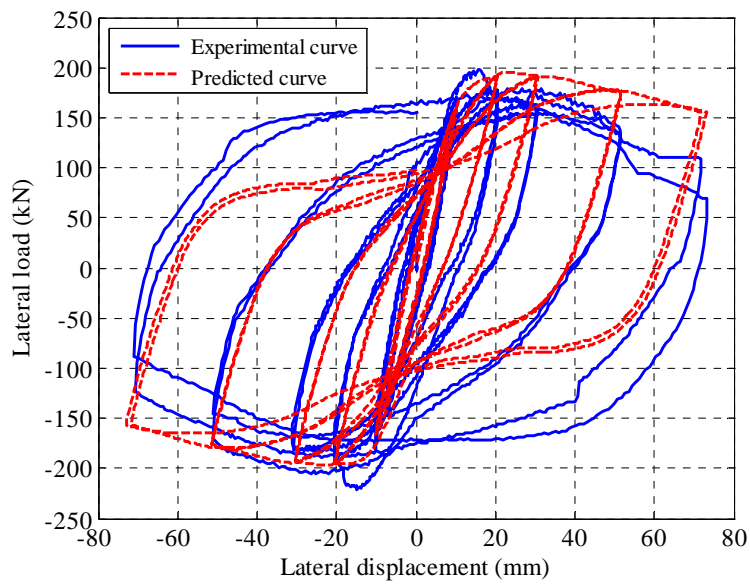


(f) D116-6-0.2

Figure 8.8: Hysteretic behavior analysis (continued)



(g) D116-6-0.4



(h) D116-10-0.4

Figure 8.8: Hysteretic behavior analysis (continued)

CHAPTER 9

CONCLUSIONS

9.1 INTRODUCTION

Hybrid FRP-concrete-steel double-skin tubular columns (hybrid DSTCs) are a new form of hybrid columns proposed by Prof. J.G. Teng of The Hong Kong Polytechnic University. This new form of hybrid columns consists of a layer of concrete sandwiched between an outer tube made of FRP (fiber-reinforced polymer) and an inner tube made of steel. In a hybrid DSTC, the FRP tube, containing fibers oriented close to the hoop direction, offers mechanical resistance primarily in the hoop direction to confine the concrete and to enhance the shear resistance of the column; the steel tube acts as the main longitudinal reinforcement and prevents the concrete from inward spalling. Hybrid DSTCs may be constructed in-situ or precast, with the two tubes serving as the stay-in-place form. The three constituent materials are combined in an optimal manner to achieve excellent ductility and hence seismic behavior, excellent durability, ease for construction as well as reduced self-weight.

This thesis has presented the results of a systematic research program on the behavior of hybrid DSTCs under static and cyclic loading, and represents a major step forward by extending the existing research on several fronts, including: (1) the use of high strength concrete (HSC) in hybrid DSTCs; (2) the use of

filament-wound FRP tubes as the confining material; (3) the effect of column size; (4) the behavior of hybrid DSTCs under cyclic axial compression; as well as (5) the behavior of hybrid DSTCs under combined axial compression and cyclic lateral loading.

9.2 CONCRETE-FILLED FRP TUBES UNDER CYCLIC AXIAL COMPRESSION

Following the introductory and the literature chapters of the thesis, Chapters 3 and 4 presented the first part of the research program which was concerned with the experimental behavior and theoretical modeling of concrete filled FRP tubes (CFFTs) under cyclic axial compression. This part of the study was motivated by the need to understand the cyclic stress-strain behavior of confined normal strength concrete (NSC) and HSC in hybrid DSTCs.

Chapter 3 presented an experimental study on the cyclic axial behavior of CFFTs with a filament-wound FRP tube, where the strength of concrete (i.e. 54.1 MPa ~ 104.4 MPa) was a key variable. All specimens had a characteristic diameter of 200 mm (outer diameter of the concrete core) and a height of 400 mm. The test results were compared with Teng *et al.*'s (2009) monotonic stress-strain model and Lam and Teng's (2009) cyclic stress-strain model. The experimental results and discussions allowed the following conclusions to be drawn:

- (1) The rupture of fibers in a filament-wound FRP tube, starting from the outermost ply, is a progressive process which is different from the failure of concrete confined with an FRP wrap;
- (2) The cyclic axial stress-strain behavior of concrete in CFFTs is generally similar to that of concrete confined with an FRP wrap;

- (3) Teng *et al.*'s (2009) monotonic stress-strain model is capable of providing accurate predictions for HSC in CFFTs, given that the FRP tube has a sufficient circumferential stiffness to ensure a monotonically ascending axial stress-strain curve; and
- (4) Lam and Teng's (2009) cyclic stress-strain model is applicable to NSC in CFFTs, but is not sufficiently accurate for HSC in CFFTs.

Although Lam and Teng's (2009) cyclic stress-strain model was developed on the basis of a relatively large database, several issues could not be readily resolved using the test database available to them at that time. Chapter 4 thus presented a critical assessment of Lam and Teng's (2009) model against the new test results of cyclically loaded CFFTs presented in Chapter 3 as well as those from studies on FRP-confined concrete with an FRP wrap published after Lam and Teng's (2009) study. The assessment revealed that:

- (1) The degree of non-linearity of unloading paths of FRP-confined HSC is different from that of FRP-confined NSC. Lam and Teng's (2009) model cannot provide accurate predictions for the unloading paths of FRP-confined HSC;
- (2) The relationship between the plastic strain $\varepsilon_{pl,1}$ and the envelope unloading strain $\varepsilon_{un,env}$ does not seem to be significantly affected by the unconfined concrete strength. Lam and Teng's (2009) equations, which take the unconfined concrete strength as a key parameter, fail to predict $\varepsilon_{pl,1}$ closely for FRP-confined HSC;
- (3) Lam and Teng's (2009) model is inaccurate in predicting the effect of repeated loading cycles (i.e. $\omega_{n,ful}$ and $\phi_{n,ful}$); and
- (4) The proposed cyclic stress-strain model corrects the above deficiencies of Lam and Teng's (2009) model, and can provide reasonably accurate

predictions for both NSC and HSC confined with either an FRP wrap or an FRP filament-wound tube.

9.3 HYBRID DSTCS UNDER MONOTONIC OR CYCLIC AXIAL COMPRESSION

Chapters 5 and 6 presented the second part of the research program which was concerned with the behavior of hybrid DSTCs filled with NSC/HSC subjected to monotonic/cyclic axial compression. Previous studies on the axial compressive behavior of hybrid DSTCs were generally limited to small-scale specimens (i.e. with a diameter < 200 mm) filled with NSC and confined with a wet lay-up FRP tube. The present experimental investigation was thus focused on three issues: (1) the effect of using HSC; (2) the effect of using a filament-wound FRP tube; and (3) the effect of specimen size. The concrete strength used in these hybrid DSTCs were 40.9 MPa ~ 104.6 MPa. Large-scale specimens (with a characteristic diameter of 300 mm and a height of 600 mm) were included in the experimental study. The majority of the hybrid DSTC specimens were designed with a realistically large void ratio (i.e. 0.73 or 0.795).

Chapter 5 presented the results from an experimental study on hybrid DSTCs under monotonic axial compression, which allowed the following conclusions to be drawn:

- (1) Hybrid DSTCs process excellent ductility even when high strength concrete is used;
- (2) The localization of damage (i.e. concrete crushing, steel buckling and/or FRP rupture), which occurred in all the specimens, appeared to be more pronounced for specimens with a higher concrete strength and/or a thinner

FRP tube;

- (3) Three types of axial stress-strain curves of concrete in hybrid DSTCs were found in the present study: (a) axial stress-strain curves with a bilinear ascending shape; (b) axial stress-strain curves with a stress fluctuation; (c) axial stress-strain curve with a sudden stress drop;
- (4) The sudden stress drop, more pronounced in hybrid DSTCs with a higher concrete strength and/or a weaker FRP tube, was found to be initiated by the local damage of concrete, which led to highly non-uniform deformation over the cross-section of concrete;
- (5) Yu *et al.*'s (2010) model is capable of providing reasonably accurate predictions for specimens with a bilinear ascending stress-strain curve and specimens with slight fluctuations in the axial stress, but it overestimates the results of specimens with a sudden load drop.

Chapter 6 first presented the results from an experimental study on hybrid DSTCs under cyclic axial compression. The experimental results and discussions in Chapter 6 allow the following conclusions to be drawn:

- (1) The envelope curve of the concrete in a cyclically loaded hybrid DSTC is almost the same as the stress-strain curve of the concrete in the corresponding monotonically loaded specimen;
- (2) The hoop rupture strain (either $\varepsilon_{h,rupt1}$ or $\varepsilon_{h,rupt2}$) of a monotonically loaded specimen is generally larger than that of the corresponding cyclically loaded specimen; and
- (3) The unloading/reloading behavior of concrete in cyclically loaded hybrid DSTCs is generally similar to that of the concrete in FRP-confined solid columns.

Chapter 6 also presented a comparison of the unloading/reloading paths between the test results and the predictions of the cyclic stress-strain model proposed in Chapter 4 for FRP-confined concrete. The comparison showed that the model proposed in Chapter 4 can also provide reasonably accurate predictions for the unloading/reloading paths of the concrete in hybrid DSTCs, provided that the envelope stress-strain curve is accurately defined.

9.4 HYBRID DSTCS UNDER COMBINED AXIAL COMPRESSION AND CYCLIC LATERAL LOADING

Chapters 7 and 8 presented the last part of the research program which was focused on the seismic behavior of hybrid DSTCs filled with NSC/HSC.

In the experimental study presented in Chapter 7, eight hybrid DSTCs were tested under combined axial compression and cyclic lateral loading. The test columns had a relatively large column section (i.e. with a section diameter of 300 mm) and a realistically large void ratio (i.e. 0.73) to achieve close representation of real column behavior. All these specimens had a circular section with a characteristic diameter of 300 mm and a void ratio of 0.73. The height was 1350 mm from the point of lateral loading to the top of the stiff RC column footing, leading to a shear span ratio of 4.5. The test results provide valuable data needed for the verification of theoretical models for the seismic behavior of hybrid DSTCs, particularly when they are filled with HSC. The test results and discussions presented in this chapter also allow the following conclusions to be drawn:

- (1) Hybrid DSTCs possess excellent ductility and seismic resistance even when high strength concrete with a cylinder compressive strength of around 120 MPa is used;

- (2) Hybrid DSTCs with a higher concrete strength generally have a higher moment capacity but a smaller deformation capacity;
- (3) A thicker FRP tube leads to a slightly larger moment capacity and better ductility for hybrid DSTCs;
- (4) The axial load ratio has a significant effect on both the lateral load capacity and the ductility of hybrid DSTCs;
- (5) Column damage is concentrated in a small plastic hinge region near the column end, and the height of this region is similar to the column diameter;
- (6) The performance of hybrid DSTCs can be enhanced by partially filling the inner steel tube with concrete near the column end.

In Chapter 8, a numerical model employing Yu *et al.*'s (2010) stress-strain model in conjunction with equations of unloading/reloading paths proposed in Chapter 4 is presented for simulating the behavior of hybrid DSTCs under combined axial compression and cyclic lateral loading. This numerical model was implemented into "Open System for Earthquake Engineering Simulation" (OpenSees 2009) using its force-based "NonLinearBeamColumn" element considering both geometric nonlinearity and material nonlinearity. The following conclusions were reached based on the results of numerical simulations:

- (1) The "DSTCconcrete" material, which was developed based on the current understanding of concrete in hybrid DSTCs subjected to monotonic/cyclic axial compression, is capable of predicting the cyclic lateral/seismic behavior of hybrid DSTCs, demonstrating the success of the approach;
- (2) The comparisons between the present numerical simulation results and the test results presented in Chapter 8 showed that this numerical column model, which can generally yield reasonably accurate but conservative results for moment-curvature, monotonic pushover and hysteretic responses, is

sufficiently accurate for predicting the seismic behavior of hybrid DSTCs.

9.5 FUTURE RESEARCH

While the research presented in this this thesis has greatly advanced our understanding of the cyclic/seismic behavior of hybrid DSTCs and our ability to model this behavior, much further research is still needed on these columns before complete confidence is gained in the practical implementation of these columns. Some of the issues that need further research are detailed below:

- (1) Further research is needed to clarify the mechanism behind the sudden axial load drop observed in some of the column specimens tested under axial compression. A theoretical model for these columns that can account for this phenomenon should also be developed;
- (2) Hybrid DSTCs of other section forms (i.e. with non-circular sections for either the outer FRP tube or the inner steel tube) should be studied for reasons of aesthetics or mechanical resistance;
- (3) Buckling of the inner steel tube in hybrid DSTCs needs to be well understood so that a limit on the steel tube diameter-to-thickness ratio can be established to avoid significant local buckling deformations that may degrade column performance;
- (4) The durability of hybrid DSTCs (i.e. the durability of the outer FRP tube and the column as a whole) in severe environments should be studied to demonstrate/confirm the excellent long-term performance of hybrid DSTCs; and
- (5) Reliable construction details (e.g., connections between hybrid DSTCs and beams, and connections between hybrid DSTCs and footings) should be devised and studied for practical implementation.

9.6 REFERENCES

- Lam, L. and Teng, J. G. (2009). “Stress-strain model for FRP-confined concrete under cyclic axial compression”, *Engineering Structures*, 31(2), 308-321.
- OpenSees. (2009). *Open System for Earthquake Engineering Simulation*, Pacific Earthquake Engineering Research Center, University of California, Berkeley, <http://opensees.berkeley.edu>.
- Teng, J. G., Jiang, T., Lam, L. and Luo, Y. Z. (2009). “Refinement of a design-oriented stress-strain model for FRP-confined concrete”, *Journal of Composites for Construction*, ASCE, 13(4), 269-278.
- Yu, T., Teng, J.G. and Wong, Y.L. (2010). “Stress-strain behavior of concrete in hybrid double-skin tubular columns”, *Journal of Structural Engineering*, ASCE, 136(4), 379-389.